Chasing the Brightest Cosmic Explosions with ROTSE-III

by

Fang Yuan

A dissertation submitted in partial fulfillment
of the requirements for the degree of
Doctor of Philosophy
(Physics)
in The University of Michigan
2010

Doctoral Committee:

Professor Carl W. Akerlof, Chair
Professor Fred Adams
Professor Timothy A. McKay
Professor Bing Zhou
Assistant Professor Jon M. Miller

To my family

ACKNOWLEDGEMENTS

First of all, I can never express my gratitude enough to Carl Akerlof, who has taught me so much in and beyond the field of physics. Carl's wonderful mentoring has made my PhD study such an enjoyable experience.

As a proud member of the ROTSE group, I am grateful to all these brilliant people, Eli Rykoff, Tim McKay, Heather Flewelling, Sarah Yost, Wiphu Rujopakarn, Don Smith and many more, that have worked with ROTSE and have made it such a superb instrument and fun project to work with. It has been a great pleasure to work with the friendly and capable observatory staffs, in particular David Doss, Toni Hanke, Tuncay Özışık and Andre Phillips.

A critical part of this thesis has been made possible through collaboration with an excellent group of researchers in the University of Texas. It all began with the ingenious idea of Robert Quimby, from whom I have gained invaluable technical and mental support when starting RSVP. I am indebted to Craig Wheeler for all the wise insights and generous encouragement. I also thank Jozsef Vinko for all the kindly help. The success of RSVP has relied on the efforts from many undergraduates, including Jamie Aretakis, Dan Chamarro, Matt Sisson and Amelia Uecker.

I would like to acknowledge Weikang Zheng and Shashi Pandy for taking graceful care of ROTSE when I am busy finishing up this thesis.

I wish to thank my parents for their unconditional love and support that make me feel safe and connected whatever I do wherever I am. Finally, thank you Qiaoqiao for making me a very happy person.

Part of chapter 3 of this thesis is accepted for publication in the Astrophysical Journal. Part of chapter 4 is based on Yuan & Akerlof (2008). Part of chapter 5 has been submitted to the Astrophysical Journal.

TABLE OF CONTENTS

LIST OF FIGURES

Figure

LIST OF TABLES

Table

LIST OF ABBREVIATIONS

ROTSE the Robotic Optical Transient Search Experiment

GRB Gamma-Ray Burst

SN SuperNova

CC Core Collapse

GCN the GRB Coordinates Network

CGRO the Compton Gamma-Ray Observer

BASTE the Burst And Transient Source Experiment

EGRET the Energetic Gamma Ray Experiment Telescope

HETE the High Energy Transient Explorer

BAT the Burst Alert Telescope

XRT the X-ray Telescope

UVOT the UV/Optical Telescope

FGST the Fermi Gamma-ray Space Telescope

LAT the Large Area Telescope

GROND the Gamma-Ray Burst Optical/NearInfrared Detector

HET the Hobby-Eberly Telescope

PSF Point Spread Function

FWHM Full Width at Half Maximum

SED Spectral Energy Distribution

MW the Milky Way

LMC the Large Magellanic Cloud

SMC the Small Magellanic Cloud

IGM Inter-Galactic Medium

CSM Circum-Stellar Medium

RSVP the ROTSE Supernova Verification Project

TSS the Texas Supernova Search

LOSS the Lick Observatory Supernova Search

SNfactory the Nearby Supernova Factory

SCP the Supernova Cosmology Project

SDSS the Sloan Digital Sky Survey

NED the NASA/IPAC Extragalactic Database

CBET the Central Bureau for Astronomical Telegrams

ATEL the Astronomer's Telegram

ABSTRACT

Gamma-ray bursts (GRBs) and supernovae (SNe) are two of the most spectacular types of cosmic explosions in the transient sky. Both phenomena are associated with the death of massive stars or disruption of compact objects. Our knowledge of these events is thus closely related to the understanding of stellar evolution across the universe. These energetic events are also used as probes of the ionization and star formation history and powerful tools to measure the cosmic expansion.

This thesis presents the follow-up observations of GRBs and the discoveries of SNe by the ROTSE-III robotic optical systems. With automated operation and fast slewing, ROTSE-III has made unique contributions to the study of GRBs by providing very early optical observations. A large fraction of ROTSE-III's burst responses started during the gamma-ray emission phase. These "prompt" optical detections and limits are invaluable for constraining the burst properties and the immediate environment surrounding the progenitor. I discuss examples of multi-wavelength studies of GRBs with an emphasize on the transition phase from the burst to the afterglow.

The ROTSE Supernova Verification Project (RSVP) is an extension of the effort initiated by the Texas Supernova Search (TSS). By scanning a large portion of the sky nightly without bias towards bright galaxies, RSVP discovered over 40 SNe in about

two years and a relatively large fraction of peculiar events. Among these, two SNe, 2008am and 2008es, belong to the ultra-luminous type that was not known before TSS and one event, 2007if, was an over-luminous Type Ia SN and a candidate for a super-Chandrasekhar mass explosion. With ROTSE-III, we hope to discover and monitor more ultra-luminous SNe to understand their extraordinary energy output, whether they are powered by ejecta-circumstellar medium interactions or thermonuclear reactions triggered by pair instability. In the case of SNe Ia, it is not likely that a single parameter, e.g. the amount of radioactive nickel produced, is able to account for their diversity. Circumstellar medium interaction, as a probable source of excess luminosity, is investigated.

CHAPTER I

Introduction

The Robotic Optical Transient Search Experiment (ROTSE-III) is a set a four 45 cm fully robotic optical telescopes, installed at Siding Spring Observatory, Australia (ROTSE-IIIa), McDonald Observatory, Texas (ROTSE-IIIb), H.E.S.S. site, Namibia (ROTSE-IIIc) and TUBITAK National Observatory, Turkey (ROTSE-IIId) (see Akerlof et al., 2003, for a detailed description of the project). The main goal of the project is to rapidly follow-up gamma-ray bursts (GRBs). Thus, they are designed to operate fully automatically and with the ability to slew to any location on the sky in typically 5 to 7 seconds. With its combination of sensitivity and fast response, ROTSE-III has made critical contributions to the study of GRBs by obtaining a unique set of very early optical observations probing the region close to the central engine. In the first part of this thesis, I will present the ROTSE-III observations of GRBs and discuss how these observations, along with detections in other wavelengths, have helped us to better understand the phenomena of GRBs.

The second part of my thesis work is the ROTSE Supernova Verification Project (RSVP). The world-wide coverage provided by the four telescopes has ensured that at least one ROTSE-III site is dark at any time of the day. This has greatly increased the chance of observation for GRBs occurring at random times and random locations.

Even so, GRBs are relatively rare and the detections of GRBs rely on satellite missions with finite fields of view. During operation, ROTSE-III telescopes survey the sky and observe lists of selected targets for the collaborators while GRBs take instant priority over any other ongoing observations.

Although the project is led by the group in Michigan, operation of ROTSE-III is made possible by the kind support from local institutes. As partial compensation, each host is allocated 30% of telescope time for discretion. The remaining 70% is used by the ROTSE collaboration, mostly for transient surveys, and, upon request, is available for specific targets proposed by collaboration members.

To carry out efficient surveys, ROTSE-III is designed to have a large, $1.85^\circ \times 1.85^\circ$, field-of-view. The first survey that took advantage of this feature was the search for "orphan" GRB afterglows, i. e. the optical counterparts to off-axis GRBs (Rykoff et al., 2005a). A byproduct of this search was the discovery of several supernovae and cataclysmic variables.

ROTSE-III telescopes were not initially contemplated as ideal instruments for discovering supernovae partly because their coarse pixel scale ($3.3''$) would blend supernovae events with the light from their galactic hosts. Robert Quimby, as a graduate student at University of Texas, Austin, nevertheless, made this attempt using the ROTSE-IIIb discretionary telescope time and achieved remarkable success (Quimby, 2006). With a carefully designed image subtraction pipeline, he not only discovered over 30 supernovae during the two and half years of operation, but also unexpectedly uncovered the brightest supernovae ever observed (Quimby et al., 2007e; Ofek et al., 2007) and a new category of ultra-bright events. After his graduation, we decided to continue this fruitful effort and extend this search to all four telescopes.

A new image subtraction software was developed to work with the under-sampled

ROTSE-III images. A new transient search pipeline was installed on a dedicated computer at each of the telescope sites. Between August 2007 and September 2009, RSVP discovered about 40 new SNe, including two of the most luminous events and one ultra-luminous Type Ia supernova, 2007if. As a third candidate for a SN Ia exploding beyond the Chandrasekhar mass limit, SN 2007if provides us a valuable chance to explore the diversity of Type Ia SNe. A detailed discussion of its characteristics will be presented in this thesis.

ROTSE-III systems are running unfiltered to maximize the detection sensitivity. In the study of GRBs, observations are compared across the electromagnetic spectrum, spanning up to 15 decades of frequency. Sensitivity is thus preferable over spectral resolution. Indeed, GRBs are energetic probes to the early universe and ROTSE-III's wide response range extending to near infra-red has enabled it to detect bright afterglows above redshift 5. This sensitivity also helps in detecting supernovae at early times. The tradeoff is that comparison of supernovae lightcurves to measurements in standard filters becomes less straightforward.

In the following chapters, I will start with a brief review of the GRB phenomenon and theories in Chapter 2, emphasizing the progress since the launch of the Swift mission. A selected sample of early ROTSE-III observations of GRBs during year 2007 and 2008 will be presented in Chapter 3, together with Swift multi-wavelength observations. The background and design of the ROTSE Supernova Verification Project (RSVP) will be described in Chapter 4. This discussion is followed by RSVP discoveries and observations of supernovae in Chapter 5. Finally, conclusions are drawn and future perspectives are outlined in Chapter 6.

CHAPTER II

GRB and the Fireball Model

2.1 Introduction

Gamma-ray bursts are among the most energetic explosions in the universe. These short and intense flashes of gamma-rays were discovered unexpectedly in the late 1960s by the US Vela satellites (Klebesadel et al., 1973) which were designed to detect nuclear explosions in space. In the next several decades, little information was obtained to support or reject the hundreds of theoretical models proposed including the popular belief of association with neutron stars. This situtation was changed by the launch of the Compton Gamma-Ray Observer (CGRO) in 1991 (Fishman et al., 1993). During the ten years of operation, its Burst And Transient Source Experiment (BATSE) instrument detected more than 2700 bursts. The resulting GRB catalog (Paciesas et al., 1999) remains the largest sample available for statistical studies. Early BATSE observations revealed a uniform distribution of GRBs over the entire sky contradicting the expectation from a local galactic population. But the cosmological origin of the bursts was not confirmed until the detections of X-ray and optical afterglows another few years later. The first optical afterglow detection was obtained for GRB 970228 thanks to the precise localization by the Italian-Dutch BeppoSAX satellite. The first redshift measurement followed for the afterglow of GRB 970508.

Its redshift of 0.835 became direct evidence that the GRBs are extra-galactic. Since then, great progress has been made towards understanding the phenomenon from studying the multi-wavelength emissions, sometimes extending to radio. Table 2.1 lists the major satellite missions that have contributed to GRB detections in the last two decades.

In particular, the *Swift* mission (Gehrels et al., 2004), launched in 2004, has revolutionized the field of GRB study in the last 5 years. Its wide-field hard X-ray survey instrument, BAT, localizes bursts to within $3'$ and distributes the coordinates with a delay comparable to the typical duration of long GRBs. This capability has enabled ground-based robotic systems, such as ROTSE-III, to start imaging the field during the burst or shortly after its cessation. *Swift* also has a fast slewing ability to repoint its narrow field X-ray Telescope (XRT) and UV/Optical Telescope (UVOT) in $\sim$ 70 sec. Besides revealing interesting features themselves, detections by these instruments with few-arcsec resolutions allow large ground-based systems to react quickly and obtain deeper follow-ups and spectroscopic observations at the earliest possible time.

The pre-*Swift* understandings of GRBs, including phenomelogy and the popular

Table 2.1. GRB satellite missions

Satellite/ Instrument	Operation Period	Field of View	Energy Range	Error Radius	Trigger Delay	Detection Rate
CGRO/BATSE	1991-2000	full sky	20-2000 keV	4°	5s	1/day
Beppo-Sax/WFC	1996-2002	0.1 Sr	2-30 keV	$5'$	2-5hr	10/yr
HETE-2/WXM	2000-2006	2 Sr	2-25 keV	$10'$	10-5h	1/month
INTEGRAL	2002-2012*	0.25 Sr	15 keV-10 MeV	$3'$	1min-3hr	1/month
Swift/BAT	2004-2012*	1.4 Sr	15-150 keV	$3'$	13-30s	2/week
FGST/GBM	2008-2018†	8 Sr	8 keV-40 MeV	10°	10-300s	20/month
FGST/LAT	2008-2018†	2 Sr	20 MeV-100 GeV	$20'$	2-32s	5/yr

*currently supported to

†planned to

theoretical model, the so-called fireball model, are presented in §2.2 and §2.3. New discoveries and recent progress in the *Swift*-era are presented in §2.4.

2.2 Pre-*Swift* Phenomenology

2.2.1 Prompt Burst Emission

Our knowledge about the burst emission in gamma-rays is mostly from the CGRO/ BATSE observations. The GRB lightcurves (i.e. light intensities as functions of time) show rapid variations on milisecond to second time-scales. The emission, lasting from less than 1 ms to over 1000 sec, is composed of one, several or many pulses with complex temporal structures that may reflect the geometry of the emitting regions. The duration (usually defined as T90, the time during which 90% of the counts are detected above the background) of GRBs have a bimodal distribution. The short ones lasting less than about 2 seconds tend to have harder spectra (Kouveliotou et al., 1993). These bursts, named short hard GRBs, are likely a different catagory of events, distinct from the long GRBs. Given the difficulty of observing short GRBs in longer wavelengths, our later discussion will mostly focus on long GRBs.

BATSE responded to an energy range of 20 to 2000 keV. Within this range, the observed spectra are non-thermal and can usually be fit by an exponentially damped broken power-law model (Band et al., 1993, the Band function,), where the typical low energy power-law index α $\sim$-1, the typical high energy power-law index β $\sim$-2.3 and the break energy $\sim$200 keV(Preece et al., 2000). Notice that the distribution of the high energy power-law index has a significant tail harder than -2. For these events, a spectral cut-off at high energy is required to avoid the unphysical prediction of an unbounded fluence.

2.2.2 Afterglow

Observations of the afterglow emission in longer wavelengths typically started hours after the burst for Beppo-Sax triggers because of instrument limitations. These observations usually showed decaying lightcurves characterized by single or broken power-laws in both optical and X-rays. The introduction of a fast coordinate distribution system (BACODINE, later renamed GCN, Barthelmy et al., 1998) and the subsequent development of moderate-sized robotic telescopes have enabled earlier optical follow-ups for BATSE and HETE-2 triggers. In 1999, ROTSE-I detected a bright optical flash during but not correlated with gamma-rays for GRB 090123 (Akerlof et al., 1999). In the next few years, a handful of optical observations were obtained starting within a few minutes from the bursts. These early observations showed deviation from simple power-law decay, and sometimes even an early rise. Hints of optical flashes were also observed, but never as spectacular as that for GRB 090123.

2.2.3 SNe Association

Observational evidence associating a GRB with a supernova was first reported for GRB 980425/SN 1998bw (Galama et al., 1998). Further associations were suggested when a red bump was observed in the optical afterglow lightcurves of several GRBs (e.g. GRB 980326, Bloom et al., 1999 and GRB 011121, Bloom et al., 2002b; Garnavich et al., 2003). The first unambiguous spectroscopic identification was obtained for GRB 030329/SN 2003dh (Stanek et al., 2003). The associations with the broad-lined core-collapse SNe provide strong evidence that most long-duration GRBs originate from massive stellar explosions. Woosley & Bloom (2006) present an excellent review on this subject.

2.3 The Fireball Model

The most popular model to date, explaining the basic properties of GRBs, is the so-called fireball model (Paczyński, 1986; Goodman, 1986 and see Piran, 1999, 2004; Meszaros, 2006 for comprehensive reviews). In this model, the central engine ejects multiple shells at ultra-relativistic speed. The shells, with different Lorenz factors, collide with each other, producing the intense and highly variable prompt gamma-ray emission. At a significant distance from the central engine, the ejecta runs into the external medium and the external shocks produce the long-lasting afterglow emission in wavelengths spanning from X-ray to radio.

2.3.1 Relativistic Outflow

Highly relativistic motion is required as a solution to the compactness problem, inferred by the small region for emission indicated by the short-time-scale variablity of the prompt lightcurves. The optical depth estimated for gamma-ray photons will be extremely large due to pair production and contradicts the non-thermal spectra observed. This apparent discrepancy is resolved if the source of radiation is moving towards an observer with a relativistic velocity characterized by a Lorentz factor, γ $>\sim$100. In the co-moving frame of the source, the photon energy is lowered by a factor of γ, quenching the pair-production process. Relativistic effects also allow the radius of the emission region to be γ^2 larger.

2.3.2 Emission Mechanisms

The most likely radiation process in GRBs is synchrotron emission. The emission is determined by the photon energy distribution and the micro-physical parameters, ϵ_B and ϵ_e, the fractions of shock energy in magnetic fields and relativistic electrons. For a power-law electron distribution with a power index p and a minimal Lorentz

factor $\gamma_{e,min}$, the integrated synchrotron spectrum can be described by piece-wise power-laws joined by three break frequencies, the cooling frequency (ν_c), the characteristic synchrotron frequency (ν_m) and the self-absorption frequency (ν_a) (e.g. Sari & Piran, 1999; Granot & Sari, 2002). All three frequencies evolve over time and the lightcurve observed at any specific wave-length decays as power-laws with temporal breaks occurring when the break frequencies pass through the spectral observation window. In general, this predicted behavior agrees with the afterglow observations in the pre-*Swift* era. In particular, the model predicts relationships between the temporal and spectral indices, α and β (see Racusin et al., 2009, and references therein for the "closure relations" in a number of possible scenarios).

Inverse Compton (IC) scattering can potentially modify the spectral shape. At high energy range, the up-scattered photons may dominate the emission. At the typical observed energy, IC provides an additional cooling process and reduces the radiation efficiency. The effect of IC scattering is not yet directly confirmed by observation, altough it is hard to understand the GeV emission without it.

2.3.3 Jets

The typical total energy release of a gamma-ray burst is in the order of 10^{54} erg, assuming isotropic emission. This energy is equivalent to the entire mass of the sun and 100 times higher than the nuclear energy release from burning one solar mass of hydrogen to iron. This is also three orders of magnitude higher than a supernova detected over weeks to months. Rather than a significant energy budget, an alternative explanation is that the emission is concentrated in a jet with a small opening angle (e.g. Frail et al., 2001; Bloom et al., 2003). Bipolar jets powered by accretion disks around black holes have been directly observed in AGNs (e.g. Schwartz et al., 2000), and are thus reasonable assumptions for GRBs where similar relativistic

process may be involved.

Achromatic steepening of the lightcurve is considered evidence for collimated ejecta in GRBs. Such "jet break" is likely produced by two effects. First, radiation from relativistically moving ejecta is beamed in the direction of the motion to within an angle $1/\gamma$. As the ejecta decelerates, the beaming angle increases and eventually exceeds the actual jet opening angle, causing a sudden increase in the flux decay rate. At about the same time, sideways expansion of the ejecta becomes significant (e.g. Sari et al., 1999). Both effects are geometrical and do not have energy dependence. Achromatic jet breaks have been observed in optical/near-infrared for a few pre-*Swift* GRBs (e.g. Kulkarni et al., 1999; Harrison et al., 2001; Klose et al., 2004). The typical jet opening half-angles inferred from lightcurve steepening range from a few to a few tens of degrees, resulting in tightly clustered corrected total energy release around 10^{51} erg (Frail et al., 2001; Bloom et al., 2003).

2.3.4 Very High Energy Emission

A handful of GRBs were observed above a few tens of MeV by the Energetic Gamma Ray Experiment Telescope (EGRET) as a part of Compton Gamma-ray Observatory. Dingus (2001) reported four cases of high-energy detections. Among them, GRB 940217 is an exceptional case. Emission as high as 20 GeV was recorded for this burst 4500s after the end of BATSE detected emission. Later, for GRB 941017, González et al. (2003) discovered a high energy component contemporaneous with the prompt emission but extending up to 200 MeV. This component did not follow the temporal behavior of the lower energy gamma-rays. In about 100 s from the trigger, the hundreds KeV gamma-ray emission of GRB 941017 decayed by three orders of magnitude while the hundreds MeV flux stayed roughly constant.

Low significance excesses at high energies beyond the GRB durations measured

by BATSE were noticed for a few bursts (Dingus, 2001), but it is hard to determine the duration of the very high energy emission with such limited statistics. Dingus (2001) showed that the four bursts detected by EGRET turned out to be among the brightest bursts in its field-of-view as determined by BATSE. Therefore the question arises as to whether all GRBs have high energy emission during the prompt phase and most of them are just too weak to be detected by EGRET. The spectra of the bursts detected by EGRET posed a question about the radiation mechanism as they showed no indication of deviations from power laws up to energies of 10 GeV.

The nature of the high energy emission is closely related to the intrinsic character of the bursts and their relation with other astrophysical events. The high energy observations alone, however, are hard to explain. Within the scope of the fireball model, the very high energy emission was suggested to be from the very early afterglow (Granot & Guetta, 2003; Pe'er & Waxman, 2004). This emission is generally considered to be due to inverse Compton scattering but there is no agreement on the origins of the background photons and the energetic electrons. Several combinations yield the right energy range, including SSC emission from the reverse shocks (Granot & Guetta, 2003), IC scattering of the self-absorbed synchrotron photons of the reverse shocks by the electrons in the forward shocks (Pe'er & Waxman, 2004) and IC scattering of the hundreds of keV emission by the electrons in the reverse shock at the fireball deceleration radius (Beloborodov, 2005).

Very early optical observations appear to be one of the keys to constrain the explosion parameters and differentiate the above models. It is noticed that different scenarios accounting for the high-energy component, as well as different model parameters in a given scenario, lead to different predictions for the fluxes at optical bands (Pe'er & Waxman, 2004). Some models predict very high energy radiation

accompanied by optical emission while others predict suppression in optical band during very high energy activity (Wang et al., 2005). Unfortunately, the EGRET high energy data had no simultaneous low energy observations.

2.4 The *Swift*-era

2.4.1 Bursts Statistics

Because of the lower energy coverage (15-150 KeV) of *Swift*/BAT than BATSE (20-2000 KeV), comparison of the burst populations are not straightforward. The short and long duration groups are identified in the *Swift* bursts (Lin, 2009, but see also Horváth et al., 2008; Huja et al., 2009 for the existence of an intermediate group). The fraction of short bursts, about 10%, detected by *Swift* is lower than the 25% detected by BATSE, due to the softer energy coverage and image trigger algorithm (see Gehrels et al., 2009, for a summary of *Swift* observations). With a higher sensitivity and the ability to trigger rapid afterglow follow-up with good localization, *Swift* has been detecting GRBs at a higher average redshift ($\langle z \rangle \sim 2.5$) than the earlier missions ($\langle z \rangle \sim 1.2$) (Le & Dermer, 2007; Gehrels et al., 2009).

The basic burst characteristics, e.g. distribution of hardness ratio, fluence and isotropic-equivalent energy release, appear to be consistent for *Swift* and pre-*Swift* events (Lin, 2009). For the various correlations between the burst temporal and spectral parameters, especially the E_{peak}-E_{iso} relation (initially found by Amati et al., 2002, for BeppoSAX events), no significant difference has been found for *Swift* and pre-*Swift* populations (Cabrera et al., 2007; Nava et al., 2008; Ghirlanda et al., 2008; Krimm et al., 2009).

2.4.2 Canonical X-ray Lightcurves

Observations obtained by the Swift/XRT has made revolutionary contributions to the studies of GRBs. More than 95% of the *Swift* GRBs have been detected in the X-rays. A canonical X-ray lightcurve (Nousek et al., 2006; Zhang et al., 2006; O'Brien et al., 2006) starts with a rapidly decaying phase that is too steep to be explained by the standard external blast wave model. This phase is often followed by a slowly decaying period, shallower than expected from the same external shock model. Only after this, the lightcurves show the normal decay and sometimes a late break, often interpreted as a jet break (see e.g. Willingale et al., 2007; Liang et al., 2008; Racusin et al., 2009; Evans et al., 2009), as observed for the pre-*Swift* bursts.

Another common but unexpected phenomena are the X-ray flares (Chincarini et al., 2007; Falcone et al., 2007) superimposed on the smoothly decaying segments observed for about half of the bursts. Their short time-scale variability is hard to produce externally at a large distance from the progenitor.

All the above features, perhaps explained by the delayed large angle internal emission (e.g. Kumar & Panaitescu, 2000; Liang et al., 2006; Zhang et al., 2007), continuous injection of energy (e.g. Rees & Meszaros, 1998; Sari & Mészáros, 2000; Zhang et al., 2006; Liang et al., 2007), delayed internal shocks or central engine activity (Chincarini et al., 2007; Falcone et al., 2007; Krühler et al., 2009, and references therein), suggest associations with central engine properties. It is likely that the central engine is active for much longer than previously believed.

2.4.3 Very Early Optical Observations

At optical wavelengths, an initial rising optical counterpart is detected for a significant fraction of bursts (Molinari et al., 2007; Panaitescu & Vestrand, 2008; Oates

et al., 2009; Klotz et al., 2009; Rykoff et al., 2009; Krühler et al., 2009; Greiner et al., 2009b; Guidorzi et al., 2009). The temporal behaviors generally agree with predictions of the fireball forward shock model (Sari & Piran, 1999; Meszaros, 2006) before the onset of the shock deceleration. In such a scenario, the peak time can be used to determine the Lorentz factor of the shock at the deceleration radius (Molinari et al., 2007). The estimated Lorentz factors of a few hundred (Molinari et al., 2007; Oates et al., 2009; Rykoff et al., 2009) agree in order of magnitude to the constraints from the prompt emission.

Alternatively, a rising afterglow can be attributed to emission in a collimated afterglow, viewed from outside the initial jet opening angle, when the shock decelerates and the relativistic beaming angle widens (Panaitescu & Vestrand, 2008). A variety of lightcurve shapes, including ones with a wide peak or plateau phase, can be accommodated in this model by combination of the jet geometry and the viewing angle. Such signature of early external shock emission is not observed in X-ray, because the accompanying X-ray emission is likely obscured by the dominating internal emission. Optical observations thus provide important clues about the onset of the afterglow because emission from the external shock appears to dominate the optical emission from early times.

During the burst, optical flares apparently correlated with the hard X-ray emission are observed for several events (Vestrand et al., 2005, 2006; Page et al., 2007; Yuan et al., 2008w). High time-resolution data plays a key role in studying the real correlation between the low and high energy emission. Such observations in optical, however, are only feasible for either a once-in-a-decade event, like the "naked eye" burst GRB 080319B (Racusin et al., 2008c), which was bright enough to be detected by a surveying very-wide-field optical instrument, or a bright burst lasting

long enough in a usual follow-up scenario (including when the *Swift*/BAT is triggered by a pre-cursor). For GRB 080319B, the extraordinary optical luminosity is orders of magnitude higher than extrapolation from the high energy spectra, implying a separate emission component. While the compatible timescales of the resolved pulses in optical and high energy point to a common origin, the varying phase offset between the different energy bands imply a possibility that they are produced by related but different mechanisms (Kumar & Narayan, 2009). We have yet to see if more bursts with typical energetics follow this behavior.

For a number of other events, an optical flare unrelated to the high energy emission is detected (e.g. Akerlof et al., 1999) or a monotonic decaying transient is observed at a flux level consistent with back-extrapolation from later observations (e.g. Rykoff et al., 2005b). These provide evidence that, at least in some cases, emission from the external shock dominates the prompt optical observations. Such diverse behaviors suggest that both internal and external shock emission may contribute to the prompt optical detections but their relative strengths vary from event to event. The identification of optical emission from the same origin as the gamma-ray emission puts considerable leverage on constraining the burst emission mechanism, but it is not always easy to separate the different components with limited understanding of neither the internal nor the early external emission.

2.4.4 Missing Jet Breaks?

An important signature of collimated outflows from GRBs is the achromatic steepening of lightcurves occurring when the relativistic beaming angle becomes comparable to the jet opening angle. Such "jet breaks" have been observed in optical in the pre-*Swift* era and are expected to manifest in the X-ray lightcurves detected by *Swift* along with the optical observations. However, there seems to be an apparent lack of

jet breaks in the *Swift* bursts. Only about 20% of the X-ray lightcurves display a post-jet-break decay, while for about half of the other events, observations terminated before the expected jet break time (Gehrels et al., 2009).

Studies in the X-ray regime have suggested modifications to the conventional models, e.g. energy injection across the break, and the existence of hidden breaks (Racusin et al., 2009). But when both X-ray and optical observations are considered, even fewer events show achromatic breaks (Liang et al., 2008). To explain the chromatic behavior, it has been proposed that the jet-break can be obscured or delayed by an additional IC scattering component in the X-ray band (Chandra et al., 2008). For most of the cases, a probable explanation for the missing jet breaks is that they may be occurring at late times and faint flux levels for typical *Swift* bursts and thus are hard to detect by standard ground- and space-based campaigns.

For identified jet-breaks or limits, somewhat smaller jet opening angles and lower collimated energy release are inferred compared to the pre-*Swift* sample (Racusin et al., 2009). Some of these effects might be attributed to the lower energy coverage and superior sensitivity of the Swift/BAT.

Several events stand out as their lightcurves show no deviation from single power-law decay across the entire expected jet break time window. For example, a well-sampled steep decay ($\alpha \sim 1.7$) is observed for GRB 061007 in the optical and X-rays from 80 s after the burst to 11 days later when the afterglow dropped below the detection threshold of XRT (Schady et al., 2007). For this energetic event, either an excessively large kinetic energy ($> 10^{54}$ erg) is required or the outflow is highly collimated ($\theta_j < 0.8^{\circ}$).

2.4.5 High Redshift Bursts

Besides detecting bursts at a high average redshift, *Swift* has seen 6 GRBs spectroscopically identified beyond redshift 5. The record-holder GRB at redshift ∼8.2 (Tanvir et al., 2009; Salvaterra et al., 2009), occurred when the universe was only about five percent of its current age and is more distant than any known galaxy (Iye et al., 2006) or quasar (Willott et al., 2003). The extreme brightness of GRBs and their afterglows allow them to be detectable out to redshift ∼10, making them potential tools to explore the early universe. For example, they can be powerful probes of the intergalactic medium (IGM) up to the re-ionization epoch (e.g. Kawai et al., 2006; Tanvir et al., 2009). Given their association with the death of massive stars, GRBs are also promising tracers of star formation history (e.g. Bromm & Loeb, 2006; Fynbo et al., 2006a), even if they might be biased against dust regions or towards low metallicity (e.g. Modjaz et al., 2008).

ROTSE-III's broad response curve has enabled it to detect the bright afterglow of GRB 060927 at z = 5.47. If the burst population at high redshift is similar to that at low redshift, fainter afterglows from distant GRBs would be expected and they would be hard to observe in optical (because of the Lyman-alpha break) before decaying. Although the fraction of optically faint GRBs from high redshift is not likely high (probably a few percent in the *Swift* sample while most of the "dark" bursts may result from local dust extinction, e.g. Grupe et al., 2007; Ruiz-Velasco et al., 2007; Perley et al., 2009), their detections bear high cosmological significance. Robotic infrared/near-infrared instruments that can respond to *Swift* triggers in a short time scale are essential for distinguishing these faint afterglows due to distance.

2.4.6 Host

Host detections have not only helped to establish redshift measurements for GRBs but also provided important clues to the nature of their progenitors. Associations with blue galaxies and active star forming regions have confirmed the connection between long soft GRBs and the very massive stars (e.g Bloom et al., 2002a; Fruchter et al., 2006). Meanwhile, detections of short GRBs in elliptical galaxies (Gehrels et al., 2005; Berger et al., 2005; Bloom et al., 2006) are consistent with the expectation that they are from mergers of compact objects (neutron star-neutron star or neutron star-black hole).

While redshift is directly measured for only a small fraction of GRBs, most of the host identifications rely solely on their alignment with GRB locations in a two-dimensional space (especially for the short GRBs). This poses a potential problem of chance superposition. For an optical afterglow identified with a precision of less than $1''$, the probability of chance alignment is reasonably small ($\sim$1%, Bloom et al., 2002a; Cobb & Bailyn, 2008) and should not alter the results of statistical studies of the host properties. However, caution should be taken when studying individual event or a small sample. Besides, this chance is dramatically increased when only X-ray afterglow localization is available with an accuracy of about $2''$ (Cobb & Bailyn, 2008).

2.4.7 Progenitor

The two types of probable progenitors, core collapse of massive stars and compact binary mergers, naturally produce two categories of GRBs. In a collapsar model, the fallback timescale is 10s of seconds (MacFadyen & Woosley, 1999). In a compact merger, the typical accretion timescale is 0.01-0.1 s (Aloy et al., 2005). These pre-

dicted durations support the classification of long and short GRBs. However, such a purely phenomenological division is highly dependent on the detector response and sensitivity and blurred by the detections of intermediate cases.

In particular, a number of well-observed bursts discovered by *Swift* appear controversial. For example, GRB 060614, a long-duration burst (T_{90} ∼100) at redshift 0.125, does not reveal a underlying SN to deep limits (Gehrels et al., 2006; Fynbo et al., 2006b; Della Valle et al., 2006; Gal-Yam et al., 2006). Its lightcurve started with a short/hard spike that resembles a typical short/hard burst. It is likely that GRB 060614 is associated with a compact merger event, with extended soft emissions that sometimes seen in short/hard GRBs.

Furthermore, the original classification was based on properties in the observer's frame. A relatively short burst occurring at a high redshift will appear stretched and softened. Two remarkable examples are GRB 080913 at z=6.7 (Greiner et al., 2009a) and GRB 090423 at z=8.2 (Tanvir et al., 2009; Salvaterra et al., 2009), the farthest GRBs detected so far. They would both have hard spectra and last shorter than 2 s in their rest frame or if observed at a much lower redshift. When additional criteria are investigated, their prompt emission characteristics and afterglow properties are statistically consistent with being in the long category (Greiner et al., 2009a; Zhang et al., 2009). Additionally, the detection of two such events contradicts the low expected rate of bright mergers at the distance (Zhang et al., 2009). If they are indeed associated with death of massive stars, it is not yet clear whether they represent an intrinsic trend of short duration core collapse events at high z.

Above all, the controversy reflects our incomplete understanding of the link between the observational properties and their physical origin, especially for the short/hard GRBs.

CHAPTER III

Observations of GRBs by ROTSE-III

3.1 Introduction

GRBs localized by satellites are telemetered to the ground and distributed through the GRB Coordinates Network (GCN). Upon receiving such notice, a ROTSE-III telescope or a similar robotic instrument will determine whether it is able to follow-up the burst immediately based on the target location and site condition. The fast and precise localizations of gamma-ray bursts (GRBs) provided by the *Swift*/BAT (Gehrels et al., 2004) in hard X-rays have enabled follow-up observations in longer wavelengths during the burst or shortly after its cessation for an increasing number of events. These observations, both from ground and from the narrow-field instruments onboard *Swift*, have revealed features that were not observed in the pre-*Swift* era.

By end of August 2009, ROTSE-III has responded to over 100 *Swift* bursts ($\sim$1/3 of the triggers). Optical counterparts were detected in $\sim$30% of the responses. For 22 bursts, optical emission was detected during the prompt burst phase, while a similar number of prompt optical limits were obtained.

In this chapter, multi-wavelength studies of selected GRBs are presented. In §3.2, GRB 081008 provides a good example of a well-observed GRB studied in both temporal and spectral domain. ROTSE-III and early *Swift* observations for another 10

individual events are summarized in §3.3. The general behavior of these selected GRBs is discussed in §3.4. Throughout the chapter, we adopt the convention that the flux density can be described as $f_\nu \propto t^{-\alpha}\nu^{-\beta}$, where α and β are the corresponding temporal and spectral power-law indices. Note that a negative α represents a rising lightcurve while a positive β, equal to the photon index minus one, corresponds to a spectrum that falls with increasing energy. We assume a standard cosmology model with the Hubble parameter H_0=70 km s^{-1} Mpc^{-1} and the density parameters Ω_m=0.3, Ω_Λ=0.7. All quoted errors are 1-sigma (68% confidence), unless otherwise stated.

3.2 GRB 081008: from Burst to Afterglow and the Transition Phase in Between

GRB 081008 is a typical long-lasting burst detected by *Swift*/BAT that provides a rare opportunity to study the optical characteristics during the prompt phase. ROTSE-IIIc started imaging only 42 s after the burst trigger and before the second epoch of major γ-ray emission. An initially rising optical transient was observed, followed by two peaks, the latter coincident with a gamma-ray peak. *Swift* slewed immediately, and the XRT and the UVOT started observing during the second optical peak, providing well-sampled data at early times and following the event until it dropped below the detection threshold (see Figure 3.1). At about 13 ks after the burst, GROND started observing the afterglow in its 7 optical/IR channels. The excellent energy coverage from IR to X-ray allows us to model the spectral energy distribution with an intrinsic broken power-law, although the evolution of the spectral shape is not restricted. The overall behavior of the observed afterglow is consistent with being achromatic, while there is some hint of a slightly steeper temporal decay in the X-rays after the break.

We first summarize the *Swift*, ROTSE-III and GROND observations in §3.2.1. We then present the multi-wavelength spectral and temporal analysis at selected epochs during the prompt and afterglow phases in §3.2.2. We next discuss the interpretations of the observations in §3.2.3. and conclude in §3.2.4.

3.2.1 Observations and Data Reduction

3.2.1.1 BAT

Swift BAT was triggered by GRB 081008 on 19:58:09.4 UT (Trigger 331093, Racusin et al., 2008b). We refer to this time as the trigger time, $T_{trigger}$. The BAT data were analyzed using the standard analysis software distributed within FTOOLS, version 6.5.1. The command *batgrbproduct* was first run to provide the basic set of products. This analysis found the emission to be detected from $T_{trigger}$-65.2 s and we therefore adopt this time as the onset of the burst T_0. Such a shift of the reference time only affects our analysis of the prompt and the very early afterglow, but we use it throughout the paper to be consistent.

Figure 3.1 shows the BAT flux density (at 71 keV) interpolated using the mean spectral index. The counts are binned with a minimum signal-to-noise ratio of 6 and maximum bin size of 20 s. The lightcurve displays a weak component decaying from T_0, two bright structured peaks at T_0+$\sim$65 s and T_0+$\sim$175 s and a fainter peak at T_0+$\sim$125 s. The emission drops below the BAT detection threshold at T_0+$\sim$270 s. The T90 (15-350 keV) of the burst is measured to be 185 ± 39 s. Spectral hardening and subsequent softening are observed during the first broad peak at T_0+$\sim$70 s. The average spectrum of the burst (from T_0 to T_0+263.3 s) is well fit by a power-law with exponential cutoff model. The best fit photon index and cutoff energy are 1.26(-0.32,+0.24) and 117(-50,+83) keV (with 90% confidence). At a redshift of 1.967 (Cucchiara et al., 2008c; D'Avanzo et al., 2008), the isotropic equivalent

energy release (0.1 keV-10 MeV) is $\sim 6.3 \times 10^{52}$ erg while the total fluence estimated is $\sim 6.7 \times 10^{-6}$ erg cm^{-2}.

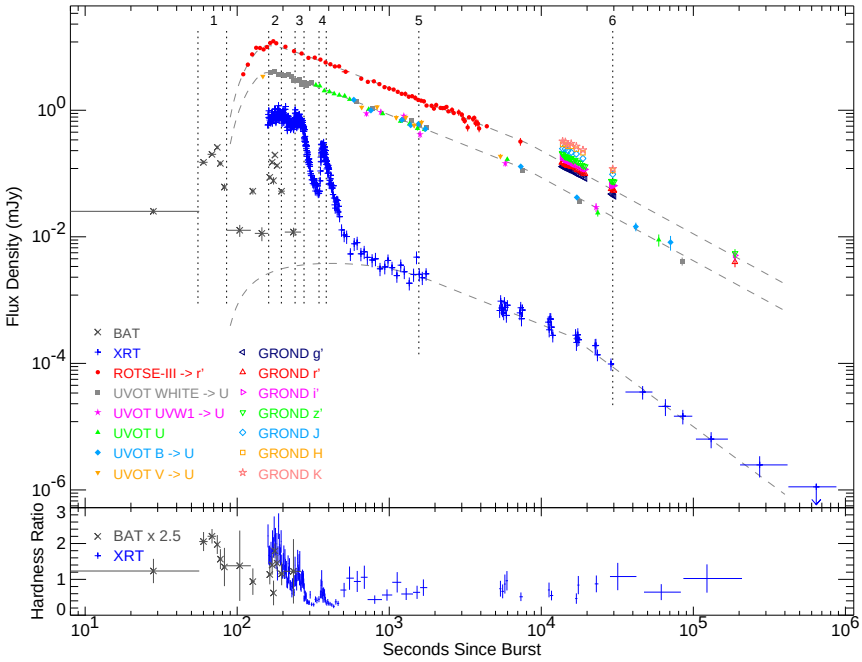

Fig. 3.1.—: Multi-wavelength lightcurve of GRB 081008. The UVOT flux densities are scaled to the u-band using the normalizations determined from the simultaneous temporal fit. The ROTSE-III unfiltered data are scaled to the GROND r'-band using the normalization from the same temporal fit. The exponential to power-law decay models (Willingale et al., 2007) for the afterglow components are over-plotted in dashed lines. Selected epochs or time intervals for spectral analysis are labeled with corresponding indices in Figure 3.2.

3.2.1.2 XRT

Swift slewed to this burst immediately and the XRT began observing in window timing (WT) mode at T_0+152.3 s. A bright uncatalogued X-ray counterpart was identified and its position distributed via a GCN alert notice. As the count rate dropped, XRT switched to photon counting (PC) mode at T_0+476 s.

The XRT lightcurve was obtained from the *Swift*/XRT GRB lightcurve repository (Evans et al., 2007). The spectra were extracted from the XRT team repository, from the new products outlined in Evans et al. (2009). The X-ray flux densities at 2.77 keV

were calculated using mean photon indices for WT and PC mode accordingly. This chosen frequency is the weighted mean of the X-ray emission assuming β=1, a typical spectral index observed, which is also similar to the afterglow spectral index of GRB 081008. The interpolations are thus not very sensitive to small changes in the photon index and the data from the two modes join smoothly. Three peaks are seen in the XRT lightcurve in Figure 3.1. The first two have complex structures and the first peak is at a similar time as the last BAT detected pulse. The third peak is a flare superimposed on the steep decay after the second peak. After that, the lightcurve smoothly declined and steepened at T_0+$\sim$10 ks.

As observed for the first bright BAT peak, the XRT hardness ratio (1.5-10 keV/0.3-1.5 keV) curve shows a similar structure as the early lightcurve, displaying visible hardening during the flares (see Burrows et al., 2005; Falcone et al., 2006; Romano et al., 2006, for other examples of such behavior). In general, there is also a trend of softening over time. This behavior, together with the rapid variation, indicates that the early X-ray detections are dominated by continuing burst activity, e.g. emission produced in the internal shocks. Detailed spectral analysis will be presented in § 3.2.2.

3.2.1.3 UVOT

UVOT began observations of the field at T_0+142.7 s. The observing sequence started with a 10 s v band settling exposure and a 150 s *white* (160-650 nm) finding chart exposure. These were followed by a 250 s u band exposure, after which the filter wheel rotated through all filters, taking short 20 s exposures. One more 150 s *white* band finding chart observation was taken at T_0+792 s. After 5 ks, longer exposures were obtained in all filters.

The optical counterpart was detected in *white*, v, b, u and $uvw1$ bands, but not in

uvm2 and uvw2 bands. This is consistent with the Lyman-α break at the measured redshift. In Figure 3.1, all UVOT observed fluxes are scaled to u band using the normalizations determined from the simultaneous temporal fit described in §3.2.2.4. Initial analysis of the late time *white* filter data shows the decay of the afterglow becomes very shallow after 100 ks. Cucchiara et al. (2008b) pointed out the presence of an extended source 2 arcsec away from the afterglow, which is within the 3 arcsec extraction radii used for UVOT. To measure the effect of this probable host galaxy, target-of-opportunity observations in the *white* filter were requested on Nov. 13th. After removing the host contribution from the *white* band photometry, no detections after 90 ks remain above 3 sigma. Such a correction is not attempted in other bands, given the negligible contribution from the underlying host galaxy during these earlier observations.

3.2.1.4 ROTSE-III

ROTSE-IIIc (Akerlof et al., 2003), at the H.E.S.S. site in Namibia, responded to GRB 081008 automatically upon receiving the GCN notice. The first 5-seconds exposure started 107.1 s after T_0 (8.3 s after receiving the alert). An initially brightening optical counterpart was detected and reported in Rykoff (2008a).

ROTSE-IIIc took a total of 10×5 s, 10×20 s and 144×60 s exposures before the target elevation dropped below the observing limit. The first ten 5-seconds exposures were taken in sub-frame mode with 3 seconds readout gap in between, instead of the 6 seconds full-frame readout time for later images. We took the first 70 single images and co-added the later images into sums of 5 to 10 depending on the image quality. The ROTSE-IIIc images were bias-subtracted and flat-fielded by the automated pipeline. Initial object detections were performed by SExtractor (Bertin & Arnouts, 1996). The images were then processed with our custom RPHOT pho-

tometry program based on the DAOPHOT (Stetson, 1987) PSF-fitting photometry package (Quimby et al., 2006b). A reference image was constructed from images taken on October 18th when the OT had faded below our detection limit.

Due to ROTSE-III's large pixel scale (3.3″), the optical counterpart is slightly blended with four surrounding objects in the ROTSE-IIIc images. To remove the possible contamination, we tried several different methods. First, we used the RPHOT functionality to subtract four PSF-scaled point sources around the OT. The lightcurve did appear to be steeper than obtained without subtraction. The two objects north of the OT are blended sources themselves but not resolved by ROTSE-IIIc. They may not be completely removed using the point source approximation, but the residual should be negligible compared to the bright OT. To confirm this, we attempted an alternative subtraction method described in Yuan & Akerlof (2008). Each burst image was cross-convolved with the reference to a common PSF and the difference between the two was taken. The brightness of the OT in the difference images were then measured by matching their PSF to the stars in the convoluted reference images. The results were consistent with the RPHOT subtraction method within the uncertainties. We report here the RPHOT PSF-fitting results with the 4 contaminating sources removed. Given the above comparison, the systematic error from subtraction is smaller than the statistical errors and is not included in the reported uncertainties.

The unfiltered thinned ROTSE-III CCDs have a peak sensitivity in the R band wavelength range. We thus calibrate the zero point magnitudes using the median offset from the USNO B1.0 R band measurements of selected field stars. In Figure 3.1, the ROTSE-III flux densities are scaled to match the GROND r'-band measurements using the offsets from the simultaneous temporal fit described in §3.2.2.4.

3.2.1.5 GROND

The Gamma-Ray Burst Optical/NearInfrared Detector (GROND, Greiner et al., 2008) mounted at the 2.2 m ESO/MPI telescope at LaSilla observatory (Chile) imaged the field of GRB 081008 simultaneously in $g'r'i'z'JHK$ starting 13.6 ks after T_0, after local sunset under clear sky conditions. A total of 28 $g'r'i'z'$ images with integration times of 66 s, 115 s and 375 s were obtained during the first night post burst. At the same time, the NIR channels were operated with a constant exposure of 10 s. In addition, the field was observed with GROND at day 2, 5 and 10 after the trigger. Data reduction and relative photometry was carried out using standard IRAF tasks (Tody, 1993), similar to the procedure outlined in Krühler et al. (2009). To exclude a possible contamination of the measured afterglow brightness with light from the host 2.2″ away, the results from the PSF photometry were checked against measurements taken using small apertures (0.3 and 0.5×FWHM) where an aperture correction was applied. Image subtraction, using the frame taken 10 days after the burst as reference, further confirmed that the contamination is negligible. Absolute photometry was measured with respect to the primary Sloan standards SA107-1006 and SA112-805 in $g'r'i'z'$ (Smith et al., 2002b), observed under photometric conditions and 2MASS field stars in JHK (Skrutskie et al., 2006).

The position of the afterglow is determined as R.A. = $18^h39^m49^s.88$ Decl. = $-57°25'52".8$ (J2000), with a 90% uncertainty of 0.3 arcsec. We adopt this as the best burst localization. Along the line of sight to this position, the Galactic extinction is E(B-V)=0.095 (Schlegel et al., 1998), and the Galactic column density is 7.1×10^{20} cm^{-2} (Kalberla et al., 2005).

3.2.2 Spectral and Temporal analysis

3.2.2.1 Prompt Spectral Evolution

We first examine the spectral evolution of the burst. Available BAT and/or XRT data are extracted in three time intervals, T_0+55 s to T_0+85 s, T_0+161 s to T_0+195 s and T_0+245 s to T_0+270 s (as marked in Figure 3.1), centered on the two broad peaks detected by BAT and the one X-ray peak shortly afterward. Because of the strong hardness ratio evolution, we limited the width of the chosen time intervals. The spectra were modeled with either a power-law or a power-law with exponential cutoff. When X-ray data were available, we included in the model a fixed Galactic absorption component and an additional variable system at the host redshift. The fit parameters for the best models are listed in Table 3.1. We tried modeling the spectra including a high energy power-law tail using a Band function (Band et al., 1993), but the power-law index above the cut-off energy is not well constrained by our data. The best fit spectral models at each epoch are plotted (with labeled offset for clarity) in Figure 3.2 as solid lines.

In both interval 2 and 3, the high energy spectra are well described by a power-law with exponential cutoff model where the cutoff energy drops from above 60 keV in interval 2, to 15 keV in interval 3, and the photon index softens. The measured local column densities ($1.06(-0.27,+0.32)\times10^{22}$ cm^{-2} and $1.01(-0.26,+0.29)\times10^{22}$ cm^{-2}) show good agreement between intervals. During interval 1, the BAT data are fit by a power-law model with a relatively hard photon index ($\Gamma \sim 1.33$). Given the general trend of softening, it is likely that the cutoff energy at this early epoch is close to or above 150 keV and thus not well constrained by the BAT energy coverage. Sakamoto et al. (2009) has demonstrated that a reasonable estimate of the peak energy (in νf_ν space) can be achieved using the power-law photon index in the BAT energy range

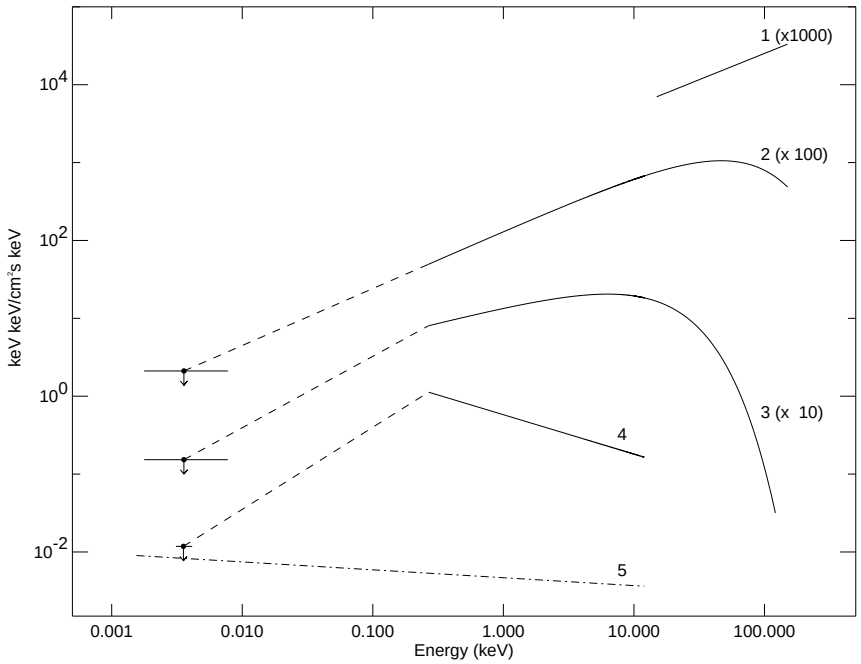

Fig. 3.2.—: Spectral models in the selected time intervals of GRB 081008. Interval 1, 2 and 3 (offset for clarity) correspond to the first 3 prompt peaks. Interval 4 corresponds to the bright X-ray flare seen by the XRT and 5 is the X-ray afterglow. Optical fluxes are corrected for Galactic extinction, but are not included in the model fit in intervals 1 to 4, because the optical fluxes are likely dominated by the external forward shock and thus not related to the high energy emission. We include these points as upper limits to constrain the internal emission component in the optical. The dashed lines, connecting the data points in the X-ray and the optical regions in the same interval, do not represent the actual spectral shape. During interval 5, the emission is entirely from the afterglow and the spectrum is plotted in dashed-dot line.

if the latter is between 1.3 and 2.3. Our value of 1.33 for the 1st interval is just inside this range and corresponds to a peak energy of 196(-47,+587) keV, assuming a cutoff power-law model as the actual spectral form. For the later two intervals, the peak energies can be explicitly calculated as $(1-\beta)E_{cut}$, which are $\sim$47 keV and $\sim$6 keV respectively. These numbers agree with the estimates following the method in Sakamoto et al. (2009), although the BAT-alone power-law photon index in the 3rd interval is not well constrained and exceeds 2.3.

During the 2nd and 3rd intervals, optical data are also available, but they are not included in the spectral fit for two reasons. First, emission from a different origin

(e.g. external forward shock) is likely dominating the optical data (see §3.2.2.3 and §3.2.2.4). Second, only data in the *white* filter (or unfiltered) is available, thus any optical deficit below the extrapolation from high energy observations can be compensated by an arbitrary value of local extinction, while any optical excess is hard to accommodate within the chosen models. Instead, we plot the *white* band fluxes (corrected for Galactic extinction and plotted with the same offsets as the corresponding high energy spectra) in Figure 3.2 and connect them directly to their high energy counterparts with dashed lines, just to show how they compare. The optical detections are considered as upper limits to constrain the internal emission component. If internal emission has contributed to at least part of the optical observations, they do not exceed the extrapolations from XRT and BAT detections at any time.

3.2.2.2 X-ray Flare

A bright single X-ray flare is superimposed on the rapid decay phase after the second broad X-ray peak. It has a similar hardness ratio evolution as the earlier peaks. It also shows a fast-rise-exponential-decay (FRED) profile that is typical of a GRB pulse. Its rapid rise and decay supports an identification with extended central engine activity. We thus analyze the flare within the same frame as the prompt emission.

Table 3.1. Best-fit spectral parameters to the burst and the flares

Interval	T_{range}-T_0 (s)	Host nH (10^{22} cm^{-2})	β	E_{cut} (keV)	χ^2/dof	Instrument
1	55 - 85	···	0.33 ± 0.07	···	58/56	BAT
2	161 - 195	$1.06^{+0.32}_{-0.27}$	$0.26^{+0.04}_{-0.05}$	$63.2^{+13.3}_{-9.8}$	201/184	BAT & XRT
3	240 - 275	$1.01^{+0.29}_{-0.26}$	$0.58^{+0.12}_{-0.14}$	$14.9^{+8.5}_{-5.3}$	200/194	BAT & XRT
4	345 - 385	$1.77^{+0.38}_{-0.32}$	$1.51^{+0.13}_{-0.12}$	···	97/75	XRT

Note. — All errors quoted correspond to 90% confidence intervals.

We extract the X-ray spectrum from T_0+345 s to T_0+385 s (noted as interval 4), centering on the flare. UVOT v band and ROTSE-III detections are available during this period, but there is no sign of a flare in the optical indicating that the emission is dominated by the afterglow. So we fit the XRT data alone. The spectrum is reasonably fit by a single power-law model with a photon index of 2.5 (see Table 3.1), which is much softer than the prompt emission and agrees with the softening trend. The inferred column density is somewhat higher than those from the earlier times, probably caused by curvature in the real spectral shape. This would suggest that E_{peak} is near or within the XRT energy range at this time.

3.2.2.3 Early Optical Afterglow

The ROTSE-III observations show an initially rising optical transient with two peaks at T_0+ ∼135 s and T_0+ ∼170 s (see Figure 3.1 and 3.3). The later one is almost simultaneous with the BAT and XRT peaks and may be attributed to a related prompt optical flare. The first one, however, does not appear to be correlated with the high energy emission. As shown in §3.2.2.4, the overall optical lightcurve is well-fit by one dominating component. We therefore interpret this first peak in terms of external shock emission. A detailed discussion of this interpretation will be presented in §3.2.3.1.

Figure 3.3 shows a close look at the BAT, XRT and optical lightcurves before T_0+345 s. The BAT and XRT data are binned in intervals determined by Bayesian block analysis (Scargle, 1998). For BAT, this analysis is carried out by *battblock* on the 1 s-binned lightcurve data. For XRT, only WT data are used and the background (∼1 ct/s) is negligible compared to the bright signal. We thus adapted the algorithm used in *battblock* for event files and consider only the change points resulting in time bins longer than half a second to ensure comparable signal to noise ratios. The

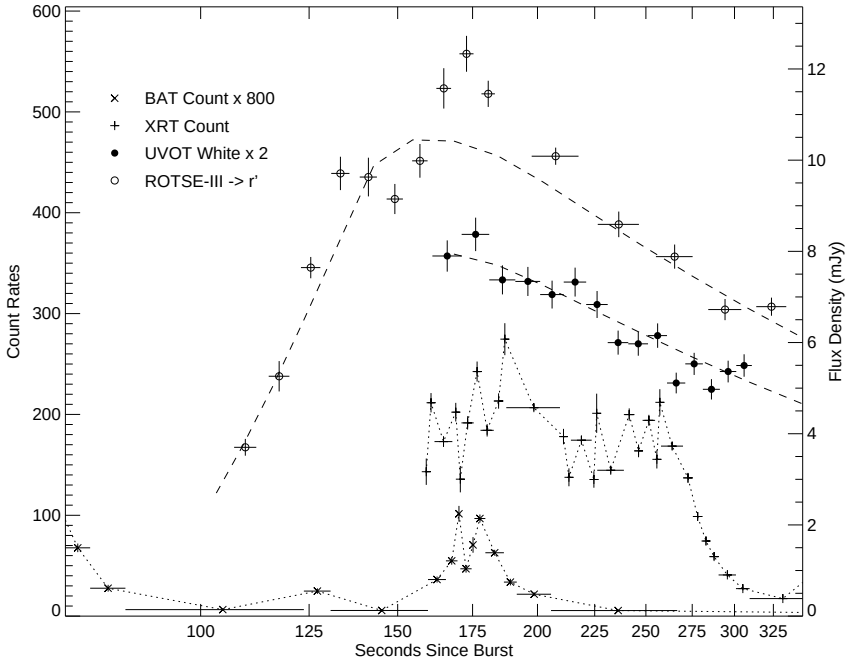

Fig. 3.3.—: Contemporaneous BAT, XRT and optical observations of GRB 081008. Time bins for the BAT and XRT data are determined by Bayesian block analysis (see text). The high energy data points are connected by dotted lines as guidance to the eye. The UVOT event data is binned in 10s intervals. The smooth rise and decay model is plotted over the optical to show that no significant deviation is detected.

high energy lightcurves show significant variations on a similar time-scale; while no convincing short-time-scale variability is detected in optical. This is not surprising though, as the optical curve connects smoothly into a monotonic decline afterward.

3.2.2.4 Multi-wavelength Afterglow

We adopt the two component exponential to power-law decay model in Willingale et al. (2007, Eq (2) and descriptions within) to characterize the temporal flux evolution in X-ray and optical. In this model, the first component corresponds to the prompt emission, and the second relates to the afterglow emission. All optical observations are sufficiently fit by one afterglow component. In the X-rays, the second component is not revealed until the end of the last flare. So the rise time (t_a) of this second component is fixed to 130 s according to the optical fit. The best fit models

for the afterglow components are over-plotted in Figure 3.1 and the parameters are tabulated in Table 3.2.

For both optical and X-ray, a later temporal break is required in the model. The break times in the two energy ranges (15870±8623 s and 7834±2160 s) are consistent at 90% confidence, but the final decay (α_2 in Table 3.2) in the X-ray is significantly faster than in the optical. We further attempted fitting all energy bands after T_0+750 s simultaneously with a smoothly joined broken power-law model (f(t)=$a[(t/t_b)^{-s\alpha_1}+(t/t_b)^{-s\alpha_2}]^{1/s}$), with a small smoothness factor, s∼1. Although the overall fit is acceptable, giving a reduced Chi-squared of 1.17 for 239 degrees of freedom (see Table 3.2 for the best fit parameters), the fit parameters are dominantly determined by the well-confined optical data. Some systematic deviations from the model, not reflected in the Chi-squared statistics, are noticed in the X-rays. Between T_0+7 ks and T_0+28 ks, the X-ray points are mostly above the model, and after T_0+30 ks, the X-ray data are all below the model. Our data are thus consistent with displaying a smooth achromatic temporal break, but a chromatic behavior is not confidently ruled out in case of a subtle evolution.

We then examine the spectral energy distributions (SEDs) in selected afterglow

Table 3.2. Afterglow temporal best-fit parameters

Energy Range	Rise time t_a(s)	Start of Decay T_a(s)	α_1	T_{break} (s)	α_2
X-ray	130*	1800**	0.96 ± 0.10	15870 ± 8623	1.78 ± 0.25
Optical/IR	130*	136 ± 18	0.96 ± 0.03	7834 ± 2160	1.313 ± 0.048
X-ray & Optical/IR ***	···	···	0.81 ± 0.07	15139 ± 8150	1.71 ± 0.13

*Fixed parameters, to a value estimated from the optical fit.

**The plateau is hidden by the prompt emission, thus no error is estimated.

***Only data after T_0+750s are fit by a smoothly joined broken power-law model, with a smooth factor, s=1.

Note. — All errors quoted correspond to 90% confidence intervals.

epochs. In the X-rays, no significant spectral or hardness ratio changes can be detected. In the optical, the UVOT detections before the break and the GROND observations after the break are poorly fit by one power-law spectral index plus the same amount of local extinction. This is caused either by spectral evolution or a spectral break at the red (blue) end of the UVOT (GROND) coverage, at around 2.5 eV. This latter conjecture is confirmed by further analysis.

The overall shapes of the SEDs are modeled from optical/IR to X-ray with all available data before and after the break. Assuming they belong to the same synchrotron emission component, we allow either one or no spectral break within the energy range. Before the break, we extract an X-ray spectrum in the time interval from T_0+765 s to T_0+1778 s (first orbit) and from T_0+5286 s to T_0+7562 s (second orbit) to maximize the signal to noise ratio, given that no significant spectral or hardness ratio changes is detected in the X-rays. This spectrum is scaled to the X-ray count rate at T_0+1.5 ks to minimize the interpolation of the UVOT data. The UVOT mean count rates at T_0+1.5 ks are estimated by fitting the nearby data points (within 500 s on each side) in each band with power-laws. The errors are estimated using a bootstrap approach, where each data point is randomly re-sampled from a Gaussian distribution centered on the observed count rate with a sigma equal to the measured error. The UVOT count rates are converted to XSPEC compatible spectral files with the corresponding response matrices downloaded from the HEASARC Calibration Database (version 20041120v104).

The SED can be fit by a single power-law model with fixed Galactic dust and gas absorption and additional dust and gas absorption at the host redshift (see Table 3.3). This model is supported by the well-matched initial temporal power-law decay indices (α_1 $\sim$0.96) in the optical and the X-ray. The relatively small amount

of host extinction required and the lack of coverage at the rest-frame 2175Å Galactic absorption feature do not allow us to distinguish between the Milky Way (MW), Large Magellanic Cloud (LMC) or Small Magellanic Cloud (SMC) environment.

After the break, another X-ray spectrum is constructed between T_0+16 ks and the last detection at T_0+400 ks. This spectrum alone has a relatively low signal to noise. We scale this X-ray spectrum to the latest epoch where the afterglow was detected in the J, H and K bands (at T_0+$\sim$29.5 ks) and convert the contemporaneous GROND detections to XSPEC compatible files. The UVOT u and b band rates are also interpolated to this epoch by fitting the neighboring two detections (about 30 ks apart) with power-laws as described above.

A single power law model does not produce an acceptable fit to the overall SED, regardless of the choice of local dust and gas absorption. At least one spectral break is required between X-ray and optical. Our best fit model (see Table 3.3) constrains a break at $\sim$2.4 eV, in the UVOT v-band. Such a low break frequency is not well covered by the earlier UVOT data, and the two SEDs thus have consistent shapes. A MW extinction curve is used because it provides a best fit and is marginally preferred during the earlier epoch. Nevertheless, we do not consider this as a conclusive property of the environment because of the possible uncertainty in our selected intrinsic

Table 3.3. Best-fit afterglow spectral parameters

T-T_0 (ks)	Energy Range	Host Type	Host Extinction E(B-V)	nH (10^{22} cm^{-2})	β_{opt}	E_{break} (eV)	β_x	χ^2/dof
1.5	XRT only	...	...	$0.47^{+0.36}_{-0.33}$	...	...	$1.06^{+0.14}_{-0.13}$	46/43
1.5	XRT & UVOT	MW	$0.15^{+0.04}_{-0.03}$	$0.62^{+0.25}_{-0.23}$	1.14 ± 0.05	...	1.14 ± 0.05	52/46
1.5	XRT & UVOT	LMC	$0.11^{+0.02}_{-0.03}$	$0.58^{+0.25}_{-0.22}$	1.12 ± 0.04	...	1.12 ± 0.04	53/46
1.5	XRT & UVOT	SMC	0.08 ± 0.02	$0.54^{+0.24}_{-0.22}$	1.10 ± 0.04	...	1.10 ± 0.04	55/46
29.5	XRT, UVOT & GROND	MW	$0.18^{+0.09}_{-0.07}$	$0.97^{+0.85}_{-0.60}$	$-0.13^{+0.30}_{-0.41}$	2.4 ± 0.2	$1.12^{+0.11}_{-0.08}$	11/14
1.5 & 29.5	XRT, UVOT & GROND	MW	$0.16^{+0.04}_{-0.03}$	$0.65^{+0.24}_{-0.21}$	$-0.06^{+0.17}_{-0.18}$	$2.4^{+0.2}_{-0.1}$	1.14 ± 0.05	72/63

Note. — All errors quoted correspond to 90% confidence intervals.

spectral shape, e.g. the smoothness of the break is not considered in our model.

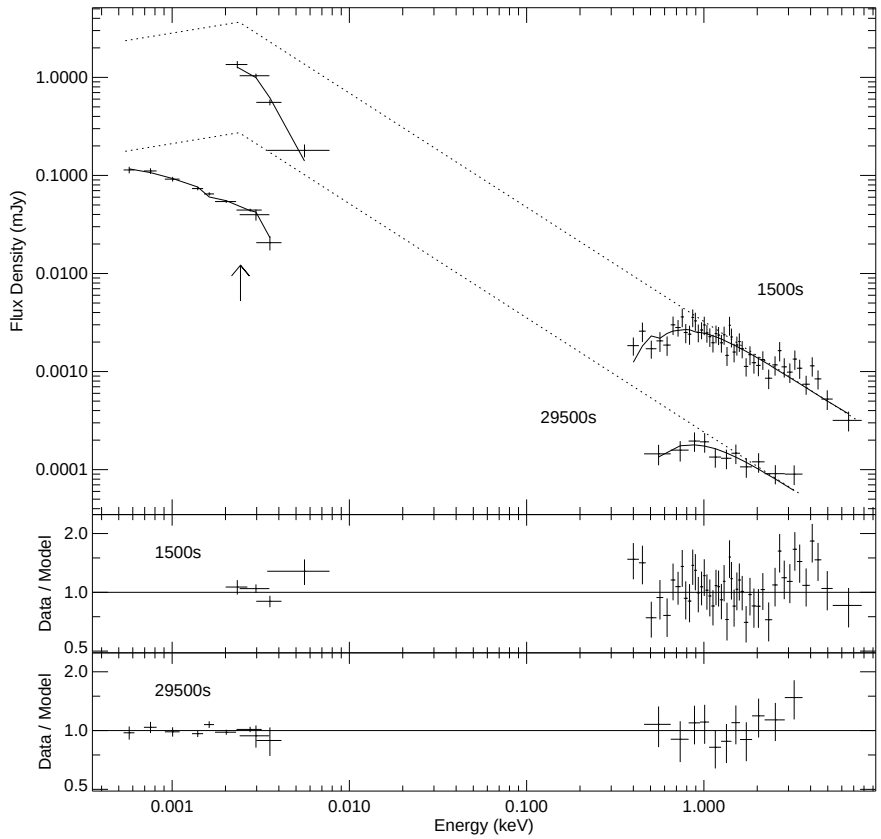

Fig. 3.4.—: Combined XRT, UVOT and GROND afterglow spectral analysis of GRB 081008 (epoch 5 and 6). The local extinction and absorption properties are tied. The fit parameters are listed in Table 3.3. The absorbed models are over-plotted in the upper panel. Dotted lines show the intrinsic power-law and broken-power-law components. The location of a spectral break is indicated by an upward arrow. The residual ratios are plotted in the bottom panels.

Figure 3.4 shows a simultaneous fit of the two SEDs with a broken power-law model with Galactic dust and gas absorption and dust and gas absorption at the host redshift. We tie the dust (following a MW extinction law) and gas properties for a consistent environment throughout the afterglow phase. The fit is fairly good except in the $uvw1$ band. A plausible explanation for the under-estimate in $uvw1$ is that our model applies a sharp cutoff above the Lyman-break which might not be true. The best fit model parameters are consistent within errors with the estimates obtained

in narrower energy bands and smaller time coverages as described above. Also, the column density derived is consistent with the estimate during prompt interval 2 and 3 (see Table 3.1).

In summary, the observed optical and X-ray afterglow emission started off following similar temporal decay rates (α_1 $\sim$0.96) and displayed smooth temporal breaks at similar times (at $\sim$15 ks). While the two SEDs before and after the break were characterized intrinsically by a power-law model and a broken power-law model respectively, they had consistent shapes because the low break frequency was not well covered during the first epoch. Besides, the optical/IR observations by GROND between T_0+13 ks and T_0+30 ks do not show evidence of a moving spectral break. The overall afterglow behavior was consistent with being achromatic. Nonetheless, there is some hint of a slightly steeper decay in the X-rays after the break. Because the afterglow was not observed in IR and near-IR at early times, probable evolution of the spectral break is not constrained, e.g. it could have increased over time from below optical to the observed 2.4 eV.

3.2.3 Discussion

3.2.3.1 Early Optical Afterglow

Reverse or Forward Shock For the initial optical observations, fixing the beginning of the external shock to the burst time T_0 yields a temporal rise index of $\alpha = -5.0 \pm 0.6$. This is too rapid to be considered as the pre-deceleration phase of the forward shock (t^2 or t^3 in ISM, slower than $t^{1/2}$ in a wind medium, see Panaitescu & Vestrand, 2008), but agrees well with the prediction for a reverse shock rising in a thin shell case when the burst duration is less than the deceleration time (Kobayashi, 2000; Zhang et al., 2003). Back-extrapolation from late time afterglow observation shows that the reverse shock and forward shock must have comparable peak luminosities.

The analysis of the later afterglow emission suggests the forward shock characteristic synchrotron frequency (ν_m) may have passed below the optical by T_0+200 s. If the micro-physical parameters are comparable in the reverse and forward shock regions, the reverse shock should have a much lower characteristic synchrotron frequency (Sari & Piran, 1999) and thus have a very weak optical emission. The detection of reverse shock emission would then point to a more magnetized reverse shock region (Zhang et al., 2003; Kumar & Panaitescu, 2003; Jin & Fan, 2007).

There are several questions to be asked for this interpretation. First, is the thin shell assumption correct? Although the overall prompt BAT and XRT detections extend to after the beginning of the optical detections, the second epoch of strong burst activity emerged once the initial rapid rise in the optical had stopped. The temporal and spectral similarity between the flares indicate that the second epoch of high energy emission was from the same emitting region as the earlier bursts of emission, i.e. closer to the central engine than external medium. This later part of the ejecta would then run into the external medium after the initial shock has been established. We thus can ignore the effect of this later injected kinetic energy when considering the early rising lightcurve. Suppose the bulk of kinetic energy was injected into the external medium by the materials producing the first flare ending at T_0+100 s, the shock can be reasonably considered impulsive.

This leads to the second question: whether the onset of the afterglow is chosen correctly as T_0? Quimby et al. (2006b) have pointed out that different choices of time origin may lead to different interpretations of the early data (also see Tagliaferri et al., 2005, for a discussion in the X-rays). Lazzati & Begelman (2006) explored how varying central engine activity would affect the self-similar evolution in the early afterglow and its lightcurve. Their simulation is limited to a power-law energy release, but gives

a good schematic picture. They found that if the burst energy release is concentrated toward the end of the burst duration, the self-similar evolution would deviate from one simple power-law behavior. For GRB 081008, the emission at T_0+65 s is about one order of magnitude higher than at T_0, it is therefore proper to choose a delayed time origin in a power-law fit. Such a small time shift has a negligible effect on the temporal index inferred for the later smooth decay. But if we choose the reference time to be T_0+45 s, the initial rise phase would have a temporal index of -3.1 ± 0.4, fully consistent with the pre-deceleration of the forward shock. For any choice of reference between T_0+25 s and T_0+62 s (including the beginning of the first big pulse detected by BAT), the estimated temporal power-law index is consistent with -3 within 2 sigma. Given the earlier discussion about the reverse shock and the fact that the lightcurve is well fit by one smooth rise and fall component, we prefer the external forward shock interpretation for this rising lightcurve observed by ROTSE-III.

Assuming the first emission peak in the optical marks the onset of the forward shock deceleration, we can apply the adjusted rise time (T_0+135 s - T_0+45 s) of 90 s and the energy released before T_0+135 s (see 3.5) into Eq (1) in Molinari et al. (2007) to obtain a Lorentz factor of $\Gamma_{\rm dec} \sim$250 at the deceleration radius and an initial Lorentz factor Γ_0 of $\sim$500 ($\sim 2\Gamma_{\rm dec}$; Meszaros, 2006). We have assumed a particle density n=1 cm^{-3} and a radiative efficiency μ=0.2. The deceleration radius is then estimated as $\sim 2\Gamma^2 ct \sim 3 \times 10^{17}$ cm.

Refreshed Shock? After the forward shock start decelerating, the passing of the synchrotron frequency and/or cooling frequency across the optical band may produce temporal breaks. But a second peak, as observed for GRB 081008, is hard

to explain in a model involving only one external forward shock component. The temporal coincidence with a high energy flare suggests possible contribution from internal emission. This scenario is hard to rule out given the slight optical excess ($\sim$4 sigma) above the afterglow model seen in Figure 3.3. However, the lightcurve also shows a probable dip below the smooth, one component model, and the decay after the second peak joins smoothly into the later phase. We thus explore other interpretations for the double peaked lightcurve.

In a reasonable contemplation in the frame of the fireball model, the shells of material producing the late burst activity would reach the external medium and catch up with the early decelerated shells at some moment and re-energize the forward shock. This later scenario results in an irregular "step" structure, as additional energy is injected over a time period comparable or longer than the second epoch of burst activity. It has been noted that refreshed shocks from slow or late shells may alter the shape of the afterglow lightcurves (Rees & Meszaros, 1998; Kumar & Piran, 2000). It is, however, hard to directly relate such structure with the internal emission as they are produced by different mechanisms at different regions. Here, we provide a simplest possible test on this speculation.

If a second batch of kinetic energy is injected into the forward shock, a new self-similar solution would be established sometime after the cessation of all burst activity. Indeed, we didn't observe any apparent deviation from a power-law decay after T_0+200 s. We try to estimate the synchrotron emission before and after the refreshed shocks. Without the additional energy injection, we can assume the afterglow would decay monotonically after the first peak at the same rate as observed in the later afterglow. At a time after T_0+200 s, the observed flux is 50-60% higher than this extrapolation, including uncertainties from the flux measurement at the first peak

and the normalization of the later decaying lightcurve.

We then estimate the energy release in the prompt emission before and after T_0+135 s (the first optical peak). We estimate the fluence between 0.1 keV and 10 MeV in the rest frame. In the observer's frame, the 0.1 keV lower bound fits nicely within the XRT sensitivity range. Before T_0+135 s, only BAT observations are available and the average spectrum can be fit by a power-law with exponential cutoff model. The cutoff energy at 157 keV, although above the BAT energy threshold, agrees well with calculation using the power-law photon index following Sakamoto et al. (2009). We estimate the fluence during this period to be $\sim 4.7 \times 10^{-6}$ erg cm^{-2}. The hard X-ray emission dropped below the BAT detection threshold at T_0+$\sim$265 s, but it is likely that the central engine activity continued with softer emission detected mainly in soft X-rays. Between T_0+155 s and T_0+210 s, simultaneous XRT and BAT detections constrain the spectral shape well, and using a power-law model with an exponential cutoff, we estimate a total fluence of $\sim 2.5 \times 10^{-6}$ erg cm^{-2}. After this, the peak energy shifts further toward lower energies and the fluence in the next 100s is only one fourth of the previous interval (with cutoff energy at $\sim$10 keV). The additional energy release between T_0+135 s and T_0+155 s is even smaller. From T_0+135 s to T_0+$\sim$310 s, we estimate a total prompt fluence of $\sim 3.4 \times 10^{-6}$ erg cm^{-2}. This is about 70% of the total energy released before T_0+135 s, and consistent with the flux increase calculated within the large uncertainties.

The X-ray flare at T_0+$\sim$400 s is likely generated by the same internal mechanism. We can estimate its emission in the same energy range as above. The spectrum is so soft (with spectral index greater than 2) that we can directly integrate it in the high energy range. No extrapolation below the XRT energy is necessary with our choice of energy range, so we do not have to worry about a spectral break below 0.3 keV. The

"bolometric" fluence calculated is two orders of magnitude lower than the previous prompt emission. Therefore, if the contribution to the forward shock is proportional to the prompt luminosity, the change in the forward shock emission is comparable to the error bars in the optical measurements and too small to be noticed.

A caveat for this calculation is the assumption that the relative radiative efficiency in the internal and external processes is constant although the relationship between the two is not straightforward. During the burst, the peak emission frequency down-shifted from γ-ray to X-ray. The X-ray emission could be from slower or delayed ejecta, or alternatively from collisions with a smaller Lorentz factor dispersion and thus lower efficiency in converting the kinetic energy. At the forward shock front, the conversion efficiency may depend on the condition of the previously shocked medium and therefore requires a detailed simulation to determine. Another overlooked factor is the evolution of the synchrotron spectral shape, as the flux is estimated in a narrow optical band.

Vestrand et al. (2006) showed that the early optical lightcurve of GRB 050820A can be modeled with a prompt component tracing the γ-ray emission and two afterglow components. The afterglow components, correspondingly produced by the precursor and the main event ejecta, have consistent ratios between the prompt fluence and afterglow amplitude. This agrees with our finding although their first afterglow component is faint and not well-sampled for a detailed study. A similar double peaked prompt lightcurve is observed for GRB 061007 (Rykoff et al., 2009). The overlapping high energy pulses indicate continuous energy input into the external shock and thus modeling of the early lightcurve in a thick shell case may be more appropriate. For that event, the initial very rapid rise of the optical emission is also problematic in the current forward shock model.

3.2.3.2 Late Afterglow Evolution

Before the break and above ∼2.4 eV, optical and X-ray appear on the same segment of a synchrotron spectrum, we thus use the method described in Racusin et al. (2009) to find all scenarios consistent with the observed temporal and spectral indices. The temporal decay (α=0.96±0.03) marginally agrees with the value expected ((3β-1)/2∼1.2, for β ∼1.1) for above the cooling and characteristic synchrotron frequencies, regardless of slow or fast cooling regime and the external medium density profile. In such a scenario, both the cooling frequency and the characteristic frequency are below or close to the optical by T_0+200 s.

For all the other closure relations considered, the temporal decay is shallower than predicted if no energy injection is present. In terms of the canonical X-ray lightcurve (Nousek et al., 2006; Zhang et al., 2006; O'Brien et al., 2006), this decay index is within the range observed for the shallow decay phase (phase II). This phase, detected in a significant fraction of the bursts, is generally explained as due to prolonged energy injection. However, the source of energy is unclear as well as the mechanism for fine tuning the input energy into the forward shock smoothly over such long period of time.

We apply the evolution constraints in Racusin et al. (2009) to the X-ray data and find the cause of the break is consistent with either a jet geometry or the cessation of energy injection. For both types of break, achromatic behavior extending to the optical range is expected, consistent with our observations.

The spectral break at 2.4 eV is hard to be accommodated in the standard fireball model. A synchrotron spectrum is characterized by three possible break frequencies, a cooling frequency (ν_c), a characteristic frequency (ν_m) and a self-absorption frequency (ν_a) (e.g. Sari & Piran, 1999; Granot & Sari, 2002). All three frequencies should

evolve over time. The observed break at 2.4 eV is too high to be a self-absorption frequency. Given a spectral index below the break (-0.13{-0.41,+0.30}) consistent with -1/3, the shape of the spectrum can be expected in a slowing cooling regime ($\nu_m < \nu_c$) around ν_m (Granot & Sari, 2002). However, ν_m should always decease over time as the forward shock decelerates, unless the shock is reenergized by significant late-time injection, which does not seem to be the case here. We do not observe the expected rise or flat evolution in IR (below the break) and do not detect a higher break frequency in our earlier SED. Finally, our data do not rule out an increasing break frequency, as expected for a cooling break in a wind medium (Chevalier & Li, 2000), but the spectral index difference across the break ($\sim$1) is much larger than the predicted amount of 0.5.

If some chromatic effect exists around the temporal break, the passage of a cooling frequency in a wind medium produces the correct trend of a break moving from optical to X-ray. The expected temporal index change of 0.25 is similar to the observed value in the optical ($\sim$0.3) but not enough to account for the amount of change detected in the X-rays ($\sim$0.8). In any case, the temporal break at T_0+15 ks is not likely to be caused by the movement of the observed spectral break, because there is no evidence that the break frequency has yet reached the X-ray regime by T_0+29.5ks, as would be expected in such a case.

In short, the observed temporal break is consistent with being a jet break or the cessation of energy injection. Before the break, the multi-wavelength observations are best interpreted by the cooling and characteristic synchrotron frequency being below the optical. No satisfactory explanation is found for the later spectral shape and its probable evolution. It is viable to assume that the spectral break has increased over time, as the cooling frequency in a wind medium, but such evolution is not likely to

be responsible for the observed temporal break.

3.2.3.3 Burst Energetics

If the temporal break at T_0+$\sim$15 ks is interpreted as a jet break, the jet opening angle can be estimated as 2.1° or 2.4° for ISM (Sari et al., 1999) or a wind medium (Bloom et al., 2003) respectively. In the calculations, we have assumed a particle density n=1cm^{-3}, a characteristic wind density A$_*$=1, a radiative efficiency μ=0.2 and a kinetic energy $E_k = E_{\rm iso}/\mu$. The collimation corrected total gamma-ray energy release (E$_\gamma$) is hence 4.2×10^{49} erg and 5.5×10^{49} erg for ISM and wind medium respectively. This number should be slightly larger if early X-ray detections are also considered.

For a jet break, the change of the temporal index ($\sim$0.8) favors an ISM-like medium (Panaitescu, 2005). Both the inferred opening angle and the collimated energy output are on the small side but well within the distribution for *Swift* detected GRBs (e.g. Liang et al., 2008; Racusin et al., 2009). The nature of the break is, however, uncertain given the previous discussions on a probable secondary chromatic effect. A later jet break, occurring close to or shortly after the afterglow dropped below the detection threshold of all our instruments ($\sim$400 ks), would also give a sensible estimate of the opening angle and E$_\gamma$.

3.2.4 Conclusions

With energetics typical among *Swift* detected events, GRB 081008 happens to last long enough to have overlapping phases with the early follow-up observations in X-ray and optical. It is well behaved in the sense that all early canonical phases in X-ray and optical were detected. A key feature of the high energy emission is the hardness ratio evolution in accordance with the flux fluctuation throughout the burst and the

X-ray flares. The temporal continuity and spectral softening suggest that early X-ray observations originate from extended internal activities, but either with a gradually decreasing efficiency or a declining energy output from the central engine.

In the optical, the detections seem to be dominated by afterglow emission at all times. An intriguing question to ask is what happens to the material producing the late burst emission. In the frame of the fireball model, they will run into the ambient medium and refresh the external shock. Whether this signature is observed for GRB 081008 is uncertain. If such early refreshed shocks can be observed, their relative strength to the prompt emission provide important clues to the burst mechanism and production of the afterglow. Refreshed shocks have been used to explain late-time lightcurve bumps (Granot et al., 2003; Jóhannesson et al., 2006). In those cases, slow shells catch up with the forward shock front hours to days after the initial burst. The existence and properties of the slow shells are only inferred from the lightcurve shapes. Observations directly linking the ejecta material and refreshed shocks are achievable for long bursts with discrete episodes of activities or for events with very bright X-ray flares if they are produced in a similar way as the prompt burst emission. The latter cases may produce cleaner chasers of the refreshed shock with less contamination from internal optical emission (however, see Krühler et al., 2009). Falcone et al. (2006) have attempted to relate the subsequent bumps in the X-ray lightcurve with the bright X-ray flare in GRB 050502B. No solid evidence of refreshed shocks associated with flares has been observed in the optical so far, probably due to limited time coverage of the data or incomplete understanding of the modification to the afterglow lightcurve.

The importance of well-sampled multi-wavelength data has been demonstrated. In general, the observed afterglow emission is consistent with displaying an achromatic temporal break. Such a break can be interpreted as due to a collimated outflow

(jet) or the end of energy injection. However, there is a hint of a steeper decay in the X-rays after the break. While for GRB 081008, the deviation is rather subtle, similar steeper decay in the X-rays than in the optical has been observed for some other events (e.g. Rykoff et al., 2006; Page et al., 2009). Using data from GROND, UVOT and XRT, we are able to model the SED of the afterglow from IR to X-ray and constrain a spectral break within the optical regime. As many other well-studied bursts, the overall temporal and spectral behavior of the afterglow is hard to explain in the frame of the standard fireball model.

3.3 Other GRBs Observed by ROTSE-III

3.3.1 Data Reduction

For all the following bursts, the Swift/BAT data were analyzed using the standard analysis software distributed within FTOOLS, version 6.5.1. The command *batgrbproduct* was first run to provide the basic set of products. The displayed lightcurves are binned with a minimum interval of 5 sec and minimum signal noise of 6. The flux densities (at 71 keV) were interplated using the mean BAT photon indices. Count rates are also extracted for intervals overlapping with optical observations.

The XRT lightcurves and spectra were obtained from the public archive (Evans et al., 2007). The flux densities (at 2.77 keV) were calculated using mean photon indices for WT and PC mode accordingly. Given the choice of the frequency, the interpolations are not very sensitive to the photon indices and the data from two modes usually join smoothly.

The ROTSE-III images were bias-subtracted and flat-fielded by the automated pipeline. Initial object detections were performed by SExtractor (Bertin & Arnouts, 1996). The images were then processed with our custom RPHOT photometry program based on the DAOPHOT (Stetson, 1987) psf-fitting photometry package (Quimby

et al., 2006b). Reference images were constructed from images taken on at least 12 hours later when the OT has faded below our detection limit. The unfiltered thinned ROTSE-III CCDs have a peak sensitivity in the wavelength range of R band. We thus calibrate the zero point magnitudes using the median offset from the USNO B1.0 R band measurements of selected field stars.

Swift/UVOT data were analyzed using the standard analysis software distributed within FTOOLS, version 6.5.1. For event data, the task 'coordinator' is first run with an aspect-corrected attitude file to convert the events to sky positions. 'uvotscreen' is then used to select only events with angular distance less than 100, elevation greater 10, SAA=0 and quality flag 0. 'uvotevtlc' is used to obtain a lightcurve in selected time bins. For the image data, if keyword ASPCORR is not set to 'T', 'uvotskycorr' is first used for aspect correction. The images in each filter are then summed ('uvotimsum') and searched for optical counterpart detections. 'uvotsource' is used to extract the count rates in selected source and background region. For both observation mode, 5″ extraction aperture is used for counterpart brighter than about 15 magnitude and 3″ aperture is used for fainter sources. Whenever 3″ aperture is used, aperture correction is necessary to obtain standard UVOT photometry. This is done by doing photometry on several chosen point sources in each image field with both 3″ and 5″ aptures. The median magnitude difference is obtained between two aperture sizes and used to correct the OT photometry estimated in the non-standard smaller aperture.

For some bursts, observations in other wavelength ranges, from the GCN circular reports, are also included to show the complete picture of the events. These filtered observations are convereted to flux density using conversion factor from Bessell (1990); Smith et al. (2002a); Cohen et al. (2003).

For all the events, the optical and X-ray lightcurves (excluding apparent flares) are simultaneously fit by power-laws or smoothly joint broken power-laws. Even for the cases no satisfactory fit can be found, a selected model is over-plotted in the multi-wavelength lightcurves figure as guidance to the eye.

3.3.2 GRB 071025

GRB 071025 triggered Swift/BAT at 04:08:53.7 UT (Trigger 295301, Pagani et al., 2007). *Swift* slewed immediately to the burst. The XRT began observing the field 146 seconds after the BAT trigger in WT mode and detected a bright uncatalogued X-ray source. UVOT started a finding chart exposure with the White filter at 155 seconds after the trigger but detected no afterglow to deep limits (21-22 magnitude) in the ∼10 ks observations (Kuin & Pagani, 2007). The BAT mask-weighted lightcurve shows a broad peak composed of several overlapping sub-peaks decaying out to T+422 sec, beyond which no information is available due to observing constraint (Barthelmy et al., 2007). T90 (15-350 keV) is at least 109 ± 2 sec. The fluence in the 15-150 keV band is $6.5 \pm 0.2 \times 10^{-6} erg/cm^2$.

ROTSE-IIIb, located at McDonald Observatory, Texas, responded automatically upon receiving the GCN notice, starting the first exposure at 04:10:14.0 UT, 80.3 s after the burst (6.0 s after the GCN notice time). A 19.2 magnitude fading source, not visible in the DSS red plate, was detected at RA = $23^h40^m17^s.19$ Dec = $+31°46'42".64$ (J2000) and reported via GCN circular (Rykoff et al., 2007a). Refined analysis and re-calibration to USNO-B1.0 R-band found the optical counterpart to rise initially and peak at 17.3 magnitude (Rykoff et al., 2007b).

We adopt the best burst location as RA = $23^h40^m17^s.078$ Dec = $+31°46'42".87$ (J2000), with an uncertainty of 0.25 arcsec in both axes (Bloom, 2007). Along the line of sight to this position, the galactic extinction is E(B-V)=0.074 (Schlegel et al.,

1998), and the galactic column density is $5.1 \times 10^{20} cm^{-2}$ (Kalberla et al., 2005).

Figure 3.6 presents the multi-wavelength lightcurves of GRB 071025. Narrow-band optical/IR data were collected from the GCN circular reports as observed by REM (Covino et al., 2007), PAIRITEL (Bloom, 2007), Mt.Lemmon (Im et al., 2007), Super-LOTIS (Williams & Milne, 2007), SQIID (Jiang et al., 2007), Kuiper (Milne & Williams, 2007), and MAGNUM (Minezaki et al., 2007). The X-ray and ROTSE-III data were simultaneously fit by a smoothly joint broken power-law model. The best fit paramters are listed and the modeled curve is overploted in Figure 3.6. The ROTSE-III and X-ray observations do not overlap and they each exist during one segment of the model (except for the last ROTSE-III detection). Nevertheless,they together constrain the break time. Such an achromatic model, in particular after the break, is supported by the optical/IR detections reported in GCNs (the thin dotted lines in Figure 3.6 are scaled to minimize the median distance between data in each filter and the correponding model). Before the break, the ROTSE-III lightcurve shows hints of two mild peaks, in consistent with the behavior reported by Bloom et al. (2007). The first preliminary J and H band data points lie below the model lightcurve, indicating bluer emission than later times, possibily related to intrinsic spectral evolution or change of extinction.

In the X-ray, the first orbit observation is contemporanous with the BAT detections. This early part of the X-ray lightcurve is shallower than the gamma-ray decay but slightly steeper than later X-ray decay. It also shows deviation from a power-law, which could be interpreted by the addition of a prompt and a afterglow components.

No redshift is directly measured for this burst. UVOT non-detection in v suggests the Lyman break lies close to 600 nm and a redshift around 5.5. This is confirmed by modeling the afterglow spectral energy distribution. No significant hardness ratio

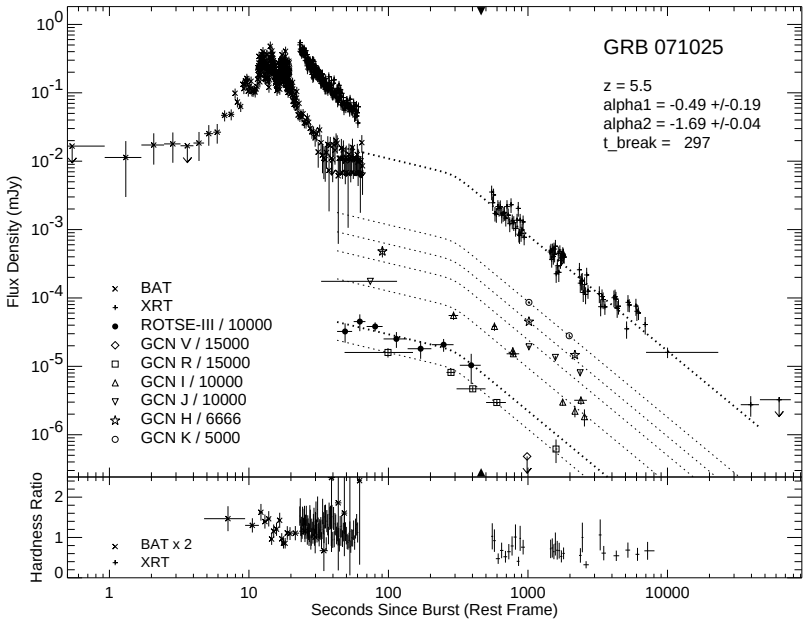

Fig. 3.5.—: Multi-wavelength lightcurve of GRB 071025. A smoothly joint broken power-law model is over-plotted in dotted lines. Filled triangles on the X-axis mark the time when spectral index is calculated between optical and X-ray for Figure 3.16. Narrow-band optical/IR data were collected from the GCN circular reports (see text). Thin dotted lines are scaled to minimize the median distance between data in each filter and the correponding model.

variation is detected after the lightcurve break. We thus use the X-ray spectra including all PC mode data between T+3.5ks and T+300ks. The R, I, J, H ,K data are interplated/extrapolated using the dotted line model in Figure 3.6 to the mean X-ray photon arrival time at T+12850 s. Absorption by inter-galactic medium (IGM) is corrected using the model from Meiksin (2005) and response curves from Bessell (1990); Cohen et al. (2003). At redshift 5.5, the deficit in R and I band compared to a power-law extrapolation from J, H and K detections is well accounted by the IGM absorption. Additional local extinction is needed so an intrinsic broken power-law model can explain both the optical and the X-ray data. The local extinction model, amount of extinction and the intrinsic break frequency are selected manually to obtain a reasonable match judged by eye. Given the prelimanary optical/IR data, these quantities are only suggestive. Qualitatively, two conclusions can be made. There is

significant local extinction and a spectral break, close to the lower energy threshold of XRT, exists between optical and X-ray.

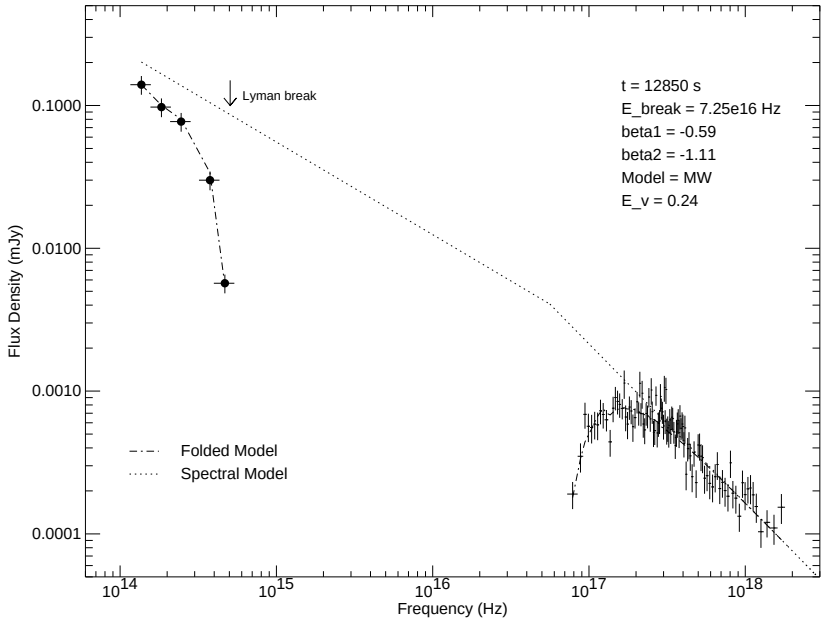

Fig. 3.6.—: Afterglow spectral energy distribution of GRB 071025. The R, I, J, H ,K data from the GCN circulars are interplated/extrapolated using the dotted line model in Figure 3.6 to the mean X-ray photon arrival time at T+12850 s. Error bars on the optical data points are approximated at 15% for each dimension. The model paramters are selected manually to obtain a reasonable match judged by eye.

3.3.3 GRB/XRF 080330

GRB 080330 triggered Swift/BAT at 03:41:16.9 UT (Trigger 308041, Mao et al., 2008). *Swift* slewed immediately to the burst. The XRT began observing the field 70.5 seconds after the BAT trigger in WT mode and detected a bright, fading, uncatalogued X-ray source. UVOT started a finding chart exposure with White filter at 82 seconds after the trigger and detected a 18.8 magnitude afterglow candidate. The BAT masked-weighted lightcurve shows four peaks between ∼T+0 sec to ∼T+70 sec (Markwardt et al., 2008b). T90 (15-350 keV) is 61 ± 9 sec. The fluence in the 15-150 keV band is $3.4 \pm 0.8 \times 10^{-7} erg/cm^2$. Based on the fluence ratio in the 25-50 keV

band and the 50-100 keV band and its low E_{peak} (Markwardt et al., 2008b; Guidorzi et al., 2009), this burst is classified as a X-ray flash according to (Sakamoto et al., 2008e).

Malesani et al. (2008) measured a redshift for this burst of z=1.51 and was confirmed by Cucchiara (2008). We adopt the best burst location as RA = $11^h17^m04^s.496$ Dec = $+30°37'23".53$, with an uncertainty of 0.7 arcsec (Bloom & Starr, 2008). Along the line of sight to this position, the galactic extinction is E(B-V)=0.017 (Schlegel et al., 1998), and the galactic column density is $1.2 \times 10^{20} cm^{-2}$ (Kalberla et al., 2005).

ROTSE-IIIb, located at McDonald Observatory, Texas, responded automatically upon receiving the GCN notice, starting the first exposure at 03:41:39.2 UT, 22.4 after the burst (7.2 s after the GCN notice time). A optical flare followed by a slow rising afterglow was detected at RA = $11^h17^m04^s.5$ Dec = $+30°37'24".0$ (J2000) and reported via GCN circular (Schaefer & Guver, 2008). Complete ROTSE-III lightcuve and the *Swift* high energy detections were shown in (Yuan et al., 2008w) together with the observations of GRB 080413A.

Figure 3.7 presents the multi-wavelength lightcurves of GRB 080330. A smoothly joint double broken power-law model is used to fit simultanously the optical detections after T+100s and the XRT detections after T+300s in the observer's frame. A complete study of the multi-wavelength observations of this burst is presented by (Guidorzi et al., 2009). The afterglow behaves accromatically from IR to X-ray. They also detected a late bump in the optical lightcurve after the emission dropped below ROTSE-III's detection threshold.

In the X-rays, the early emission can again be modeled with a rapid decaying prompt compoent and a afterglow rises as the same time as the optical afterglow. There might be a faint X-ray flare at T+200s (rest frame), displaying slightly harder

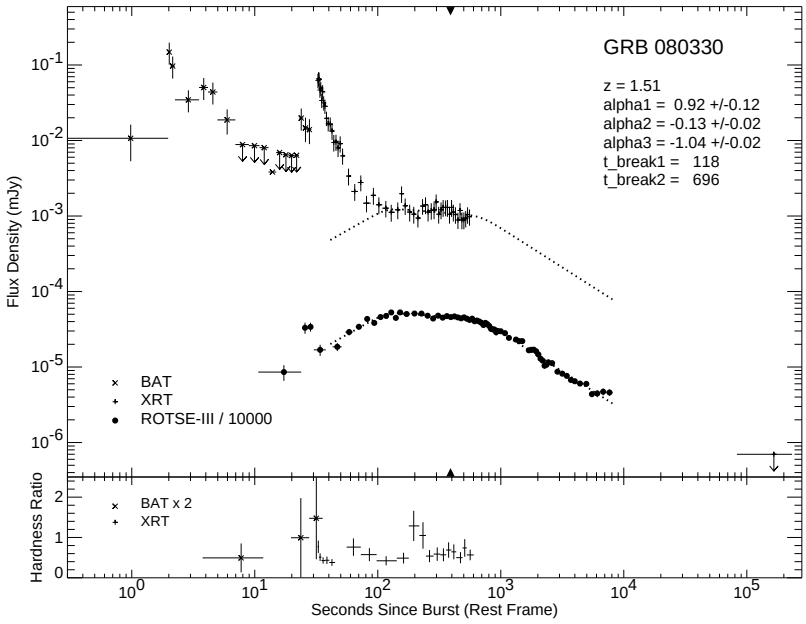

Fig. 3.7.—: Multi-wavelength lightcurve of GRB 080330. A smoothly joint double broken power-law model is over-plotted in dotted lines. Filled triangles on the X-axis mark the time when spectral index is calculated between optical and X-ray for Figure 3.16.

hardness ratio than the underlying afterglow. The X-ray lightcurve of this event was also discussed in (Zhang, 2009).

The late rise of the afterglow can either be explained as deceleration of forward shock with a low Lorentz factor or a senario where a structrued jet is observed off-axis. Both of these explanation can be related to the fact that this burst is classified as a XRF and the XRFs form a continous but apparently less energetic population than the GRBs.

3.3.4 GRB 080413A

GRB 080413A triggered Swift/BAT at 02:54:19.3 UT (Trigger 309096, Beardmore et al., 2008). *Swift* slewed immediately to the burst. The XRT began observing the field 60.7 seconds after the BAT trigger in WT mode and detected a bright uncatalogued X-ray source. UVOT started a finding chart exposure with White filter

at 76 seconds after the trigger and detected a 15.2 magnitude afterglow candidate. The BAT masked-weighted lightcurve shows four peaks between T-0.1 sec and ∼T+80 sec (Tueller et al., 2008a). T90 (15-350 keV) is 46 ± 1 sec. The fluence in the 15-150 keV band is $3.5 \pm 0.1 \times 10^{-6} erg/cm^2$. Joint spectrum from Suzaku/WAM and Swift/BAT between T-1 sec and T+22 sec is well fit by a power-law with exponential cutoff model, with photon index -1.2 and Epeak 170(-40,+80) keV (Ohno et al., 2008).

Thoene et al. (2008b) measured the absorption redshift of the burst to be z=2.433, which was confirmed by Cucchiara et al. (2008a). We adopt the best burst location as RA = $19^h09^m11^s.76$ Dec = $-27°40'40".27$, with an uncertainty of 0.5 arcsec (90% confidence, Oates & Marshall, 2008). Along the line of sight to this position, the galactic extinction is E(B-V)=0.155 (Schlegel et al., 1998), and the galactic column density is $8.7 \times 10^{20} cm^{-2}$ (Kalberla et al., 2005).

ROTSE-IIIc, located at the H.E.S.S. site at Mt. Gamsberg, Namibia, responded automatically upon receiving the GCN notice, starting the first exposure at 02:54:39.7 UT, 20.4 s after the burst (6.7 s after the GCN notice time). A 12.8 magnitude fading source, not visible in the DSS red plate, was detected at RA = $19^h09^m11^s.8$ Dec = $-27°40'41".6$ (J2000) and reported via GCN circular (Rykoff & Rujopakarn, 2008).

Figure 3.8 presents the multi-wavelength lightcurves of GRB 080413A. Both the optical and the X-ray lightcurves deviate from the broken power-law model over-plotted as dotted lines. The prompt burst emission displayed multiple flares. This flaring behavior continued in the X-ray band after the gamma-ray emission ended. In the optical, the emission dropped rapidly from the first to the second detection. This is followed by a flare, coincident with a gamma-ray peak. The optical lightcurve then decayed slowly and steepened smoothly, until about 100 s after the burst in the rest frame, when the flux slightly increased and started another shallow-to-steeper decay.

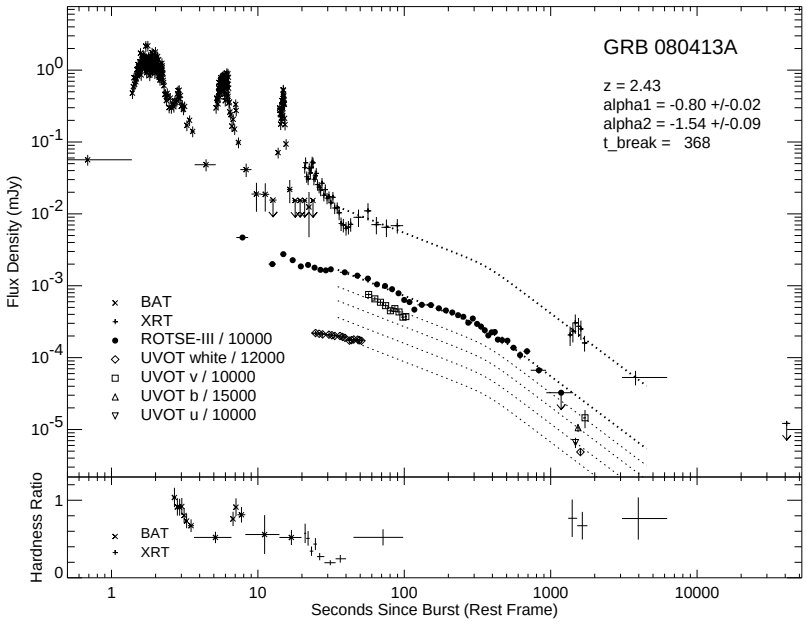

Fig. 3.8.—: Multi-wavelength lightcurve of GRB 080413A. A smoothly joint broken power-law model is over-plotted in dotted lines. Filled triangles on the X-axis mark the time when spectral index is calculated between optical and X-ray for Figure 3.16.

While the initial optical decay and flare may be associated with the prompt emission, the later smooth optical lightcurve is likely dominated by the afterglow emission in the forward shock. Given the complex lightcurve of the burst, the broad optical bump after 100 s could be due to additional energy injection into the forward shock by the late shells. It is, however, hard to directly compare the prompt and the afterglow structures.

3.3.5 GRB 080603B

GRB 080603B triggered Swift/BAT at 19:38:13.3 UT (Trigger 313087, Mangano et al., 2008a). *Swift* slewed immediately to the burst. The XRT began observing the field 68 seconds after the BAT trigger in WT mode and detected a bright uncatalogued X-ray source. UVOT started a finding chart exposure with the White filter at 72 seconds after the trigger and detected a 15.9 magnitude afterglow candidate. The

BAT masked-weighted lightcurve shows three clusters of peaks between T-1 sec and ∼T+80 sec (Tueller et al., 2008b). T90 (15-350 keV) is 60 ± 4 sec. The total fluence in the 15-150 keV band is $2.4 \pm 0.1 \times 10^{-6} erg/cm^2$. Konus-Wind was triggered by this burst on 19:38:12.4 UT (Golenetskii et al., 2008b) and measured the average E_{peak} to be around 100 keV. At redshift z=2.69 (Fynbo et al., 2008; Cucchiara & Fox, 2008a), the isotropic energy release is $E_iso \sim 7.7 \times 10^{52} erg$.

We adopt the best burst location as RA = $11^h46^m07^s.66$ Dec = $+68°03'39".99$, with an uncertainty of 0.3 arcsec (Kuin & Mangano, 2008). Along the line of sight to this position, the galactic extinction is E(B-V)=0.013 (Schlegel et al., 1998), and the galactic column density is $1.2 \times 10^{20} cm^{-2}$ (Kalberla et al., 2005).

ROTSE-IIId, located at the TUBITAK National Observatory at Bakirlitepe, responded automatically upon receiving the GCN notice, starting the first exposure at 19:38:36.2 UT, 22.9 s after the burst (8.3 s after the GCN notice). A 14.1 magnitude fading object, not visible in the DSS red plate, was detected at RA = $11^h46^m07^s.8$ Dec = $+68°03'39".9$. (J2000) and reported via GCN circular (Rujopakarn et al., 2008).

Figure 3.9 presents the multi-wavelength lightcurves of GRB 080603B. The UVOT detections and the R-band data obtained from the GCN circulars (Klotz et al., 2008b; Castro-Tirado et al., 2008; Klotz et al., 2008a; Xin et al., 2008; Kann et al., 2008; Rumyantsev & Pozanenko, 2008; Klunko & Pozanenko, 2008; Rumyantsev et al., 2008; Ibrahimov et al., 2008) are scaled to match the ROTSE-IIIb detections during overlapping periods, to demonstrate the overall optical evolution. The optical lightcurve shows a flare with similar temporal shape as the contemporaneous high energy emission. The two ROTSE detections before the flare may either be associated with prompt emission or part of a underlying decaying component. The optical lightcurve after the flare (starting about 200 s since burst in the rest frame) can be charac-

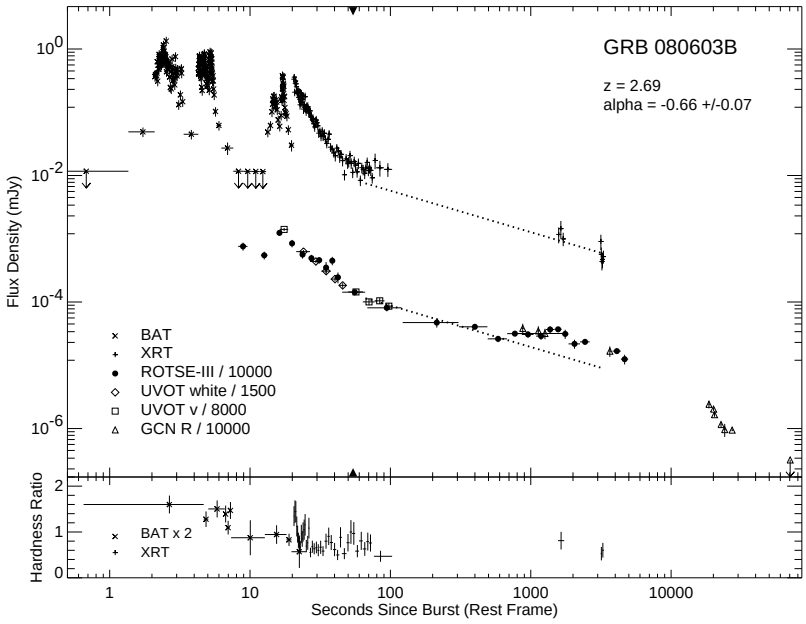

Fig. 3.9.—: Multi-wavelength lightcurve of GRB 080603B. A single power-law model is over-plotted in dotted lines. Filled triangles on the X-axis mark the time when spectral index is calculated between optical and X-ray for Figure 3.16.

terized by three segments of power-laws with two steepening breaks, which could be explained as cessation of energy injection and a jet break respectively. There is also a hint of an additional steep to shallow break or a slight rise in flux at around 600 s in the rest frame. The X-ray observation is too sparse at the time to see whether it behaves similarly as in the optical. With no color information, the increase of optical flux could be due to late energy injection or change of local extinction.

3.3.6 GRB 080607

GRB 080607 triggered Swift/BAT at 06:07:27.0 UT (Trigger 313417, Mangano et al., 2008c). *Swift* slewed immediately to the burst. The XRT began observing the field 82.1 seconds after the BAT trigger in WT mode and detected a bright uncatalogued X-ray source. UVOT started a finding chart exposure with the White filter at 92 seconds after the trigger and detected a 19.7 magnitude afterglow candidate. The

BAT masked-weighted lightcurve shows multiple peaks from ∼T-1 sec out to ∼T+180 sec (Stamatikos et al., 2008). T90 (15-350 keV) is 79 ± 5 sec. The fluence in the 15-150 keV band is $2.4 \pm 0.0 \times 10^{-5} erg/cm^2$. Konus-Wind was triggered by this burst on 06:07:23.3 UT (Golenetskii et al., 2008b) and measured the E_{peak} to be around 400 keV. At redshift z=3.036 (Prochaska et al., 2008), the estimated isotropic energy release, $E_iso = 1.87(-0.10, +0.11) \times 10^{54} erg$ is among the largest ever measured and the peak luminosity of $2.27 \pm 0.46 \times 10^{54} erg/s$ is the highest ever reported.

We adopt the best burst location as RA = $12^h59^m47^s.20$ Dec = $+15°55'10".74$, with an uncertainty of 0.5 arcsec (90% confidence, Mangano et al., 2008b). Along the line of sight to this position, the galactic extinction is E(B-V)=0.023 (Schlegel et al., 1998), and the galactic column density is $1.7 \times 10^{20} cm^{-2}$ (Kalberla et al., 2005).

ROTSE-IIIb, located at McDonald Observatory, Texas, responded automatically upon receiving the GCN notice, starting the first exposure at 06:07:49.0 UT, 22.0s after the burst (6.0 s after the GCN notice time). A 14.8 magnitude fading source, not visible in the DSS red plate, was detected at RA = $12^h59^m47^s.3$ Dec = $+15°55'10".8$ (J2000) and reported via GCN circular (Rujopakarn & Rykoff, 2008a).

Figure 3.10 presents the multi-wavelength lightcurves of GRB 080607. The prompt emission of this burst appears highly variable, displaying numerous resolved peaks, the last two of which were also detected in the X-rays. Hints of flaring can be seen before and after the XRT orbital gap. The optical detection, although starting during the burst, shows only low significance deviation from a smooth curve, probably due to insufficient time resolution. The last two ROTSE-IIIb detections showed higher optical flux above the earlier power-law decay. This might be due to a flare, with a possible X-ray counterpart whose tail was detected at around 1 ks in the rest frame. However, this conjecture is valid only if the flux drops back to the underlying power-

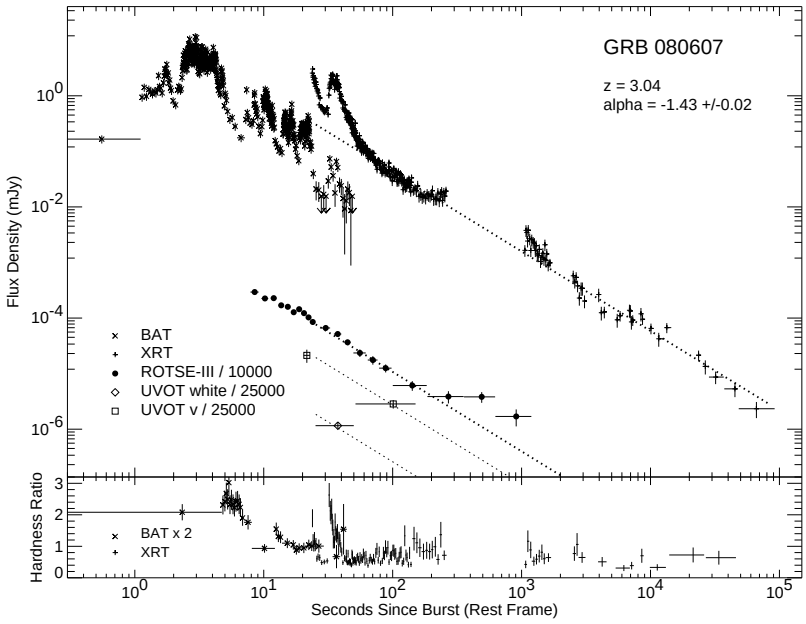

Fig. 3.10.—: Multi-wavelength lightcurve of GRB 080607. A single power-law model is over-plotted in dotted lines. Filled triangles on the X-axis mark the time when spectral index is calculated between optical and X-ray for Figure 3.16.

law decay, which is beyond the range of our data.

Spectroscopic observations of the bright afterglow of GRB 080607 have enabled direct studies of the star forming region at a high redshift. Through its line of sight, molecular gas was detected for the first time in a GRB host galaxy (Prochaska et al., 2009). Interestingly, GRB 080607 can be classified as a "dark burst" (Jakobsson et al., 2004) based on its shallow optical-to-X-ray spectral index (β_{ox} $\sim$0.2, see Figure 3.16). Prochaska et al. (2009) thus suggested that at least some of the "dark bursts" can be explained as intrinsically faint afterglows observed through intersecting molecular clouds. In another study by Sheffer et al. (2009), evidence of vibrationally excited H_2 was found toward the burst, confirming the predicted interaction between GRB and its intermediate environment.

3.3.7 GRB 080703

GRB 080703 triggered Swift/BAT at 19:00:11.5 UT (Trigger 315819, Ziaeepour et al., 2008). *Swift* slewed immediately to the burst. The XRT began observing the field 104 seconds after the BAT trigger in PC mode and detected a bright uncatalogued X-ray source. UVOT started a finding chart exposure with the White filter at 100 seconds after the trigger and detected a 17.6 magnitude afterglow candidate. The BAT masked-weighted lightcurve shows a single peak between ∼T-5 sec and ∼T+4 sec (Sakamoto et al., 2008a). T90 (15-350 keV) is 3.4 ± 0.8 sec. The fluence in the 15-150 keV band is $2.0 \pm 0.3 \times 10^{-7} erg/cm^2$.

We adopt the best burst location as RA = $06^h47^m12^s.639$ Dec = $-63°13'08".96$, with an uncertainty of 0.5 arcsec (Ward & Ziaeepour, 2008). Along the line of sight to this position, the galactic extinction is E(B-V)=0.071 (Schlegel et al., 1998), and the galactic column density is $5.1 \times 10^{20} cm^{-2}$ (Kalberla et al., 2005).

ROTSE-IIIa, located at Siding Spring Observatory, Australia, responded upon receiving the GCN notice, starting the first exposure at 19:00:45.1 UT, 31.5 s after the burst (11.1 s after the GCN notice time). A 14.7 magnitude source, not visible in the DSS red plate, was detected at RA = $06^h47^m12^s.7$ Dec = $-63°13'08".6$ (J2000) and reported via GCN circular (Rykoff & Schaefer, 2008).

Figure 3.11 presents the multi-wavelength lightcurves of GRB 080703. The prompt emission for this burst is relatively faint and composed of a single peak. The afterglow, however, has complicated structure. A broad hump, from about 30 to 100 s in the burst rest frame, is visible in both the optical and the X-ray lightcurves. An earlier bump is seen in optical and there is hint of a short flare at around 100 s. Additional flaring is suggested by the X-ray detection between 200 and 400 s, when the optical data is comparatively less well sampled. The time-scale of the variability is in the

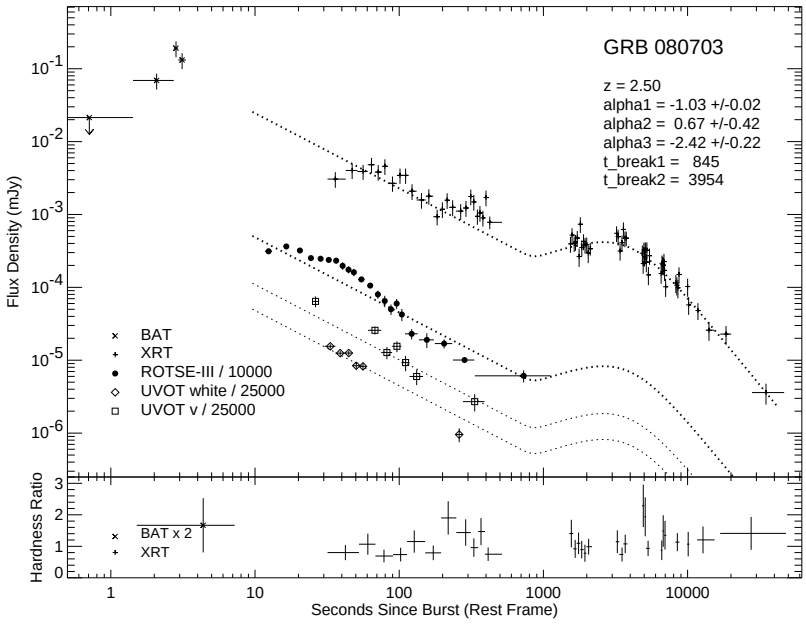

Fig. 3.11.—: Multi-wavelength lightcurve of GRB 080703. A smoothly joint double broken power-law model is over-plotted in dotted lines. Filled triangles on the X-axis mark the time when spectral index is calculated between optical and X-ray for Figure 3.16.

order of a few tens of seconds. The early fluctuating emission can thus be the results of forward shock going through a clumpy external medium near the burst location.

After about 1 ks post-burst, only X-ray observation is available and the lightcurve becomes relatively smooth. Although the broken power-law model over-plotted in Figure 3.11 suggests a rise between 1 and 4 ks, this is likely affected by our choice to include the early data in the fit. A flat curve should describe this segment equally well. The steepening at 4 ks can be explained as the end of continuous energy injection into the forward shock, while the last segment of the lightcurve decays fast as expected after a jet-break.

3.3.8 GRB 080804

GRB 080804 triggered Swift/BAT at 23:20:14.7 UT (Trigger 319016, Racusin et al., 2008a). *Swift* slewed immediately to the burst. The XRT began observing the field

99 seconds after the BAT trigger in WT mode and detected a bright uncatalogued X-ray source. UVOT started a finding chart exposure with the White filter at 109 seconds after the trigger and detected a 16.8 magnitude afterglow candidate. The BAT masked-weighted lightcurve shows one main peak between ∼T-10 sec and ∼T+100 sec (Markwardt et al., 2008a). T90 (15-350 keV) is 34 ± 16 sec. The fluence in the 15-150 keV band is $3.6 \pm 0.2 \times 10^{-6} erg/cm^2$. Thoene et al. (2008a) measured an absorption redshift of z=2.2045 for this burst, which was confirmed by Cucchiara et al. (2008e).

We adopt the best burst location as RA = $21^h54^m40^s.20$ Dec = $-53°11'04".6$, with an uncertainty of 0.4 arcsec (90% confidence, Kuin & Racusin, 2008). Along the line of sight to this position, the galactic extinction is E(B-V)=0.016 (Schlegel et al., 1998), and the galactic column density is $1.6 \times 10^{20} cm^{-2}$ (Kalberla et al., 2005).

ROTSE-IIIc, located at the H.E.S.S. site at Mt. Gamsberg, Namibia, responded automatically upon receiving the GCN notice, starting the first exposure at 23:20:34.3 UT, 19.6 s after the burst (6.3 s after the GCN notice time). A 17.2 magnitude brightening source, not visible in the DSS red plate, was detected at RA = $21^h54^m40^s.1$ Dec = $-53°11'03".8$ (J2000) and reported via GCN circular (Rujopakarn & Rykoff, 2008b).

Figure 3.12 presents the multi-wavelength lightcurves of GRB 080804. r-band detections by GROND from the GCN circular (Kruehler et al., 2008) are scaled to match the last ROTSE-IIIc points. The optical lightcurve of GRB 080804 has a similar shape as that of GRB 080330, rising initially, followed by a shallow decay and subsequent steepening. Additional flattening is suggested after 1 ks by the late GROND and UVOT observations (Kruehler et al., 2008, α measured as 0.87±0.03 in). However, no change in the decay rate is detected in the X-rays from 100 to 10^5 s

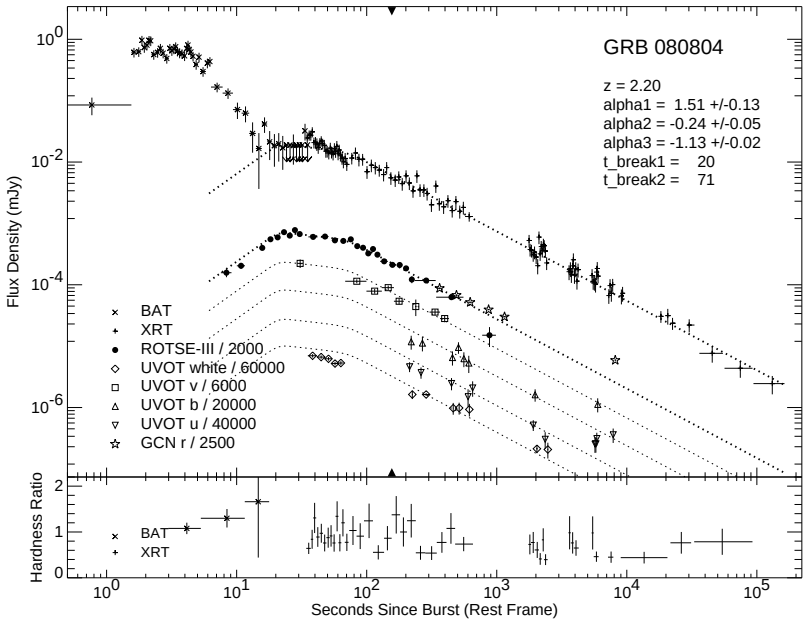

Fig. 3.12.—: Multi-wavelength lightcurve of GRB 080804. A smoothly joint double broken power-law model is over-plotted in dotted lines. Filled triangles on the X-axis mark the time when spectral index is calculated between optical and X-ray for Figure 3.16.

post-burst.

3.3.9 GRB 080928

GRB 080928 triggered Swift/BAT at 15:01:32.9 UT (Trigger 326115, Sakamoto et al., 2008c). *Swift* slewed immediately to the burst. The XRT began observing the field 170 seconds after the BAT trigger in WT mode and detected a bright uncatalogued X-ray source. UVOT started a finding chart exposure with the White filter at 179 seconds after the trigger and detected a 19.2 magnitude afterglow candidate. The BAT masked-weighted lightcurve shows two faint peaks at ∼T+0 sec and ∼T+60 sec and the main emission is between ∼T+170 sec and ∼T+400 sec(Fenimore et al., 2008). T90 (15-350 keV) is 280 ± 30 sec. The fluence in the 15-150 keV band is $2.5 \pm 0.2 \times 10^{-6} erg/cm^2$. Fermi GBM was triggered by this event at 15:04:56 UT (Paciesas et al., 2008). The fluence between 50 and 300 keV during the 87 seconds

duration is $(1.5 \pm 0.1) \times 10^{-6} erg/cm^2$.

Vreeswijk et al. (2008) measured an absorption redshift of z=1.692 for this burst, which was confirmed by Cucchiara & Fox (2008b). We adopt the best burst location as RA = $06^h20^m16^s.836$ Dec = $-55°11'58".95$, with an uncertainty of 0.5 arcsec (90% confidence, Kuin et al., 2008). Along the line of sight to this position, the galactic extinction is E(B-V)=0.067 (Schlegel et al., 1998), and the galactic column density is $5.6 \times 10^{20} cm^{-2}$ (Kalberla et al., 2005).

ROTSE-IIIa, located at Siding Spring Observatory, Australia, responded automatically upon receiving the GCN notice, starting the first exposure at 15:03:44.9 UT, 132.0 s after the burst (7.9 s after the GCN notice time). A fluctuating optical counterpart was detected at RA = $06^h20^m17^s.0$ Dec = $-55°11'58".8$ (J2000) and reported via GCN circular (Rykoff et al., 2008).

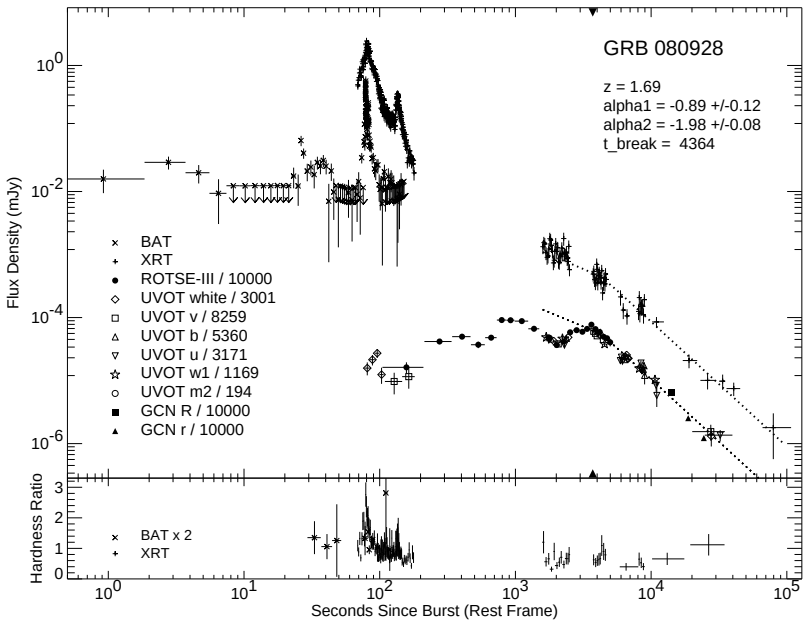

Fig. 3.13.—: Multi-wavelength lightcurve of GRB 080928. A smoothly joint broken power-law model is over-plotted in dotted lines. Filled triangles on the X-axis mark the time when spectral index is calculated between optical and X-ray for Figure 3.16.

Figure 3.13 presents the multi-wavelength lightcurves of GRB 080928. The UVOT

detections, the r and R-band data obtained from the GCN circulars (Rossi et al., 2008; Ferrero et al., 2008) are scaled to match the ROTSE-IIIa detections during overlapping periods, to demonstrate the overall optical evolution. The early optical lightcurve of this burst is highly unusual with at least three broad peaks detected by ROTSE-IIIa. The variation may either be related to high energy flares or due to fluctuation in the external forward shock, e.g. from late energy injection. Lack of contemporaneous X-ray data and broad-band optical observation makes it hard to test the different possibilities. The X-ray lightcurve, starting about 2 ks in the rest frame, however, does not show a corresponding rise as in the optical. This is probably because the X-ray emission is from a different origin, e.g. dominated by internal emission, before it started to decay at a same rate as in the optical after 5 ks.

The gamma-ray emission of this burst was detected by both *Swift* and Fermi/GBM. (Rossi et al., 2010) present the broadband observations of the event and interpret the rising optical lightcurve shortly after 2 ks as the onset of afterglow. Using the late time multi-wavelength data, they model the afterglow emission as from forward shock propagating in a ISM medium with a cooling frequency above X-ray during the whole observation period.

3.3.10 GRB 081029

GRB 081029 triggered Swift/BAT at 01:43:56.1 UT (Trigger 332931, Sakamoto et al., 2008d). *Swift* did not slew to the burst immediately due to an Earth limb constraint. The BAT masked-weighted lightcurve shows a single peak between ∼T-50 sec and ∼T+300 sec (Cummings et al., 2008). T90 (15-350 keV) is 270 ± 45 sec. The fluence in the 15-150 keV band is $2.1 \pm 0.2 \times 10^{-6} erg/cm^2$. The XRT began observing the field 2711 seconds after the BAT trigger in PC mode and detected a fading X-ray afterglow. UVOT observation started 2708 sec after the trigger and

detected the afterglow in v, b and white filters (Holland et al., 2008).

D'Elia et al. (2008) measured an absorption redshift of z=3.8479 ± 0.0002 for this burst, which was confirmed by Cucchiara et al. (2008d). We adopt the best burst location as RA = $23^h07^m05^s.35$ Dec = $-68°09'19".8$, with an uncertainty of 0.5 arcsec (90% confidence, Holland et al., 2008). Along the line of sight to this position, the galactic extinction is E(B-V)=0.031 (Schlegel et al., 1998), and the galactic column density is $2.8 \times 10^{20} cm^{-2}$ (Kalberla et al., 2005).

ROTSE-IIIc, located at the H.E.S.S. site at Mt. Gamsberg, Namibia, responded automatically upon receiving the GCN notice, starting the first exposure at 01:45:22.8 UT, 86.0 s after the burst (8.8 s after the GCN notice time). A 16.5 magnitude fading source, not visible in the DSS red plate, was detected at RA = $23^h07^m05^s.36$ Dec = $-68°09'19".74$ (J2000) and reported via GCN circular (Rykoff, 2008b).

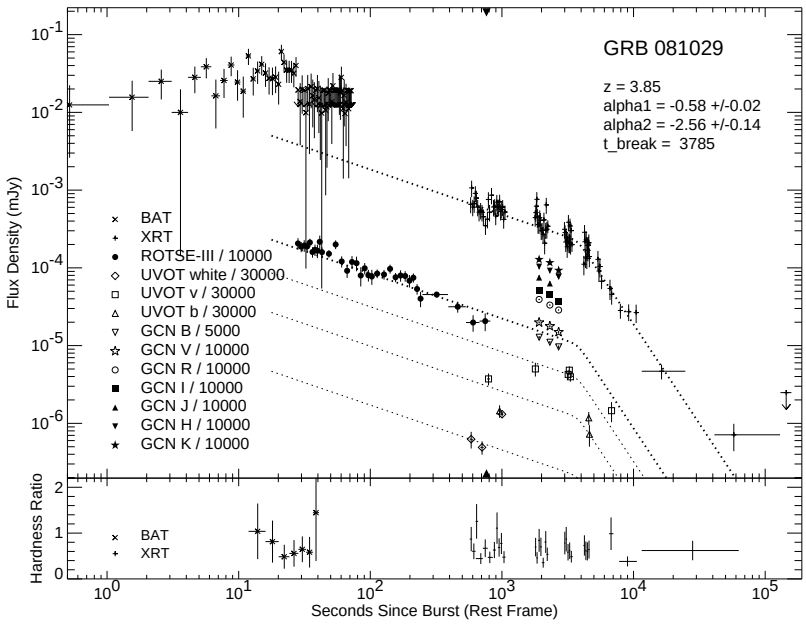

Fig. 3.14.—: Multi-wavelength lightcurve of GRB 081029. A smoothly joint broken power-law model is over-plotted in dotted lines. Filled triangles on the X-axis mark the time when spectral index is calculated between optical and X-ray for Figure 3.16.

Figure 3.14 presents the multi-wavelength lightcurves of GRB 081029, with B, V,

R, I, J, H, K-band observations from GCN circular (Cobb, 2008a). The optical and late X-ray lightcurves display a typical shallow to steep decay. Before the temporal break, the decay is too shallow to be explained as forward shock emission without contribution from continuous energy injection. The interpretation that the break results from termination of energy injection is supported by its likely achromatic behavior. Possible deviation from the smooth decay is also detected at early times, suggesting a potential connection to the internal activity.

3.3.11 GRB 081121

GRB 081121 triggered Swift/BAT at 20:35:32.8 UT (Trigger 335105, Oates et al., 2008). *Swift* did not slew to the burst immediately due to an Earth limb constraint. The BAT masked-weighted lightcurve shows a main pulse between ∼T-10 sec and ∼T+15 sec and hint of precursor starting before T-119 sec (Sakamoto et al., 2008b). T90 (15-350 keV) is 14 ± 2 sec. The fluence in the 15-150 keV band is $4.1 \pm 0.3 \times 10^{-6} erg/cm^2$. Konus-Wind was triggered by this burst at 20:35:31.4 UT and measured the E_{peak} to be around 250 keV (Golenetskii et al., 2008a). At redshift of z=2.512 (Berger & Rauch, 2008), this isotropic energy release $E_iso \sim 2.7 \times 10^{52} erg$. Fermi GBM was triggered by this event at 20:35:27.5 UT.

The XRT began observing the field 2826 seconds after the BAT trigger in PC mode and detected a fading X-ray afterglow. UVOT observation started 2816 sec after the trigger and detected the afterglow in white, v, b, u, and uvw1 filters (Oates, 2008). We adopt the best burst location as RA = $05^h57^m06^s.15$ Dec = $-60°36'10".0$, with an uncertainty of 0.6 arcsec (90% confidence, Oates, 2008). Along the line of sight to this position, the galactic extinction is E(B-V)=0.051 (Schlegel et al., 1998), and the galactic column density is $4.0 \times 10^{20} cm^{-2}$ (Kalberla et al., 2005).

ROTSE-IIIc, located at the H.E.S.S. site at Mt. Gamsberg, Namibia, responded

automatically upon receiving the GCN notice, starting the first exposure at 20:36:30.0 UT, 57.2 s after the burst (8.9 s after the GCN notice time). A 11.6 magnitude fading source, not visible in the DSS red plate, was detected at RA = $05^h57^m06^s.1$ Dec = $-60°36'10".3$ (J2000) and reported via GCN circular (Yuan & Rujopakarn, 2008).

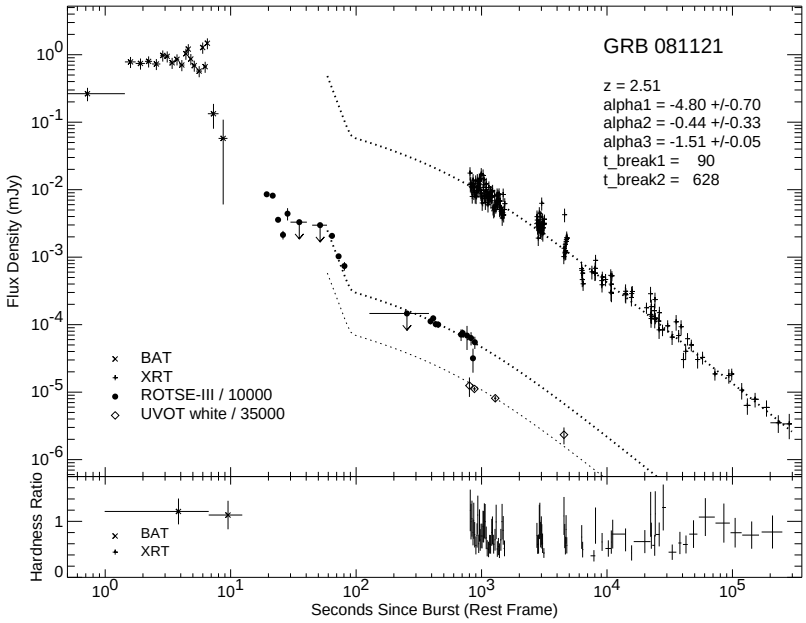

Fig. 3.15.—: Multi-wavelength lightcurve of GRB 081121. A smoothly joint double broken power-law model is over-plotted in dotted lines. Filled triangles on the X-axis mark the time when spectral index is calculated between optical and X-ray for Figure 3.16.

Figure 3.15 presents the multi-wavelength lightcurves of GRB 081121. The early optical lightcurve is highly variable, displaying at least two steep decaying segments starting at 20 and 60 s post-burst in the rest frame. Passing clouds at the ROTSE-IIIc site resulted in fluctuating seeing conditions and discontinuous temporal coverage of the OT. Nevertheless, additional variation in the optical brightness is hinted between 30 and 60 s post-burst. This behavior in the optical resembles that typically observed in the X-rays shortly after the burst, often interpreted as the soft tail of the prompt emission. Unfortunately, no contemporaneous X-ray observation is available to confirm this correlation. At $\sim$1 ks post-burst, the decay rate observed by ROTSE-IIIc

agrees with that in the X-ray. However, fluctuation in the X-ray hardness ratio curve may hint at superimposed flaring. At later times, a shallower decay in the optical is suggested by the UVOT data and as reported in the GCN circulars (Cobb, 2008b).

3.4 Early Behavior of GRBs

3.4.1 High Energy Observations

The prompt emission can be composed of single or multiple pulses. Its hardness ratio curves show correlated temporal variability with the burst lightcurve. The pulse usually hardens as it rise and then softens during the decay. Similar behavior is observed during the X-ray flares, confirming their internal origin.

3.4.2 Optical and X-ray Spectra

For each of the above bursts, the spectral index between optical and X-ray (β_{ox}) was calculated at one epoch (marked with filled triangles on the X-axis in the lightcurve figures) and compared to its X-ray spectral index (β_x) in Figure 3.16. All the X-ray spectral indices are obtained from automatic fitting of the average PC mode spectra (Evans et al., 2007), except for 080603B. For this later event, the average WT mode spectral index is used because it is consistent with but better constrained than the parameter for the PC mode.

The fluxes in optical and X-rays are obtained from the fitted models as shown in the previous lightcurve figures. The errors are estimated from sampling the model population assuming a normal distribution for each parameter. To minimize the effect of inaccurate models, the time is chosen to be as close as possible to when both optical and X-ray data points are well fitted by the model (see the lightcurve figures). For all the bursts, the hardness ratio curves show no evidence for significant spectral evolution during the time that the average spectral index is calculated, and between

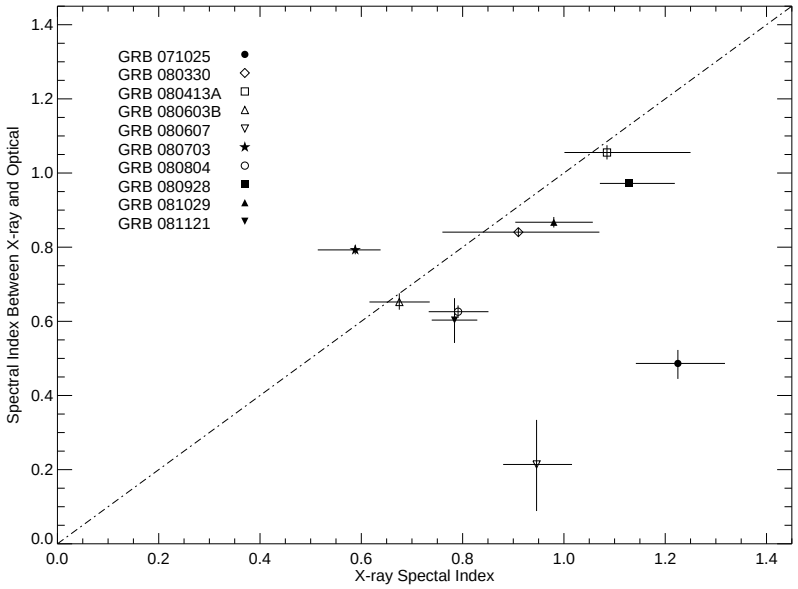

Fig. 3.16.—: Optical-to-X-ray spectral indices vs. X-ray spectral indices.

this period and the chosen epoch for β_{ox} calculation.

GRB 080703 is the only event for which β_{ox} is greater than β_x. However, broad flares are presented around the time and cannot be avoided due to the limited coverage of optical observations. Therefore the spectrum may result from multiple emission regions.

The smaller value of β_{ox} than β_x is consistent with optical and X-rays from one synchrotron component with the cooling break frequency below the optical or between optical and X-ray. This result agrees with the studies of earlier ROTSE-III observations (Rykoff et al., 2009).

3.4.3 Optical and Hard X-ray (BAT) Spectra

For selected bursts with prompt optical detections, we extract the BAT counts in the same time bins as the ROTSE-III observations and calculate the spectral index between BAT and optical for each period. These are compared with the spectral

indices within BAT energy range in Figure 3.17.

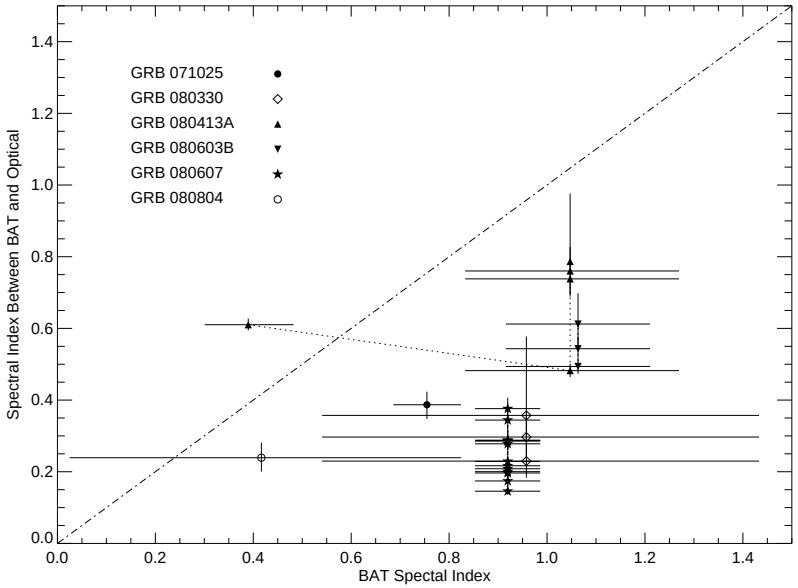

Fig. 3.17.—: Optical-to-BAT spectral indices vs. BAT spectral indices.

For all bursts except GRB 080413A, an average BAT spectral index is obtained for the entire period overlapping with the ROTSE-III observations. Breaking these spectra into smaller time bins only increases the error bar of each index, but reveals no significant evolution. For GRB 080413A, the first ROTSE-III image was taken during decay of the second to last BAT pulse which is significantly harder than the last one. This is also the only epoch for which we find an optical flux that lies above the extrapolation from BAT. In such a situation, as for GRB 080319B, the overall spectrum cannot be explained by a single synchrotron component. The distribution found here is generally consistent with earlier studies of the prompt emission spectra by (Yost et al., 2007).

3.4.4 Conclusion

Excluding the early rapid decay in X-ray and the apparent flares in either X-ray or optical, ROTSE-III observations show no contradiction to X-ray and optical fluxes following the same or similar power-law decay behavior. This is no surprise if both are from the same external forward shock origin. Correlated spectral study also support a synchrotron mechanism for the emission.

Prompt optical observations show a diversified behavior and cannot always be explained by optical and gamma-ray from the same synchrotron component. For a few events (e.g. GRB 080603B and GRB 080928), we observed broad optical flares not necessarily accompanied by X-ray counterparts. The origin of these features are still uncertain. Broadband observations will be useful to establish the color evolution during these flares and therefore constrain their nature.

CHAPTER IV

ROTSE Supernova Verification Project

4.1 Introduction

Supernovae (SNe) are luminous stellar explosions, releasing a slightly smaller amount of energy than GRBs, on the order of 10^{51} erg. They often rise to peak optical luminosity in a few weeks and then slowly decay and remain visible in optical for several weeks to months. They therefore allow studies in a longer time-scale than GRBs. SNe are exciting targets in the transient sky because of their connection to stellar evolution and possible application as tools to probe the history of the universe. At least some GRBs are associated with specific types of SNe (see §2.2.3). Their relationship provides an important clue on the nature of their progenitor.

There are several recent and ongoing dedicated supernova search projects. Some target nearby galaxies, such as the Lick Observatory Supernova Search (LOSS). Some emphasize the building of a large data set for cosmological studies, such as the Nearby Supernova Factory (SNfactory) and SuperNova Legacy Survey (SNLS). In year 2008 and early 2009, supernovae are discovered at an average rate of $\sim$1/day.

While ROTSE-III cannot compete in the depth and production rate with these surveys, ROTSE-III's 3.5deg^2 field-of-view makes it possible to monitor a large area of the sky on a daily basis and thus conduct a less spatially biased (not targeted

towards the near-by galaxies) transient survey on a daily time-scale. With a typical limiting magnitude of 18.5, a ROTSE-III telescope can discover a near-by ($\sim$100 pc) type Ia SNe within the first day of explosion and trigger spectroscopic observations at the earliest possible time. This was the goal of Robert Quimby when he started the Texas Supernova Search (TSS) (Quimby, 2006) with ROTSE-IIIb and a target-of-opportunity program with the Hobby-Eberly Telescope (HET) at the McDonald observatory. HET's location (right next to ROTSE-IIIb) and its queue-scheduled operation make it an ideal follow-up instrument for ROTSE-IIIb discoveries.

Although the goal of a first-day type Ia has not been reached, TSS has made several early discoveries of SNe that leads to multi-epoch spectral follow-ups throughout their lifetime. TSS also discovered some of the most luminous supernovae, e.g. the record holder SN 2005ap (Quimby et al., 2007e) and SN 2006gy (Ofek et al., 2007; Smith et al., 2007). It is particularly intriguing that the moderate-sized ROTSE-III are discovering a high rate of abnormal events. It was therefore worth the effort to continue this survey after Quimby graduated. Even at a time that a new generation of transient projects, such as the Palmer Transient Factory (PTF) and Pan-STARRS, are starting to produce discoveries at an unprecedented rate, ROTSE-III can make its contribution by discovering and triggering early follow-ups of interesting and unexpected events.

In this chapter, I will describe the ROTSE Supernova Verification Project (RSVP), a succession and extension of TSS, utilizing all four ROTSE-III telescopes in a quasi-realtime transient search. I will outline the science motivations of RSVP in §4.2, present our image subtraction approach in §4.3 and describe the data flow in §4.4.

4.2 Science Goals

Based on the absence or presence of hydrogen Balmer lines in their spectra at maximum brightness, SNe are respectively classified into two types, Type I and Type II. Both categories are further divided into subtypes based on spectral and lightcurve features. It is believed that Type II, Ib and Ic SNe result from the core-collapse (CC) of massive stars, while Type Ia SNe are the thermonuclear explosions of white dwarfs (see Filippenko, 1997, for a review).

RSVP is motived to discover more of the ultra-luminous SNe, enriching the data set and provide further evidence to investigate their explosion mechanism. Besides, we still seek the opportunity to better understand the physics of type Ia supernova by discovering SNe Ia at very early phases and triggering spectral follow-up throughout its evolution.

4.2.1 Ultra-luminous SNe

4.2.1.1 Making of a CC SN

Massive stars, with main sequence masses greater than about 8 solar masses ($M_\odot$) go through stages of nuclear burnings until an iron core is produced (see Woosley et al., 2002, for a nice review of the evolutions and explosions of massive stars). When the nuclear fuel is burned up, the core collapses under its own gravitational pressure. It would subsequently bounce and launch a shock (possibly revived by neutrino energy deposition, Colgate & White, 1966; Bethe & Wilson, 1985; Bethe, 1990) that explode the star. A neutron star (or sometimes a black hole) is left behind.

Mass loss, through radiatively driven winds (Kudritzki & Puls, 2000; Vink et al., 2001) or nuclear pulsations (Schwarzschild & Härm, 1959; Appenzeller, 1970; Papaloizou, 1973a,b; Glatzel & Kiriakidis, 1993; Osaki, 1986), has a critical impact on

the evolution of massive stars. For example, a Wolf-Rayet star can lose as much as 10^{-5} $M_{\odot}$ per year through strong stellar winds (Hamann et al., 1995; Hamann & Koesterke, 1998) (compared to about 10^{-14} $M_{\odot}yr^{-1}$ for the sun). If the hydrogen envelope of the progenitor is intact at the time of core collapse, a type II supernova is observed. A more massive star (with $M \gtrsim 35$ $M_{\odot}$) may shed its hydrogen envelope entirely (Schaller et al., 1992; Meynet et al., 1994) and explode as a type Ib SN. If the helium layer is also mostly removed, a type Ic is detected. The link between type II and type Ib/c is strengthened by cross-over types, e.g. SN 1993J (Filippenko et al., 1993; Schmidt et al., 1993), which started as a type II-like but evolved to resemble a type Ib. The progenitor of such a type IIb event may have shed most of its hydrogen and have a helium-rich envelope. Existence of a binary companion helps to strip the outer layers of a star through mass transfer and thus alter its evolutionary path (see Table 4.1 from Wellstein & Langer, 1999; Woosley et al., 2002).

If the remnant core mass is just slightly above the maximum stable neutron star mass, the star might explode and then collapse again into a black hole (Bethe & Brown, 1995; Pons et al., 1999). If the initial shock do not have sufficient energy to unbind the material outside the core, some matter will fall back into the remnant to make a black hole(MacFadyen et al., 2001). Otherwise, a black hole can form when the shock fails to be launched (MacFadyen et al., 2001). Accretion onto a rapidly rotating black hole may power bi-polar relativistic jets that could produce a cosmic gamma-ray burst (collapsar model, Woosley, 1993; Jaroszynski, 1996; MacFadyen & Woosley, 1999). To avoid the dissipation of jet energy, the gamma-ray burst progenitor should have depleted its hydrogen envelope prior to core collapse. GRBs are thus associated with type Ib/c SNe.

4.2.1.2 Powering of a CC SNe

CC SNe span a wide range of luminosity. Although they are typically fainter than the thermonuclear SNe (SNe Ia), exceptionally luminous CC SNe, an order of magnitude brighter than SNe Ia, have been observed. ROTSE-IIIb has made a significant constribution in this realm by discovering 5 out of 6 of the most luminous SNe (3 by TSS and 2 by RSVP, see Figure 4.1 and Table 4.2 for the details).

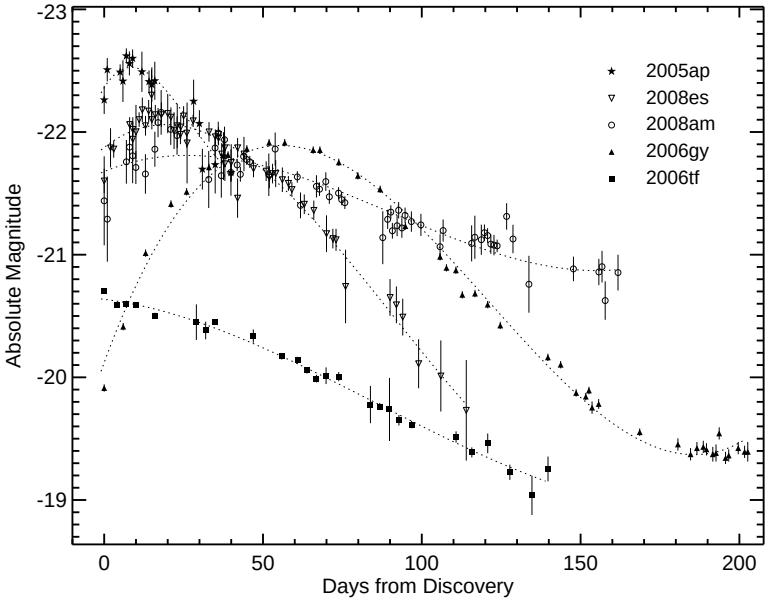

Fig. 4.1.—: Optical lightcurves of the ultra-luminous SNe (Quimby et al., 2007e; Smith et al., 2007, 2008; Gezari et al., 2009). Overplotted as dotted lines are the polynomial fit to the lightcurves.

Several mechanisms may contribute in powering the optical lightcurve of a CC SNe. Thermal emission from hydrogen recombination is believed to power the prolonged plateau phase observed in a type II-plateau supernova (SN II-P) (e.g. Popov, 1993). Interaction with optically thin circumstellar medium (CSM) can efficiently convert the blast wave energy into radiation and generate high luminosity seen in some type II supernovae exhibiting narrow emissions lines (SNe II-n) (e.g. Chevalier & Fransson, 1994; Chugai et al., 2004). Alternatively, if the shocked circumstellar envolope is

dense and opaque, thermal diffusion of the shock-deposited energy may domiate at early times (Smith & McCray, 2007). Radioactive decay of ^{56}Ni and the subsequent ^{56}Co decay provide another energy source, as supported by the observed late time lightcurve decay rates in some events (e.g. Clocchiatti & Wheeler, 1997).

Table 4.2 lists the primary power sources proposed for the ultra-luminous events. Note that for the type II-Linear (SNe II-L) events, narrow emission lines as characteristic feature of interaction with optically thin CSM, were not observed. Radioactive decay of ^{56}Ni was not sufficient to power the peak luminosity since a modest envolope mass was required by the relatively fast rise and decay. Diffusion of the shock-deposited energy in an opaque envolope thus provide an possible explanation.

SN 2006gy was an intriguing case, where although a weak H_α line was observed, the interaction between the ejecta and an optically thin CSM was too weak to account for the total luminosity, given a mass loss rate inferred from X-ray emission (Smith et al., 2007). Thermal diffusion through an opaque shell may play a role (Smith & McCray, 2007). The observed properties are also consistent with being powered by radioactive decay of $\sim$20 $M_\odot$ of ^{56}Ni (Smith et al., 2007). Such a large Ni mass would require SN 2006gy to be a pair-instability SN where the core of a massive star is obliterated.

Pair-instability explosion (Barkat et al., 1967; Bond et al., 1984; Heger & Woosley, 2002) is relevant for a main sequence star between 100 $M_\odot$ and 260 $M_\odot$. Such a star evolves into its presupernova stage with a helium core greater than 40 $M_\odot$. During contraction after helium burning, the kinetic energy is converted into creation of electron-positron pairs that leads to a runaway collapse. If nuclear burning is not sufficient to stop the contraction, the star bounces and explodes. Above 140 $M_\odot$, the core is completely disrupted. For a main sequence mass between 100 $M_\odot$ and

Table 4.1. Remnants and expected type of supernova from massive stars with solar metallicity.

Initial Mass ($M_\odot$)	Binary mass transfer Case A[1]	Case B[2]	Case C[3]	Single star
8...13			SN Ib	SN IIp
	WD	WD	NS	NS
13...16		SN Ib/Ic	SN Ib	SN IIp
	WD	NS	NS	NS
16...25	SN Ib	SN Ib	SN Ib	SN IIp
	NS	NS	NS	NS
25...35	SN Ic	SN Ic	SN Ib	SN IIL
	NS	NS	BH	BH
> 35	SN Ic	SN Ic	SN Ib	SN Ic
	NS/BH	NS/BH	NS/BH	NS/BH

[1]Case A: mass transfer occurs during core hydrogen burning;

[2]Case B: mass transfer occurs after hydrogen depletion;

[3]Case C: mass transfer occurs after helium depletion.

Note. — This table is adapted Wellstein & Langer (from 1999); Woosley et al. (from 2002).

Table 4.2. Ultra-luminous SNe.

SN name	Peak Magnitude	Type	Proposed Power Source
2005ap	-22.7[1]	II-L	CSM interaction or spin-down of a magnetar[1]
2006gy	-22.0[2,3]	II-n	pair instability SN[3,4]or CSM interaction[2,5]
2006tf	<-20.7[6]	II-n	CSM interaction[6]
2008am	-22.1[7]	II-n	CSM interaction[8]
2008es	-22.2[9]	II-L	CSM interaction[9,10]

Note. — References:(1): Quimby et al. (2007e), (2): Ofek et al. (2007), (3): Smith et al. (2007), (4): Woosley et al. (2007), (5): Smith & McCray (2007), (6): Smith et al. (2008), (7): Yuan et al. (2008s), (8): Chatzopoulos et al. (2010), (9): Gezari et al. (2009), (10): Miller et al. (2009)

140 $M_\odot$, pair instability leads to violent mass-ejection pulsations (Heger & Woosley, 2002). Collision between these ejected shells may produce a bright event.

SN 2006gy was the first observational candidate for a pair-instablitiy supernova (Smith et al., 2007). Woosley et al. (2007) also proposed pulsational pair instability as a possible interpretation. At solar metallicity, mass loss during the main-sequence and post-main-sequence phases will likely shed much of the initial mass and prevent the onset of pair instability. In the early universe, however, more massive stars can exist with lower mass loss due to low metallicity. The pair instability path is thus particular interesting for understanding the population III stars.

More ulra-luminous events are yet to be discovered by ROTSE-III and other coming synoptic surveys to improve our understanding of CC SNe and stellar evolution in diverse enviroments.

4.2.2 SNe Ia

4.2.2.1 SNe Ia Diversity

Stars with initial masses less than 8 $M_\odot$ end up as white dwarfs. Supported by electron degeneracy pressure, white dwarfs can sustain masses up to the Chandrasekhar limit of about 1.4 $M_\odot$. If a white dwarf accretes mass from a binary companion and reaches the Chandrasekhar limit, nuclear fusion is ignited and the thermal runaway reaction will generate enough energy to unbind the whole star. Since the explosions happen at the Chandrasekhar limit, all SNe Ia should release similar amounts of energy and reach the same intrinsic peak luminosity. Hence, they can be used as standard candles to measure the distance to their host galaxies and probe the expansion history of the universe. In reality, varying pre-explosion composition and burning conditions result in a dispersion in the observed lightcurve evolution. A tight correlation was found between the lightcurve width and the peak luminosity

(the Phillips relation, Phillips, 1993; Phillips et al., 1999). Using such empirical calibration, observations of type Ia SNe provided the first evidence for an accelerating universe (Perlmutter et al., 1999; Riess et al., 1998).

Although the majority of the type Ia SNe behave impressively similarly, e.g. have remarkably homogeneous optical spectra when compared at similar times relative to maximum brightness, outliers and peculiar events have been discovered at an increasing rate. Two sub-groups with distinctive spectroscopic and photometric features were discovered in the early 90s. The first one, represented by SN 1991T (Filippenko et al., 1992b; Phillips et al., 1992), has slightly wider lightcurves and somewhat higher maximum luminosity than average. Their pre-maximum spectra show no or little Si II or Ca II absorption, yet months past maximum brightness the spectra become nearly indistinguishable from that of a classical SN Ia. The other sub-group, represented by SN 1991bg (Filippenko et al., 1992a; Leibundgut et al., 1993; Turatto et al., 1996), is sub-luminous.Their lightcurves show rapid and monotonic decline and no clear secondary maximum in I-band as a normal SN Ia. They are intrinsically red and display strong Ti II absorption in spectra. Unusually low expansion velocity and ejecta mass were derived for these events. Later, SN 1999aa (Li et al., 2001b) was found to be spectroscopically similar to SN 1991T in having weak Si II and prominent Fe III lines, while it also showed apparent Ca II H and K lines that were weak in SN 1991T. It thus represents a possible intermediate type between SN 1991T-like events and normal SNe Ia. The discoveries of two peculiar SNe followed. SN 2000cx (Li et al., 2001a), whose lightcurve rose relatively fast and decayed relatively slowly, showed unusual color evolution. While its pre-maximum spectra were similar to that of SN 1991T, much higher expansion velocities were derived for both the intermediate-mass and iron-peak elements. SN 2002cx (Li et al., 2003) was also discovered to exhibit

1991T-like premaximum spectrum, but it had 1991bg-like luminosity and low expansion velocities. It posed a major challenge to the SN Ia models and was called "the most peculiar known type Ia supernova". More recently, the exceptionally bright SN 2003fg Howell et al. (2006) and SN 2006gz (Hicken et al., 2007) suggest large radioactive nickel productions that cannot be sensibly achieved in a Chandrasekhar mass progenitor.

Various sub-classification schemes were suggested, based on a combination of photometric and spectroscopic properties (Benetti et al., 2005) or spectral features observed around the maximum light (Branch et al., 2006). As the sample size increases, mildly peculiar events begin to fill up the multi-dimensional parameter space (Branch et al., 2009). Continuity between subgroups becomes evident. It is also clear that no single parameter can sufficiently describe the sequence of all SNe Ia.

4.2.2.2 Physical Origin of the Diversity

Although many of the peculiar SNe can be recognized from single-epoch of spectra near maximum and the Phillips relation (Phillips, 1993; Phillips et al., 1999) works rather well for majority of the "normal" SNe Ia sample, further cosmological constraints are limited by insufficient knowledge of the systematics. The physical origin of the above diversity is not well-understood and the contamination from outliers is hard to estimate.

First of all, there are at least two possible classes of progenitor channels. A single-degenerate (SD) progenitor involves a C/O white dwarf reaching Chandrasekhar limit by accreting mass from a non-degenerate companion; while in a double-degenerate (DD) scenario, two CO white dwarfs merge. Both channels may be contributing to the SNe Ia population. For example, direct evidence of circumstellar material in SN 2006X has supported the SD model (Patat et al., 2007a). The exceptional luminosity

of SN 2003fg (as well as 2006gz and 2007if, Howell et al., 2006; Hicken et al., 2007; Yuan et al., 2010) has suggested a super-Chandrasekhar mass progenitor, probably produced in a merger.

Initial metallicity of the progenitor may partly account for the spread because it affects the production of ^{56}Ni whose radioactive decay is the main source powering the lightcurve. On the other hand, iron-group elements, including ^{56}Ni, determine the opacity and in turn the diffusion process and the lightcurve width. The Phillips relation indeed suggests the dominance of Ni mass. The dependence on metallicity also play a key role in understanding the possible evolution of SN Ia properties with redshift.

The total amount of ^{56}Ni produced not only determines the luminosity of the SNe, but also influences the spectra by changing the effective temperature (Nugent et al., 1995). Spectral features, e.g. $\mathcal{R}$(Si II) (the ratio of the depth of Si II at 5972 and 6355 Å, Nugent et al., 1995), could thus serve as independent luminosity indicators besides photometric parameters such as Δm_{15}(B) (the decay in B-band within 15 days from maximum light, Phillips, 1993). The apparent discontinuity between the 1991bg-like events and the normal SNe Ia might be explained by a continuous temperature distribution while the Ti II signature disappears above certain temperature because of ionization (Nugent et al., 1995).

One key factor in the explosion model is how the burning front propagates (see Höflich, 2006, for a review of the physics). There are two possible modes, in which the nuclear burning propagates at a sub-sonic speed (deflagration) or a supersonic speed (detonation). The most likely scenario is delayed detonation (DD Khokhlov, 1991; Yamaoka et al., 1992; Woosley & Weaver, 1994) where the flame starts as a deflagration and turns into a detonation. The transition, however, is not well-

understood. Variation in the transition density could introduce internal dispersion in the observables. Alternatively, pure deflagration (e.g. W7 in Nomoto et al., 1984) and pulsating delayed detonation (PDD Khokhlov et al., 1993; Hoflich et al., 1995) models remain relevant in at least some events (Hoeflich & Khokhlov, 1996; Quimby et al., 2007a).

Asymmetrical structures have been supported by polarization observations (Wang et al., 2003; Leonard et al., 2005) and would produce a certain degree of dispersion (Sim et al., 2007). Furthermore, rotation of the progenitor has a potential influence on the explosion (Uenishi et al., 2003; Yoon & Langer, 2005), e.g. increasing the mass threshold for carbon ignition.

4.2.2.3 Necessity of Early Identification

The initial conditions of the progenitors are learned through the studies of the composition and dynamics of the expanding envelope. During the rapid expansion, the matter density deceases and the photosphere recedes. While this allows us to probe the structure of the entire star by monitoring the lightcurve and spectra through time, important information conveyed in the outer layers become unobservable at later times. Empirically, the observational features evolve quickly during the first days after the explosion. The diversity among SNe Ia is greatest at early times. Even the normal type with remarkable homogeneity post-maximum, show distinct spectra at 2 weeks before maximum (e.g. Branch et al., 2007). Theoretically, predictions of the popular burning models (e.g. W7, DD and PDD) are similar after maximum light but distinct at early times. The early spectroscopic observations are thus critical in understanding the diversity of the SNe Ia and distinguish the explosion models.

Unfortunately, very early spectroscopic observations are sparse given the transient nature of SNe. Surveys with a rapid cadence (less than 1 day) provide the best chance

of detecting a nearby SN Ia as early as possible. This is precisely what ROTSE-III can do with its large field-of-view and thus a continuing goal of RSVP.

4.3 Image Subtraction by Cross-Convolution

The advent of low-noise megapixel electronic image sensors, cheap fast computers, and terabyte data storage systems has enabled searches for rare astrophysical phenomena in an ever-increasing space-time volume. Among the popular targets are supernovae and transits of extra-solar planets. Discoveries of supernovae, and in general, any transient events, involve monitoring the same area of the sky on a comparable time-scale and detecting the brightness changes of objects, appearance or disappearance of sources. Image subtraction is a common tool to remove the contributions of static sources and enhance the appearance of subtle changes. It is critical for identifying variable sources in a crowded field or embedded in their host galaxies. In our case, because of the large pixel scale ($3.3''$) of ROTSE-III, SNe in normal galaxies are often blended with the host light and not resolved. In reality, images are taken under different seeing and weather conditions, with varying aberrations from the optics. These effects have to be compensated first before reliably differencing two images. A number of research groups have developed algorithms to achieve this, e.g. the publicly available ISIS image subtraction package[1] employing the method described by Alard & Lupton (1998) and Alard (2000).

Robert Quimby first addressed this challenge on ROTSE-III images. He had worked extensively with the Supernova Cosmology Project (SCP) as an undergrad at the University of California at Berkeley. The SCP image subtraction code (Perlmutter et al., 1999) was thus adapted for use with the TSS. The evident success of the TSS motivated us to examine the image subtraction problem with the goal of

[1] Available at http://www2.iap.fr/users/alard/package.html

applying this to the considerably more extensive image data available to the entire suite of ROTSE-III telescopes. The original hope of using the SCP code was abandoned following the realization that the program would not be made freely available. We attempted to adopt the ISIS package but were discouraged by the initial results. The significant under-sampling of ROTSE-III stellar images coupled with asymmetric point spread functions across the image plane created a severe challenge for making clean subtractions. These issues are not satisfactorily addressed by the Alard & Lupton (1998) and Alard (2000) algorithms for two reasons: (1) we do not always have the luxury of a substantially higher quality reference image and (2), the point spread functions (PSFs) are often approximately elliptical with the axes oriented at any angle in the image plane. For a variety of reasons, the ROTSE-III PSFs can vary with temperature and telescope orientation. Thus, the possibility that one can simply convolve a new image to an ideal reference image is not always viable. With this in mind, we sought to develop a more symmetric algorithm that would be robust enough to handle less pristine observations. The aim of this project is primarily for the reliable identification of transients in a very large database, the application in precision photometry will be discussed later in chapter 5.

4.3.1 Mathematical Method

The basic technique for image subtraction presented by Alard and Lupton depends on finding a suitable PSF smearing kernel, $K(u, v)$ that when convoluted with the reference image, $R(x, y)$, generates a transformed image, $R^*(x, y)$, that can be compared on a pixel-by-pixel basis with a new test image of lesser quality, $T(x, y)$:

$$R(x, y) \otimes K(u, v) = R^*(x, y) \tag{4.1}$$

The kernel, $K(u, v)$, is constructed by a linear superposition of basis functions of the form:

$$f_{n,p,q}(u, v) = u^p v^q e^{-(u^2+v^2)/2\sigma_n^2} \tag{4.2}$$

Alard and Lupton recommend a three-fold ensemble of terms with σ_n values spanning a 9-fold range. These functions are poor choices to synthesize an elliptical PSF at an arbitrary angle with respect to the imager sensor axes although they will be satisfactory for PSFs with close to azimuthal symmetry. The specific values for σ_n, p and q must be determined by *ad hoc* comparisons with the characteristic PSFs associated with the particular instrument in use. The set of amplitudes for the basis functions is computed by the least squares technique to minimize the pixel-by-pixel differences between R^* and T.

From this starting point, we decided to symmetrize the Alard-Lupton procedure by creating two convolution operators so that:

$$R(x, y) \otimes K_R(u, v) \approx T(x, y) \otimes K_T(u, v) \tag{4.3}$$

In the limit that the reference image is substantially better than the test image, the K_R operator smears R with the point spread function characteristic of T while K_T will be essentially equal to the identity operator so that its effect on T will be negligible. Under these conditions, the computation becomes functionally equivalent to the procedure adopted by Alard and Lupton. However, in general, the addition of a second convolution operator injects new mathematical degrees of freedom that must be constrained. The most obvious is that K_R and K_T can be multiplied by

an arbitrary constant without violating image convolution equality. This can be conveniently resolved by demanding that one or both kernels be flux-conserving, i.e.:

$$\sum K(u,v) = 1 \tag{4.4}$$

The second, more complex, problem arises from the diffusion of a stellar image if K_R and K_T approximate broad Gaussian distributions. The convoluted image equality will be maintained but the signal-to-noise ratio of the subtracted image will drastically diminish. The solution to this was found by analogy to a similar problem in the application of smoothing splines to drawing curves through data with errors. In the latter case, one can trivially create a spline curve that runs exactly through each and every data point (as long as the abscissas are distinct). Such a curve would appear very wiggly and poorly represent the trend of the data. The solution to this problem is to add a curvature penalty term to the least squares residuals so that a trade-off is reached between adequately fitting the data and inserting unnecessarily complex behavior into the smoothed interpolation. The coefficient that scales the curvature term is a measure of the stiffness of the spline. There exists an elegant method called cross-validation that determines the stiffness parameter from the standard deviation errors for each data point.

For image subtraction, the degradation of the signal-to-noise ratio is proportional to the effective number of pixels that are summed by the convolution kernel. Since each pixel has an associated variance, σ^2_{pix}, the variance for a signal diffused over N_{pix} pixels will be $N_{pix}\sigma^2_{pix}$. Assuming Gaussian distributions, we can estimate N_{pix} from the width of the effective stellar point spread function, $N_{pix} \sim 4\pi(\sigma^2_{PSF} + \sigma^2_K)$, where σ_{PSF} is the basic stellar PSF width (in pixels) and σ_K is the diffusive width of the convolution, K. If σ^2_K is evaluated by the normal formula, $\sigma^2_K = \sum K_i r_i^2$ where

K_i are the kernel element amplitudes, the sum can be deceptively small when the values for K_i alternate in sign. Noting that $\langle K_i \rangle \propto \frac{1}{\sigma_K^2}$, the value for σ_K^2 can be better estimated by $\frac{1}{2\pi} \sum K_i^2 r_i^4$ which equally penalizes both positive and negative contributions to the kernel elements. Although the scaling behavior of the penalty coefficient is understood in terms of the image size, σ_{pix}^2, and σ_{PSF}^2, we have not investigated whether there is an elegant way to evaluate this quantity analogously to the cross-validation technique for splines.

4.3.2 Computational Methods

The image preprocessing that we require is similar to that described by Alard and Lupton. Flat-fielded images are processed by SExtractor (Bertin & Arnouts, 1996) to create object lists with precise stellar coordinates. The IDL routine[2], `POLYWARP`, is used to warp the new test image to overlay stellar objects in the reference image as closely as possible. A valid pixel map is generated to avoid pixels close to the image perimeter and screen against saturated values, etc. At this point, the fundamental image subtraction code is invoked as an IDL routine which first performs image flux normalization to equalize the mean values of the two images under comparison.

The most basic choice that the user must make is the representation of the convolution kernels. We have restricted them to $n \times n$ arrays with n odd. This permits a simple representation for the convolution identity operator: $K_{[n/2],[n/2]} = 1$ while all other elements of $K_{i,j}$ are zero. For the ROTSE-III images, $n = 9$ appears to provide more than adequate coverage of stellar point spread functions under the worst conditions.

The values for the convolution kernel elements are derived from the difference image:

[2]ITT Visual Information Solutions, ITT Industries, Inc.

$$D(x,y) = \{R(x,y) \otimes K_R(u,v)\} - \{T(x,y) \otimes K_T(u,v)\} \tag{4.5}$$

Invoking the criterion that $\sum D(x,y)^2$ should be a minimum subject to the requirements for K_R and K_T generates $2(n^2-1)$ linear equations via the usual least squares procedure to solve for the independent coefficients for $K_R(u,v)$ and $K_T(u,v)$ after imposing the kernel unitarity constraints. As described earlier, these equations will not provide unique solutions for K_R and K_T because the effective width of the two convolution kernels can still be radially scaled without substantially affecting the difference image, D. Thus, the quantity to be minimized must include a penalty term for radially diffusing the convoluted images any further than necessary. Following from earlier remarks, this figure-of-merit function can be represented as:

$$Q = \sum D(x,y)^2 + \lambda \sum (u^2+v^2)^2 \{K_R(u,v)^2 + K_T(u,v)^2\} \tag{4.6}$$

where λ is a constant selected to balance the contributions of the two competing error terms. From the discussion given above, the value for λ should scale as:

$$\lambda = 2\pi N_{image} \frac{(\sigma_R^2 + \sigma_T^2)}{\sigma_{PSF}^2} \lambda' \tag{4.7}$$

where N_{image} is the total number of pixels in the image, σ_R^2 and σ_T^2 are the pixel amplitude variances, σ_{PSF} is the characteristic stellar PSF width and λ' is a constant of order unity.

With two 9×9 convolution kernels, the number of free parameters is 160 and the size of the regression matrix becomes problematic. The main concern is that if the images are essentially featureless (i.e.. no stars), the matrix elements become

indistinguishable and the inverse matrix will be singular. To avoid these effects as well as various other computational issues, a binary valued mask array is created to eliminate sampling around the image perimeter, saturated pixels and all featureless areas not associated with stellar objects as determined by SExtractor. This approach was quite successful: the degree of singularity of the regression matrix was determined during the inversion process using the IDL singular value decomposition routines `SVDC` and `SVSOL`, codes derived from *Numerical Recipes in C*(Press et al., 1992).

For our ROTSE project, computational efficiency is critical because we typically acquire 400 images per night with each telescope and these must be reduced in situ comfortably within 24 hours. It was easily verified that most of the image subtraction calculations were devoted to computing the convolution kernels regression matrix described above. Examination of the two-dimensional structure of the kernels showed that the amplitudes near the edges of the 9×9 arrays were always small and suggested that the representation could be significantly reduced from 81 values to 25 by assuming a mapping from a reduced number of wavelet functions. Thus, each convolution kernel was represented by a linear superposition:

$$K(u, v) = \sum A_i B_i(u, v)$$

with the basis functions, B_i, chosen as discrete approximations to bicubic spline functions with characteristic widths of 1, $\frac{3}{2}$ and 2 pixels, centered as shown in Figure 4.2. Using this technique shrank the regression matrix from 160×160 to 48×48 with a consequent reduction in processing time of about an order of magnitude. This brought the computation throughput to values similar to what Robert Quimby had obtained using the SCP code as adapted for his Texas Supernova Search.

Most of the image subtraction code was written in IDL with the exception of the

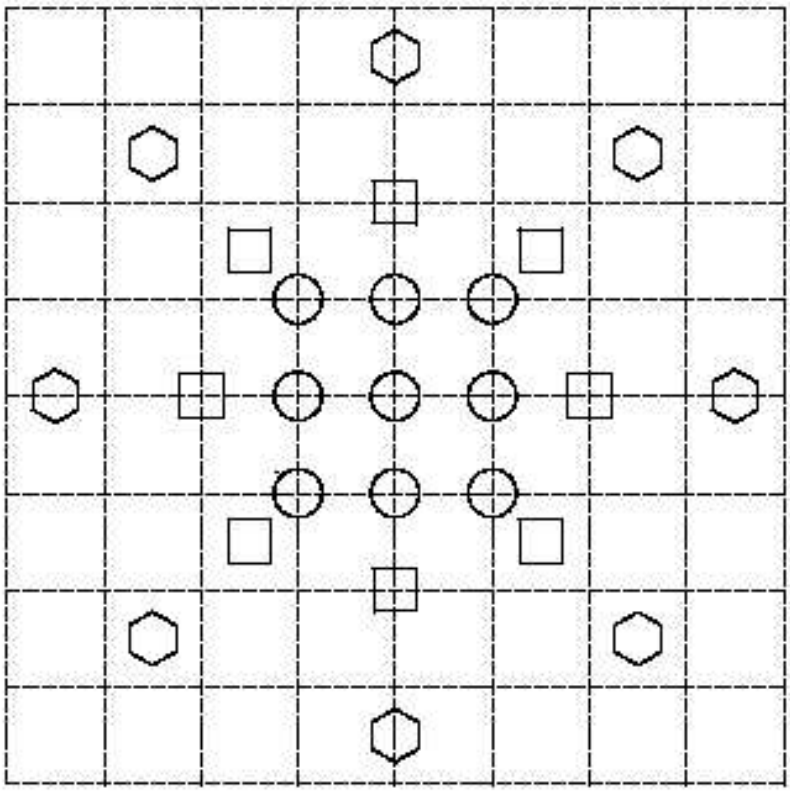

Fig. 4.2.—: Diagram of the location of the bicubic B-splines used to construct the convolution kernels. The 9 circles, 8 squares and 8 hexagons mark the centers of the B-spline maxima with widths of 1, $\frac{3}{2}$ and 2 pixels respectively. The dashed lines indicate the 9×9 grid of the underlying convolution kernels.

evaluation of the regression matrix. Since this is the core of the computational burden and IDL is not particularly efficient in handling the necessary array indexing, this portion was coded in C and linked to the rest of the IDL programs using the IDL standard external calling interface. A crucial detail, particularly important for the ROTSE-III telescopes, is the variation of the stellar PSF across the image plane. To accommodate this problem, each 2045×2049 image was subdivided into 36 sub-images of roughly equal size. The set of 50 kernel amplitude coefficients was calculated, one by one, for each of these sub-images. Cross-convolved images were obtained by bilinear interpolation for every pixel using the four nearest neighbor coefficient sets. The unitarity of the convolution kernels is guaranteed by the linearity of the interpolation

method with respect to the gridded coefficient reference values. Although this sounds somewhat complicated, the calculation was extremely efficient.

Another significant concern is the estimation of the background sky intensity. Initially, we relied on SExtractor to remove this background before subtraction. However, when applying our code to images containing large galaxies such as M31 and M33, we realized that these backgrounds are poorly estimated around the cores of bright galaxies. The solution we adopted only removes the background difference between the two images instead of the individual background for each image separately. After the images are scaled so that stellar fluxes match, a sky difference map is generated by first performing pixel by pixel subtraction. The low frequency spatial variation of this difference image is obtained by a process similar to the one used by SExtractor. The difference image is divided into 32×32 pixel sub-images and median pixel values are recursively evaluated, subject to the constraint that pixels with 3σ excursions from the median are ignored. Saturated pixels are also excluded from the median computation. The resultant slowly varying background is subtracted from one of the input images before invoking the cross-convolution algorithm. The remaining common non-zero background does not affect the estimation of the convolution kernels and the final subtracted image will be background-free.

A comparison of the results of the cross-convolution and the single convolution algorithms is shown in Figure 4.3. In the limiting case where the PSFs of the reference image are azimuthally symmetric, the two methods should produce rather similar results. However, when that condition is not satisfied, the cross-convolution method is more appropriate.

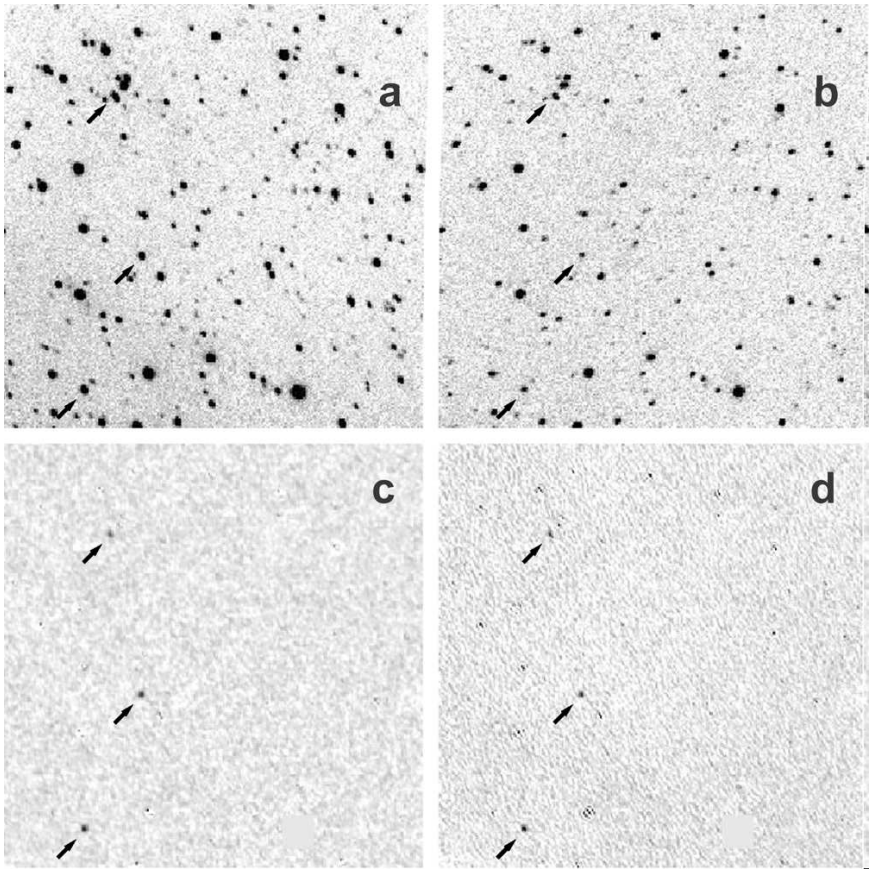

Fig. 4.3.—: Comparison of image subtractions methods. The first one uses the cross-convolution method described in this paper and the other is a single convolution method described by Alard and Lupton and implemented in the ISIS code. The initial images were obtained by the ROTSE-IIIb telescope at McDonald Observatory. Shown here are 260×260 pixel subframes centered on $\alpha = 16:50:02.21$, $\delta = +23:46:32.88$, covering a field of $0.235^\circ \times 0.235^\circ$. To demonstrate the results, three artificial "variable" stars were added to the test image (a) and the reference image (b) with PSFs appropriately matched to their respective fields. The locations are shown by black arrows. The subtracted image obtained by cross-convolution is depicted in (c) and the Alard-Lupton results are shown in (d). The bright star near the lower right corner of the images has been replaced with a uniform gray level since neither subtraction technique can extract useful information from saturated pixels.

4.3.3 Operational Experience

Subtraction of a 2045×2049 ROTSE image from a reference frame using the method described above takes approximately 4 minutes with a 2.0 GHz personal computer. If the same reference image is used multiple times, it needs to be convolved with the base kernels just once, saving computational time. Subtractions of three typical ROTSE images from the same reference frame takes $\sim$10 minutes on the same processor. It should be noted that the memory allocation for the process, mainly for storing the base kernel convoluted images, scales with the size of the image and number of kernel basis sets. For our choice of 25 kernel base vectors and a 2045×2049 image size, $\sim$ 1 GB memory is required. This is not a serious handicap for a modern desktop computer.

For 5 months since August 2007, a supernova search pipeline using this subtraction code was running on images taken by the ROTSE-IIIb telescope, in parallel with the TSS pipeline. In terms of transient recovery efficiency, both real-world and limited Monte Carlo comparisons show that our subtraction code is comparable to the modified version of the Supernova Cosmology Project search code employed by the Texas Supernova Search.

The algorithm described can be adapted for a wide variety of photometric searches for transient objects. Its performance appears to be at least as good as other codes presently in use. Since the method is designed to handle images with significantly varying quality, it should remain effective when alternative programs may fail. The drawback for the cross-convolution method is that the dispersion process widens the psf in both images and produces a larger region of correlated pixels. A signal in the difference image is more likely to be affected by imperfect subtraction in the nearby region, e.g. at the bright core of a galaxy or a saturated star. A bad pixel in either

image can produce a false point source in the difference.

For anyone wishing to employ this cross-convolution technique, the source code can be downloaded from the University of Michigan Deep Blue institutional repository [3].

4.4 Transient Search Pipeline

In March 2007, Rykoff and I traveled to Texas and installed for ROTSE-IIIb a dual-core processor computer, which combines the functionality of the ROTSE control computer and the camera computer. This update eliminated potential communication issues with the camera and improves the reliability of the system. The old control computer, with a memory upgrade to 1.5 GB, was then readily converted to run the supernova search pipeline. In July of the same year, I made another trip to Texas with Prof. Akerlof. The main task was to replace the deteriorating primary and secondary mirrors of ROTSE-IIIb with newly aluminum-coated ones. This effort improved the detection sensitivity by about one magnitude and further prepared the system for a large-volume transient search. In August 2007, the supernova search pipeline started running full-time on ROTSE-IIIb. The same system upgrade and mirror replacement were completed for ROTSE-IIIc and ROTSE-IIId in May and August 2008, following which the search pipeline began operational in July and October respectively. Finally, in December 2008, a single system control computer was installed for ROTSE-IIIa. The supernova pipeline was started in July 2009 at ROTSE-IIIa.

4.4.1 Target Fields Selection

A number of designated sky fields are monitored daily whenever visible at night and weather permitting. Majority of the fields are inherited from TSS. These include tiles covering the Virgo, Coma, Ursa Major clusters and M31 in the winter and

[3] Available at http://hdl.handle.net/2027.42/57484

areas centered on nearby spiral galaxies (IC342, M33, M74, M77, M81, NGC6946 and NGC 7331) and tiles covering the Perseus clusters in the summer. Given the more telescope time available and the southern hemisphere coverage, extended areas south to the Virgo cluster, in the Fornax cluster and selected ABELL clusters in the south are chosen. To take advantage of the rich archive of Sloan Digital Sky Survey (SDSS), 23 fields overlapping with the SDSS coverage and with relatively high density of galaxies are also selected. The coordinates of the centers of all 323 fields (sorted by RA) are listed in Table 4.3. Elliptical latitudes are shown since a number of fields have low latitudes and source contamination from astroids (although they can be effectively rejected, see §4.4.4). For each field, known galaxies are extracted from the NASA/IPAC Extragalactic Database (NED) or SDSS archive (see column N_{gal}). The numbers of nights each field is searched by each telescope from August 2007 to August 2009 are listed in the next four columns. By the end of August 2009, 3 fields in the selection are not yet searched. They are targets for the southern hemisphere sites, for which no reference can yet be built with limited images taken previously.

We also estimate the space-time volume covered by the search for type-Ia SNe using the nightly observing log. We take the typical peak brightness for a SN Ia as -19.0 absolute magnitude. For a given ROTSE-III limiting magnitude, we can calculate the luminosity distance range a supernova can be detected. For example, a limiting magnitude of 18.5 corresponds to a search depth of $\sim$300 Mpc. For each field, each night, the shallowest limit of the coadds is used (see §4.4.3 for co-addition scheme). A lower limit of 10 Mpc is set according to the saturation level of ROTSE-III CCD. A conservative field-of-view of 3 $degree^2$ is used, accounting for the difficulty of detecting transients near the edge of images where aberrations are worst. The time coverage is assumed to be 60 s for each image. The results are presented in the last column

in Table 4.3. In total, ROTSE-IIIb has searched 2654 Mpc^3 $year$ for SNe Ia from August 2007 to end of August 2009. ROTSE-IIIc has searched 579 Mpc^3 $year$ since July 2008 and ROTSE-IIId has searched 114 Mpc^3 $year$ since Oct 2008. ROTSE-IIIa has searched 8.8 Mpc^3 $year$ since July 2009. For a SN at the record brightness (-22.7 absolute magnitude for SN 2005ap), the searched volume is about 165 times as much as the above for SN Ia.

Table 4.3:: List of RSVP Target Fields

Field Name	RA J2000	DEC J2000	Ecliptic Latitude	N_{gal}	N_{nights} IIIa	N_{nights} IIIb	N_{nights} IIIc	N_{nights} IIId	Volume Mpc^3 $year$
ABELL2717	00:03:19	-35:57:00	-32.9	222	0	0	62	0	9.93
ABELL2764	00:20:28	-49:13:12	-45.9	99	0	0	40	0	2.50
ABELL44	00:29:36	+12:01:12	8.1	19	0	0	5	0	0.54
ABELL2800	00:38:00	-25:04:48	-26.6	351	0	0	73	0	12.17
A1	00:38:19	+40:26:21	33.0	22	0	256	0	52	25.89
ABELL76	00:39:48	+06:46:00	2.3	34	7	152	46	30	49.23
ABELL85	00:41:36	-09:19:48	-12.7	512	0	0	29	0	3.30
A2	00:42:44	+41:16:09	33.3	28	0	355	0	35	10.53
A3	00:47:09	+42:05:57	33.7	18	0	252	0	53	25.41
ABELL119	00:56:24	-01:16:00	-6.7	534	14	103	82	19	31.72
ABELL2854	01:00:48	-50:31:12	-50.8	86	0	0	42	0	4.86
ABELL147	01:08:12	+02:10:00	-4.7	228	8	137	64	23	32.90
ABELL151	01:08:52	-15:25:12	-20.9	190	0	0	67	0	5.16
ABELL150	01:09:12	+13:09:00	5.4	395	0	0	5	0	0.29
SDSS1	01:09:55	+13:52:12	6.0	628	0	88	0	0	10.73
ABELL154	01:11:00	+17:39:00	9.4	53	0	0	4	0	0.11
ABELL160	01:12:54	+15:31:00	7.2	705	0	222	15	36	37.46
ABELL2889	01:14:48	-48:30:00	-50.5	58	0	0	46	0	5.46
ABELL168	01:15:12	+00:15:00	-7.1	586	9	134	75	20	30.04
SDSS2	01:16:40	+13:52:12	5.3	758	0	96	0	0	13.29
SDSS3	01:23:25	+14:22:48	5.2	384	0	102	0	0	17.91
ABELL189	01:23:42	+01:39:00	-6.6	326	8	142	74	22	35.00
ABELL193	01:25:06	+08:42:00	-0.2	110	0	191	25	27	42.46
ABELL194	01:25:36	-01:30:00	-9.7	280	11	132	92	17	30.74
ABELL2911	01:26:00	-37:58:12	-42.8	71	0	0	72	0	8.18
ABELL195	01:27:40	+19:10:16	9.3	43	0	198	4	38	28.82
SDSS4	01:30:10	+14:22:48	4.6	214	0	105	0	0	20.76
M33	01:33:50	+30:39:35	19.4	26	0	291	0	47	39.22
M74	01:36:41	+15:47:00	5.3	102	0	245	7	37	40.06
ABELL225	01:38:52	+18:52:48	8.0	11	0	0	0	0	0.00
ABELL2933	01:40:43	-54:33:00	-57.7	20	0	0	24	0	2.10
SDSS5	01:49:55	+13:24:00	2.0	162	0	116	0	0	22.09
ABELL261	01:51:24	-02:13:59	-12.8	42	8	125	92	19	40.37
ABELL260	01:52:17	+33:21:25	20.4	66	0	223	0	46	35.22
ABELL262	01:52:48	+36:09:00	22.9	156	0	234	0	49	32.30
ABELL2988	02:12:55	-47:07:12	-55.1	49	0	0	41	0	4.03
ABELL2995	02:15:12	-24:49:48	-35.9	56	0	0	76	0	18.70
ABELL3009	02:22:07	-48:34:12	-57.2	45	0	0	27	0	2.60
ABELL347	02:25:48	+41:52:00	25.9	60	0	228	0	46	19.84
M77	02:42:40	-00:00:47	-15.0	210	7	233	25	21	26.29
ABELL376	02:45:48	+36:52:00	19.9	112	0	225	0	41	25.97
ABELL397	02:57:00	+15:57:00	-0.8	84	0	192	4	25	35.56
ABELL400	02:57:36	+06:01:59	-10.4	216	0	181	11	25	27.73
ABELL407	03:01:33	+35:37:33	17.7	122	0	228	0	37	26.71

Continued on Next Page. . .

Table 4.3 – Continued

Field Name	RA J2000	DEC J2000	Ecliptic Latitude	N_{gal}	N_{nights} IIIa	N_{nights} IIIb	N_{nights} IIIc	N_{nights} IIId	Volume Mpc^3 $year$
PER3	03:08:13	+42:24:42	23.8	128	0	235	0	36	18.85
ABELL3093	03:08:33	-47:14:52	-60.6	46	0	0	19	0	0.76
F17	03:12:07	-35:27:37	-50.6	56	21	0	124	0	15.16
F6	03:13:00	-32:08:25	-47.7	202	23	0	125	0	5.57
F27	03:15:04	-38:46:49	-53.9	106	18	0	49	0	2.58
F22	03:16:36	-37:07:13	-52.5	118	19	0	82	0	9.41
PER2	03:17:05	+42:24:42	23.3	334	0	248	0	35	13.24
PER5	03:17:09	+40:45:06	21.7	326	0	341	0	33	17.13
ABELL3108	03:17:33	-47:45:07	-61.9	36	0	0	8	0	0.35
F11	03:17:46	-33:48:01	-49.6	260	18	0	124	0	12.80
F16	03:20:10	-35:27:37	-51.3	196	17	0	106	0	12.15
F5	03:20:45	-32:08:25	-48.3	274	17	0	124	0	13.34
ABELL3122	03:22:16	-41:19:48	-56.8	185	0	0	17	0	1.01
F26	03:23:29	-38:46:49	-54.6	139	9	0	44	0	2.80
F21	03:24:50	-37:07:13	-53.2	196	13	0	47	0	3.31
F10	03:25:41	-33:48:01	-50.2	298	14	0	110	0	12.92
PER4	03:25:48	+40:45:06	21.3	312	0	240	0	37	15.22
PER1	03:25:57	+42:24:42	22.9	290	0	239	0	37	15.05
F15	03:28:14	-35:27:37	-52.0	380	12	0	68	0	7.93
F4	03:28:31	-32:08:25	-48.9	250	13	0	102	0	12.23
ABELL3128	03:30:12	-52:33:00	-67.0	587	0	0	1	0	0.04
F25	03:31:53	-38:46:49	-55.3	162	8	0	44	0	3.20
F20	03:33:04	-37:07:13	-53.9	458	8	0	49	0	4.74
F9	03:33:35	-33:48:01	-50.9	448	12	0	89	0	11.08
F3	03:36:17	-32:08:25	-49.5	222	11	0	90	0	10.52
F14	03:36:18	-35:27:37	-52.6	564	8	0	56	0	5.32
ABELL3144	03:37:07	-55:01:12	-69.5	329	0	0	1	0	0.05
F24	03:40:18	-38:46:49	-56.0	178	8	0	52	0	4.39
F19	03:41:17	-37:07:13	-54.5	480	8	0	55	0	4.70
F8	03:41:29	-33:48:01	-51.5	402	9	0	85	0	9.57
ABELL3158	03:43:00	-53:37:48	-69.0	359	0	0	1	0	0.05
F2	03:44:03	-32:08:25	-50.1	134	8	0	86	0	8.94
F13	03:44:21	-35:27:37	-53.2	476	8	0	69	0	7.42
IC342	03:46:48	+68:05:45	46.7	4	0	267	0	45	10.57
F23	03:48:42	-38:46:49	-56.6	132	7	0	49	0	4.44
F7	03:49:24	-33:48:01	-52.1	112	7	0	73	0	8.60
F18	03:49:31	-37:07:13	-55.2	198	7	0	56	0	4.43
F1	03:51:49	-32:08:25	-50.7	24	7	0	80	0	8.50
F12	03:52:25	-35:27:37	-53.8	100	7	0	64	0	8.29
ABELL3202	04:00:12	-53:39:00	-70.6	101	0	0	0	0	0.00
ABELL3223	04:08:36	-30:49:12	-50.5	166	0	0	49	0	8.00
ABELL3231	04:11:52	-64:35:60	-78.7	18	0	0	0	0	0.00
ABELL484	04:16:16	-07:39:00	-28.5	56	0	0	2	0	0.08
ABELL3266	04:31:12	-61:28:12	-79.1	485	0	0	0	0	0.00
ABELL496	04:33:36	-13:13:48	-34.8	425	0	0	0	0	0.00
ABELL500	04:38:52	-22:06:00	-43.7	38	0	0	0	0	0.00
ABELL3301	05:00:48	-38:40:12	-60.9	60	0	0	0	0	0.00
ABELL3341	05:25:36	-31:34:48	-54.6	128	0	0	0	0	0.00
ABELL3354	05:34:40	-28:30:00	-51.7	135	0	0	54	0	3.02
ABELL3395	06:27:31	-54:22:48	-77.4	261	0	0	0	0	0.00
ABELL688	08:37:28	+15:51:00	-2.6	2	0	0	0	0	0.00
M81	09:56:21	+69:03:55	51.6	15	0	268	0	1	14.38
ABELL957	10:14:00	-00:54:00	-11.1	595	0	0	0	0	0.00
ABELL978	10:20:28	-06:31:12	-15.7	310	0	0	24	0	2.75
ABELL1020	10:27:48	+10:24:00	0.7	250	0	0	0	0	0.00
ABELL1060	10:36:52	-27:31:12	-33.3	427	0	0	34	0	1.36
ABELL1216	11:17:40	-04:28:12	-8.3	358	0	0	0	0	0.00
U11	11:27:43	+51:36:15	43.2	184	0	219	0	36	36.38
U6	11:29:39	+53:14:03	44.7	168	0	235	0	33	14.81
U25	11:36:42	+46:42:51	39.8	112	0	259	0	36	12.22
U10	11:38:00	+51:36:15	44.1	269	0	211	0	33	34.48
U5	11:40:19	+53:14:03	45.6	266	0	194	0	5	29.26

Continued on Next Page...

Table 4.3 – Continued

Field Name	RA J2000	DEC J2000	Ecliptic Latitude	N_{gal}	N_{nights} IIIa	N_{nights} IIIb	N_{nights} IIIc	N_{nights} IIId	Volume Mpc^3 $year$
U19	11:40:43	+48:20:39	41.6	170	0	208	0	6	22.83
ABELL1356	11:42:28	+10:25:48	7.8	124	0	0	0	0	0.00
ABELL1367	11:44:31	+19:49:48	16.6	294	0	0	0	0	0.00
U24	11:46:03	+46:42:51	40.6	187	0	200	0	29	32.30
U9	11:48:18	+51:36:15	44.9	271	0	310	0	4	23.64
U14	11:48:58	+49:58:27	43.7	250	0	190	0	5	31.88
U35	11:50:12	+41:49:27	36.8	180	0	204	0	9	34.39
U18	11:50:21	+48:20:39	42.4	234	0	261	0	0	19.51
U4	11:50:59	+53:14:03	46.5	249	0	205	0	5	20.01
U32	11:51:42	+43:27:15	38.4	271	0	200	0	27	36.41
U29	11:54:09	+45:05:03	40.0	258	0	193	0	0	29.22
U1	11:54:50	+56:29:39	49.5	131	0	122	0	28	7.61
U2	11:55:00	+54:51:51	48.2	233	0	302	0	0	19.51
U23	11:55:25	+46:42:51	41.5	174	0	183	0	0	25.02
U8	11:58:35	+51:36:15	45.9	271	0	265	0	0	12.51
U34	11:58:49	+41:49:27	37.6	402	0	190	0	26	48.17
U13	11:58:55	+49:58:27	44.5	261	0	283	0	8	18.89
U17	11:59:59	+48:20:39	43.3	223	0	156	0	17	18.88
U31	12:00:33	+43:27:15	39.2	526	0	178	0	0	35.46
U3	12:01:39	+53:14:03	47.5	204	0	258	0	0	7.44
U28	12:03:15	+45:05:03	40.8	285	0	184	0	20	29.97
U22	12:04:46	+46:42:51	42.3	136	0	178	0	8	21.66
U33	12:07:27	+41:49:27	38.4	420	0	199	0	0	41.66
U12	12:08:52	+49:58:27	45.4	160	0	280	0	0	13.12
U7	12:08:52	+51:36:15	46.8	116	0	150	0	0	11.02
U30	12:09:24	+43:27:15	40.0	425	0	289	0	0	15.68
U16	12:09:37	+48:20:39	44.2	195	0	311	0	15	28.68
V13	12:11:21	+14:27:15	14.4	540	0	38	0	0	1.96
V26	12:11:26	+11:11:39	11.4	372	0	20	0	0	0.79
U27	12:12:20	+45:05:03	41.7	249	0	198	0	0	25.54
V19	12:12:42	+12:49:27	13.0	670	0	257	0	0	15.55
V32	12:13:14	+09:33:51	10.1	310	0	18	0	0	0.53
V38	12:13:33	+07:56:03	8.6	314	0	14	0	0	0.69
V7	12:13:53	+16:05:03	16.1	246	0	47	0	0	2.81
VE5	12:13:57	+01:24:51	2.7	106	0	0	11	0	2.64
U21	12:14:07	+46:42:51	43.2	210	0	195	0	0	12.64
V43	12:14:37	+06:18:15	7.2	380	0	11	0	0	0.30
V48	12:17:50	+04:40:27	6.1	294	0	10	0	0	0.20
V12	12:18:04	+14:27:15	15.0	760	0	264	0	0	13.92
V25	12:18:04	+11:11:39	12.1	652	0	22	0	0	0.47
U15	12:19:16	+48:20:39	45.0	180	0	192	0	30	18.97
V18	12:19:21	+12:49:27	13.7	806	0	259	0	0	10.10
V31	12:19:50	+09:33:51	10.7	614	0	18	0	0	0.27
V37	12:20:07	+07:56:03	9.3	656	0	216	0	0	13.65
VE6	12:20:29	+01:24:51	3.3	130	0	0	7	0	1.03
V6	12:20:38	+16:05:03	16.8	328	0	45	0	0	1.95
V42	12:21:10	+06:18:15	7.9	548	0	202	0	0	10.79
V52	12:21:17	+03:02:39	4.9	66	0	9	0	0	0.19
U26	12:21:26	+45:05:03	42.5	190	0	224	0	0	30.07
U20	12:23:28	+46:42:51	44.1	184	0	211	0	0	14.49
V2	12:23:36	+17:42:51	18.5	98	0	70	0	0	3.84
V47	12:24:22	+04:40:27	6.7	296	0	160	0	0	5.17
V24	12:24:42	+11:11:39	12.7	794	0	246	0	0	11.75
V11	12:24:46	+14:27:15	15.7	616	0	265	0	0	12.47
V17	12:26:01	+12:49:27	14.3	760	0	258	0	0	10.71
VE13	12:26:17	-00:12:56	2.4	394	0	0	4	0	0.68
V30	12:26:26	+09:33:51	11.4	806	0	236	0	0	5.00
V36	12:26:41	+07:56:03	9.9	750	0	223	0	0	13.16
VE7	12:27:00	+01:24:51	4.0	216	0	0	0	0	0.00
V5	12:27:24	+16:05:03	17.4	344	0	278	0	0	16.42
V41	12:27:43	+06:18:15	8.5	454	0	204	0	0	7.95
V51	12:27:48	+03:02:39	5.6	48	0	12	0	0	0.49

Continued on Next Page...

Table 4.3 – Continued

Field Name	RA J2000	DEC J2000	Ecliptic Latitude	N_{gal}	N_{nights} IIIa	N_{nights} IIIb	N_{nights} IIIc	N_{nights} IIId	Volume Mpc^3 $year$
VE19	12:28:50	-01:50:44	1.2	454	0	0	8	0	1.63
V1	12:30:25	+17:42:51	19.2	102	0	104	0	0	11.27
V46	12:30:54	+04:40:27	7.4	172	0	10	0	0	0.21
V23	12:31:19	+11:11:39	13.4	728	0	240	0	0	12.97
V10	12:31:28	+14:27:15	16.4	530	0	279	0	0	12.78
V16	12:32:41	+12:49:27	15.0	684	0	260	0	0	12.53
VE14	12:32:48	-00:12:56	3.1	492	0	0	0	0	0.00
V29	12:33:01	+09:33:51	12.1	760	0	236	0	0	5.31
V35	12:33:15	+07:56:03	10.6	656	0	223	0	0	8.84
VE8	12:33:31	+01:24:51	4.6	252	0	0	0	0	0.00
VE25	12:33:55	-03:28:32	0.2	490	0	0	7	0	0.63
V4	12:34:09	+16:05:03	18.1	244	0	94	0	0	10.67
V40	12:34:16	+06:18:15	9.2	414	0	19	0	0	0.47
V50	12:34:20	+03:02:39	6.2	54	0	11	0	0	0.44
VE20	12:35:22	-01:50:44	1.8	530	0	0	0	0	0.00
V45	12:37:26	+04:40:27	8.0	238	0	16	0	0	0.58
V22	12:37:57	+11:11:39	14.0	632	0	245	0	0	7.32
V9	12:38:11	+14:27:15	17.0	374	0	91	0	0	6.99
VE15	12:39:19	-00:12:56	3.7	550	0	0	0	0	0.00
V15	12:39:21	+12:49:27	15.7	582	0	270	0	0	6.62
V28	12:39:37	+09:33:51	12.7	480	0	31	0	0	0.47
V34	12:39:49	+07:56:03	11.2	352	0	25	0	0	0.92
VE9	12:40:03	+01:24:51	5.3	252	0	2	0	0	0.12
VE26	12:40:27	-03:28:32	0.8	692	0	0	3	0	0.05
V39	12:40:49	+06:18:15	9.8	284	0	20	0	0	0.86
V49	12:40:51	+03:02:39	6.8	88	0	13	0	0	0.25
V3	12:40:54	+16:05:03	18.8	132	0	280	0	0	16.06
VE21	12:41:53	-01:50:44	2.4	650	0	0	0	0	0.00
VE31	12:42:03	-05:06:20	-0.5	466	0	0	3	0	0.09
V44	12:43:58	+04:40:27	8.6	222	0	18	0	0	0.50
V21	12:44:34	+11:11:39	14.7	416	0	233	0	0	7.39
V8	12:44:53	+14:27:15	17.7	202	0	117	0	0	13.74
VE36	12:45:45	-06:44:08	-1.7	228	0	0	3	0	0.12
VE16	12:45:50	-00:12:56	4.3	540	0	0	1	0	0.02
V14	12:46:01	+12:49:27	16.3	356	0	94	0	0	7.60
V27	12:46:13	+09:33:51	13.4	206	0	53	0	0	2.87
V33	12:46:24	+07:56:03	11.9	124	0	29	0	0	1.13
VE10	12:46:34	+01:24:51	5.9	248	0	2	0	0	0.07
VE27	12:46:59	-03:28:32	1.4	712	0	1	3	0	0.13
VE2	12:47:23	+03:02:39	7.5	98	0	4	0	0	0.14
VE42	12:47:50	-08:21:56	-3.0	228	0	0	6	0	0.21
VE43	12:47:51	-09:59:44	-4.5	230	0	0	14	0	1.62
VE46	12:48:24	-11:37:32	-5.9	290	0	0	22	0	1.65
VE22	12:48:24	-01:50:44	3.1	732	0	0	0	0	0.00
VE32	12:48:35	-05:06:20	0.1	542	0	0	3	0	0.15
VE1	12:50:31	+04:40:27	9.3	134	0	5	0	0	0.06
V20	12:51:12	+11:11:39	15.3	142	0	94	0	0	8.31
VE49	12:51:27	-13:15:20	-7.1	490	0	0	26	0	2.17
C3	12:52:12	+29:41:34	32.2	660	0	211	0	0	30.69
VE37	12:52:19	-06:44:08	-1.0	210	0	0	3	0	0.13
C6	12:52:21	+28:03:46	30.7	1322	0	199	0	0	24.67
VE17	12:52:22	-00:12:56	5.0	512	0	1	2	0	0.09
C9	12:52:27	+26:25:58	29.3	1056	0	194	0	0	24.43
VE51	12:53:03	-14:53:08	-8.5	884	0	0	30	0	2.37
VE11	12:53:05	+01:24:51	6.5	218	0	4	0	0	0.06
VE28	12:53:31	-03:28:32	2.1	794	0	1	3	0	0.16
VE3	12:53:55	+03:02:39	8.1	84	0	4	0	0	0.05
ABELL3528	12:54:16	-29:01:12	-21.3	439	0	0	21	0	1.03
VE41	12:54:25	-08:21:56	-2.3	252	0	0	3	0	0.10
VE44	12:54:28	-09:59:44	-3.8	272	0	0	5	0	0.10
VE23	12:54:56	-01:50:44	3.7	726	0	1	2	0	0.17
VE47	12:55:03	-11:37:32	-5.3	356	0	0	7	0	0.28

Continued on Next Page...

Table 4.3 – Continued

Field Name	RA J2000	DEC J2000	Ecliptic Latitude	N_{gal}	N_{nights} IIIa	N_{nights} IIIb	N_{nights} IIIc	N_{nights} IIId	Volume Mpc^3 $year$
VE33	12:55:08	-05:06:20	0.7	592	0	0	3	0	0.07
VE53	12:55:11	-16:30:56	-9.8	1036	0	0	31	0	1.52
VE50	12:58:09	-13:15:20	-6.5	442	0	0	14	0	1.03
VE38	12:58:53	-06:44:08	-0.4	164	0	0	3	0	0.10
VE18	12:58:53	-00:12:56	5.6	496	0	2	2	0	0.14
VE12	12:59:37	+01:24:51	7.2	274	0	3	2	0	0.14
C2	12:59:39	+29:41:34	32.9	1102	0	231	0	0	33.35
C8	12:59:40	+26:25:58	30.0	1300	0	206	0	0	29.67
C5	12:59:41	+28:03:46	31.5	1828	0	205	0	0	27.75
VE52	12:59:48	-14:53:08	-7.8	552	0	0	23	0	1.41
VE29	13:00:03	-03:28:32	2.7	732	0	1	2	0	0.13
VE4	13:00:27	+03:02:39	8.8	130	0	5	0	0	0.04
VE40	13:01:01	-08:21:56	-1.7	112	0	0	4	0	0.10
VE45	13:01:06	-09:59:44	-3.2	122	0	0	5	0	0.14
VE24	13:01:27	-01:50:44	4.3	616	0	1	2	0	0.14
VE34	13:01:41	-05:06:20	1.4	420	0	0	2	0	0.09
VE48	13:01:42	-11:37:32	-4.7	224	0	0	13	0	0.78
VE30	13:06:35	-03:28:32	3.3	434	0	1	3	0	0.15
C7	13:06:54	+26:25:58	30.7	782	0	211	0	0	34.28
C4	13:07:00	+28:03:46	32.2	1246	0	219	0	0	35.93
C1	13:07:05	+29:41:34	33.7	942	0	229	0	51	41.44
VE39	13:07:36	-08:21:56	-1.1	36	0	0	10	0	0.64
VE35	13:08:14	-05:06:20	2.0	292	0	1	4	0	0.17
VE54	13:08:23	-16:30:56	-8.6	138	0	0	21	0	1.50
VE57	13:10:48	-19:46:32	-11.3	86	0	0	21	0	2.24
VE56	13:14:12	-18:08:44	-9.5	168	0	0	24	0	2.17
VE55	13:15:12	-16:30:56	-7.9	158	0	0	18	0	1.31
ABELL3554	13:19:31	-33:28:12	-23.2	318	0	0	23	0	1.87
ABELL3558	13:26:59	-31:27:01	-20.7	1046	0	0	11	0	0.32
ABELL3559	13:29:55	-29:31:12	-18.6	375	0	0	13	0	0.49
ABELL3560	13:31:08	-33:07:58	-21.9	982	0	0	24	0	2.00
ABELL3564	13:32:44	-35:12:36	-23.6	226	0	0	24	0	1.83
ABELL3562	13:34:25	-31:41:23	-20.3	969	0	0	20	0	0.58
ABELL3565	13:37:39	-33:58:55	-22.1	405	0	0	20	0	0.86
ABELL3566	13:40:18	-35:38:41	-23.4	220	0	0	28	0	1.64
ABELL3571	13:47:28	-32:51:00	-20.3	327	0	0	29	0	1.24
ABELL3577	13:54:16	-27:49:48	-15.1	152	0	0	33	0	1.04
ABELL3578	13:57:31	-24:43:12	-11.9	101	0	0	55	0	6.15
ABELL1827	13:58:12	+21:42:00	31.4	33	0	0	0	0	0.00
ABELL1837	14:01:48	-11:09:00	1.2	130	0	0	12	0	1.16
ABELL1913	14:26:55	+16:40:12	29.4	21	0	0	0	0	0.00
SDSS6	14:34:35	+03:27:43	17.7	554	0	17	0	0	0.22
SDSS7	14:41:07	+03:27:43	18.2	534	0	19	0	0	0.24
ABELL1983	14:52:40	+16:43:48	31.7	166	0	0	9	0	0.57
ABELL1991	14:54:31	+18:37:12	33.6	120	0	0	0	0	0.00
ABELL2040	15:12:48	+07:25:12	24.4	198	0	0	37	0	1.63
ABELL2063	15:23:00	+08:37:48	26.2	260	0	0	25	0	1.41
ABELL2107	15:39:48	+21:46:12	40.0	103	0	0	11	0	0.48
SDSS8	15:57:24	+41:48:00	60.1	204	0	77	0	0	4.32
SDSS9	16:02:48	+16:18:00	36.2	1178	0	53	0	0	1.66
SDSS10	16:17:37	+35:03:36	55.2	348	0	113	0	0	4.35
SDSS11	16:21:26	+39:15:36	59.4	1192	0	108	0	0	5.83
SDSS12	16:21:38	+40:53:24	60.9	1116	0	107	0	0	6.45
SDSS13	16:22:51	+37:37:48	57.9	586	0	121	0	0	5.94
SDSS14	16:29:56	+39:15:36	59.9	1360	0	168	0	0	8.04
SDSS15	16:30:15	+40:53:24	61.5	1242	0	150	0	0	11.41
SDSS16	16:38:53	+39:45:36	60.9	634	0	189	0	0	15.05
SDSS17	16:47:30	+39:45:36	61.3	232	0	202	0	0	17.78
SDSS18	16:50:12	+23:42:00	45.7	420	0	196	0	0	12.47
SDSS19	17:16:00	+57:18:00	79.4	181	0	121	0	0	9.86
SDSS21	17:27:40	+58:57:36	81.6	158	0	109	0	0	6.93
SDSS20	17:28:16	+56:58:12	79.7	159	0	153	0	0	10.41

Continued on Next Page...

Table 4.3 – Continued

Field Name	RA J2000	DEC J2000	Ecliptic Latitude	N_{gal}	N_{nights} IIIa	N_{nights} IIIb	N_{nights} IIIc	N_{nights} IIId	Volume $Mpc^3\ year$
ABELL3651	19:52:12	-55:04:48	-33.5	142	0	0	83	0	5.15
ABELL3667	20:12:28	-56:48:00	-35.8	225	0	0	75	0	5.91
ABELL3677	20:26:24	-33:21:00	-13.7	34	0	0	45	0	2.02
NGC6946	20:34:52	+60:09:14	71.9	2	0	316	0	75	16.88
ABELL3698	20:36:00	-25:16:12	-6.4	41	0	0	92	0	8.36
ABELL3716	20:51:31	-52:42:00	-33.6	274	0	0	73	0	3.25
ABELL3733	21:02:00	-28:03:00	-10.7	134	0	0	97	0	9.36
ABELL3744	21:07:12	-25:28:12	-8.6	148	0	0	52	0	5.64
ABELL3749	21:10:12	-45:48:00	-28.1	161	0	0	91	0	7.92
ABELL3799	21:41:36	-72:42:36	-54.0	19	0	0	35	0	1.42
ABELL2382	21:52:00	-15:37:48	-2.5	137	0	0	61	0	3.53
ABELL2399	21:57:31	-07:46:48	4.4	306	0	0	44	0	3.31
ABELL3831	22:03:19	-45:49:12	-31.5	104	0	0	102	0	8.71
SDSS22	22:15:40	+13:24:00	22.5	168	0	83	0	0	4.87
ABELL3879	22:27:48	-69:01:12	-53.2	53	0	0	36	0	2.04
ABELL2457	22:35:48	+01:28:12	9.6	105	0	0	36	0	4.10
NGC7331	22:37:04	+34:24:56	39.4	56	0	290	0	75	26.72
ABELL2469	22:40:28	+12:15:00	19.1	27	0	0	23	0	2.35
ABELL3911	22:46:04	-52:43:12	-40.8	30	0	0	87	0	7.47
ABELL2506	22:56:36	+13:19:59	18.5	124	6	207	37	43	73.78
ABELL3969	23:05:36	-44:07:48	-34.9	56	0	0	49	0	4.65
SDSS23	23:14:40	+13:57:00	17.3	190	0	113	0	0	10.02
ABELL2572	23:18:24	+18:43:59	21.3	104	6	232	15	47	40.40
ABELL3990	23:18:48	-67:46:12	-55.3	11	0	0	11	0	0.39
ABELL2589	23:24:00	+16:49:00	19.0	238	7	214	19	44	43.62
ABELL2593	23:24:30	+14:37:59	16.9	606	7	202	30	40	32.38
ABELL2634	23:37:57	+26:54:33	26.7	348	0	247	10	59	54.37
ABELL2657	23:44:54	+09:09:00	9.9	142	8	157	45	31	44.11
ABELL4038	23:47:40	-28:07:48	-24.4	676	0	0	68	0	7.17
ABELL2666	23:50:54	+27:09:00	25.6	62	0	270	9	58	64.23
ABELL4059	23:56:43	-34:40:12	-31.1	446	0	0	69	0	10.90

Note - Identification code for the field names: A = M31, C = Coma,
F = Fornax, PER = Perseus, U = Ursa Major, V = Virgo, VE = Virgo South

4.4.2 Construction of References and Bad Pixel Maps

Irregular pixels, e.g. dead pixels or hot pixels, produce non-linear responses that should not be used in image analysis based on a linear algorithm. The number of bad pixels in ROTSE-III CCDs is well under 1% and therefore not a problem for the usual data analysis focused on a small area of the image. For our transient search, however, the full image array is used and the bad pixels can affect the convolution kernel estimate or produce spurious residues in the difference image. We therefore have to first determine the locations of these problematic pixels for each CCD. For each telescope, ∼2000 images taken in the past year are randomly selected from the

archive. Background determined by SExtractor is removed from the images. At each pixel location, the median value of all images is recorded. Given the fact that the majority of pixels in an image are associated with the sky background, the resulting median array shows a relatively smooth residue sky map. Abnormal pixels with consistently high or low charges will stand out. A pixel is thus marked bad if its median value deviates far enough from the average. This procedure does a good job finding dead or constantly hot pixels but is by no means complete in finding irregular pixels. To efficiently correct for as many potentially problematic pixels as possible, we adjust the cutoff value between 3 and 4 sigma to mark a total number of 0.4% pixels. With this bad pixel map, each image can be corrected using the "image_suture" routine in IDL written by Akerlof. The questionable pixel values are replaced by local averages obtained on 3 x 3 neighborhood.

Transient events are detected based on positive changes in luminosity. A reference without the transient light or while the source is in quiescence is needed for comparison. For a supernova, the lightcurve rises in a time scale of a few weeks and the explosion is not recurrent, so all past images up until a month before the search time can be used as reference. For RSVP, each reference is constructed by coadding 30 to 40 images with best quality (at early phase of the search, a lower number of images are used based on availability). This image will be cross-convoluted with the new image to look for flux changes. High signal-to-noise is thus desirable to minimize the noise in the difference. Although the cross-convolution routine does not require better seeing in the reference, a well confined PSF helps to reduce the blurring in the difference and detection of point sources.

4.4.3 Data Flow and Automated Candidate Filtering

Every night, for each field, two sets of four dithered 60-sec exposures (20-sec for fields with bright target galaxies) are taken with a 30-minute cadence. Following the method developed by the Texas Supernova Search Quimby (see 2006, for the details), the images for each 4-exposure epoch are co-added as are the total 8 images for the night. All three co-additions are subtracted by the same reference image. The difference images are processed through SExtractor to find residual objects. To reject false detections due to bad pixels, cosmic rays, asteroids and subtraction noise, further filtering is applied. The signal-to-noise ratio of a candidate has to be above 5 in the nightly 8-fold sum and 2.5 for the sum of single epoch. The positions of a candidate in 3 subtractions must match to within one pixel for detections above 15 SNR and 1.5 pixels for those with SNR below 15. The FWHM of the candidate has to lie within the range of one pixel and twice the median FWHM for stars in the convolved reference image. Next, the flux change in a circular region with a radius of 4 pixels is checked and a cut is applied with a lower threshold for detections embedded in known galaxies and higher for those corresponding to stellar objects. This later criterion is intended to suppress variable stars. In particular, if a candidate is not consistent with the core but within 20% of semi-major axis length from the center of a galaxy, 3% change is required. If a candidate matches a star or unknown object, 60% change is required. For any other areas, 10% change is required. To reject false detections at convoluted bad pixels in the background (see §4.3.3), any candidate with flux change greater than 1000% should match a sextractor identification in the new image.

Finally, if there are too many candidates in a field, the image may have poor quality and/or the subtraction have failed. Any real transient is not likely to be found in

such cases. Therefore if over 20 candidates pass the above filters in a field, crowding of sources is checked. Objects with more than 15 neighboring candidates within 250 pixels are rejected. If there are still more than 20 candidates, the objects near the edge of images are rejected assuming the peripheral areas are prone to aberrations and fringing. This process is repeated in a shrinking area around the center of the image, until either the area is 800 pixels wide or there are less than 20 candidates left.

4.4.4 Web Scan and Follow-up Schedules

The coordinates of the final candidates are converted from their physical locations in the image according to astronometry of the reference. For preliminary analysis of the signal, aperture photometry by SExtractor is used. The magnitude zero point is determined by running SExtractor with the same aperture size on the convoluted reference image, followed by calibration to the USNO-A1.0 catalog.

Information about the remaining candidates and subframes (about $7'$ by $7'$) from the two epochs of coadd and the reference image are transfered immediately to rotse1, the ROTSE webserver. Utilizing the Perl script written for prompt GRB follow-ups, rotse1 monitors the coming files constantly and creates or updates a structure of webpages for human scanning. The layout of the scan website is designed after the transient search page by Rykoff and TSS website by Quimby. At http://www.rotse.net/supernova_search/, the user finds a list of dates, each linking to a table of all candidates of the day. The table for each day is organized by fields. By clicking on the field name, the user is redirected to an information page resembling the example in Figure 4.4. The user can also choose to go directly to an anchored position for a particular candidate in the information page by clicking on the corresponding entires in the table.

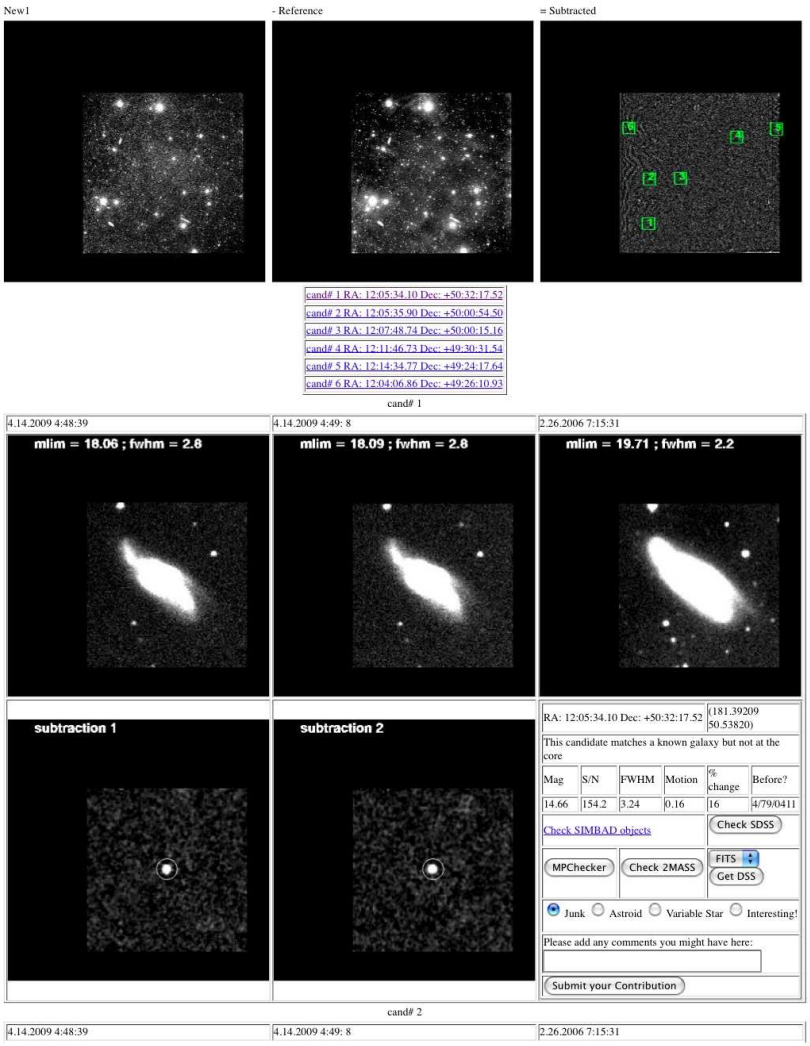

Fig. 4.4.—: Sample supernova search information page. Subimages and information table of the first candidate are shown. The complete webpage will include similar tables for all candidates.

For each candidate, critical information are tabulated to help determining its significance. The magnitude, signal to noise (S/N) and FWHM are for the source detected in the difference image between the reference and the sum of the night. The "motion" is the distance between the locations found for the two epochs, in unit of pixels. The "% change" is the relative flux change between the sum of the night and the reference within 4 pixels from the candidate location. The last column "Before?" lists the number of times a candidate is found at this location, the number of nights compared

and the last date a match is found (as three numbers divided by slashes). A candidate observed more than once has a larger significance while a detection months ago or in the past season may indicate a recurrent brightness change. Links for searching various catalogs and archives are available. SIMBAD archive can be searched within 0.01 degree from the candidate. Minor Planet Checker (MPChecker) can be queried within $5'$ to 21 visual magnitude at the time of the first image. SDSS, 2MASS and DSS images can be obtained in a comparable area as the ROTSE sub-images. Among these, MPChecker is critical for rejecting slow-moving astroids without recurrent detections between the nights. SDSS provides deep (to 23 magnitude in r band) references for identification of counterparts and sometimes redshift measurements of potential hosts. Outside SDSS coverage, DSS achieve is checked for counterpart. Although the limiting magnitude is often not much deeper than ROTSE-III reference, its better resolution helps to identify extended sources. Finally, the user can select the nature of the source and make additional comments. By submitting a comment on the information page, the user will be redirected back to the candidate table. The input comment, with the time and user's name, will be then be shown next to the candidate entry. New comment will overwrite the old ones.

Potential SN candidate determined from the above scan will be sent to HET for spectroscopic confirmation. The coordinates, approximate unfiltered magnitude and a finding chart will be supplied. This initial follow-up is time critical and requested at high priority. Confirmed SN are reported to CBET. Interesting discoveries are also sent to Astronomer's Telegram (ATEL), whose content is available to the public free of charge. In the occasional case when HET is not available, the transient is reported to CBET and/or ATEL as unconfirmed candidates.

A SN detected at a very early phase or a particularly interesting event will trigger

further HET follow-up observations. About 1 or 2 such targets are picked every tri-semester and the spectral observations usually cover every 3-7 days. The exact follow-up scheme is determined on an event-to-event basis.

CHAPTER V

RSVP supernovae

5.1 Introduction

By end of September, 2009, the RSVP pipeline identified a total of 46 SNe (including 5 first reported by other groups). Besides, 5 novae in M31 and 6 cataclysmic variables (CVs) have been reported by RSVP. More CVs have likely been detected but were not recorded given their lower priority in the project. The majority of the discoveries are from ROTSE-IIIb, while ROTSE-IIIc discovered two SNe and ROTSE-IIId discovered two SNe and one nova. This ratio is not surprising given the limited search time at IIIa, IIIc and IIId. In particular, ROTSE-IIId had suffered from lots of bad weather (mostly strong winds) at the site. Its discovery rate per search volume matches ROTSE-IIIb. At ROTSE-IIIc, mechanical problem with the focus motor resulted in an unstable and highly asymmetrical PSF which is not preferred by the search algorithm.

Observations of the 46 SNe, with data available by end of 2009, are presented in this Chapter. The data reduction method and ROTSE-III photometry are reported in §5.2. Our first discovery, SN 2007if, turns out to be a ultra-luminous type Ia event. Multiple epochs of HET observations and Keck detections of the host are presented for this particular event, followed by a discussion of its probable origin in §5.3.

5.2 ROTSE-III Observations of the SNe

5.2.1 Data Reduction

For each SN field, images taken on each available night are coadded. A reference is built using the best 30 or so images taken more than 50 days before the estimate SN maximum light or more than 200 days after the maximum. Subframes of 300 by 300 pixels around the targets are used for photometry and calibration. If the host brightness is below the detection threshold of ROTSE-III, the standard RPHOT routine is used to do PSF photometry. If the host is visible in the reference frame, image subtraction is applied (see Chapter 4 for the details). Photometry is performed at the target location in the difference image, using the PSF estimated in the convolved reference image. Photometry errors are likely underestimated given the correlated background pixels. Calibration to USNO B1.0 R-band is carried out by calculating the medium offset from the USNO B1.0 magnitudes for selected field stars.

5.2.2 Discoveries and Photometry

Basic information of the 46 SNe are tabulated in Table 5.1. Finding charts and ROTSE-III lightcurves are displayed in Figure 5.1. Description of individual events are presented below.

5.2.3 SN 2007gr

SN 2007gr was a type Ic supernova in NGC 1058, discovered on Aug. 15.51 and reported by the LOSS group (Madison & Li, 2007). It was first picked up by the RSVP pipeline on Aug. 13th and was detected on the 11th in the ROTSE-III images, but did not receive much attention because of our lack of experience at the beginning of the project. The supernova was not detected to a limit of 20.1 mag on Aug. 10.4 in the ROTSE-III images, confirming an explosion date between then and Aug. 11.4.

Table 5.1. List of RSVP SNe

IAU Name	RSVP Name	RA (J2000)	DEC (J2000)	Type	Redshift	Host	Discovery Date	RSVP Field
2007gr*	···	02:43:27.98	+37:20:45.4	Ib/c	0.0017	NGC 1058	07/08/13	ABELL376
2007if	Twilek	01:10:51.37	+15:27:40.0	Ia	0.0736	Anonymous	07/08/19	ABELL160
2007is*	···	16:47:14.61	+40:14:37.0	Ia	0.030	UGC 10553	07/09/14	SDSS17
2007iu	Rappertunie	01:25:20.15	+08:54:13.0	II	0.09	Anonymous	07/09/08	ABELL193
2007kh	Bebe	03:15:12.03	+43:10:13.7	Ia	0.05	Anonymous	07/09/07	PER2
2007nq	Alderaan	00:57:33.77	-01:23:20.3	Ia	0.045	UGC 595	07/10/21	ABELL119
2007ob	MosEisley	23:12:26.00	+13:54:49.9	Ia	0.034	SDSS J231225.99+135450.1	07/10/28	SDSS23
2007op	Givin	01:53:12.34	+33:44:33.9	Ia	0.085	Anonymous	07/10/20	ABELL260
2007qc	Randy	11:57:04.78	+53:29:55.4	Ia	0.035	Anonymous	07/10/27	U4
2007qe	pip	23:54:12.92	+27:24:32.7	Ia	0.024	Anonymous	07/11/13	ABELL2666
2007rx	Stan	23:40:11.77	+27:25:15.5	Ia	0.031	Anonymous	07/11/28	ABELL2634
2007sp	Kabe	12:04:42.32	+49:11:09.2	Ia	0.024	SDSS J120446.19+491111.6	07/11/14	U12
2007su	Ike	22:19:08.84	+13:10:38.8	Ia	0.028	SDSS J221908.85+131040.4	07/12/19	SDSS22
2007sw	Nikto	12:13:36.93	+46:29:37.3	Ia	0.025	UGC 7228	08/01/20	U21
2008E	Butters	11:25:36.81	+52:08:27.3	Ia	0.034	Anonymous	08/01/04	U11
2008ab	Goths	11:34:45.92	+53:57:50.9	Ia	0.069	SDSS J113445.89+535749.7	08/01/30	U5/U6
2008ac	Clyde	11:53:45.15	+48:25:21.4	Ia	0.053	SDSS J115345.22+482520.9	08/01/30	U18
2008ad	Token	12:49:37.12	+28:19:46.0	Ia	0.054	SDSS J124936.88+281944.8	08/01/30	C6
2008am	Timmy	12:28:36.33	+15:34:48.8	IIn	0.234	SDSS J122836.32+153449.6	08/01/10	V5
2008ar	Wendy	12:24:37.97	+10:50:17.3	Ia	0.026	IC 3284	08/02/27	V24
2008bg	Mackey	12:51:11.94	+26:17:38.4	Ia	0.06	SDSS J125111.93+261737.7	08/03/05	C9
2008bj	Thad	11:51:47.74	+46:52:29.7	II	0.019	MCG+08-22-020	08/03/12	U23
2008by	Shelly	12:05:20.84	+40:56:45.8	Ia	0.045	SDSS J120520.81+405644.4	08/04/19	U33
2008bz	Kenny	12:38:57.73	+11:07:46.9	Ia	0.060	SDSS J123858.12+110750.0	08/04/22	V22
2008cw	Craig	16:32:38.24	+41:27:32.7	IIb	0.032	SDSS J163238.15+412730.7	08/06/01	SDSS15
2008dx	Kyle	13:00:14.34	+27:57:17.1	Ia	0.023	Anonymous	08/06/24	C5
···	Jimmy	12:56:42.71	+27:30:40.4	Ia	0.023	Anonymous	08/07/12	C5
2008es	Wing	11:56:49.10	+54:27:25.2	IIL	0.202	Anonymous	08/04/26	U2
2008fh	Phillip	03:20:18.57	+41:21:44.9	Ia	0.0179	Anonymous	08/07/30	PER5
2008fm	Bradley	23:49:03.51	+26:47:39.4	IIn	0.0385	UGC 12792	08/09/05	ABELL2666
2008fn	Tweek	16:21:48.53	+37:03:41.1	Ib/c	0.030	SDSS J162148.53+370338.9	08/08/04	SDSS13
2008fo	Terrance	16:40:12.55	+39:43:56.5	Ic	0.030	SDSS J164012.94+394400.4	08/08/07	SDSS16
2008fr	Towelie	01:11:49.13	+14:38:26.9	Ia	0.039	SDSS J011149.19+143826.5	08/09/14	SDSS1
2008fs	Filmore	01:09:05.66	+14:45:16.8	Ib/c	0.039	SDSS J010905.96+144520.8	08/09/21	SDSS1
2008gd	Jason	01:20:44.00	+14:41:38.5	II	0.059	SDSS J012044.48+144139.6	08/09/27	SDSS3
2008in*	···	12:22:01.80	+04:28:48.2	II	0.0052	NGC 4303	08/12/28	V47
2008io	···	12:50:02.63	-14:42:55.2	Ia	0.013	MCG-02-33-17	08/12/27	VE51
2009L	Red	12:58:47.91	+27:40:29.4	Ia	0.028	NGC 4854	09/01/13	C5
2009dd*	···	12:05:34.13	+50:32:18.3	II	0.0025	NGC 4088	09/04/07	U12
2009dn	Garrison	11:37:39.26	+46:57:10.9	II	0.039	PGC 35993	09/04/12	U25
2009eu*	···	16:28:41.08	+39:33:11.4	Ia	0.031	NGC 6166	09/05/25	SDSS14
2009fx	Tammy	16:53:11.32	+23:57:55.5	Ia	0.048	SDSS J165311.27+235754.4	09/05/29	SDSS18
2009fy	Jimbo	23:24:05.09	+16:39:51.6	Ia	0.0408	SDSS J232405.23+163943.1	09/06/01	ABELL2589
2009hk	Maxi	20:38:37.48	-25:06:56.7	Ia	0.018	MCG-04-48-26	09/07/11	ABELL3698
2009ia	Big Al	17:26:11.34	+59:18:30.9	Ia	0.027	SDSS J172611.22+591831.1	09/07/22	SDSS21
2009iv	Chef	02:58:14.22	+05:58:19.8	Ia	0.023	2MASX J02581424+0558189	09/08/21	ABELL400

*First discovered or reported by other groups.

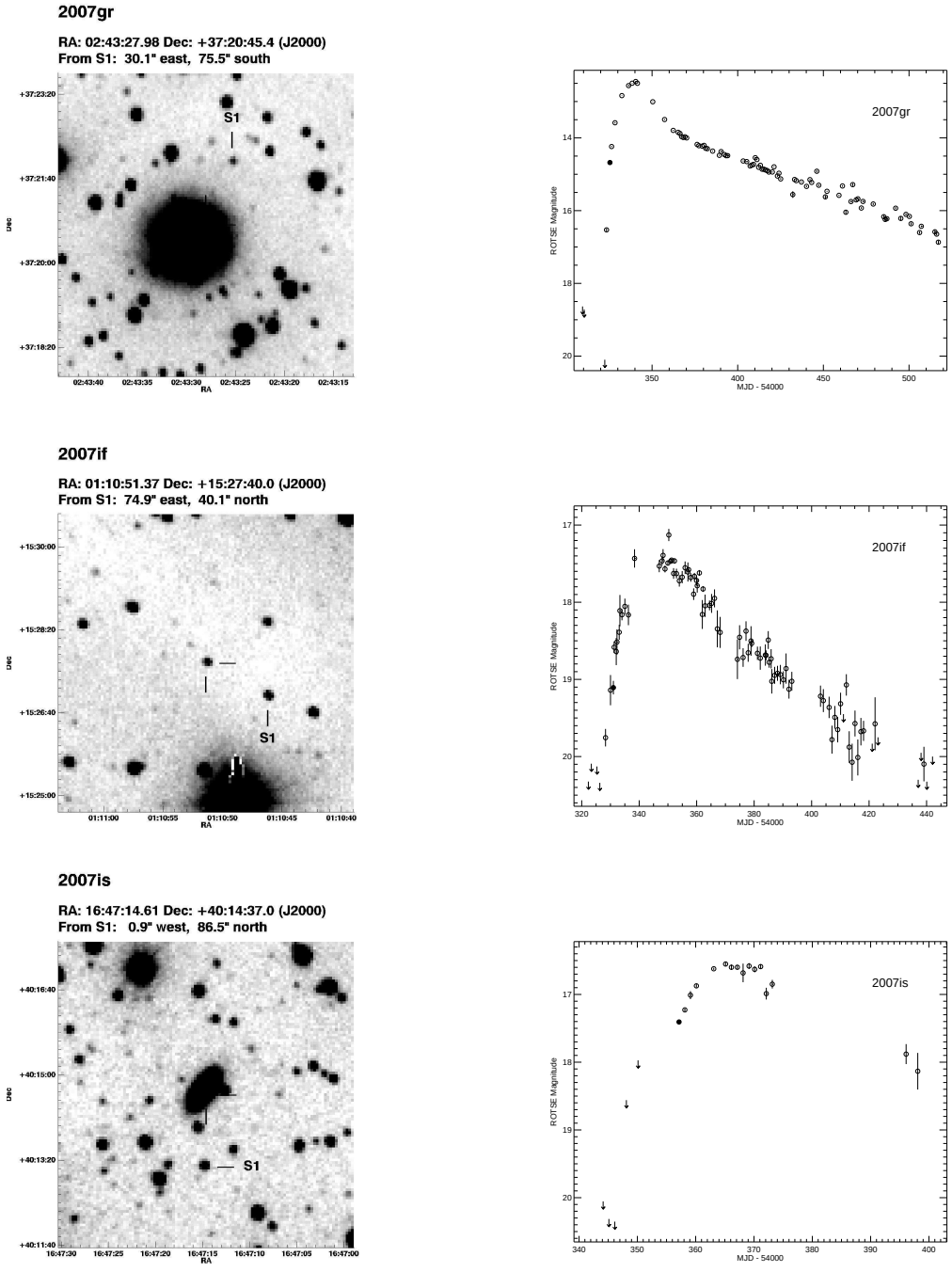

Fig. 5.1.—: ROTSE-III finding charts and lightcurves of the SNe observed by RSVP. Filled circles in the lightcurve plots represent data on the dates when the supernovae were identified in the pipeline.

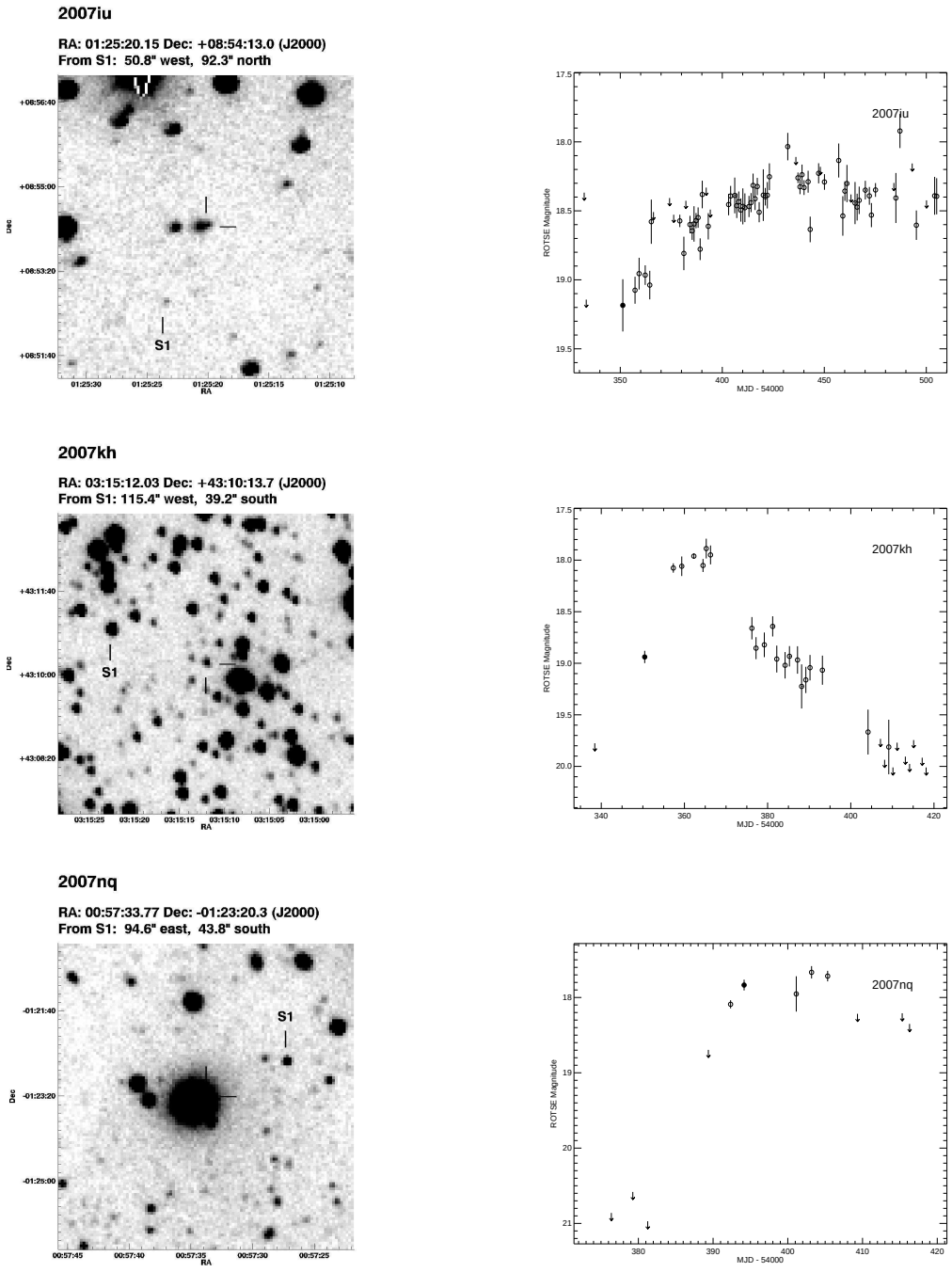

Fig. 5.1.—: ROTSE-III finding charts and lightcurves of the SNe observed by RSVP (cont'd).

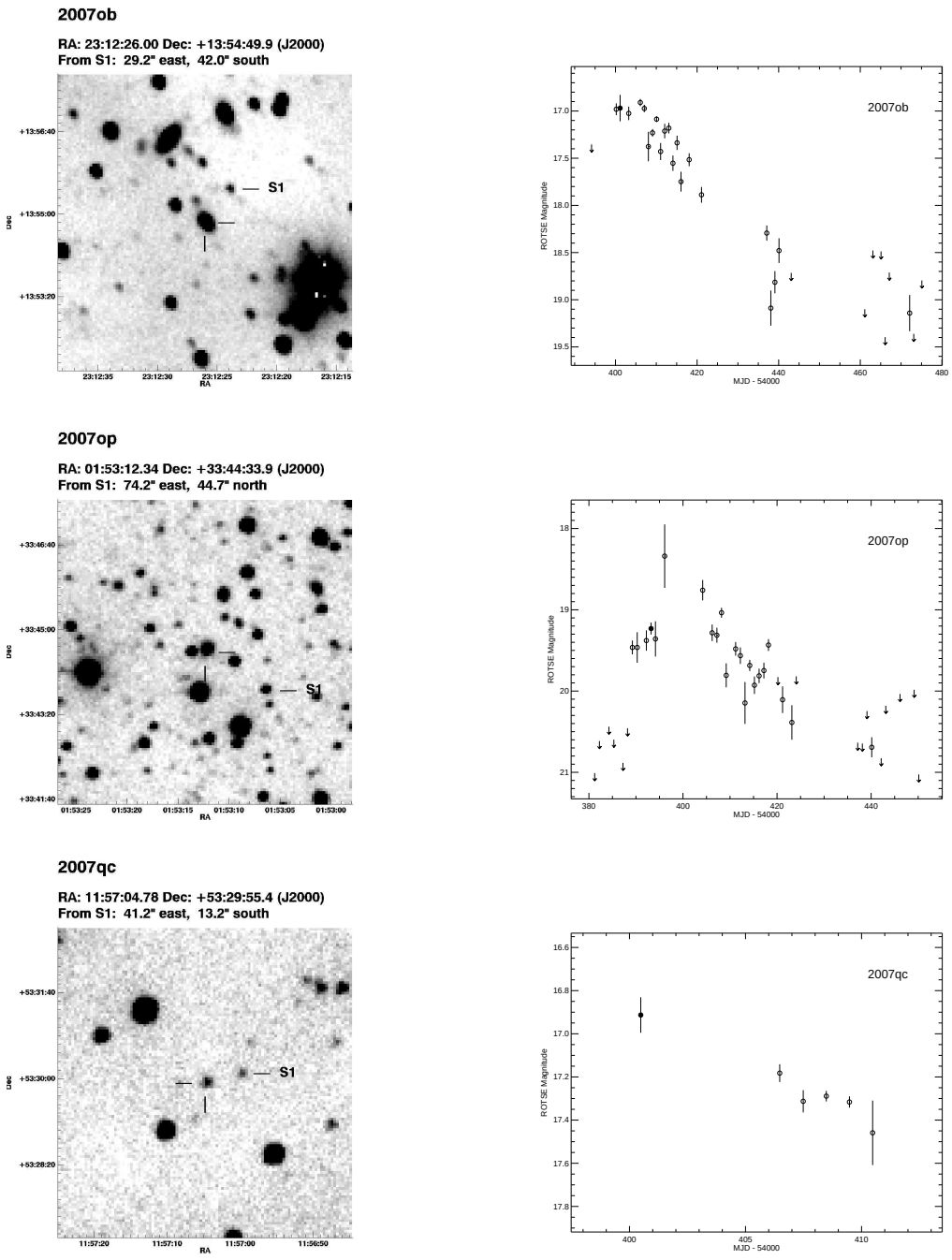

Fig. 5.1.—: ROTSE-III finding charts and lightcurves of the SNe observed by RSVP (cont'd).

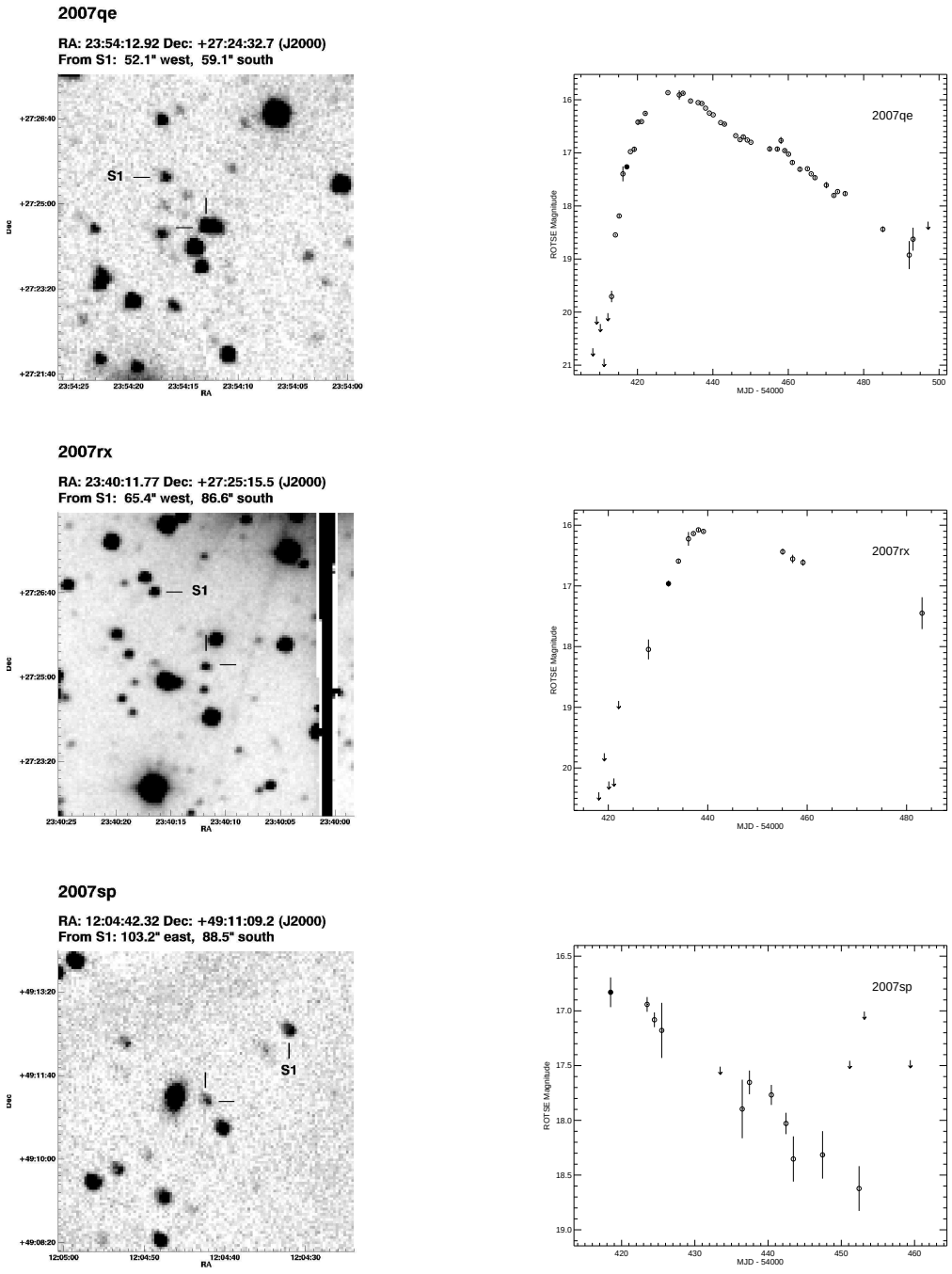

Fig. 5.1.—: ROTSE-III finding charts and lightcurves of the SNe observed by RSVP (cont'd).

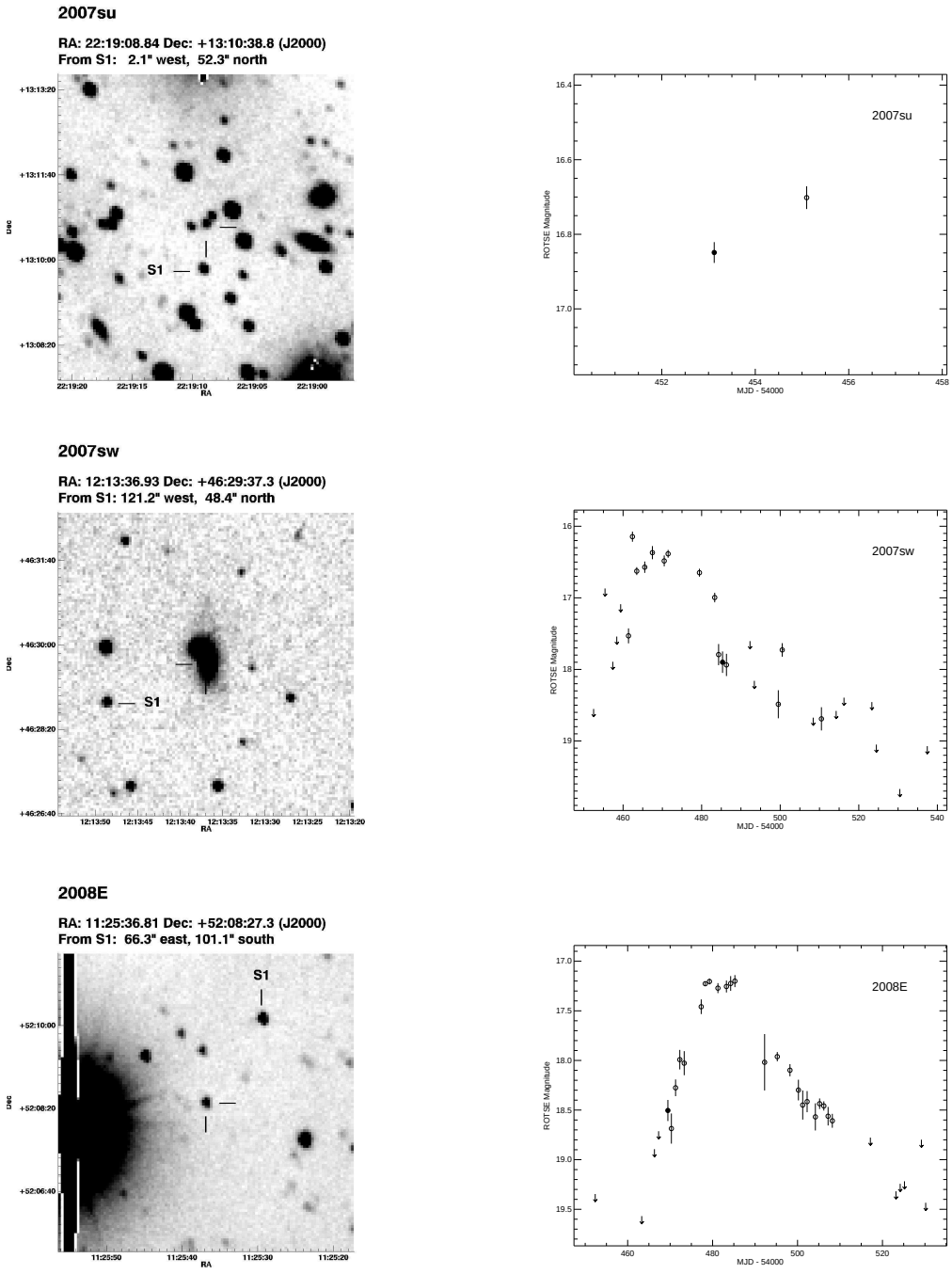

Fig. 5.1.—: ROTSE-III finding charts and lightcurves of the SNe observed by RSVP (cont'd).

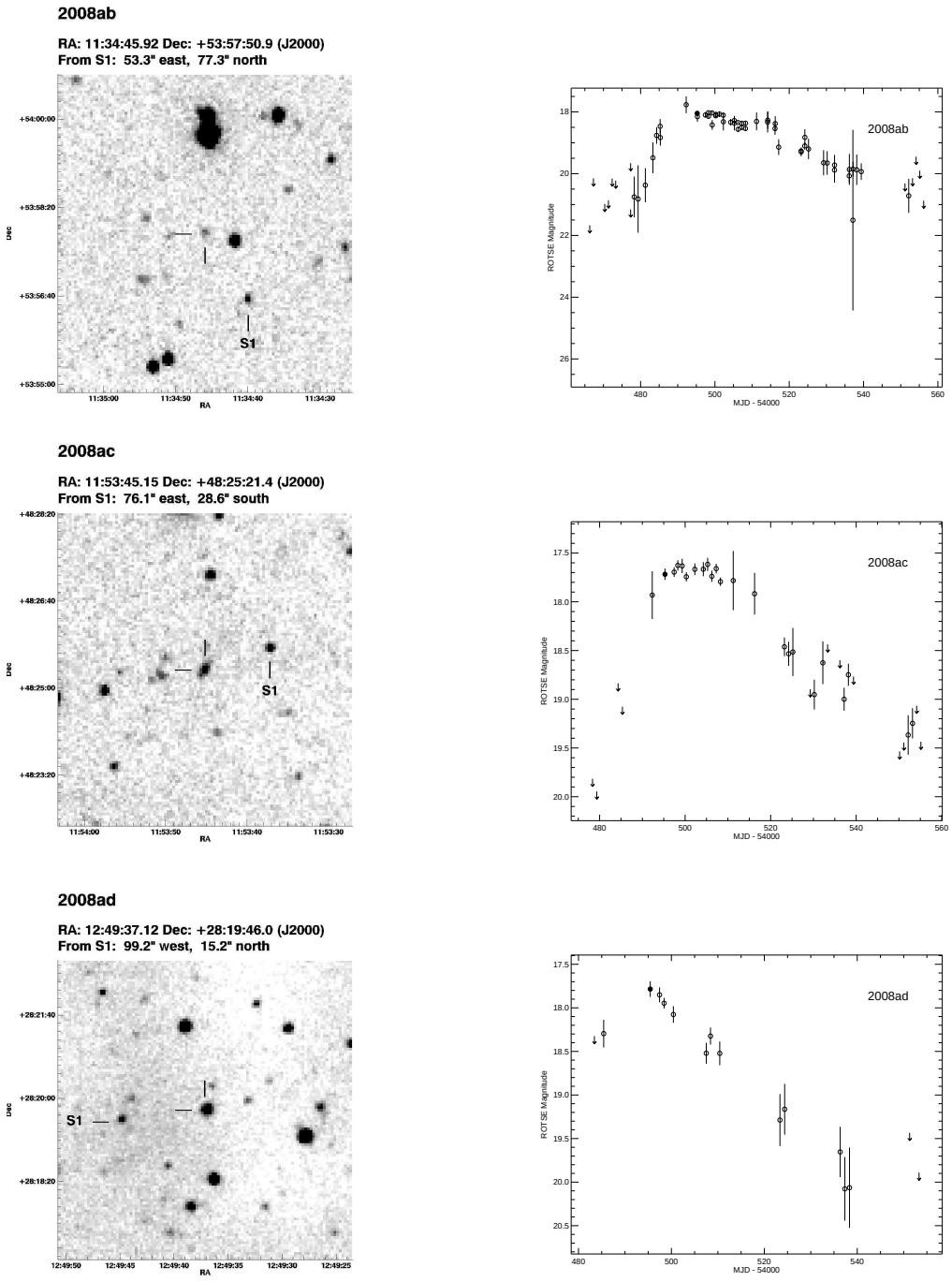

Fig. 5.1.—: ROTSE-III finding charts and lightcurves of the SNe observed by RSVP (cont'd).

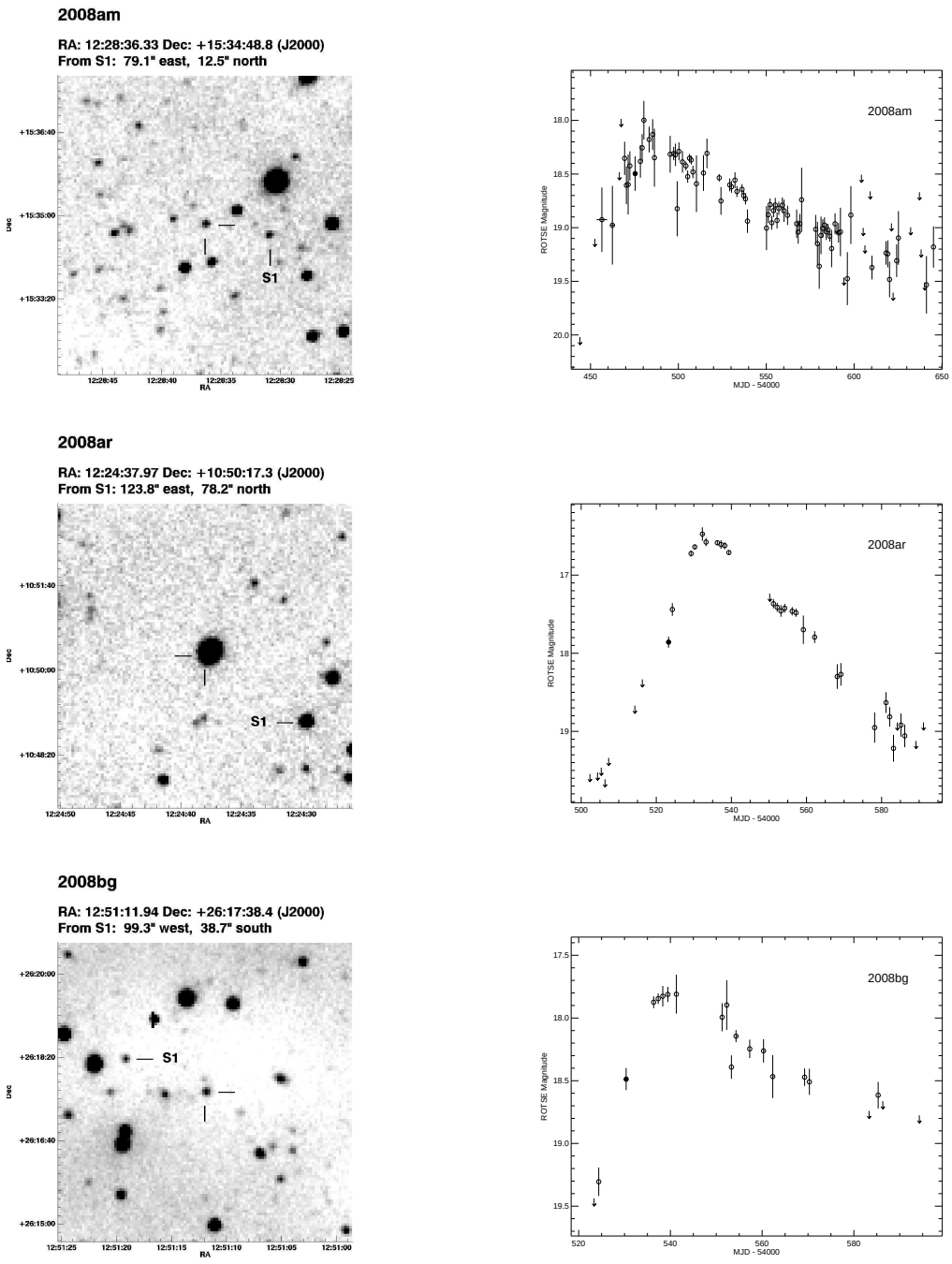

Fig. 5.1.—: ROTSE-III finding charts and lightcurves of the SNe observed by RSVP (cont'd).

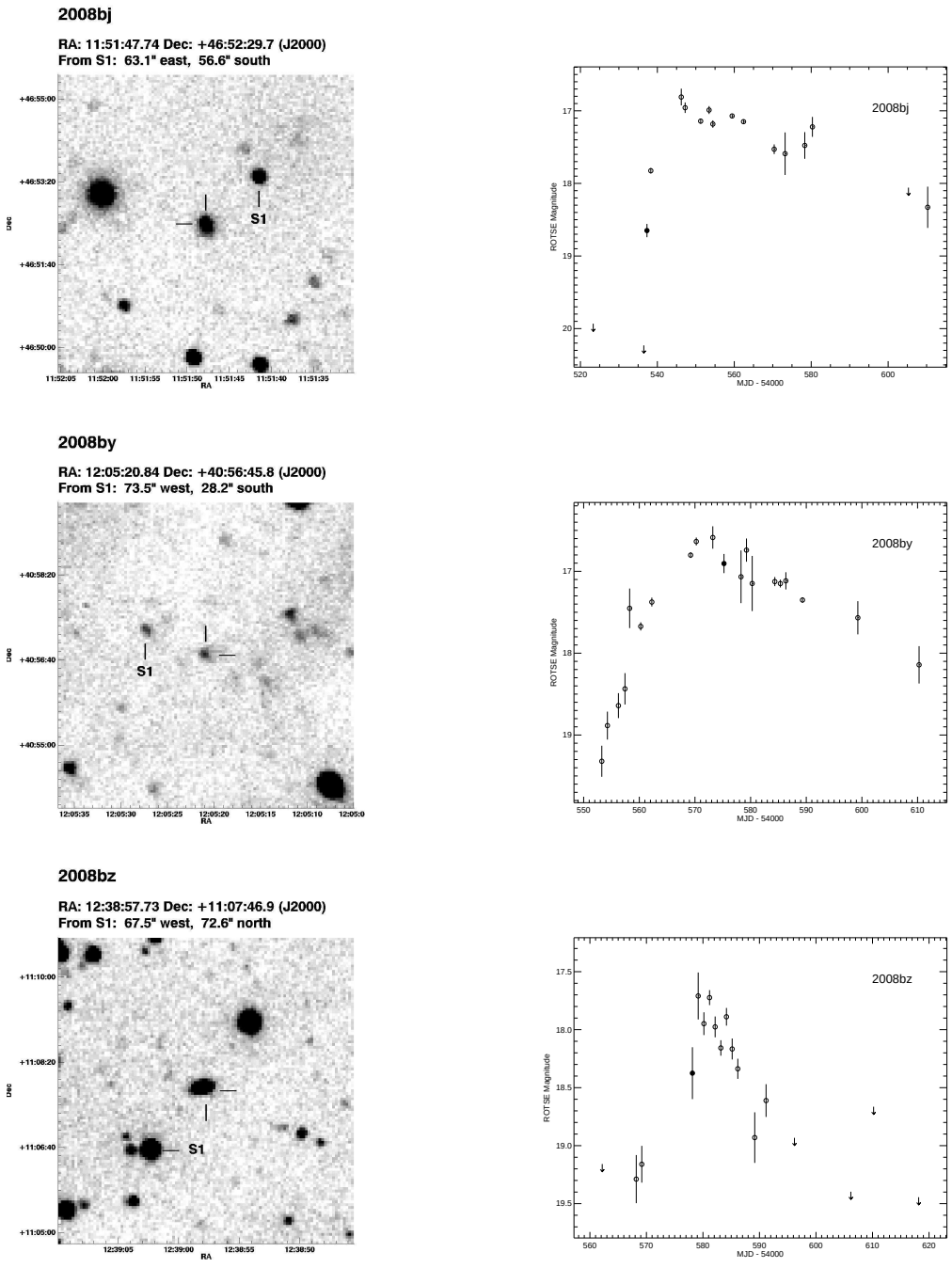

Fig. 5.1.—: ROTSE-III finding charts and lightcurves of the SNe observed by RSVP (cont'd).

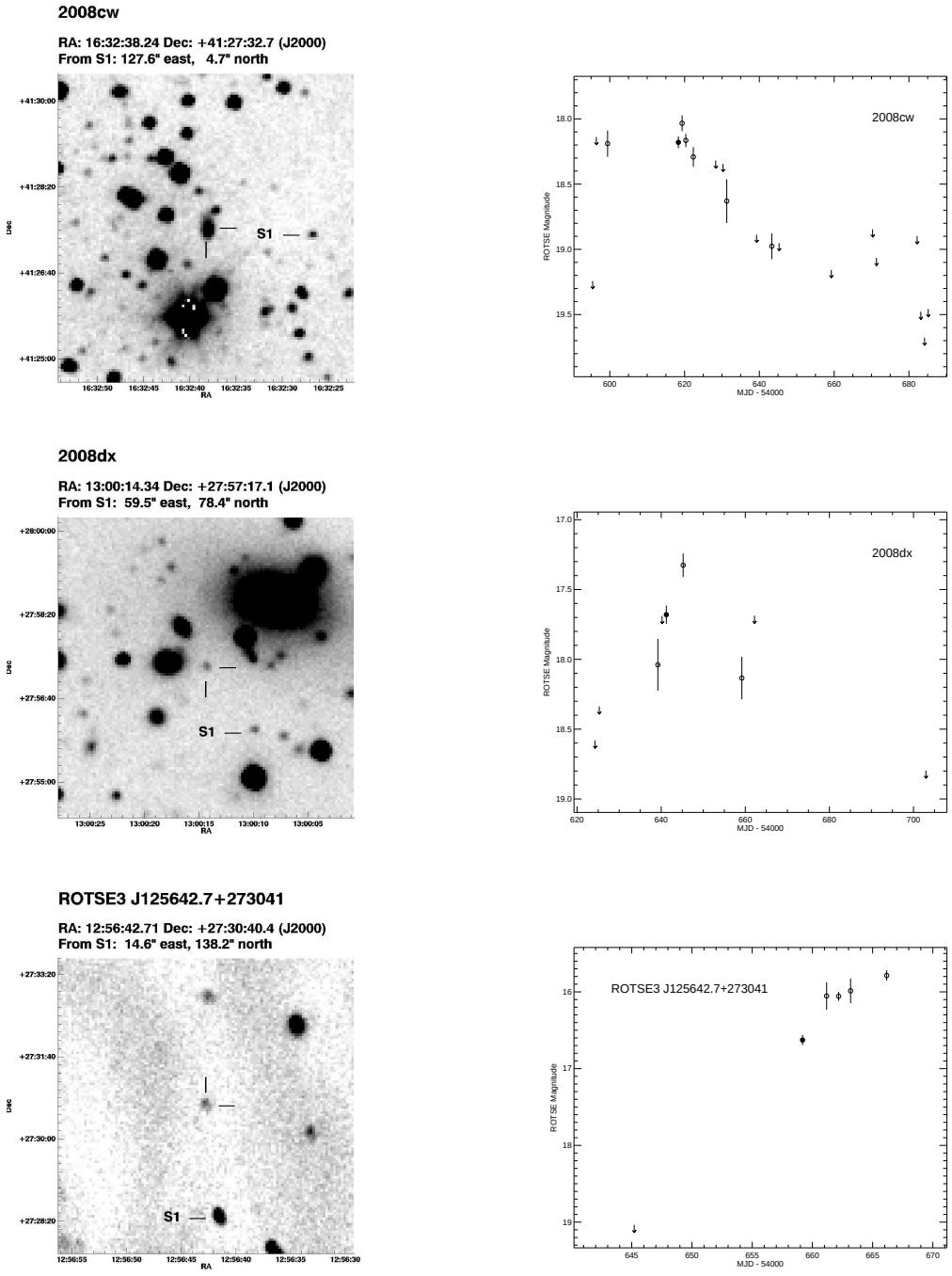

Fig. 5.1.—: ROTSE-III finding charts and lightcurves of the SNe observed by RSVP (cont'd).

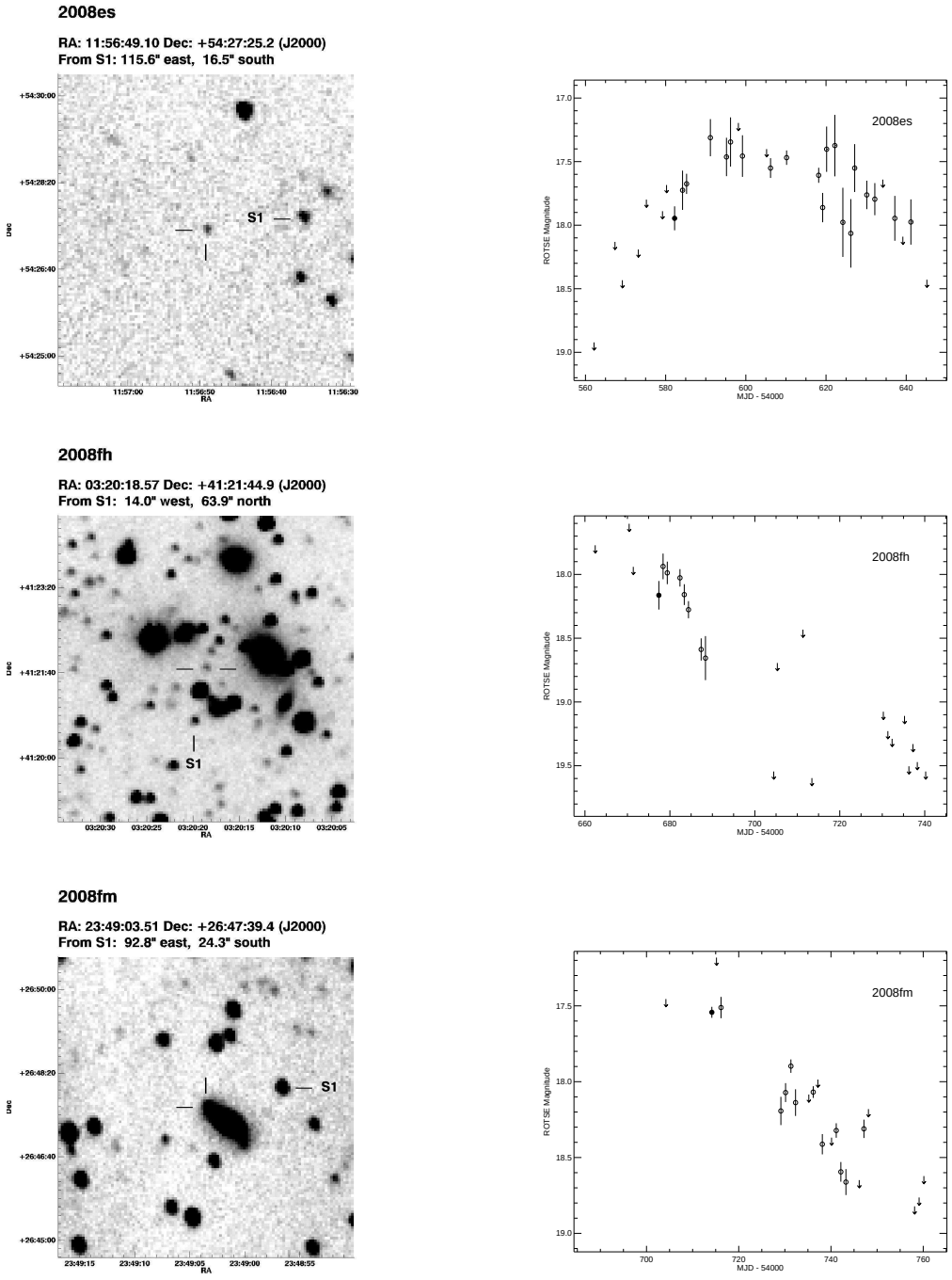

Fig. 5.1.—: ROTSE-III finding charts and lightcurves of the SNe observed by RSVP (cont'd).

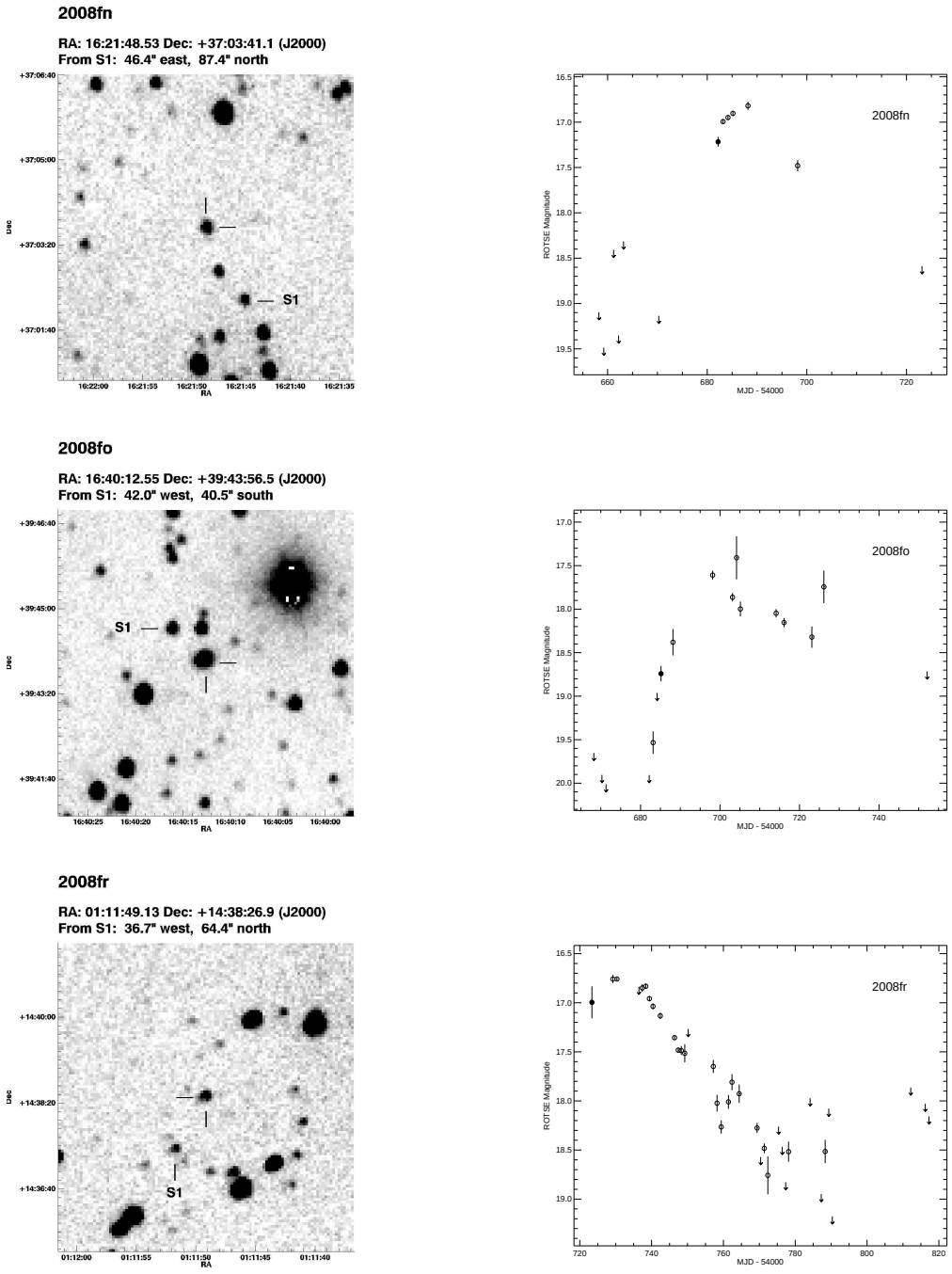

Fig. 5.1.—: ROTSE-III finding charts and lightcurves of the SNe observed by RSVP (cont'd).

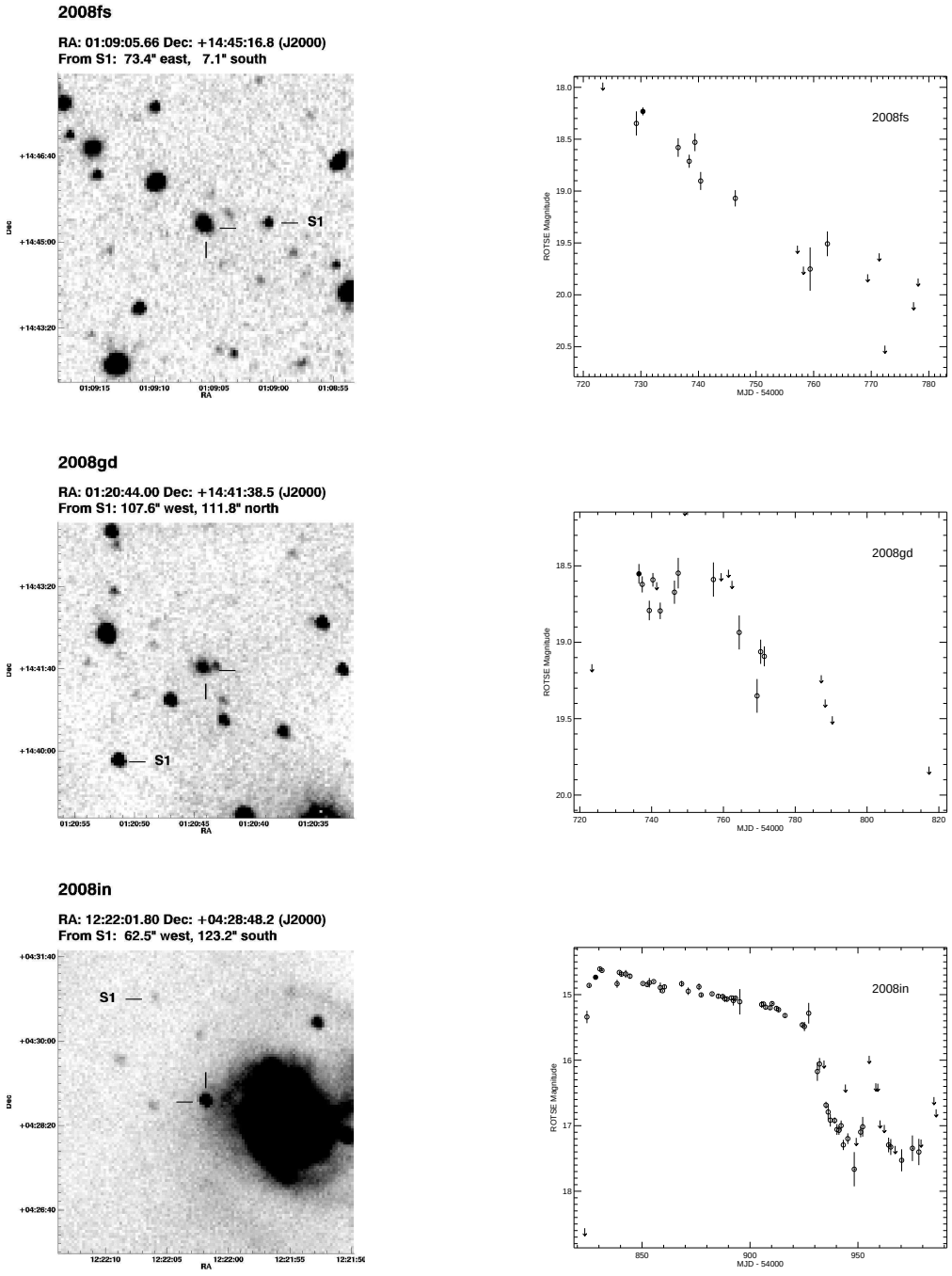

Fig. 5.1.—: ROTSE-III finding charts and lightcurves of the SNe observed by RSVP (cont'd).

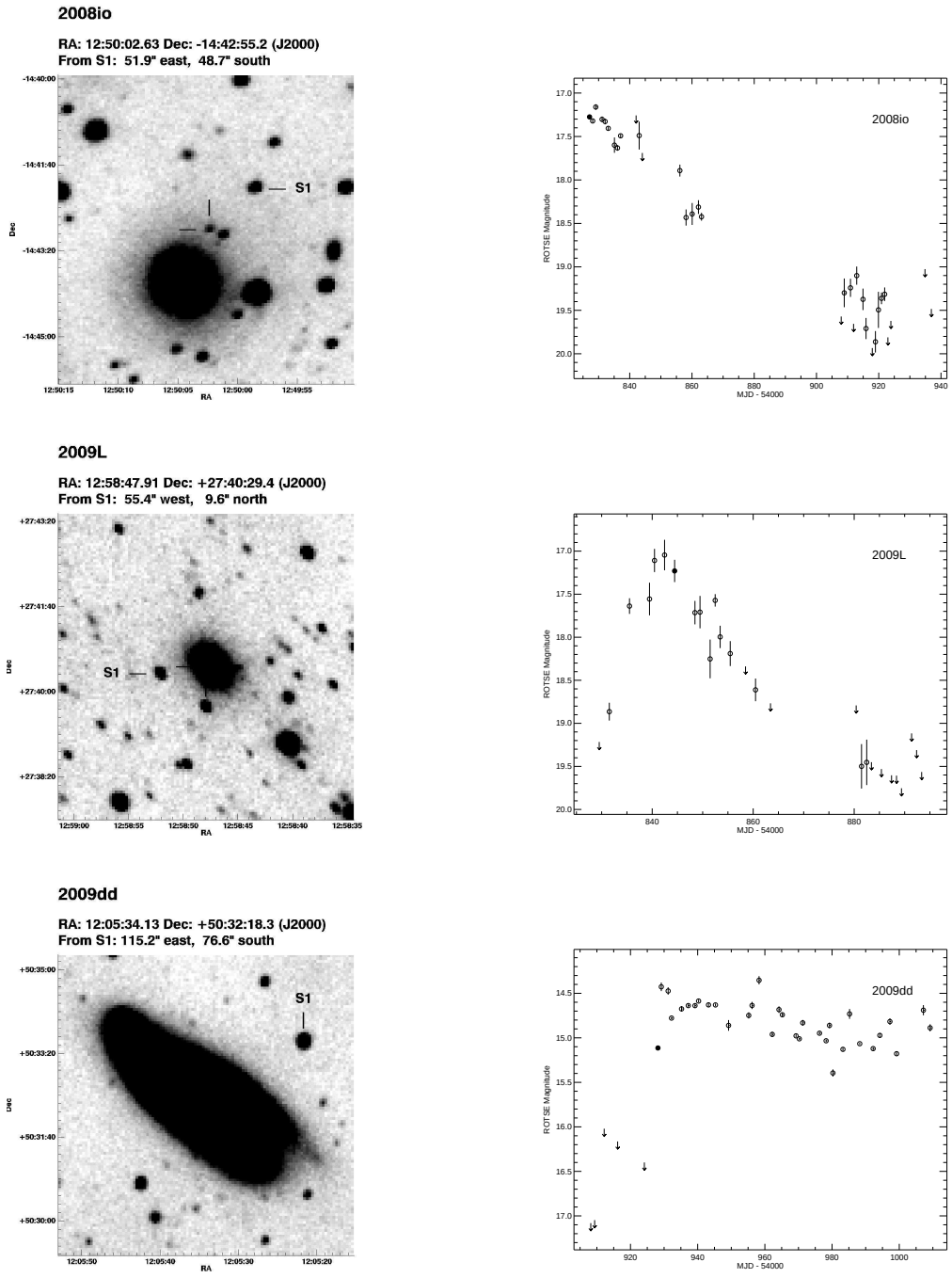

Fig. 5.1.—: ROTSE-III finding charts and lightcurves of the SNe observed by RSVP (cont'd).

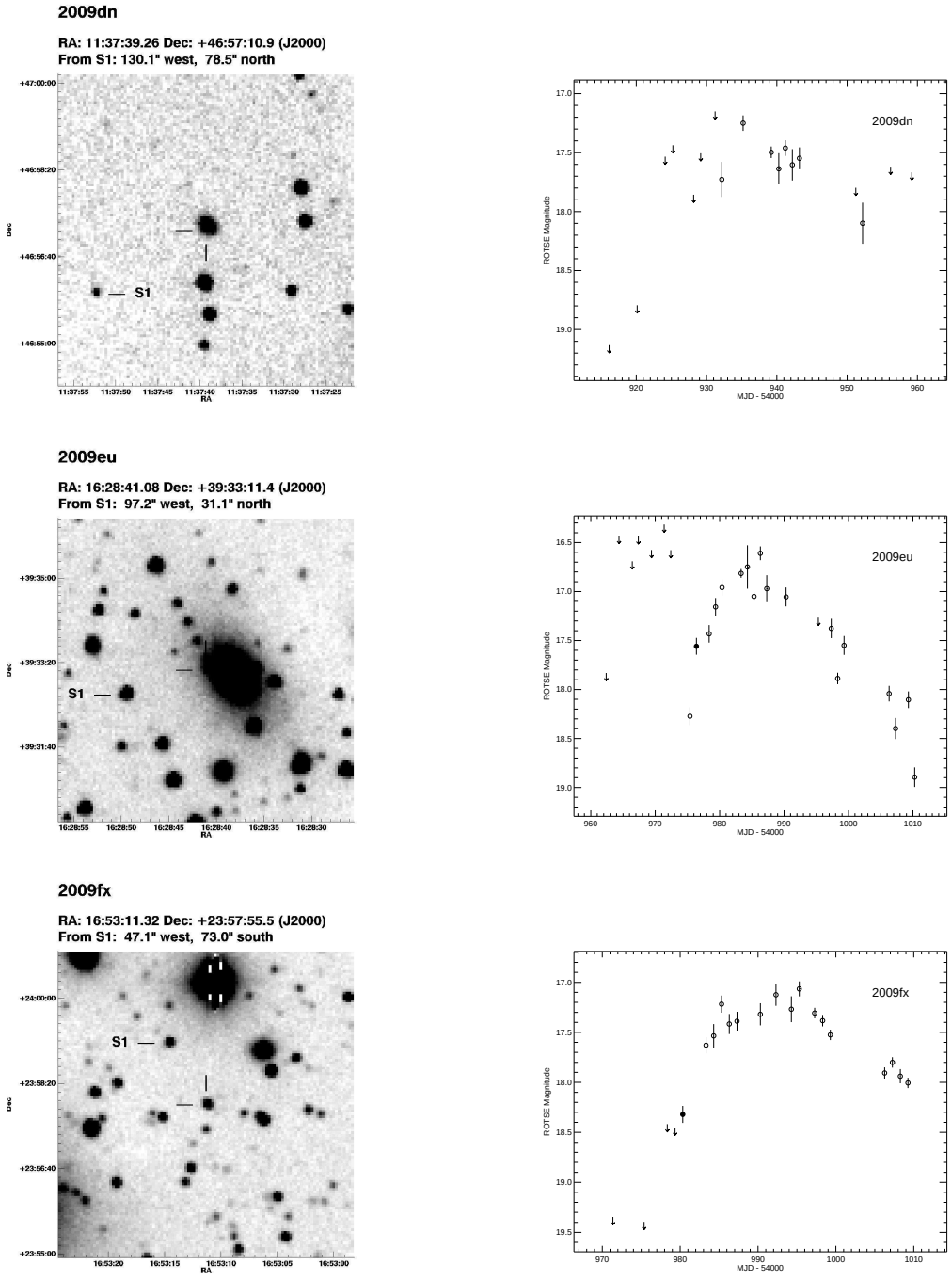

Fig. 5.1.—: ROTSE-III finding charts and lightcurves of the SNe observed by RSVP (cont'd).

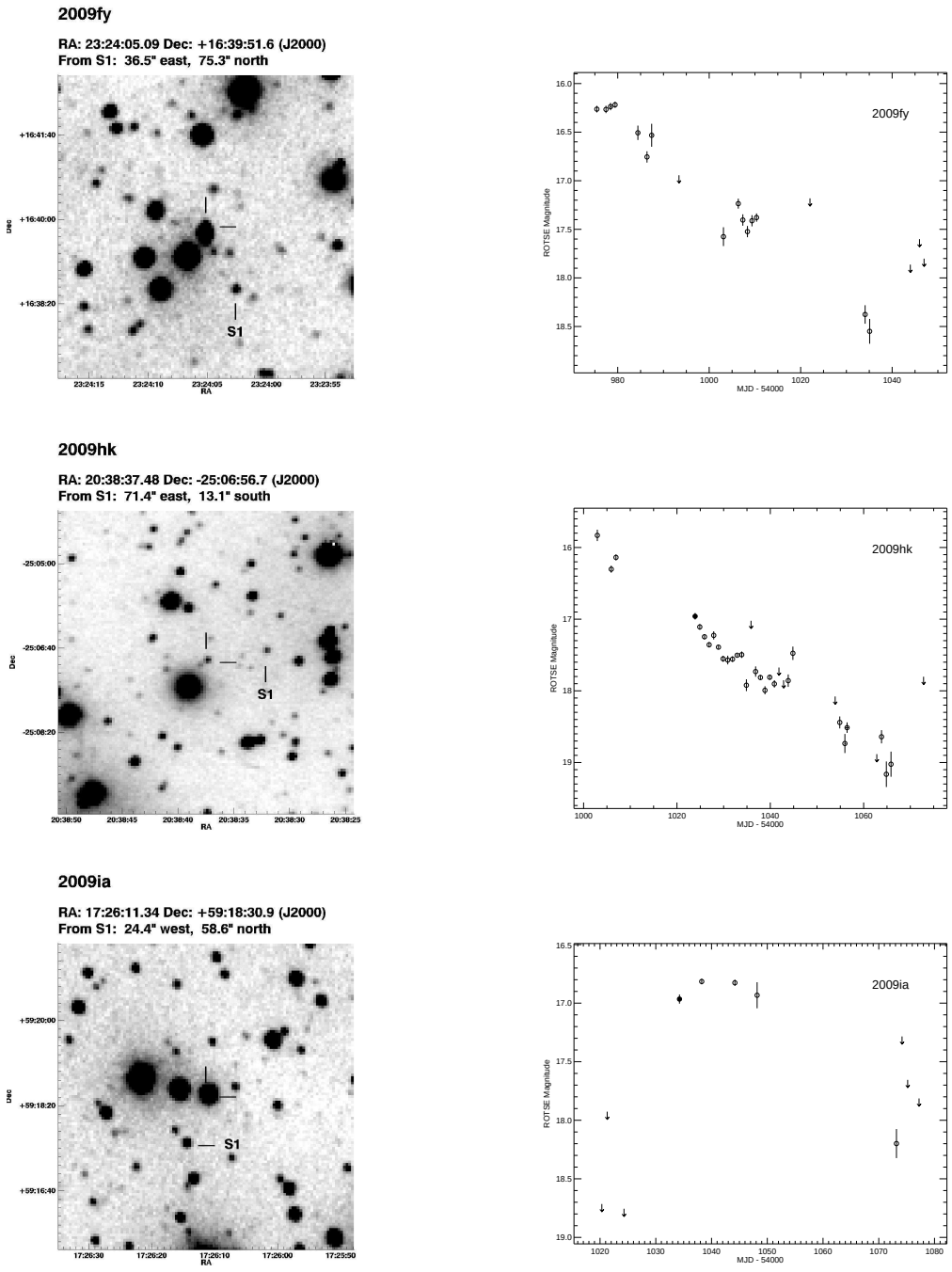

Fig. 5.1.—: ROTSE-III finding charts and lightcurves of the SNe observed by RSVP (cont'd).

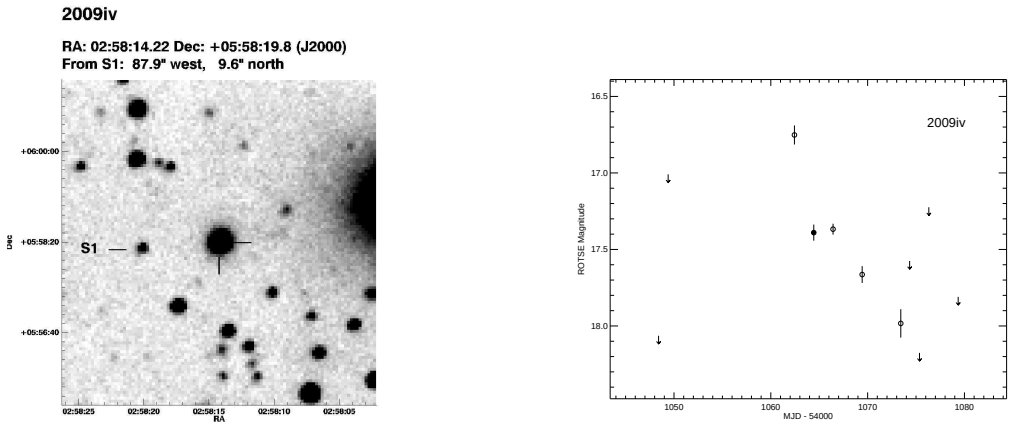

Fig. 5.1.—: ROTSE-III finding charts and lightcurves of the SNe observed by RSVP (cont'd).

Detailed photometric and spectroscopic observations of this SN were presented in Valenti et al. (2008); Hunter et al. (2009). In particular, with its narrow absorption lines and the identified evolution of carbon feature, SN 2007gr provides an important opportunity to explore the diversity among SNe Ic. Spectropolarimetry observations reported in Tanaka et al. (2008) supports a possible bipolar explosion model, although the data is not conclusive. Its nearby location also makes SN 2007gr a good candidate for a progenitor star search (Crockett et al., 2008).

5.2.4 SN 2007if

SN 2007if was independently discovered by the ROTSE-IIIb telescope on Aug 19.28 UT and the SNfactory subsequently on Aug 25.4 UT (Yuan et al., 2007a,p). Spectra taken with the MDM 2.4m telescope on Aug 22.4 UT and the HET telescope on Aug 29 failed to show significant features that could identify the nature of the transient. The features of a type Ia supernova were not recognized until Sep. 6.45 UT, when additional spectra were taken by the Hale telescope at Palomar observatory.

Another SNIFS spectrum, obtained later on Sep. 10.5 UTC, was found to match that of the ultra-luminous SN 2003fg. A redshift around 0.07 was inferred and indeed

suggest SN 2007if was over-luminous as well with an absolute magnitude approaching or above -20. Further observations obtained with HET and Keck will be presented later in this chapter, along with discussions of the probable interpretations.

5.2.5 SN 2007is

2007is was a normal type Ia supernova, discovered on Sep. 14.14 and reported by the LOSS group (Thrasher et al., 2007). It was detected and picked up by the RSVP pipeline on the same date. Silverman et al. (2007) reported its spectroscopic identification and an expansion velocity of 11600 km/s based on the Si II 635.5-nm absorption.

5.2.6 SN 2007iu

SN 2007iu was discovered on Sep. 8.24 UT with the ROTSE-IIIb telescope (Yuan et al., 2007c,b). A spectrum (420-890 nm) obtained on Sep. 15.28 UT with the 9.2-m Hobby-Eberly Telescope (+ Marcario Low-Resolution Spectrograph) by M. Shetrone, V. Riley, and F. Deglman, shows it to be a type-II supernova. Emission lines from H-alpha, H-beta, and H-gamma are detected, and a redshift of z=0.09 is inferred from the line peaks. Weak emission lines from He II 468.6-nm and possibly O III 500.7-nm are also seen. An emission peak is observed at rest wavelength 588 nm, which, if identified with Na I, would imply a blueshift relative to the Balmer lines of about 600 km/s.

5.2.7 SN 2007kh

SN 2007kh was discovered on Sept. 7.45 UT with the ROTSE-IIIb telescope (Yuan et al., 2007e,d). Nothing is visible (including a possible host galaxy) at this position in the Digitized Sky Survey image or on any USNO archive plates. A spectrum (420-890 nm) obtained on Sept. 25.29 with the 9.2-m Hobby-Eberly Telescope (+ Marcario

Low-Resolution Spectrograph) by J. Caldwell, E. Terrazas, and V. Riley, shows it to be a type-Ia supernova. The spectrum is similar to that of SN 1994D at about 3 days after maximum light (Patat et al., 1996). Using the spectrum of SN 1994D as a template, the redshift is found to be approximately z=0.05.

5.2.8 SN 2007nq

SN 2007nq was discovered on Oct. 21.15 UT using the ROTSE-IIIb telescope (Quimby et al., 2007d). A spectrum (range 420-890 nm) obtained on Oct. 23.19 with the 9.2-m Hobby-Eberly Telescope (+ Marcario Low-Resolution Spectrograph) by M. Shetrone, E. Terrazas, and V. Riley shows it to be a type-Ia supernova, similar to SN 1992A prior to maximum light (Kirshner et al., 1993). Adopting the host-galaxy redshift of z=0.045, the expansion velocity, derived from the minimum of the Si II (rest 635.5 nm) line, is 12500 km/s.

5.2.9 SN 2007ob

SN 2007ob was discovered on Oct. 28.13 UT with the ROTSE-IIIb telescope (Yuan et al., 2007m,j). A spectrum (range 420-890 nm) was obtained on Nov. 1.22 with the 9.2-m Hobby-Eberly Telescope (+ Marcario Low-Resolution Spectrograph) by J. Caldwell, V. Riley, and E. Terrazas, and though the data are heavily contaminated by galaxy light, several broad features indicative of a type-Ia supernova are detected. Specifically, an absorption trough is observed around 630 nm, which is identified as Si II 635.5-nm; correcting for the recession velocity using the host-galaxy redshift from SDSS, the expansion velocity derived from the minimum of this Si II feature is about 12000 km/s.

5.2.10 SN 2007op

SN 2007op was discovered on Oct. 20.22 with the ROTSE-IIIb telescope (Quimby et al., 2007c). A spectrum (range 420-890 nm) obtained on Nov. 8.33 with the 9.2-m Hobby-Eberly Telescope (+Marcario Low-Resolution Spectrograph) by S. Odewahn and A. Westfall, shows it to be a type-Ia supernova; the spectra are similar to those of SN 1994D at about 11 days after maximum light (Patat et al., 1996). HET spectra of the host galaxy indicate a redshift of z=0.085.

5.2.11 SN 2007qc

SN 2007qc was discovered on Oct. 27.49 UT with the ROTSE-IIIb telescope (Yuan et al., 2007n,o). A marginally detected host galaxy (magnitude r = 22.9) is seen at the location of the supernova in pre-explosion SDSS imaging. A quick reduction of the red-channel spectra (range 510-990 nm), obtained on Nov. 13.55 by A. Rau (Caltech) with the Palomar 5-m telescope (+ Double Beam Spectrograph), shows 2007qc to be a type-Ia supernova at about 2 weeks past maximum light. Using spectra of SN 1994D as a template (Patat et al., 1996), an approximate redshift of z = 0.035 is found, which would imply an absolute r magnitude fainter than about -13 for the host galaxy.

5.2.12 SN 2007qe

SN 2007qe was discovered on Nov. 13.17 UT with the ROTSE-IIIb telescope (Yuan et al., 2007l,k). A spectrum, obtained by the SNfactory on Nov. 14.3 with the SuperNova Integral Field Spectrograph on the University of Hawaii 2.2-m telescope, shows 2007qe to be a young type-Ia supernova, easily a week before peak brightness. No lines from the host were present in the "Integral Field Unit" to determine the redshift. Compared to other supernova spectra at similar epochs, the redshift velocity

should be less than 3000 km/s. However, (Garnavich et al., 2007) measured a host redshift of 0.024 and estimated an expansion velocity of 28500±1500 km/s from a high-velocity Ca II component (see also Marion & Garnavich, 2007).

5.2.13 SN 2007rx

SN 2007rx was discovered on Nov. 28.11 UT with the ROTSE-IIIb telescope (Yuan et al., 2007g,f). A spectrum (range 420-890 nm) obtained on Dec. 6.16 with the 9.2-m Hobby-Eberly Telescope (+ Marcario Low-Resolution Spectrograph) by S. Odewahn and A. Westfall, shows it to be a type-Ia supernova. The spectra are similar to those of SN 1994D just prior to maximum light (Patat et al., 1996). Using the 1994D spectrum as a template, an approximate redshift of z=0.03 is estimated. This redshift is compatible with the nearby Abell 2634 galaxy cluster (z=0.031, Oegerle & Hill, 2001).

5.2.14 SN 2007sp

SN 2007sp was discovered on Nov. 14.50 UT with the ROTSE-IIIb telescope (Yuan et al., 2007h). A spectrum (420-890 nm) obtained on Dec. 13.45 with the 9.2-m Hobby-Eberly Telescope (+ Marcario Low-Resolution Spectrograph) by S. Rostopchin and E. Terrazas, shows it to be a type-Ia supernova about two months after maximum light; the shift of the spectral lines is consistent with the SDSS redshift for the nearby galaxy (z=0.024).

5.2.15 SN 2007su

SN 2007su was discovered on Dec. 19.10 with the ROTSE-IIIb telescope (Yuan et al., 2007i). A spectrogram (range 420-890 nm) obtained on Dec. 23.05 with the 9.2-m Hobby-Eberly Telescope (+Marcario Low-Resolution Spectrograph) by M. Shetrone and F. Deglman, shows it to be a type-Ia supernova around maximum light.

Adopting the recession velocity of the host galaxy (z=0.028, taken from SDSS), the minimum of the Si II 635.5-nm feature is blushifted by 11700 km/s.

5.2.16 SN 2007sw

SN 2007sw was discovered on Dec. 29.49 UT using the ROTSE-IIIb telescope in the TSS pipeline (Quimby et al., 2007b), but the RSVP pipeline did not pick it up until about 20 days later because of the severe blending with the host light. A spectrum (range 420-890 nm) obtained on Dec. 30.39 with the 9.2-m Hobby-Eberly Telescope (+ Marcario Low-Resolution Spectrograph) by S. Odewahn and E. Terrazas, shows it to be a type-Ia supernova. The spectra are similar to that of SN 2005ir (Frieman et al., 2005b,a) a few days prior to maximum light. Adopting the redshift of the apparent host (z=0.025; Updated Zwicky Catalog, via NED), the expansion velocity derived from the minimum of the Si II (rest 635.5 nm) line is about 14000 km/s.

5.2.17 SN 2008E

SN 2008E was discovered on Jan. 4.47 UT with the ROTSE-IIIb telescope (Yuan et al., 2008b). A spectrum (range 420-890 nm) obtained on Jan. 7.35 with the 9.2-m Hobby-Eberly Telescope (+ Marcario Low-Resolution Spectrograph) by S. Odewahn and E. Terrazas, shows it to be a type-Ia supernova. The spectrum is similar to that of SN 1992A a few days before maximum light (Kirshner et al., 1993), and is consistent with the redshift of the nearby galaxy cluster (z=0.034).

5.2.18 SN 2008ab

SN 2008ab was discovered on Jan 30.23 UT with the ROTSE-IIIb telescope (Yuan et al., 2008u). A quick reduction of the red-channel (530-1000 nm) spectra obtained on Feb. 1.34 by E. Ofek with the Palomar 5-m telescope (+Double Beam Spectrograph), shows narrow emissions lines, likely from the host galaxiy, that yield a redshift of

z=0.069. Correcting for the host redshifts, the minima of the Si II 635.5-nm features are blue-shifted by 10600 km/s.

5.2.19 SN 2008ac

SN 2008ac was discovered on Jan 30.27 UT with the ROTSE-IIIb telescope (Yuan et al., 2008u). A quick reduction of the red-channel (530-1000 nm) spectra obtained on Feb. 1.34 by E. Ofek with the Palomar 5-m telescope (+Double Beam Spectrograph), shows narrow emissions lines, likely from the host galaxy, that yield a redshift of z=0.053. Correcting for the host redshifts, the minima of the Si II 635.5-nm features are blue-shifted by 11000 km/s.

5.2.20 SN 2008ad

SN 2008ad was discovered on Jan 30.42 UT with the ROTSE-IIIb telescope (Yuan et al., 2008u). A spectrum (range 420-890 nm) obtained on Jan. 31.34 UT with the 9.2-m Hobby-Eberly Telescope (+ Marcario Low-Resolution Spectrograph) by S. Rostopchin and F. Deglman, is heavily contaminated by the host-galaxy light; correcting for the recession velocity of the host galaxy (z = 0.054 from narrow H II region lines in the host), the minimum of the Si II 635.5-nm feature is blue-shifted by 11700 km/s.

5.2.21 SN 2008am

SN 2008am was discovered on Jan 10.41 with the ROTSE-IIIb telescope (Yuan et al., 2008s,t). Optical spectra (range 420-890 nm) obtained on Jan. 29.35 under poor conditions and again on Jan. 30.35 with the 9.2-m Hobby-Eberly Telescope (+ Marcario Low-Resolution Spectrograph) by S. Rostopchin and V. Riley, show it to be a type-II supernova. The spectra consist of blue continua superposed by hydrogen Balmer emission lines (narrow and broad). Overall, the spectra are similar to those

of the type-IIn supernova 1996L at early times (Benetti et al., 1999). The Jan. 30 data also clearly show narrow emission features from O III 495.9-and 500.7-nm and O II 372.7-nm. All narrow features are consistent with a systematic redshift of z = 0.234.

A spectrogram (range 330-980 nm), obtained on Jan. 31.50 UT by E. Ofek (CIT) with the Palomar 5-m telescope (+ Double Beam Spectrograph), and another one obtained on Feb. 8.12 by J. S. Bloom, R. J. Foley, M. Modjaz, and A. A. Miller (UCB) with the 10-m Keck I telescope (+ LRIS), confirm the behavior described above; these spectra also exhibit narrow He I emission lines and weak, narrow absorption features corresponding to the Mg II 279.6- and 280.4-nm doublet. The He I lines are further confirmation that the object is a supernova and not an active galactic nucleus. The Mg II absorption sets the minimum redshift for the supernova at z = 0.234. The narrow [O II] 372.7-nm emission is more extended along the slit in the two-dimensional spectrogram (i.e., the extension is seen in the direction orthogonal to the dispersion) than is the supernova continuum, and it is offset as well; this indicates that 2008am is offset from its host galaxy and that the host light may contribute to the narrow emission features.

Target-of-opportunity observations of 2008am were obtained with the Swift XRT satellite (+ UVOT) on Feb. 6, 7, and 13 UT. No x-ray emission was detected at the position of the supernova. The 1100-s cleaned observation on Jan. 6 yields a 3-sigma upper limit of 2×10^{13} erg/cm^2/s in the energy range 0.3-10 keV, assuming a power-law spectrum with photon index of 2. SN 2008am was also observed by UVOT in all filters.

At the redshift derived above, SN 2008am reached a peak absolute magnitude of -22.3, comparable to that of 2006gy, the second brightest supernova observed (Ofek

et al., 2007; Smith et al., 2007). The narrow emission features in the spectra suggest its exceptional luminosity is powered by ejecta-circumstellar matter interaction. Detailed analysis and modeling of this supernova will be presented in Chatzopoulos et al. (2010).

5.2.22 SN 2008ar

SN 2008ar was discovered on Feb. 27.25 UT with the ROTSE-IIIb telescope (Yuan et al., 2008d,h). A spectrogram (range 420-890 nm) obtained on Feb. 28.29 with the 9.2-m Hobby-Eberly Telescope (+ Marcario Low-Resolution Spectrograph) by S. Rostopchin and A. Westfall, shows it to be a type-Ia supernova. The data are similar to the pre-maximum spectra of normal type-Ia supernovae, such as SN 1992A (Kirshner et al., 1993), but with features significantly extended to the blue. Correcting for the SDSS redshift of the host (z=0.026), the minimum of the Si II 635.5-nm feature is blueshifted by 14300 km/s. The Ca II infrared absorption is unusually strong, and the line minimum is blueshifted by 23600 km/s.

5.2.23 SN 2008bg

SN 2008bg was discovered on Mar. 5.34 UT with the ROTSE-IIIb telescope (Yuan et al., 2008y,x). The CfA Supernova Group reported the spectroscopic identification of this object as a type Ia supernova, with a redshift consistent with the host (z=0.063) and expansion velocity of roughly 10300 km/s from the Si II absorption line around maximum light.

5.2.24 SN 2008bj

SN 2008bj was discovered on Mar. 12.28 UT with the ROTSE-IIIb telescope (Yuan et al., 2008e). A spectrogram (range 420-890 nm) obtained on Mar. 25.16 with the 9.2-m Hobby-Eberly Telescope (+ Marcario Low-Resolution Spectrograph)

by J. Caldwell and V. Riley, shows it to be a type-II supernova. The spectra are similar to that of SN 2006bp at about 12 days after explosion (Quimby et al., 2007f).

5.2.25 SN 2008by

SN 2008by was discovered on Apr. 19.21 UT with the ROTSE-IIIb telescope (Yuan et al., 2008f). Spectroscopy (420-890 nm) of 2008by, obtained on Apr. 22.10 with the 9.2-m Hobby-Eberly Telescope (+ Marcario Low-Resolution Spectrograph) by S. Rostopchin and V. Riley, shows it to be a type-Ia supernova. The spectra are similar to those of SN 2005cg at about five days after explosion (Quimby et al., 2006a). Narrow emission lines of H-alpha and O III (likely from the host galaxy) indicate a redshift of z=0.045.

5.2.26 SN 2008bz

SN 2008bz was discovered on Apr. 22.14 UT with the ROTSE-IIIb telescope (Yuan et al., 2008f). A spectrum (range 420-890 nm) obtained on Apr. 23.13 with the 9.2-m Hobby-Eberly Telescope (+ Marcario Low-Resolution Spectrograph) by S. Rostopchin and F. Deglman, shows it to be a type-Ia supernova. The spectra are similar to those of SN 1992A around maximum light (Kirshner et al., 1993). Correcting for the SDSS redshift of the host galaxy (z=0.06), the minimum of the Si II 635.5-nm feature is blueshifted by 11300 km/s.

5.2.27 SN 2008cw

SN 2008cw was discovered on June 1.33 UT with the ROTSE-IIIb telescope (Yuan et al., 2008g,c). A spectrum (420-890 nm) obtained on June 3.15 with the 9.2-m Hobby-Eberly Telescope (+ Marcario Low-Resolution Spectrograph) by M. Shetrone and E. Terrazas, shows it to be a supernova. The spectral features are roughly similar to those of the peculiar type-Ib supernova 2005bf at 32 days before maximum light

(Folatelli et al., 2006), except that the 560- to 600-nm region is more similar to that of the type-Ic supernova 1994I around 5 days before maximum light (Filippenko et al., 1995). Blondin et al. (2008) reported additional spectral observations and identified SN 2008cw as a type IIb event with blue-shifted H_α, H_β and He I absorption.

5.2.28 SN 2008dx

SN 2008dx was discovered on June 24.20 with the ROTSE-IIIb telescope (Chamarro et al., 2008b,a). It is located at about 339″ east and 94″ south from the center of the Coma cluster and 45″ west and 3″ south from the center of the nearest galaxy seen in SDSS (2MASX J13001768+2757192). The CfA Supernova Group identified it to be a type Ia supernova at redshift 0.035, with expansion velocity of about 13500 km/s from Si II line around one week before maximum light. Its spectra were mostly similar to the sub-luminous type Ia supernova 2000cn, although the ROTSE-III photometry shows SN 2008dx to be comparable in brightness to a normal type Ia supernova.

5.2.29 ROTSE3 J125642.7+273041

ROTSE3 J125642.7+273041 was discovered on Jul. 12.18 UT by the ROTSE-IIIb telescope (Yuan et al., 2008a). This object does not have an apparent host in the SDSS images, but it is in the field of Coma cluster and about 41′ west and 28′ south from the center of the cluster. Gal-Yam & Simon (2008) identified it as a probable type Ia supernova, at a redshift consistent with the Coma cluster (Abell 1656, z=0.023)

5.2.30 SN 2008es

SN 2008es was discovered on Apr. 26.23 UT with the ROTSE-IIIb telescope (Yuan et al., 2008r,q). It is located near a group of galaxies at z=0.062 in SDSS images, but no counterpart is visible at the position of 2008es. The closest SDSS source

is a galaxy (magnitude r=23.1) some 8″ away. There are no known x-ray or radio sources catalogued via NED or SIMBAD at the location of the optical transient. Given the early featureless blue spectra, the transient was initially reported as a possible background active galactic nucleus (Yuan et al., 2008q). A tidal disruption scenario was proposed by Gezari & Halpern (2008). Through the later development of spectral features (including a broad H_α emission), the object was identified as a type-II supernova (Miller et al., 2008a; Gezari et al., 2008; Miller et al., 2008b; Chornock et al., 2008).

At redshift z∼0.21, SN 2008es reached a peak absolute magnitude of -22.2. Based on its linearly decaying lightcurve, 2008es was further classified as a type IIL, in the same category as the brightest SN 2005ap. Two groups have presented their analysis and discussed the nature of this event. Gezari et al. (2009) favor a progenitor star with a low-mass extended hydrogen envelope and a dense stellar wind; while Miller et al. (2009) suggest strong interaction with a dense, optically thick circumstellar medium as the main powering mechanism.

5.2.31 SN 2008fh

SN 2008fh was discovered independently by ROTSE-IIIb on July 30.36 UT (Yuan et al., 2008p,l) and by the LOSS group. There is no apparent host seen in the Digitized Sky Survey image, but the location is in the middle of a group of galaxies in the Perseus cluster. Spectra (range 420-890 nm) obtained under poor conditions on Aug. 21.37 by M. Shetrone and A. Westfall, and under improved conditions on Aug. 26.37 by J. Caldwell and V. Riley, with the 9.2-m Hobby-Eberly Telescope (+Marcario Low-Resolution Spectrograph) show broad (FWHM about 10000 km/s) emission features similar to those in spectra of type-Ia supernovae in the nebular phase. The best-fit match from SNID (Blondin & Tonry, 2007), is to spectra of

SN 1991bg arround 30 days past maximum light; however, the fit is imperfect and results in a formal redshift estimate of z=0.008±0.008. By eye, the data longward of 630 nm are similar to those of 1991bg around 50 days past maximum, but with a much stronger emission peak at about 870 nm (observed). From this fit, a redshift of approximately z=0.01 is estimated. If the object is in the Perseus galaxy cluster (Abell 426, z=0.0179, Struble & Rood, 1999), then the peak absolute magnitude, corrected for Galactic extinction, would correspond to about -16.7. This would be consistent with a subluminous, 1991bg-like supernova at this distance.

5.2.32 SN 2008fm

SN 2008fm was discovered on Sept. 5.16 UT with the ROTSE-IIIb telescope (Yuan et al., 2008v). A spectrum (range 420-890 nm) obtained on Sept. 7.20 with the 9.2-m Hobby-Eberly Telescope (+ Marcario Low-Resolution Spectrograph) by J. Caldwell and E. Terrazas, shows it to be a type-IIn supernova. The redshift derived from the hydrogen Balmer emission lines is consistent with that of the presumed host, UGC 12792 (z=0.0385, Zabludoff et al., 1990).

5.2.33 SN 2008fn

SN 2008fn was discovered on Aug. 4.17 UT as an apparent supernova with the ROTSE-IIIb telescope (Yuan et al., 2008n,m). Spectroscopic observations show it to be a probable type Ib/c supernova.

5.2.34 SN 2008fo

SN 2008fo was discovered on Aug. 7.15 UT with the ROTSE-IIIb telescope (Yuan et al., 2008o). Spectra (range 420-890 nm) were obtained on Sept. 5.13 with the 9.2-m Hobby-Eberly Telescope (+ Marcario Low-Resolution Spectrograph) by S. Odewahn and V. Riley. SNID (Blondin & Tonry, 2007) indicates that the spectra of 2008fo

best matches that of the type-Ic supernova 2004aw at 23 days after maximum, at z=0.027±0.005, which is consistent with the redshift of its apparent host. The best match found with the "superfit" supernova spectral identification code (Howell et al., 2005) is to the type-Ic supernova 1991A.

5.2.35 SN 2008fr

SN 2008fr was discovered on Sep. 14.27 UT with the ROTSE-IIIb telescope (Yuan et al., 2008j). Spectra (range 420-890 nm) were obtained on Sept. 22.26 UT with the 9.2-m Hobby-Eberly Telescope (+ Marcario Low-Resolution Spectrograph) by J. Caldwell and A. Westfall. The spectra, compared via SNID (Blondin & Tonry, 2007), shows 2008fr to be a type-Ia supernova around maximum light at z=0.039±0.002. The minimum of the Si II 635.5 nm feature is blueshifted by 11000 km/s in the restframe.

5.2.36 SN 2008fs

SN 2008fs was discovered on Sep. 21.28 UT with the ROTSE-IIIb telescope (Yuan et al., 2008j). Spectra (range 420-890 nm) were obtained on Sept. 22.23 UT with the 9.2-m Hobby-Eberly Telescope (+ Marcario Low-Resolution Spectrograph) by J. Caldwell and A. Westfall. Comparison via SNID (Blondin & Tonry, 2007) shows 2008fs's spectra to be best matched by that of SN 1999ex at nine days after maximum at z = 0.049±0.004. An average redshift of 0.044±0.005 was obtained from matching to type-Ib/c-supernovae spectra templates around ten days after maximum. This redshift is roughly consistent within uncertainty to that of the apparent SDSS host galaxy (z=0.0386±0.0002, measured by SDSS).

5.2.37 SN 2008gd

SN 2008gd was discovered on Sept. 27.46 UT with the ROTSE-IIIb telescope (Yuan et al., 2008k). A spectrum (range 420-890 nm), obtained on Oct. 1.21 with

the 9.2-m Hobby-Eberly Telescope (+ Marcario Low-Resolution Spectrograph) by S. Odewahn and A. Westfall, shows 2008gd to be a type-II supernova. Weak H-alpha, H-beta, and He I/Na I lines are detected. Reference to SNID (Blondin & Tonry, 2007) indicates that the spectra are similar to that of type-IIP supernovae around maximum light or to the type-IIL supernova 1979C at 11 days after maximum, both at redshift consistent with the host. The shape of the lightcurve is not well constrained by the ROTSE photometry with its alimited signal-to-noise.

5.2.38 SN 2008in

SN 2008in was discovered on Dec. 26.79 by Nakano et al. (2008). Spectroscopic identifications of it being a type II supernova were reported by several groups (Chakraborti et al., 2008; Foley, 2008; Stritzinger, 2008). The supernova was first detected in the ROTSE-III3b images on Dec. 28.46.

5.2.39 SN 2008io

SN 2008io was discovered on Dec. 27.09 UT with the ROTSE-IIIc telescope (Yuan et al., 2008i). This field was not observed by any ROTSE-III telescope between July 2007 and the discovery date. Nothing is visible at this position in the Digitized Sky Survey images (limiting mag 20.5) or in the ROTSE reference image built from images taken between March and May 2007 (limiting mag 19.2). (Challis et al., 2008) confirmed it to be a normal type-Ia supernova about 50 days past maximum light.

5.2.40 SN 2009L

SN 2009L was discovered on Jan. 13.44 UT with the ROTSE-IIIb telescope (Yuan et al., 2009e). A spectrum (range 340-1080 nm) obtained on Jan. 15.34 with the 9.2-m Hobby-Eberly Telescope (+ Marcario Low-Resolution Spectrograph) by J. Caldwell and A. Westfall, shows it to be a type-Ia supernova. SNID (Blondin & Tonry, 2007)

indicates that the spectra best match the spectra of SNe 1999by and 1991bg at 3 days after maximum and at a redshift consistent with that of NGC 4854. The expansion velocity, derived from the minimum of the Si II (rest 635.5 nm) line, is about 11000 km/s. The (580 nm)/(615 nm) line-depth ratio (Nugent et al., 1995) for Si II is about 0.5, indicating a subluminous type-Ia event. Strong, broad absorption features at 760 and 850 nm (attributed to O I and Ca II) are also present, which strongly supports this classification (Garnavich et al., 2004).

5.2.41 SN 2009dd

SN 2009dd was discovered on Apr. 13.97 and Apr. 13.05 independently by two groups (Cortini & Dimai, 2009). Elias-Rosa et al. (2009) identifies it as a type II supernova. X-ray emission from the supernova was detected by Swift/XRT (Immler et al., 2009). The supernova was first picked up by the RSVP pipeline on Apr. 7.13, although the image quality was not ideal. The ROTSE-III photometry was greatly affected by the bright host galaxy (NGC 4088).

5.2.42 SN 2009dn

SN 2009dn was discovered on Apr. 12.78 UT with the ROTSE-IIId telescope (Yuan et al., 2009c,d). It was also detected with the ROTSE-IIIb telescope. This discovery was confirmed by D. W. Bishop and J. Brimacombe, who reported observation of the new object at mag 16.9 on Apr 20.17 using a 51-cm telescope in New Mexico. No spectra were obtained immediately following the discovery because Hobby-Eberly Telescope was offline for upgrade and maintenance.

5.2.43 SN 2009eu

SN 2009eu was discovered on May 21.43 by the LOSS group (Rex et al., 2009). It was identified as a normal type-Ia supernova, with an expansion velocity of 9900 km/s

from the Si II 635.5-nm line (Foley et al., 2009). The supernova was first detected in the ROTSE-III images on May 24.37 and first picked up by the RSVP pipeline on May 25.29.

5.2.44 SN 2009fx

SN 2009fx was discovered on May 29.34 with the ROTSE-IIIb telescope (Vinko et al., 2009a). A spectrum (range 420-1020 nm) obtained on June 6.40 with the 9.2-m Hobby-Eberly Telescope (HET; + Marcario Low-Resolution Spectrograph) by S. Rostopchin, shows 2009fx to be a type-Ia supernova. The spectrum contains the Si II 635.5-nm line and also other S II/Mg II/Fe II features that are characteristic of type-Ia supernovae. SNID software (Blondin & Tonry, 2007) indicates that the spectrum best matches the spectra of normal type-Ia supernovae between -6 and +2 days relative to maximum, at a redshift consistent with that of the presumed host (z=0.04766). This age estimate is supported by the ROTSE-III lightcurve, which shows that 2009fx brightened before the spectroscopic observation and stayed roughly constant (at mag about 17.5) between June 5.3 and 8.3. However, the Si II 635.5-nm feature is weak compared to the majority of type-Ia supernovae, and the Si II 580.0-nm feature is not detected. The spectrum is noisy at longer wavelengths, but there is no evidence for the O I 770-nm feature, and the Ca II infrared triplet is weak or absent. This suggests that 2009fx belongs to the subclass of 1991T-like, shallow-silicon supernovae (Filippenko, 1997; Branch et al., 2006), and it is slightly before or at maximum light. The expansion velocity, derived from the minimum of the Si II 635.5-nm line, and correcting for the host-galaxy redshift, is about 10000 km/s.

5.2.45 SN 2009fy

SN 2009fy was discovered on June 1.04 with the ROTSE-IIId telescope (Vinko et al., 2009a), and it was also observed by ROTSE-IIIb since May 24.43, although the transient-search pipeline software did not identify it due to a nearby saturated object. An HET/LRS spectrum obtained by S. C. Odewahn on June 8.44 shows 2009fy to be a type-Ia supernova about two weeks after maximum. According to SNID (Blondin & Tonry, 2007), the spectrum best resembles those of SN 1991T (16 days after maximum) and SN 1997br (+12 days). The Si II 635.5-nm line appears to be slightly blended with Na I D. There is no O I feature at 770 nm, and the Ca triplet is weak. The redshift measured by SNID is z = 0.042, which is consistent with the redshift of the host(z=0.0408, according to NED). The photospheric velocity, estimated from the minimum of the Si II 635.5-nm feature, and corrected for the host-galaxy redshift, is about 8700 km/s.

5.2.46 SN 2009hk

SN 2009hk was discovered as an apparent supernova on July 11.90 UT with the ROTSE-IIIc telescope (Yuan et al., 2009b,a). It is slightly blended with an object (of red magnitude about 18.2 in the USNO-B1.0 catalogue) to its southeast in the ROTSE-III images. No source was detected at this position in the Digitized Sky Survey images or a ROTSE-III reference image (limiting magnitude about 19.3) constructed from images taken between June and Aug. 2008. Turatto et al. (2009) confirmed it to be a type-Ia supernova, similar to SN 2005cf at 38 days past maximum on July 16.14 UT .

5.2.47 SN 2009ia

SN 2009ia was discovered on July 22.25 UT with the ROTSE-IIIb telescope (Vinko et al., 2009b). An optical spectrum, obtained on Aug. 1.22 at McDonald Observatory with the 9.2-m Hobby-Eberly Telescope (+ Marcario Low-Resolution Spectrograph) by M. Shetrone, shows that 2009ia is a type-Ia supernova, but the spectrum looks peculiar. There is a strong, narrow H-alpha emission line superimposed on the supernova spectrum, which is consistent with the host galaxy, being a strong H-alpha emitter. The SiI I 635.5-nm and 580.0-nm features are both weak, suggesting a pre-maximum phase; their ratio is R(Si II) = 0.4, which is higher than the usual value of 0.1-0.3 for normal type-Ia events close to maximum light (Benetti et al. 2004, MNRAS 348, 261). The O I 777-nm feature is not detected. The Ca II infrared triplet is present but weak. According to the SNID code (Blondin & Tonry, 2007), the spectrum most resembles those of SNe 2003du and 2002er at roughly 10 days before maximum, assuming a redshift of z = 0.03, which is consistent with that of the host galaxy (z=0.027, as measured by SDSS). The ROTSE unfiltered light curve, however, does not show significant brightening after Aug. 1, thus, it does not support the spectroscopic age determination. The expansion velocity, calculated from the absorption minimum of the Si II 635.5-nm line, after correcting for host-galaxy redshift, is 11000 km/s.

5.2.48 SN 2009iv

SN 2009iv was discovered on Aug. 21.43 UT with the ROTSE-IIIb telescope and was also detected by ROTSE-IIId (Chatzopoulos et al., 2009). Two spectra (range 420-1020 nm), obtained on Aug. 29.43 and Sept. 9.72 with the Low Resolution Spectrograph on the 9.2-m Hobby-Eberly Telescope, show 2009iv to be a type-Ia

supernova. The spectra contain the Si II 635.5-nm line, and also other S II/Mg II/Fe II features characteristic of type-Ia events, but they are heavily contaminated by the host galaxy. An E0-galaxy spectrum template was used to remove the contamination by the host galaxy. SNID (Blondin & Tonry, 2007) identified the transient as a type-Ia supernova 28 days after maximum.

5.3 The Exceptionally Luminous Type Ia Supernova 2007if

At redshift z$\sim$0.074, SN 2007if reached a peak absolute magnitude exceeding -20 and is one of the most luminous Type Ia supernova ever observed. In the following sections, we first summarize the photometric and spectroscopic observations of SN 2007if and its host in §5.3.1. We then discuss the possible interpretation of the observed features in §5.3.2. This is followed by our conclusions in §5.3.3. We assume a standard cosmology model with the Hubble parameter H_0=70 km s^{-1} Mpc^{-1} and the density parameters Ω_m=0.3, Ω_Λ=0.7. All quoted errors are 1-sigma (68% confidence), unless otherwise stated.

5.3.1 Observations and Analysis

5.3.1.1 Photometric Observations by ROTSE-III

ROTSE-IIIb (at the McDonald Observatory) and ROTSE-IIIc (at the H.E.S.S. site at Mt. Gamsberg, Namibia) monitored the field of SN 2007if on a daily basis, weather permitted. The supernova was observed above detection threshold between August 16.29 UT and December 5.08 UT in 2007. The ROTSE-III images were bias-subtracted and flat-fielded by the automated pipeline. Initial object detections were performed by SExtractor (Bertin & Arnouts, 1996). The images were then processed with our custom RPHOT photometry program based on the DAOPHOT (Stetson, 1987) psf-fitting photometry package (Quimby et al., 2006b). The host galaxy, with

a R-band magnitude of 22.7 (see §5.3.1.3), is well below ROTSE-III's detection limit and does not affect our photometry of the supernova.

The unfiltered thinned ROTSE-III CCDs have a peak sensitivity in the R band wavelength range. We estimate the magnitude zero-point by obtaining the median offset from well-measured SDSS r-band magnitudes of selected field sources. The color distribution of these references covers almost the entire SN Ia color space. The standard deviation of the offsets is about 0.20 magnitude. This value provides an estimate of our zero-point uncertainty.

To find the lightcurve maximum, the ROTSE-III data were fit with a lightcurve template, that is constructed from spectral templates (Hsiao et al., 2007) and by weighing the g, r and i band lightcurves with the approximate ROTSE-III CCD efficiency curve. The rise and decay phases are fit with two different stretch factors for two reasons. First, the best fit stretch factor is smaller during the rise (1.12 ± 0.05) than during the decay (1.53 ± 0.03). Hayden et al. (2010) have also noticed that the rise and decay stretches are not necessarily correlated. Second, a typical SN Ia becomes progressively redder just after the maximum. Although the color of SN 2007if is not well constrained by our data, there is no evidence that it is not following a similar trend. Fitting the rise and decay separately minimizes the effect of color evolution on the determination of the lightcurve peak. Due to the uncertainties in constructing the unfiltered template, the errors in our lightcurve fitting are likely under-estimated.

The best fit maximum date (relative to a B-band template) is found to be September 1.8 UT, with an error of about 0.9 day (90% confidence, but not including uncertainty from possible color effects). The explosion date is estimated to be around September 9.4 UT, assuming a pre-stretch template rise time of 19.5 days. Our fitting is constrained by an upper limit at August 14.3 UT and the 22-days rise in the rest

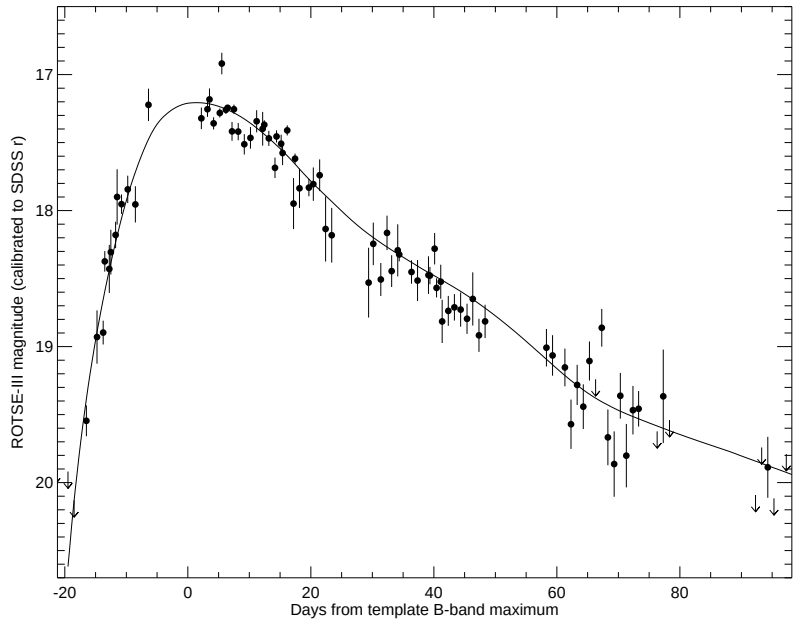

Fig. 5.2.—: Unfiltered optical lightcurve of SN 2007if. Observations by ROTSE-IIIb and ROTSE-IIIc. The fitted template (Hsiao et al., 2007, see text) is overplotted as a solid line.

frame is among the typical range for SNe Ia (Hayden et al., 2010).

Given a reliable detection at 17.18±0.08 mag (corrected for the Galactic extinction of 0.21 magnitude in the r-band) by ROTSE-IIIb on September 5, SN 2007if, at a redshift 0.0736 (see §5.3.1.3), reached about -20.4 absolute magnitude, without host reddening correction. This is one magnitude brighter than the average peak brightness of SNe Ia, even considering the zero-point uncertainty in our r-band calibration. Note that the post-maximum stretch factor obtained is quite large. Based on the lightcurve width and luminosity relationship derived from fainter events (Perlmutter et al., 1997; Phillips et al., 1999), SN 2007if was over-luminous by about 0.4 magnitude for its decline-phase stretch.

5.3.1.2 Spectroscopic Observations

Photometric Phase Ten spectra were obtained with the HET from Aug. 28 to Nov. 10, 2007 (see Table 5.2), covering 4 days before until 70 days after the estimated

maximum light of Sep. 1.8 UT. These spectra were reduced using standard *IRAF* procedures. They are presented in Figure 5.3 and Figure 5.4 in comparison with other SN Ia spectra at similar epochs, obtained from the SUSPECT database [1]. The blue and red ends, where the spectra are dominated by noise, are truncated.

The spectrum taken at about four days before maximum had relatively low signal to noise and is smoothed for display in Figure 5.3. It shows a blue continuum with a probable broad and shallow absorption between 4700 and 6000 Å but no distinguishable features that can be associated with a SN Ia. At day -3, shallow P-Cygni profiles are visible around 4300, 5000 and 6100 Å, consistent with the Fe III multiplets around λ4404 and λ5129 and Si II λ6355. These defining features of a SN Ia become more evident in the spectrum taken just past maximum, at day +1. The lack of O I λ7773 and strong Ca IR-triplet absorptions argue against SN 2007if being a Type Ic. Contributions from Si III, Mg II, Fe II and S II can also be identified in the day +1 spectrum along with a probable trace of C II (see Figure 5.3). Although the C II feature is uncertain, it has been detected in other luminous SNe Ia before or around maximum light (Howell et al., 2006; Hicken et al., 2007; Yamanaka et al., 2009).

Shallow Si II features are usually seen in over-luminous SNe Ia (i.e. the 1991T-like class) before and around maximum. For SN 2007if, the Fe signatures are not particularly strong. The relative strength of Fe seems to be between a normal SN Ia and a 1991T-like event. The shallow features may be caused by high temperatures in the outer layers that ionize Si II and Fe II (Mazzali et al., 1995; Nugent et al., 1995). Indeed, Figure 5.3 shows that the spectral shape of SN 2007if is similar to that of the pre-maximum SN 2005hk (Phillips et al., 2007), which displayed significantly less blueshifted absorptions and was a peculiar sub-luminous event with a high initial

[1] http://bruford.nhn.ou.edu/∼suspect/

Table 5.2. Spectroscopic observations of SN 2007if

Age* (days)	MJD	Telescope /Instrument	Wavelength Range (Å)	Expo. Time (s)	Reso-lution
-4	54340.30	HET/LRS	4100-9200	1800	300
-3	54341.32	HET/LRS	4100-9200	900	300
+1	54345.31	HET/LRS	4100-9200	900	300
+15	54359.44	HET/LRS	4100-9200	900	300
+18	54362.44	HET/LRS	4100-9200	900	300
+20	54365.23	HET/LRS	4100-9200	900	300
+29	54374.22	HET/LRS	4100-9200	900	300
+39	54384.18	HET/LRS	4100-9200	900	300
+42	54387.18	HET/LRS	4100-9200	900	300
+70	54414.30	HET/LRS	4100-9200	900	300
+339	54683.58	Keck/LRIS	3400-9200	1800	1000
+688†	55032.60	Keck/LRIS	3100-10000	4200	1000

*Relative to the estimate maximum light of Sep. 1.8 UT.

†Observation of the host.

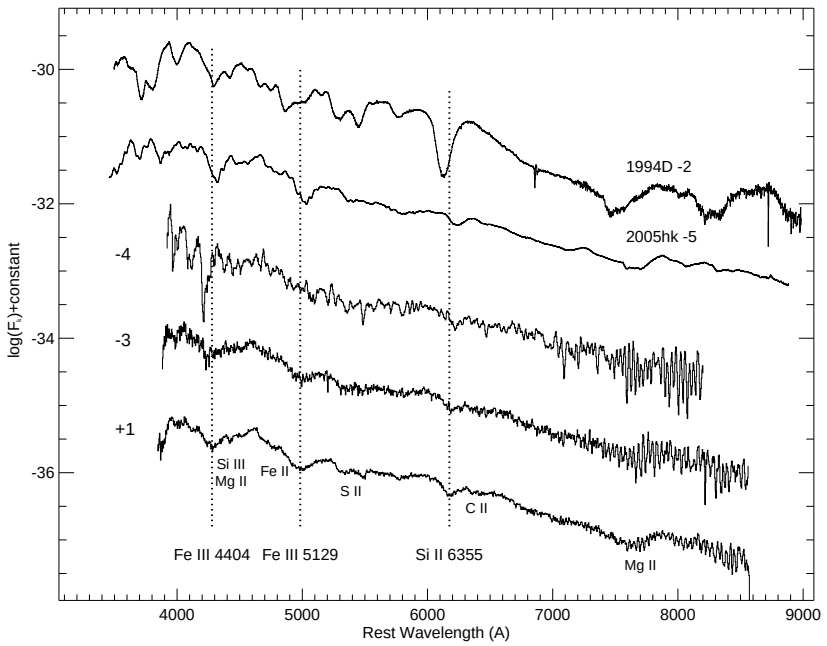

Fig. 5.3.—: Early spectra of SN 2007if observed by HET. They are plotted against spectra at similar epochs for a normal Ia, SN 1994D (Patat et al., 1996) and a peculiar Ia, SN 2005hk (Phillips et al., 2007). The vertical dotted lines mark Fe III λ4404, λ5129 and Si II λ6355 blueshifted by 8500 km/s

temperature. Another probable explanation for shallow features is dilution by an underlying continuum emission. This prospect will be further discussed in §5.3.2.

The spectroscopic resemblance of SN 2007if to SN 2003fg was pointed out in Yuan et al. (2007a), where a spectrum of 2007if taken on Sep. 10.5 by the SNfactory was reported to closely match that of SN 2003fg at 2 days post-maximum. We note that at day +1, closer to the phase when SN 2003fg was observed, the features have not yet grown to be as strong as seen in SN 2003fg, probably suggesting a even higher temperature or more dilution in SN 2007if.

The expansion velocity measured from the Si II λ6355 absorption minimum at 1 day post-maximum is 8500$\pm$400 km/s. This photospheric velocity is confirmed if Fe II λ4404 and Fe II λ5129 are mainly responsible for the minima of the other two major absorption features on the blue side. Such a velocity, clearly slower than in a typical SN Ia (Figure 5.3) and much slower than for a luminous 1991T-like event, is consistent with that measured for SN 2003fg at a similar epoch around maximum (Howell et al., 2006). This further strengthens the proposition that SN 2007if is in the same category as 2003fg.

Between day +15 and day +70, the spectral evolution of SN 2007if closely resembles that of a normal SN Ia during similar epochs (e.g. SN 2003du Stanishev et al., 2007, a normal Type Ia with good spectroscopic coverage, see Figure 5.4). Overall, the spectra of SN 2007if have less contrast than those of 2003du. One remarkable deviation is the weak features from intermediate mass elements in SN 2007if. The relatively slow Si II λ6355 absorption disappears into a blend with Fe II lines by day +29, while its core is often visible until day +40 or later for normal SN Ia. The Ca II IR triplet can be identified at around 8300Å after day +15, but is also considerably weaker than typically observed.

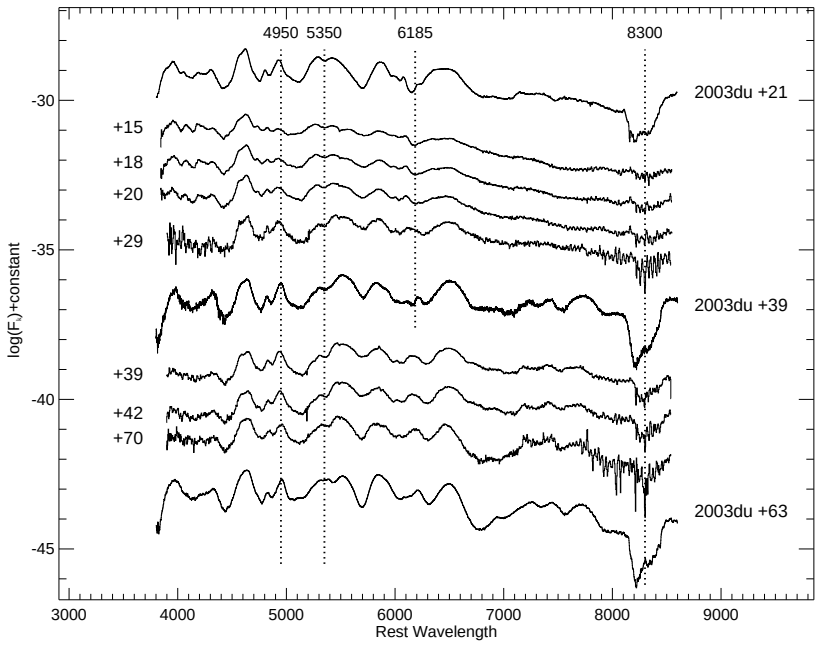

Fig. 5.4.—: Spectra series of SN 2007if observed by HET. They are plotted against spectra at selected epochs for a normal Ia, SN 2003du (Stanishev et al., 2007).

Another noticeable difference is at around 4950Å, where the spectra of SN 2007if appear comparatively flat before day +20. The peak at 4950Å grows stronger over time and becomes indistinguishable from a typical SN Ia by day +29. Such a trend, together with the rapidly decreasing blue-to-red peak ratio around 5350Å, is observed for SN 1994D from 2 to 4 weeks post-maximum (see Figure 7 in Branch et al., 2005) and was modeled as due to strengthening Fe II and Cr II lines.

The photospheric velocity evolution is not constrained from the Si II λ6355 absorption as it is not resolved in our later observations, but we note that the other absorption minima show similar line velocities to normal events. The inner layers of the SN 2007if ejecta thus do not necessarily have low kinetic energy.

Nebular Phase SN 2007if was observed in the nebular phase by Keck on Aug. 5, 2008. At day +339, the spectrum shows a broad bump on the blue side and a probable broad emission feature just above 7000Å. While the general shape of the

spectrum is similar to that of other SNe Ia in nebular phase (see Figure 5.5), the typical narrow emission features at 4700 and 5300Å are not as prominent. These two features are usually modeled as dominated by [Fe III] and a combination of [Fe II] and [Fe III] forbidden lines in the blue and red respectively (Mazzali et al., 1997, 1998). The slightly higher ratio of flux density at these two wavelengths may indicate a somewhat higher temperature in the inner layers of SN 2007if than a normal SN Ia.

Further quantitative analysis is complicated by the contamination from the host galaxy. We find that the total SN plus host galaxy flux as observed in the g-band by Keck/LRIS on Aug. 4, 2008 was only 0.4 mag brighter than the host flux alone (see §5.3.1.3). As for the featureless pre-maximum spectra, dilution by an additional continuum may also play a role.

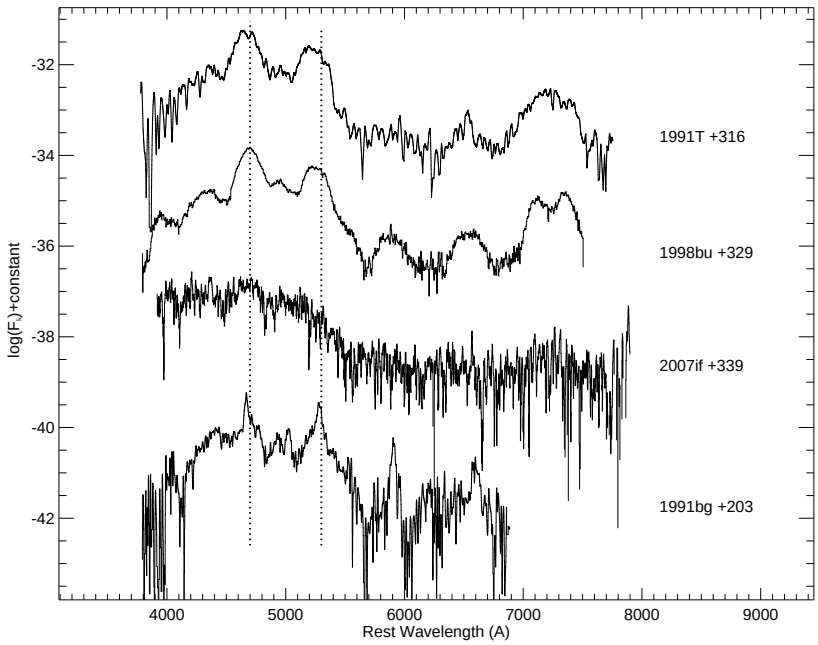

Fig. 5.5.—: Nebular spectrum of SN 2007if observed by Keck. It is smoothed and plotted against spectra at similar epochs for the over-luminous SN 1991T (Gómez & López, 1998), normal SN 1998bu (Cappellaro et al., 2001) and the sub-luminous SN 1991bg (Turatto et al., 1996).

A similarly featureless nebular spectrum in the blue region was observed for another luminous supernova, 2006gz (Maeda et al., 2009). However, in the latter case,

relatively strong emission was detected at ∼7200-7300Å (probably due to [Ca II]), indicating yet different composition and conditions.

5.3.1.3 Observations of the Host Galaxy

The host of SN 2007if was imaged by Keck on June 26.6, 2009, long after the SN had faded away. An R-band magnitude of 22.70±0.08 and g magnitude of 23.03±0.13 (corrected for Galactic extinction) were estimated by calibrating to the SDSS measurements of nearby objects. Based on the g-R color, the host of SN 2007if is among the bluest objects within the 3′ neighborhood.

A spectrum of the host was also obtained by Keck on July 20.6, 2009. Because of the faintness of the host, the spectrum was dominated by sky emissions. After removing the sky lines, a single emission feature was identified as H_α at redshift 0.0736 (Figure 5.6). This redshift is fully consistent with the estimation from cross-correlating the spectra with templates in SNID (Blondin & Tonry, 2007). We therefore adopt this as the redshift of SN 2007if.

At the measured redshift, the host has an absolute R magnitude of -14.91. The host spectrum is best-matched by an SB3 - SB4 galaxy template at redshift 0.07 using "superfit" (Howell et al., 2005) (see Figure 5.7), but the H_α emission is much weaker than that in the star forming template.

5.3.2 Discussion

If the supernova lightcurve is entirely powered by radioactive decay of Ni, the luminosity of the supernova at maximum light would roughly equal the instantaneous energy deposition from Ni. The peak brightness of the supernova thus provides an estimate of the amount of Ni synthesized in the explosion (Arnett, 1982).

A precise estimate of the bolometric luminosity is not possible without multi-

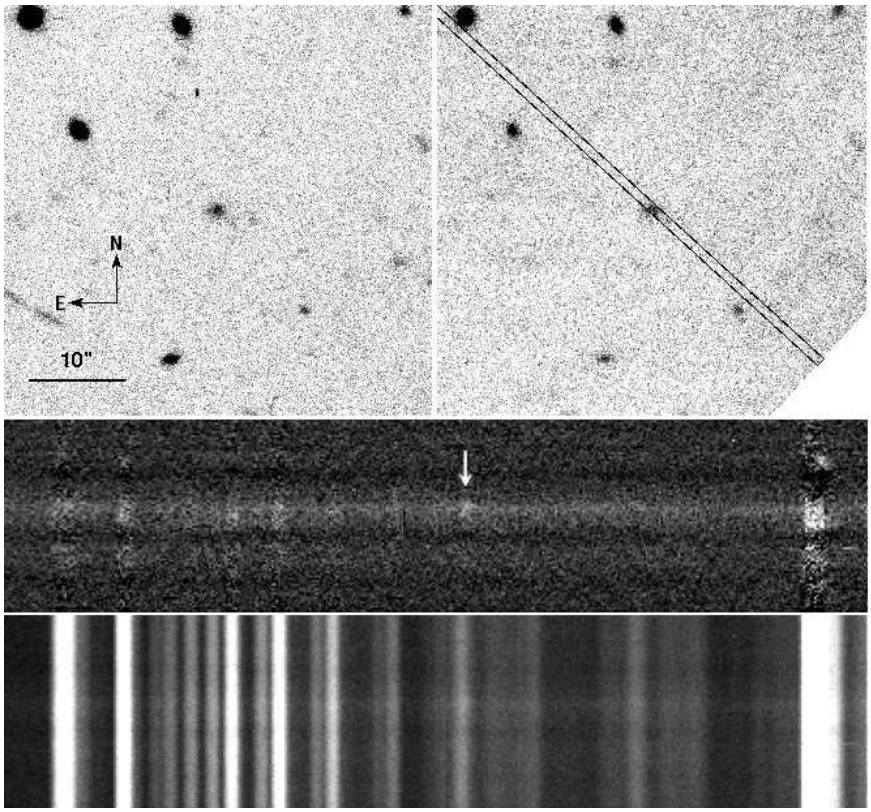

Fig. 5.6.—: Optical images and spectra of the host of SN 2007if. All data are taken by Keck/LRIS two years after the SN discovery. The top two panels show the R-band (left) and unfiltered blue channel (right) images, with the slit position marked in the latter. The middle panel shows the sky subtracted two-dimensional spectrum. The remaining emission feature, identified as H_α, is marked with a downward arrow. The original spectrum, dominated by strong sky features, is displayed in the bottom panel.

band photometry. Since the observed evolution is quite similar for SN 2007if and a normal brightness SN Ia, we can simply scale its Ni production with the peak luminosity. At one magnitude brighter than average, SN 2007if would require about 1.5 $M_\odot$of Ni compared to a typical 0.6 $M_\odot$(Leibundgut, 2000). The weak features from intermediate mass elements may indicate a more complete burning and thus less total mass required. Even considering the large uncertainty associated with such an estimate, the amount of Ni is far beyond that which can be synthesized in a 1.4 $M_\odot$white dwarf progenitor.

Howell et al. (2006) discussed a large progenitor mass and hence a large bind-

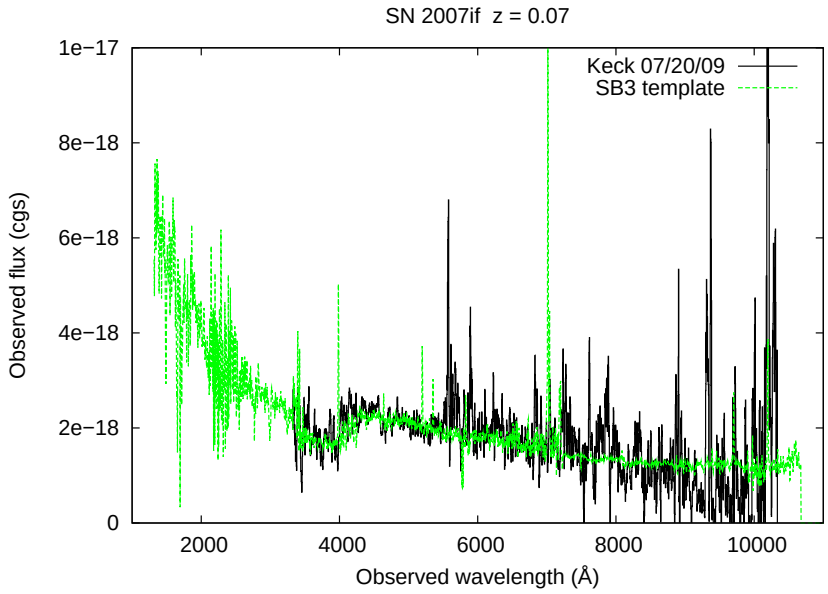

Fig. 5.7.—: Host spectrum of SN 2007if plotted against a SB3 galaxy template at redshift 0.07. The spectrum is truncated on the noisy blue side.

ing energy as the explanation for the apparent discrepancy between the exceptional brightness and a low photospheric velocity of SN 2003fg. A similar situation is noticed for SN 2007if. In addition, we observe shallow features in the early spectra, suggesting high ionization and high temperature. At later times, the spectral evolution of SN 2007if follows that of a typical SN Ia, indicating similar physical processes.

Despite the resemblance to SN 2003fg, the spectra of SN 2007if clearly differ from that of another ultra-luminous SN Ia with a proposed super-Chandrasekhar progenitor, 2006gz. For the latter case, prominent narrow absorption features were observed from 2 weeks before maximum light. Maeda & Iwamoto (2009) investigated the different properties between SN 2003fg and 2006gz, and suggested that they might be from the same type of progenitor but observed at different angles. They propose that the shallow spectral features can be explained as due to less shocked material at the pole. However, polarimetric observations of a recent luminous SN Ia, 2009dc, which has similar observational features as SN 2003fg, do not support the aspherical

explosion hypothesis (Tanaka et al., 2009).

As an alternative, we consider the interaction between the ejecta and the circumstellar medium (CSM) that may produce extra luminosity. Detection of a CSM signature may provide important clues about the mass transfer process leading to the SN Ia explosion. A CSM played a domninant role in SN 2002ic (Hamuy et al., 2003; Wang et al., 2004) that had an underlying SN Ia spectrum, but a strong (asymmetric) Type IIn CSM interaction. SN 2006X (Patat et al., 2007b), SN 1999cl (Blondin et al., 2009) and SN 2007le (Simon et al., 2009) showed variable Na D lines that indicated the presence of a more dilute CSM. Many SN Ia show high-velocity Ca II features (Wang et al., 2003; Gerardy et al., 2004; Mazzali et al., 2005) that may hint at a CSM. Perhaps "super Chandrasekhar" events reveal excess luminosity from CSM interaction. In such a scenario, the continuum emission above the photosphere produces a "toplighting" effect (Branch et al., 2000). As modeled in Branch et al. (2000), when the external light has comparable intensity as the photospheric emission, the spectral features are strongly "muted." The shallow features observed in SN 2007if could then be a consequence of luminous emission from circumstellar interaction, roughly doubling the total luminosity. It is potentially possible that deceleration by the reverse shock results in shifted absorption minima and apparently low photospheric velocity. Any CSM interaction must satisfy the constraint that narrow emission lines are not observed in SN 2007if. In addition, any CSM cannot correspond to a steady-state wind since an r^{-2} density profile would substantially affect the early light curve in a manner that is not observed. Such a CSM might be reminiscent of the expanding gas identified in novae by Williams et al. (2008) or a common envelope in a DD model (Khokhlov et al., 1993). Modeling of the exact distribution of the CSM and the propagation of forward/reverse shocks is beyond the scope of this paper.

5.3.3 Conclusions

SN 2007if was one of the first discoveries of the ROTSE Supernova Verification Project (RSVP) (Yuan & Akerlof, 2008), which extends the efforts of the Texas Supernova Search (TSS, Quimby, 2006) and uses all four ROTSE-III telescopes.

The peak unfiltered magnitude of SN 2007if (calibrated to SDSS r-band) measured by ROTSE-IIIb, corresponds to an absolute magnitude of -20.4 at redshift 0.074. This is by far the brightest SN Ia observed. If powered by Ni decay, the exceptional brightness of SN 2007if requires a total Ni mass close to or even exceeding the Chandrasekhar mass of a non-rotating white dwarf. The photospheric expansion velocity derived around maximum is comparable to the estimate for SN 2003fg and suggests a relatively low kinetic energy. After two weeks post-maximum, the spectral evolution of SN 2007if become indistinguishable from a normal SN Ia, except for "muted" features and weak absorptions due to Si and Ca. Late time observations show that SN 2007if occured in a low luminosity host, similar to that of SN 2003fg.

The observed properties of SN 2007if may suggest that it had a massive progenitor, well above 1.4 $M_{\odot}$, as proposed for a few other luminous SNe Ia. Super-Chandrasekhar explosions have been investigated for systems with rapid rotations (Uenishi et al., 2003; Yoon & Langer, 2005). Both a single WD or a merger of two degenerate stars can sustain a larger mass if rapidly rotating.

CSM interaction may provide another interpretation for the excess luminosity. In the presence of such emission above the photosphere, shallow spectral features are predicted, consistent with our observation of SN 2007if. However, it is noted that the spectra of other luminous SNe, such as 2003fg and 2006gz are not similarly "muted." Further studies are needed to see whether the observed lightcurve can be reproduced.

So far, the few most luminous SNe Ia show diverse behaviors. In general, the events

follow a positive correlation between peak brightness and stretch factor, except for SN 2003fg (Howell et al., 2006), which was among the brightest but showed a relatively fast decay. SN 2009dc (Yamanaka et al., 2009) and 2007if had similarly slow photospheric velocity derived from Si II 6355 as for SN 2003fg. SN 2006gz (Hicken et al., 2007) and 2004du (Contreras et al., 2009) appear as close cousins, with relatively high photospheric velocity. Suppression of the silicon velocity was also noticed at early times for SN 2006gz (Hicken et al., 2007). Although rare, over-luminous SNe Ia show significant deviations in brightness when the normal parametrization method is applied in cosmological studies (Folatelli et al., 2010). More luminous events, polarimetric observations, X-ray monitoring and detailed simulations in the future may help to understand the category as a whole.

CHAPTER VI

Conclusions and Future Prospectives

6.1 Ongoing Projects

6.1.1 Optical Follow-up of Neutrino Multiplets

Starting Fall 2008, ROTSE-III has been used to follow up neutrino multiplet triggers from the IceCube Detector (Franckowiak et al., 2009). This effort has been pursued in a collaboration with Dr. Marek Kowalski and Anna Franckowiak in Humboldt University, Berlin.

The collapsar (theoretical) model predicts high energy neutrino emission from the ultra-relativistic jets of GRBs. While only a small fraction of core-collapse SNe are associated with GRBs, the others may also produce mildly relativistic jets, from which radiation is not observed because of the dense outer layers in the progenitor. For this later hypothesis, detection of the escaping high energy neutrinos provides a crucial test. However, identifying such weak neutrino signals above the terrestrial atmospheric background is inevitably challenging. An optical follow-up program would enhance the sensitivity of such detections (Kowalski & Mohr, 2007) and also help to determine the type of emission source. If a fast decaying GRB afterglow-like transient is discovered, the GRB theory is verified. If a SN is observed without GRB emission, the hidden jet scenario is confirmed and the link between CC SNe and GRBs is

reaffirmed.

To restrain the rate of triggers so that any transient detection is significantly greater than chance probability, the neutrino events are filtered on-site at the South Pole. When two or more muon-neutrinos are detected from the same direction (less than 4° away) within a 100 s time window, the weighted average of the reconstructed location is sent to ROTSE-III. These criteria limit the trigger frequency to about 25 per year.

In the first 7 months, ROTSE-III has received 34 neutrino triggers, among which 14 warrant further analysis. Given the current trigger delay time of about 8 hours it is more feasible to detect a slow rising SN than a rapidly decaying GRB afterglow. Upon receiving a trigger, any ROTSE-III telescope that can observe the target will take a series of 30 60-s exposures. In the following 14 days, ROTSE-III will observe the target every day whenever possible. Images from each night are co-added and the first available set is used to construct a reference to be subtracted from all later co-added frames. The images are processed through the supernova search pipeline as described in Chapter 4. Similar filters and cuts are applied except that probable counterparts in the reference images are identified as galaxy or star based on the FWHM measured by SExtractor, because no catalog is obtained for these random fields beforehand.

No interesting candidate has been found so far in the search pipeline. This is partly due to the difficulty of controlling the quality of the reference frame. As of October 2009, additional observations are being carried out for fields without good reference images. Careful re-analysis of early images are also being conducted. In addition, numerical simulation is required to estimate the efficiency of the detection pipeline and consequently the significance of any detection or limit constrained by

non-detection.

6.1.2 GRB Studies in the Fermi era

With the launch of the Fermi Gamma-ray Space Telescope (FGST) in June 2008, GRB research entered the Fermi era. In particular, the Large Area Telescope (LAT) onboard Fermi is sensitive to photons with energies from 20 MeV to over 100 GeV. This provides an invaluable opportunity to explore the poorly-understood very high energy emission from GRBs, following EGRET's pioneering effort a decade ago. Prior to the launch of FGST, a number of groups, including us, have estimated the LAT performance based on extrapolation from low energies. For about a dozen bursts per year, LAT should detect and provide localizations suitable for ground-based optical follow-ups, although the error boxes degrade with decreasing numbers of photons. ROTSE-III's large field-of-view and global coverage makes it a competitive instrument to provide early optical observations of LAT bursts. Such detections will enable observations from bigger telescopes and help to interpret the high energy emission.

The GCN position notice from LAT was not enabled until the end of February 2009. Since then, only one GRB (090510) triggered the instrument. In its first year of operation, the LAT detection rate turned out to be much lower than expected. By December 2009, LAT detected signals from 13 bursts, out of which only four were bright enough to be identified onboard. Fortunately, Target-of-Opportunity (ToO) observations by *Swift* revealed afterglow emission for 6 of these bursts, enabling additional follow-ups and determination of redshifts.

Meanwhile, the GBM onboard Fermi detected around 300 hundred events, mostly with error boxes in the order of many degrees that prevented follow-up from optical instruments. The recent detection of the optical afterglow by ROTSE-IIIa, in response to the Fermi/GBM trigger for GRB 090902B, was encouraging. The event was very

bright in high energy gamma-rays and in optical. With a delay of about 80 minutes, it is the earliest optical detection of any LAT burst that has no corresponding prompt *Swift* detection. With improved GBM localization in future, more optical detections are possible with a shorter delay.

6.2 Concluding Remarks

6.2.1 GRBs

ROTSE-III has made significant contributions in uncovering the very early and prompt optical behavior of *Swift* GRBs. With *Swift* currently funded to 2012, ROTSE-III will help increase the sample of well-observed events.

In general, we have learned in the *Swift* era that the GRB afterglows behave similarly in X-ray and optical, except at very early times when X-ray detections seem to be dominated by extended internal emission while optical emission is most likely from external shocks. The canonical shallow decay phase and flaring seen in X-rays are observed in the optical as well. However, the optical and X-ray lightcurves do not necessarily track each other for the same event, i.e. X-ray flares without optical counterparts or optical flares without X-ray counterparts are sometimes observed. Although they follow similar decaying behavior, the decay indices are often resolvably different when accurate data is available. The observations do support correlated optical and X-ray emission, but probably not always from the same emitting region.

Quite unexpectedly, ROTSE-III has also contributed to the studies of dark bursts and X-ray flashes (XRFs). In both cases, the optical afterglows are significantly fainter than normal bursts, but by observing early, ROTSE-III was able to detect emission from these faint events, e.g. GRB 080607 and GRB 080330. In the earlier case, the ROTSE-III detection constrained the spectral energy distribution and supported the suggestion that the apparent low optical luminosity was caused by high

local extinction (see §3.3.6). In the latter case, a rising lightcurve, as seen for a few other XRFs, was observed. The late rise of the afterglow emission, probably related to a low Lorentz factor or a collimated outflow being viewed off-axis, may provide a hint of the connection between XRFs and GRBs. If the XRFs are from an extended population of GRBs, they allow studies of GRB progenitors in a wider parameter space.

My work has emphasized the study of the transition phase from prompt to afterglow emission, uniquely probed by the early optical observations. Through multi-wavelength studies, I have explored the origin of the early optical detections and their probable connection to the gamma-ray radiation. It is likely that both prompt and early afterglow emission contribute to the total optical luminosity. The observed diversity of behavior originates from the varying relative strengths. Although the prompt component might be identified according to its short timescale variability, the optical data do not often have adequate temporal resolution. Different sampling rates at high energy and optical make direct comparisons hard. More data in the future may improve the statistics and help to reveal the underlying connection.

The field of GRB research has developed quickly in the recent years. The amount of data has been increasing at an ever growing speed. New degrees of freedoms have been added to the model continuously, but the fundamental picture has not changed since the fireball model was proposed. No competing theories offer better interpretation for the whole range of data. Additional observational hints may come from future missions that measure the polarization systematically. Detection of gravitational waves, as predicted in the current theory, will verify the assumed origin of short duration bursts and significantly enhance our understanding of the progenitor. Other clues about the progenitor type would most likely come from the studies of

the burst environment. At the same time, high quality spectroscopic data along the GRB sightlines provide powerful tools to probe the composition and evolution of the universe. They allow studies of metallicity and star formation activities in distant galaxies that are too faint to be directly detected. They provide measurements of the hydrogen neutral fraction in the IGM and thus trace the history of reionization out to a distance exceeding any other cosmological source. More ambitious projects are on the way to fully exploit the bright optical beams from GRBs.

6.2.2 SNe

In the field of supernova, a wealth of data has been produced by RSVP and the follow-up campaign by HET. Among the 46 SNe detected by ROTSE-III, a relatively large fraction turned out to be peculiar events of rare types. Densely sampled ROTSE-III lightcurves have been critical to constrain the explosion dates of these SNe. In the near future, further studies of interesting individual events will be carried out and the statistical properties of the RSVP SNe will be investigated.

While the ultra-luminous events are intrinsically rare, RSVP and the coming synoptic surveys will help to increase the sample size by searching in a larger spatial volume. Given the diversity of their behavior, there might be more than one mechanism that produces such spectacular explosions. Whether the extraordinary luminosity is powered by interaction with circumstellar medium or nuclear burning triggered by pair instability, studies of these extreme SNe would improve our understanding of the evolution of massive stars. The discovery of these objects also offer an inspiring perspective on how alternative search algorithm can still uncover unknown transient phenomena.

Early SNe Ia detection remains an important goal of RSVP. Constraints on the early photometric and spectral behavior help break the degeneracy among the ex-

plosion models. In addition, high velocity spectral features observed in early phases provide useful tools to explore the circumstellar environment and the mass transfer process in the progenitor system. Circumstellar interaction has been identified in at least some events, but it is not yet clear whether significant component of luminosity can be produced in the optical and whether it introduces a potential source of systematic error in using SNe Ia as standard candles.

Finally, collaboration with IceCube is ongoing and, whether or not any SNe will be discovered by responding to the neutrino triggers, we will put interesting constraints on the theory.

6.2.3 Ultimate ROTSE-III Experience

The work described in this thesis has been carried out in the course of a few years and in collaboration with a number of people from various institutes. As a member of the small group leading the ROTSE project in Michigan, I have been deeply involved in the operation and maintenance of the telescopes. While ROTSE-III has been one of the most successful robotic telescope project, its smooth performance has relied on both organized and voluntarily efforts from the whole collaboration.

The status of the ROTSE-III telescopes are monitored through web servers in quasi realtime. Image thumbnails are retrieved as soon as available for quick quality check. In case of a problem, a group member will log in to the remote system to diagnose the fault. If no connection can be made, local staff will be contacted. Instructions are provided via emails or on the phone to assist the staff to solve the problem. Occasionally, parts are shipped back to Michigan for tests or required replacements are ordered and distributed from Michigan.

To maximize the chance of observing, ROTSE enclosures are open as much as possible, exposing the optical assembly to rough weather conditions. About twice

a year, the secondary mirror is adjusted to ensure consistent alignment and focus quality. A common failure mode for the telescope mount control system occurs when one of the shaft position sensors detects drive motor slippage or overrun of an axis rotation limit. To guard against damage, the control system cuts the electric drive power immediately and human intervention is required for recovery. The fix is often as easy as turning the mount by hand and rebooting the computers. Occasionally, the rubber shaft driving the mount is worn out and needs to be replaced. A trickier but much infrequent task is to align the mount encoder reader that is knocked out of place over time. Most of these services can be easily carried out by one person. However, unexpected situations can happen at the remote ROTSE-III sites. In Australia, the circuit is constantly tripped by visiting/residing ants or lightning strikes. In Turkey, it is important to keep spare hurricane-proven wind cups and wind vanes because they are blown away or destroyed every winter.

Due to limited bandwidth at the remote sites, the large amount of data (as much as 6 Gigabytes per night) cannot all be transfered over the internet. Instead, all the images are copied to a removable hard drive. The filled disks are shipped to Michigan, where the data are archived and indexed.

With most of the required maintenance work done through the help of the locals, we have been able to keep ROTSE-III running at close to 90% of the time. For important upgrades, Michigan members will travel to the observatory sites, about once every year to Texas and about once every two years to the foreign sites. The most recent such upgrades were the re-coating of the primary mirrors and the installations of dedicated computers running the RSVP pipeline. For the later task, we took the opportunity to upgrade the telescope control, combining the pipeline and the camera functions into one dual-core system. I have participated in these efforts at all of the

ROTSE sites, traveling to each location, except for ROTSE-IIIa, for which the work was done remotely by sending a fully configured computer.

During normal operation, whenever a GRB is detected by a satellite mission and is observable by any of the ROTSE-III telescope, the ROTSE team members will receive email messages and be paged on the phone. Anyone among the Michigan group and a few passionate collaborators that has access to a computer and network will log in to the ROTSE webserver, where web pages have been created showing thumbnails and preliminary reduction as soon as the images are processed through the pipeline and the data is transfered to Michigan. If the webpage does not appear or the images are not taken, the cause will be investigated immediately. For many cases, a quick fix is attempted and data is obtained with short delay. If an optical counterpart is identified or if the observation starts early enough to warrant interesting limits, a brief GCN circular will be generated using pre-typed templates. Counterpart identification is often achieved by comparing the sources in the ROTSE-III images to the optical catalogs. A comparison to the USNO A1.0 catalog is automated for relatively bright objects (brighter than about 17.5 magnitude). For error boxes smaller than a few arcminutes, such as those provided by the *Swift*/BAT, Digitized Sky Survey red plates are downloaded and the images can be compared by eye with the assistance of automated source identifications. X-ray detections by *Swift*/XRT and sometimes other optical/IR counterpart identifications significantly improve the GRB localizations. These coordinates can be used to query the specific areas of the ROTSE-III images to confirm identifications or look for faint or blended objects. If no proper GRB counterpart is recognized in a ROTSE-III image, the limiting magnitude is roughly estimated as the magnitude below which 10% of the sources in the image are measured.

GRB responses request dedicated efforts because fast reactions are demanded while bursts often occur outside normal working hours. People usually have to wake up at night and log in from home voluntarily. A chat room function has been built to allow communication about burst observations. The first person logged in will often take the lead to generate a circular, but all members are involved in identifying optical counterparts and solving problems. Discussions are particularly valuable when the situation is not straightforward. Through these exciting moments, the ROTSE team has maintained an excellent record of distributing GCN circulars as soon as within minutes from receiving the satellite triggers.

The RSVP pipeline is maintained in a different manner. A few undergraduate students and myself take turns to examine the new candidates on a daily basis. Any noticeable problem in the images or the data processing will be investigated as soon as possible. Focus and alignment issues result in the failure of the image subtraction process, the pipeline thus provides a sensitive monitor on the image quality. The search is designed to be near real time and uses only the most recent image data in the telescope pipeline. These data are moved to a different hard drive and become invisible to the RSVP computer before scheduled observing starts the next night. This time frame constrains the pipeline design, especially the time consuming subtraction process, but ensures the data to be handled in a timely fashion. Delays in the data processing are not favorable because they may cause fraction of the night's imaging efforts to be ignored. When necessary, pipeline routine can be initiated by hand to process missed data. At the early stage of the project, the candidate filtering method is constantly improved by changing or adding parameters. The few supernovae first detected by other groups provide useful targets to test our strategy. The goal is to be sensitive enough to detect faint objects embedded in host galaxies and discard

most of the artifacts, which can be identified through quality checks on the residue shapes and features in the original images. For the interesting candidate found in the the RSVP pipeline, spectroscopic observations are triggered by collaborators in the University of Texas, who have also played important roles in the reduction of the spectral data and participated in the writing of the CBET reports.

The automated data reduction, although critical for quickly informing the community to organize follow-ups, is seldom adequate for journal publications. Careful analysis of the data is required, especially when the target is faint or blended with nearby objects. For both GRBs and SNe, valuable observations come from a range of instruments. The most interesting constraints on the model are often from multi-wavelength data analysis. By leading the data interpretation for GRB 081008 and SN 2007if, I have thus gained experience in temporal and spectral analysis in both optical and high energy.

During the course of my PhD, I have worked with many collaborators and observatory staffs both remotely and shoulder to shoulder. This has allowed me to directly experience the diverse cultures behind the success of the ROTSE enterprise, of which I have felt fortunate to be a part. I have also worked with many eminent groups in the area of GRBs and SNe through specific projects. All these experiences have helped me to understand and appreciate how great discoveries and exciting progress are achieved in modern astrophysics, and this is probably the most valuable lesson I have learned.

Bibliography

Akerlof, C., et al. 1999, Nature, 398, 400

Akerlof, C. W., et al. 2003, PASP, 115, 132

Alard, C. 2000, A&AS, 144, 363

Alard, C. & Lupton, R. H. 1998, ApJ, 503, 325

Aloy, M. A., Janka, H., & Müller, E. 2005, A&A, 436, 273

Amati, L., et al. 2002, A&A, 390, 81

Appenzeller, I. 1970, A&A, 5, 355

Arnett, W. D. 1982, ApJ, 253, 785

Band, D., et al. 1993, ApJ, 413, 281

Barkat, Z., Rakavy, G., & Sack, N. 1967, Physical Review Letters, 18, 379

Barthelmy, S. D., et al. 1998, in American Institute of Physics Conference Series, Vol. 428, Gamma-Ray Bursts, 4th Hunstville Symposium, ed. C. A. Meegan, R. D. Preece, & T. M. Koshut, 99–103

Barthelmy, S. D., et al. 2007, GCN, 6996

Beardmore, A. P., et al. 2008, GCN, 7594

Beloborodov, A. M. 2005, ApJ, 618, L13

Benetti, S., et al. 2005, ApJ, 623, 1011

Benetti, S., Turatto, M., Cappellaro, E., Danziger, I. J., & Mazzali, P. A. 1999, MNRAS, 305, 811

Berger, E., et al. 2005, Nature, 438, 988

Berger, E. & Rauch, M. 2008, GCN, 8542

Bertin, E. & Arnouts, S. 1996, A&AS, 117, 393

Bessell, M. S. 1990, PASP, 102, 1181

Bethe, H. A. 1990, Rev. Mod. Phys., 62, 801

Bethe, H. A. & Brown, G. E. 1995, ApJ, 445, L129

Bethe, H. A. & Wilson, J. R. 1985, ApJ, 295, 14

Blondin, S., Challis, P., Falco, E., Calkins, M., & Berlind, P. 2008, CBET, 1408, 1

Blondin, S., Prieto, J. L., Patat, F., Challis, P., Hicken, M., Kirshner, R. P., Matheson, T., & Modjaz, M. 2009, ApJ, 693, 207

Blondin, S. & Tonry, J. L. 2007, ApJ, 666, 1024

Bloom, J. S. 2007, GCN, 6989

Bloom, J. S., Butler, N. R., Perley, D. A., Starr, D. L., & Foley, R. 2007, GCN, 7002

Bloom, J. S., Frail, D. A., & Kulkarni, S. R. 2003, ApJ, 594, 674

Bloom, J. S., Kulkarni, S. R., & Djorgovski, S. G. 2002a, AJ, 123, 1111

Bloom, J. S., et al. 1999, Nature, 401, 453

Bloom, J. S., et al. 2002b, ApJ, 572, L45

Bloom, J. S., et al. 2006, ApJ, 638, 354

Bloom, J. S. & Starr, D. L. 2008, GCN, 7542

Bond, J. R., Arnett, W. D., & Carr, B. J. 1984, ApJ, 280, 825

Branch, D., Baron, E., Hall, N., Melakayil, M., & Parrent, J. 2005, PASP, 117, 545

Branch, D., Dang, L. C., & Baron, E. 2009, PASP, 121, 238

Branch, D., et al. 2006, PASP, 118, 560

Branch, D., Jeffery, D. J., Blaylock, M., & Hatano, K. 2000, PASP, 112, 217

Branch, D., et al. 2007, PASP, 119, 709

Bromm, V. & Loeb, A. 2006, ApJ, 642, 382

Burrows, D. N., et al. 2005, Science, 309, 1833

Cabrera, J. I., Firmani, C., Avila-Reese, V., Ghirlanda, G., Ghisellini, G., & Nava, L. 2007, MNRAS, 382, 342

Cappellaro, E., Patat, F., Mazzali, P. A., Benetti, S., Danziger, J. I., Pastorello, A., Rizzi, L., Salvo, M., & Turatto, M. 2001, ApJ, 549, L215

Castro-Tirado, A. J., et al. 2008, GCN, 7796

Chakraborti, S., Prabhu, T., Anupama, G. C., Kaur, A., Uday Kumar, G., & Ray, A. 2008, CBET, 1638, 1

Challis, P., Calkins, M., & Berlind, P. 2008, CBET, 1640, 1

Chamarro, D., Uecker, A., Yuan, F., Sisson, M. D., Akerlof, C., McKay, T., Quimby, R., & Wheeler, J. C. 2008a, ATEL, 1590

Chamarro, D., Uecker, A., Yuan, F., Sisson, M. D., Akerlof, C., McKay, T., Quimby, R., & Wheeler, J. C. 2008b, CBET, 1427, 1

Chandra, P., et al. 2008, ApJ, 683, 924

Chatzopoulos, E., et al. 2010, in preparation, 00

Chatzopoulos, E., Vinko, J., Yuan, F., Quimby, R., Chamarro, D., Sisson, M. D., Akerlof, C., Pandey, S. B., & Wheeler, J. C. 2009, CBET, 1940, 2

Chevalier, R. A. & Fransson, C. 1994, ApJ, 420, 268

Chevalier, R. A. & Li, Z.-Y. 2000, ApJ, 536, 195

Chincarini, G., et al. 2007, ApJ, 671, 1903

Chornock, R., Miller, A. A., Perley, D. A., & Bloom, J. S. 2008, ATEL, 1644

Chugai, N. N., Blinnikov, S. I., Cumming, R. J., Lundqvist, P., Bragaglia, A., Filippenko, A. V., Leonard, D. C., Matheson, T., & Sollerman, J. 2004, MNRAS, 352, 1213

Clocchiatti, A. & Wheeler, J. C. 1997, ApJ, 491, 375

Cobb, B. E. 2008a, GCN, 8452

Cobb, B. E. 2008b, GCN, 8547

Cobb, B. E. & Bailyn, C. D. 2008, ApJ, 677, 1157

Cohen, M., Wheaton, W. A., & Megeath, S. T. 2003, AJ, 126, 1090

Colgate, S. A. & White, R. H. 1966, ApJ, 143, 626

Contreras, C., et al. 2009, ArXiv e-prints

Cortini, G. & Dimai, A. 2009, CBET, 1764, 1

Covino, S., et al. 2007, GCN, 6988

Crockett, R. M., et al. 2008, ApJ, 672, L99

Cucchiara, A. 2008, GCN, 7547

Cucchiara, A. & Fox, D. B. 2008a, GCN, 7815

Cucchiara, A. & Fox, D. B. 2008b, GCN, 8304

Cucchiara, A., Fox, D. B., & Cenko, S. B. 2008a, GCN, 7616

Cucchiara, A., Fox, D. B., Cenko, S. B., & Berger, E. 2008b, GCN, 8372

Cucchiara, A., Fox, D. B., Cenko, S. B., & Berger, E. 2008c, GCN, 8346

Cucchiara, A., Fox, D. B., Cenko, S. B., & Berger, E. 2008d, GCN, 8448

Cucchiara, A., Fox, D. B., Cenko, S. B., & Berger, E. 2008e, GCN, 8065

Cummings, J. R., et al. 2008, GCN, 8447

D'Avanzo, P., D'Elia, V., & Covino, S. 2008, GCN, 8350

D'Elia, V., Covino, S., & D'Avanzo, P. 2008, GCN, 8438

Della Valle, M., et al. 2006, Nature, 444, 1050

Dingus, B. L. 2001, in American Institute of Physics Conference Series, Vol. 558, American Institute of Physics Conference Series, ed. F. A. Aharonian & H. J. Völk, 383–391

Elias-Rosa, N., van Dyk, S. D., Agnoletto, I., & Benetti, S. 2009, CBET, 1765, 1

Evans, P. A., et al. 2009, MNRAS, 397, 1177

Evans, P. A., et al. 2007, A&A, 469, 379

Falcone, A. D., et al. 2006, ApJ, 641, 1010

Falcone, A. D., et al. 2007, ApJ, 671, 1921

Fenimore, E., et al. 2008, GCN, 8297

Ferrero, A., French, J., & Melady, G. 2008, GCN, 8303

Filippenko, A. V. 1997, ARA&A, 35, 309

Filippenko, A. V., et al. 1995, ApJ, 450, L11

Filippenko, A. V., Matheson, T., & Ho, L. C. 1993, ApJ, 415, L103

Filippenko, A. V., et al. 1992a, AJ, 104, 1543

Filippenko, A. V., et al. 1992b, ApJ, 384, L15

Fishman, G. J., Meegan, C. A., Wilson, R. B., Paciesas, W. S., Pendleton, G. N., Harmon, B. A., Horack, J. M., Kouveliotou, C., & Finger, M. 1993, A&AS, 97, 17

Folatelli, G., et al. 2006, ApJ, 641, 1039

Folatelli, G., et al. 2010, AJ, 139, 120

Foley, R. J. 2008, CBET, 1638, 2

Foley, R. J., Challis, P., Groner, T., Silverman, J. M., Cenko, S. B., Filippenko, A. V., & Li, W. 2009, CBET, 1817, 2

Frail, D. A., et al. 2001, ApJ, 562, L55

Franckowiak, A., Akerlof, C., Cowen, D. F., Kowalski, M., Lehmann, R., Schmidt, T., Yuan, F., for the IceCube collaboration, & for the ROTSE collaboration. 2009, ArXiv e-prints

Frieman, J., Quimby, R., Sellers, M., Castro, F., Puckett, T., & Sostero, G. 2005a, IAU Circ., 8629, 1

Frieman, J., Quimby, R., Sellers, M., Castro, F., Shetrone, M., & Terrazas, E. 2005b, CBET, 277, 1

Fruchter, A. S., et al. 2006, Nature, 441, 463

Fynbo, J., Quirion, P.-O., Malesani, D., Thoene, C. C., Hjorth, J., Milvang-Jensen, B., & Jakobsson, P. 2008, GCN, 7797

Fynbo, J. P. U., et al. 2006a, A&A, 451, L47

Fynbo, J. P. U., et al. 2006b, Nature, 444, 1047

Gal-Yam, A., et al. 2006, Nature, 444, 1053

Gal-Yam, A. & Simon, J. 2008, ATEL, 1617

Galama, T. J., et al. 1998, Nature, 395, 670

Garnavich, P., Marion, H., Challis, P., Blondin, S., & Kirshner, R. 2007, CBET, 1176, 1

Garnavich, P. M., et al. 2004, ApJ, 613, 1120

Garnavich, P. M., et al. 2003, ApJ, 582, 924

Gehrels, N., et al. 2004, ApJ, 611, 1005

Gehrels, N., et al. 2006, Nature, 444, 1044

Gehrels, N., Ramirez-Ruiz, E., & Fox, D. B. 2009, ARA&A, 47, 567

Gehrels, N., et al. 2005, Nature, 437, 851

Gerardy, C. L., Höflich, P., Fesen, R. A., Marion, G. H., Nomoto, K., Quimby, R., Schaefer, B. E., Wang, L., & Wheeler, J. C. 2004, ApJ, 607, 391

Gezari, S., et al. 2008, ATEL, 1578

Gezari, S. & Halpern, J. P. 2008, ATEL, 1524

Gezari, S., et al. 2009, ApJ, 690, 1313

Ghirlanda, G., Nava, L., Ghisellini, G., Firmani, C., & Cabrera, J. I. 2008, MNRAS, 387, 319

Glatzel, W. & Kiriakidis, M. 1993, MNRAS, 263, 375

Golenetskii, S., Aptekar, R., Mazets, E., Pal'Shin, V., Frederiks, D., Oleynik, P., Svinkin, D., Ulanov, M., & Cline, T. 2008a, GCN, 8548

Golenetskii, S., Aptekar, R., Mazets, E., Pal'Shin, V., Frederiks, D., Oleynik, P., Ulanov, M., Svinkin, D., & Cline, T. 2008b, GCN, 7862

Gómez, G. & López, R. 1998, AJ, 115, 1096

González, M. M., Dingus, B. L., Kaneko, Y., Preece, R. D., Dermer, C. D., & Briggs, M. S. 2003, Nature, 424, 749

Goodman, J. 1986, ApJ, 308, L47

Granot, J. & Guetta, D. 2003, ApJ, 598, L11

Granot, J., Nakar, E., & Piran, T. 2003, Nature, 426, 138

Granot, J. & Sari, R. 2002, ApJ, 568, 820

Greiner, J., et al. 2008, PASP, 120, 405

Greiner, J., et al. 2009a, ApJ, 693, 1610

Greiner, J., et al. 2009b, ApJ, 693, 1912

Grupe, D., Nousek, J. A., vanden Berk, D. E., Roming, P. W. A., Burrows, D. N., Godet, O., Osborne, J., & Gehrels, N. 2007, AJ, 133, 2216

Guidorzi, C., et al. 2009, A&A, 499, 439

Hamann, W.-R. & Koesterke, L. 1998, A&A, 335, 1003

Hamann, W.-R., Koesterke, L., & Wessolowski, U. 1995, A&A, 299, 151

Hamuy, M., et al. 2003, Nature, 424, 651

Harrison, F. A., et al. 2001, ApJ, 559, 123

Hayden, B., et al. 2010, submitted to ApJ

Heger, A. & Woosley, S. E. 2002, ApJ, 567, 532

Hicken, M., Garnavich, P. M., Prieto, J. L., Blondin, S., DePoy, D. L., Kirshner, R. P., & Parrent, J. 2007, ApJ, 669, L17

Hoeflich, P. & Khokhlov, A. 1996, ApJ, 457, 500

Höflich, P. 2006, Nuclear Physics A, 777, 579

Hoflich, P., Khokhlov, A. M., & Wheeler, J. C. 1995, ApJ, 444, 831

Holland, S. T., Sakamoto, T., & Rykoff, E. S. 2008, GCN, 8450

Horváth, I., Balázs, L. G., Bagoly, Z., & Veres, P. 2008, A&A, 489, L1

Howell, D. A., et al. 2006, Nature, 443, 308

Howell, D. A., et al. 2005, ApJ, 634, 1190

Hsiao, E. Y., Conley, A., Howell, D. A., Sullivan, M., Pritchet, C. J., Carlberg, R. G., Nugent, P. E., & Phillips, M. M. 2007, ApJ, 663, 1187

Huja, D., Mészáros, A., & Řípa, J. 2009, A&A, 504, 67

Hunter, D. J., et al. 2009, A&A, 508, 371

Ibrahimov, M., Karimov, R., Rumyantsev, V., & Pozanenko, A. 2008, GCN, 7975

Im, M., Lee, I., & Urata, Y. 2007, GCN, 6994

Immler, S., Russell, B. R., & Brown, P. J. 2009, ATEL, 2106

Iye, M., et al. 2006, Nature, 443, 186

Jakobsson, P., Hjorth, J., Fynbo, J. P. U., Watson, D., Pedersen, K., Björnsson, G., & Gorosabel, J. 2004, ApJ, 617, L21

Jaroszynski, M. 1996, A&A, 305, 839

Jiang, L., Bian, F., & Fan, X. 2007, GCN, 7003

Jin, Z. P. & Fan, Y. Z. 2007, MNRAS, 378, 1043

Jóhannesson, G., Björnsson, G., & Gudmundsson, E. H. 2006, ApJ, 647, 1238

Kalberla, P. M. W., Burton, W. B., Hartmann, D., Arnal, E. M., Bajaja, E., Morras, R., & Pöppel, W. G. L. 2005, A&A, 440, 775

Kann, D. A., Laux, U., & Ertel, S. 2008, GCN, 7823

Kawai, N., et al. 2006, Nature, 440, 184

Khokhlov, A., Mueller, E., & Hoeflich, P. 1993, A&A, 270, 223

Khokhlov, A. M. 1991, A&A, 245, 114

Kirshner, R. P., et al. 1993, ApJ, 415, 589

Klebesadel, R. W., Strong, I. B., & Olson, R. A. 1973, ApJ, 182, L85

Klose, S., et al. 2004, AJ, 128, 1942

Klotz, A., Boer, M., & Atteia, J. L. 2008a, GCN, 7799

Klotz, A., Boer, M., & Atteia, J. L. 2008b, GCN, 7795

Klotz, A., Boër, M., Atteia, J. L., & Gendre, B. 2009, AJ, 137, 4100

Klunko, E. & Pozanenko, A. 2008, GCN, 7890

Kobayashi, S. 2000, ApJ, 545, 807

Kouveliotou, C., Meegan, C. A., Fishman, G. J., Bhat, N. P., Briggs, M. S., Koshut, T. M., Paciesas, W. S., & Pendleton, G. N. 1993, ApJ, 413, L101

Kowalski, M. & Mohr, A. 2007, Astroparticle Physics, 27, 533

Krimm, H. A., et al. 2009, ApJ, 704, 1405

Kruehler, T., Schrey, F., Greiner, J., Yoldas, A., Clemens, C., McBreen, S., Kupcu Yoldas, A., & Szokoly, G. 2008, GCN, 8075

Krühler, T., et al. 2009, ApJ, 697, 758

Kudritzki, R.-P. & Puls, J. 2000, ARA&A, 38, 613

Kuin, N. P. M. & Mangano, V. 2008, GCN, 7808

Kuin, N. P. M. & Pagani, C. 2007, GCN, 7000

Kuin, N. P. M. & Racusin, J. L. 2008, GCN, 8069

Kuin, N. P. M., Sakamoto, T., & Holland, S. 2008, GCN, 8298

Kulkarni, S. R., et al. 1999, Nature, 398, 389

Kumar, P. & Narayan, R. 2009, MNRAS, 395, 472

Kumar, P. & Panaitescu, A. 2000, ApJ, 541, L51

Kumar, P. & Panaitescu, A. 2003, MNRAS, 346, 905

Kumar, P. & Piran, T. 2000, ApJ, 532, 286

Lazzati, D. & Begelman, M. C. 2006, ApJ, 641, 972

Le, T. & Dermer, C. D. 2007, ApJ, 661, 394

Leibundgut, B. 2000, A&A Rev., 10, 179

Leibundgut, B., et al. 1993, AJ, 105, 301

Leonard, D. C., Li, W., Filippenko, A. V., Foley, R. J., & Chornock, R. 2005, ApJ, 632, 450

Li, W., et al. 2003, PASP, 115, 453

Li, W., et al. 2001a, PASP, 113, 1178

Li, W., Filippenko, A. V., & Riess, A. G. 2001b, ApJ, 546, 719

Liang, E.-W., Racusin, J. L., Zhang, B., Zhang, B.-B., & Burrows, D. N. 2008, ApJ, 675, 528

Liang, E. W., et al. 2006, ApJ, 646, 351

Liang, E.-W., Zhang, B.-B., & Zhang, B. 2007, ApJ, 670, 565

Lin, Y.-Q. 2009, Research in Astronomy and Astrophysics, 9, 682

MacFadyen, A. I. & Woosley, S. E. 1999, ApJ, 524, 262

MacFadyen, A. I., Woosley, S. E., & Heger, A. 2001, ApJ, 550, 410

Madison, D. & Li, W. 2007, CBET, 1034, 1

Maeda, K. & Iwamoto, K. 2009, MNRAS, 394, 239

Maeda, K., Kawabata, K., Li, W., Tanaka, M., Mazzali, P. A., Hattori, T., Nomoto, K., & Filippenko, A. V. 2009, ApJ, 690, 1745

Malesani, D., Fynbo, J. P. U., Jakobsson, P., Vreeswijk, P. M., & Niemi, S.-M. 2008, GCN, 7544

Mangano, V., et al. 2008a, GCN, 7794

Mangano, V., Cummings, J., Barthelmy, S. D., Sbarufatti, B., Schady, P., Burrows, D. N., Roming, P., & Gehrels, N. 2008b, GCN Report, 147, 1

Mangano, V., Cummings, J. R., Cusumano, G., Gehrels, N., La Parola, V., Markwardt, C. B., Osborne, J. P., Sbarufatti, B., & vanden Berk, D. E. 2008c, GCN, 7847

Mao, J., et al. 2008, GCN, 7537

Marion, H. & Garnavich, P. 2007, CBET, 1145, 1

Markwardt, C., et al. 2008a, GCN, 8067

Markwardt, C., et al. 2008b, GCN, 7549

Mazzali, P. A., et al. 2005, ApJ, 623, L37

Mazzali, P. A., Cappellaro, E., Danziger, I. J., Turatto, M., & Benetti, S. 1998, ApJ, 499, L49

Mazzali, P. A., Chugai, N., Turatto, M., Lucy, L. B., Danziger, I. J., Cappellaro, E., della Valle, M., & Benetti, S. 1997, MNRAS, 284, 151

Mazzali, P. A., Danziger, I. J., & Turatto, M. 1995, A&A, 297, 509

Meiksin, A. 2005, MNRAS, 356, 596

Meszaros, P. 2006, Reports on Progress in Physics, 69, 2259

Meynet, G., Maeder, A., Schaller, G., Schaerer, D., & Charbonnel, C. 1994, A&AS, 103, 97

Miller, A. A., et al. 2008a, ATEL, 1576

Miller, A. A., Chornock, R., Bloom, J. S., Modjaz, M., Filippenko, A. V., Li, W., Foley, R. J., Butler, N. R., & Perley, D. A. 2008b, ATEL, 1593

Miller, A. A., et al. 2009, ApJ, 690, 1303

Milne, P. A. & Williams, G. G. 2007, GCN, 7011

Minezaki, T., Price, P. A., Yoshii, Y., Cowie, L., & Kakazu, Y. 2007, GCN, 7018

Modjaz, M., Kewley, L., Kirshner, R. P., Stanek, K. Z., Challis, P., Garnavich, P. M., Greene, J. E., Kelly, P. L., & Prieto, J. L. 2008, AJ, 135, 1136

Molinari, E., et al. 2007, A&A, 469, L13

Nakano, S., Kadota, K., & Wells, W. 2008, CBET, 1636, 1

Nava, L., Ghirlanda, G., Ghisellini, G., & Firmani, C. 2008, MNRAS, 391, 639

Nomoto, K., Thielemann, F.-K., & Yokoi, K. 1984, ApJ, 286, 644

Nousek, J. A., et al. 2006, ApJ, 642, 389

Nugent, P., Phillips, M., Baron, E., Branch, D., & Hauschildt, P. 1995, ApJ, 455, L147

Oates, S. R. 2008, GCN, 8544

Oates, S. R., et al. 2008, GCN, 8537

Oates, S. R. & Marshall, F. E. 2008, GCN, 7607

Oates, S. R., et al. 2009, MNRAS, 395, 490

O'Brien, P. T., et al. 2006, ApJ, 647, 1213

Oegerle, W. R. & Hill, J. M. 2001, AJ, 122, 2858

Ofek, E. O., et al. 2007, ApJ, 659, L13

Ohno, M., et al. 2008, GCN, 7630

Osaki, Y. 1986, PASP, 98, 30

Paciesas, B., Briggs, M., & Preece, R. 2008, GCN, 8316

Paciesas, W. S., et al. 1999, ApJS, 122, 465

Paczyński, B. 1986, ApJ, 308, L43

Pagani, C., et al. 2007, GCN, 6986

Page, K. L., et al. 2009, MNRAS, 400, 134

Page, K. L., et al. 2007, ApJ, 663, 1125

Panaitescu, A. 2005, MNRAS, 362, 921

Panaitescu, A. & Vestrand, W. T. 2008, MNRAS, 387, 497

Papaloizou, J. C. B. 1973a, MNRAS, 162, 143

Papaloizou, J. C. B. 1973b, MNRAS, 162, 169

Patat, F., Benetti, S., Cappellaro, E., Danziger, I. J., della Valle, M., Mazzali, P. A., & Turatto, M. 1996, MNRAS, 278, 111

Patat, F., et al. 2007a, Science, 317, 924

Patat, F., et al. 2007b, Science, 317, 924

Pe'er, A. & Waxman, E. 2004, ApJ, 603, L1

Perley, D. A., et al. 2009, AJ, 138, 1690

Perlmutter, S., et al. 1999, ApJ, 517, 565

Perlmutter, S., et al. 1997, ApJ, 483, 565

Phillips, M. M. 1993, ApJ, 413, L105

Phillips, M. M., et al. 2007, PASP, 119, 360

Phillips, M. M., Lira, P., Suntzeff, N. B., Schommer, R. A., Hamuy, M., & Maza, J. 1999, AJ, 118, 1766

Phillips, M. M., Wells, L. A., Suntzeff, N. B., Hamuy, M., Leibundgut, B., Kirshner, R. P., & Foltz, C. B. 1992, AJ, 103, 1632

Piran, T. 1999, Phys. Rep., 314, 575

Piran, T. 2004, Reviews of Modern Physics, 76, 1143

Pons, J. A., Reddy, S., Prakash, M., Lattimer, J. M., & Miralles, J. A. 1999, ApJ, 513, 780

Popov, D. V. 1993, ApJ, 414, 712

Preece, R. D., Briggs, M. S., Mallozzi, R. S., Pendleton, G. N., Paciesas, W. S., & Band, D. L. 2000, ApJS, 126, 19

Press, W. H., Teukolsky, S. A., Vetterling, W. T., & Flannery, B. P. 1992, Numerical recipes in C: The art of scientific computing. Cambridge University Press, Cambridge, 2d edition

Prochaska, J. X., et al. 2009, ApJ, 691, L27

Prochaska, J. X., Shiode, J., Bloom, J. S., Perley, D. A., Miller, A. A., Starr, D., Kennedy, R., & Brewer, J. 2008, GCN, 7849

Quimby, R., Höflich, P., Kannappan, S. J., Rykoff, E., Rujopakarn, W., Akerlof, C. W., Gerardy, C. L., & Wheeler, J. C. 2006a, ApJ, 636, 400

Quimby, R., Höflich, P., & Wheeler, J. C. 2007a, ApJ, 666, 1083

Quimby, R., Yuan, F., Akerlof, C., Wheeler, J. C., Odewahn, S., & Terrazas, E. 2007b, CBET, 1185, 1

Quimby, R., Yuan, F., Akerlof, C., Wheeler, J. C., Odewahn, S., & Westfall, A. 2007c, CBET, 1124, 1

Quimby, R., Yuan, F., Akerloff, C., Wheeler, J. C., Shetrone, M., Terrazas, E., & Riley, V. 2007d, CBET, 1106, 1

Quimby, R. M. 2006, PhD thesis, University of Texas, USA

Quimby, R. M., Aldering, G., Wheeler, J. C., Höflich, P., Akerlof, C. W., & Rykoff, E. S. 2007e, ApJ, 668, L99

Quimby, R. M., et al. 2006b, ApJ, 640, 402

Quimby, R. M., Wheeler, J. C., Höflich, P., Akerlof, C. W., Brown, P. J., & Rykoff, E. S. 2007f, ApJ, 666, 1093

Racusin, J. L., et al. 2008a, GCN, 8057

Racusin, J. L., et al. 2008b, GCN, 8344

Racusin, J. L., et al. 2008c, Nature, 455, 183

Racusin, J. L., Liang, E. W., Burrows, D. N., Falcone, A., Sakamoto, T., Zhang, B. B., Zhang, B., Evans, P., & Osborne, J. 2009, ApJ, 698, 43

Rees, M. J. & Meszaros, P. 1998, ApJ, 496, L1

Rex, J., Cenko, S. B., Li, W., & Filippenko, A. V. 2009, CBET, 1813, 1

Riess, A. G., et al. 1998, AJ, 116, 1009

Romano, P., et al. 2006, A&A, 450, 59

Rossi, A., et al. 2010, in preparation

Rossi, A., Clemens, C., Greiner, J., Yoldas, A., Kruehler, T., Filgas, R., Yoldas, A. K., & Szokoly, G. 2008, GCN, 8296

Ruiz-Velasco, A. E., et al. 2007, ApJ, 669, 1

Rujopakarn, W., Guver, T., & Smith, D. A. 2008, GCN, 7792

Rujopakarn, W. & Rykoff, E. S. 2008a, GCN, 7846

Rujopakarn, W. & Rykoff, E. S. 2008b, GCN, 8056

Rumyantsev, V., Antoniuk, K., & Pozanenko, A. 2008, GCN, 7974

Rumyantsev, V. & Pozanenko, A. 2008, GCN, 7869

Rykoff, E. S. 2008a, GCN, 8343

Rykoff, E. S. 2008b, GCN, 8436

Rykoff, E. S., et al. 2005a, ApJ, 631, 1032

Rykoff, E. S., et al. 2009, ApJ, 702, 489

Rykoff, E. S., et al. 2006, ApJ, 638, L5

Rykoff, E. S. & Rujopakarn, W. 2008, GCN, 7593

Rykoff, E. S. & Schaefer, B. E. 2008, GCN, 7935

Rykoff, E. S., et al. 2005b, ApJ, 631, L121

Rykoff, E. S., Yuan, F., & McKay, T. A. 2008, GCN, 8293

Rykoff, E. S., Yuan, F., Schaefer, B. E., Swan, H., & Quimby, R. 2007a, GCN, 6987

Rykoff, E. S., Yuan, F., Schaefer, B. E., Swan, H., & Quimby, R. 2007b, GCN, 6992

Sakamoto, T., et al. 2008a, GCN, 7938

Sakamoto, T., et al. 2008b, GCN, 8539

Sakamoto, T., et al. 2008c, GCN, 8292

Sakamoto, T., et al. 2008d, GCN, 8435

Sakamoto, T., et al. 2008e, ApJ, 679, 570

Sakamoto, T., et al. 2009, ApJ, 693, 922

Salvaterra, R., et al. 2009, Nature, 461, 1258

Sari, R. & Mészáros, P. 2000, ApJ, 535, L33

Sari, R. & Piran, T. 1999, ApJ, 520, 641

Sari, R., Piran, T., & Halpern, J. P. 1999, ApJ, 519, L17

Scargle, J. D. 1998, ApJ, 504, 405

Schady, P., et al. 2007, MNRAS, 380, 1041

Schaefer, B. E. & Guver, T. 2008, GCN, 7538

Schaller, G., Schaerer, D., Meynet, G., & Maeder, A. 1992, A&AS, 96, 269

Schlegel, D. J., Finkbeiner, D. P., & Davis, M. 1998, ApJ, 500, 525

Schmidt, B. P., Kirshner, R. P., Eastman, R. G., Grashuis, R., dell'Antonio, I., Caldwell, N., Foltz, C., Huchra, J. P., & Milone, A. A. E. 1993, Nature, 364, 600

Schwartz, D. A., et al. 2000, ApJ, 540, L69

Schwarzschild, M. & Härm, R. 1959, ApJ, 129, 637

Sheffer, Y., Prochaska, J. X., Draine, B. T., Perley, D. A., & Bloom, J. S. 2009, ApJ, 701, L63

Silverman, J. M., Ganeshalingam, M., & Filippenko, A. V. 2007, CBET, 1075, 1

Sim, S. A., Sauer, D. N., Röpke, F. K., & Hillebrandt, W. 2007, MNRAS, 378, 2

Simon, J. D., et al. 2009, ApJ, 702, 1157

Skrutskie, M. F., et al. 2006, AJ, 131, 1163

Smith, J. A., et al. 2002a, AJ, 123, 2121

Smith, J. A., et al. 2002b, AJ, 123, 2121

Smith, N., Chornock, R., Li, W., Ganeshalingam, M., Silverman, J. M., Foley, R. J., Filippenko, A. V., & Barth, A. J. 2008, ApJ, 686, 467

Smith, N., et al. 2007, ApJ, 666, 1116

Smith, N. & McCray, R. 2007, ApJ, 671, L17

Stamatikos, M., et al. 2008, GCN, 7852

Stanek, K. Z., et al. 2003, ApJ, 591, L17

Stanishev, V., et al. 2007, A&A, 469, 645

Stetson, P. B. 1987, PASP, 99, 191

Stritzinger, M. 2008, CBET, 1638, 3

Struble, M. F. & Rood, H. J. 1999, ApJS, 125, 35

Tagliaferri, G., et al. 2005, Nature, 436, 985

Tanaka, M., Kawabata, K. S., Maeda, K., Hattori, T., & Nomoto, K. 2008, ApJ, 689, 1191

Tanaka, M., et al. 2009, ArXiv e-prints

Tanvir, N. R., et al. 2009, Nature, 461, 1254

Thoene, C. C., de Ugarte Postigo, A., Vreeswijk, P. M., Malesani, D., & Jakobsson, P. 2008a, GCN, 8058

Thoene, C. C., Malesani, D., Vreeswijk, P. M., Fynbo, J. P. U., Jakobsson, P., Ledoux, C., & Smette, A. 2008b, GCN, 7602

Thrasher, P., Winslow, D., & Li, W. 2007, CBET, 1067, 2

Tody, D. 1993, in Astronomical Society of the Pacific Conference Series, Vol. 52, Astronomical Data Analysis Software and Systems II, ed. R. J. Hanisch, R. J. V. Brissenden, & J. Barnes, 173

Tueller, J., et al. 2008a, GCN, 7604

Tueller, J., et al. 2008b, GCN, 7806

Turatto, M., Benetti, S., Cappellaro, E., Danziger, I. J., Della Valle, M., Gouiffes, C., Mazzali, P. A., & Patat, F. 1996, MNRAS, 283, 1

Turatto, M., Bufano, F., Agnoletto, I., Inserra, C., Pastorello, A., & Benetti, S. 2009, CBET, 1877, 1

Uenishi, T., Nomoto, K., & Hachisu, I. 2003, ApJ, 595, 1094

Valenti, S., et al. 2008, ApJ, 673, L155

Vestrand, W. T., et al. 2005, Nature, 435, 178

Vestrand, W. T., et al. 2006, Nature, 442, 172

Vink, J. S., de Koter, A., & Lamers, H. J. G. L. M. 2001, A&A, 369, 574

Vinko, J., Yuan, F., Marion, H., Quimby, R., Chamarro, D., Sisson, M. D., Akerlof, C., Wheeler, J. C., & Chatzopoulos, E. 2009a, CBET, 1837, 1

Vinko, J., et al. 2009b, CBET, 1901, 1

Vreeswijk, P., Malesani, D., Fynbo, J., Jakobsson, P., Thoene, C., Sollerman, J., Watson, D., & Milvang-Jensen, B. 2008, GCN, 8301

Wang, L., et al. 2003, ApJ, 591, 1110

Wang, L., Baade, D., Höflich, P., Wheeler, J. C., Kawabata, K., & Nomoto, K. 2004, ApJ, 604, L53

Wang, X. Y., Cheng, K. S., Dai, Z. G., & Lu, T. 2005, A&A, 439, 957

Ward, P. & Ziaeepour, H. 2008, GCN, 7941

Wellstein, S. & Langer, N. 1999, A&A, 350, 148

Williams, G. G. & Milne, P. A. 2007, GCN, 6995

Williams, R., Mason, E., Della Valle, M., & Ederoclite, A. 2008, ApJ, 685, 451

Willingale, R., et al. 2007, ApJ, 662, 1093

Willott, C. J., McLure, R. J., & Jarvis, M. J. 2003, ApJ, 587, L15

Woosley, S. E. 1993, ApJ, 405, 273

Woosley, S. E., Blinnikov, S., & Heger, A. 2007, Nature, 450, 390

Woosley, S. E. & Bloom, J. S. 2006, ARA&A, 44, 507

Woosley, S. E., Heger, A., & Weaver, T. A. 2002, Reviews of Modern Physics, 74, 1015

Woosley, S. E. & Weaver, T. A. 1994, ApJ, 423, 371

Xin, L. P., et al. 2008, GCN, 7814

Yamanaka, M., et al. 2009, ApJ, 707, L118

Yamaoka, H., Nomoto, K., Shigeyama, T., & Thielemann, F.-K. 1992, ApJ, 393, L55

Yoon, S. & Langer, N. 2005, A&A, 435, 967

Yost, S. A., et al. 2007, ApJ, 669, 1107

Yuan, F., et al. 2007a, ATEL, 1212

Yuan, F. & Akerlof, C. W. 2008, ApJ, 677, 808

Yuan, F., Aretakis, J., Akerlof, C., & Quimby, R. 2007b, ATEL, 1217

Yuan, F., Aretakis, J., Akerlof, C., & Quimby, R. 2007c, CBET, 1069, 1

Yuan, F., Aretakis, J., Akerlof, C., Quimby, R., & Wheeler, J. C. 2007d, ATEL, 1224

Yuan, F., Aretakis, J., Akerlof, C., Quimby, R., Wheeler, J. C., Caldwell, J., Terrazas, E., & Riley, V. 2007e, CBET, 1089, 1

Yuan, F., Chamarro, D., Sisson, M. D., Uecker, A., Akerlof, C., McKay, T., Quimby, R., & Wheeler, J. C. 2008a, ATEL, 1615

Yuan, F., Quimby, R., Akerlof, C., & Wheeler, J. C. 2007f, ATEL, 1321

Yuan, F., Quimby, R., Akerlof, C., & Wheeler, J. C. 2007g, CBET, 1157, 1

Yuan, F., Quimby, R., Akerlof, C., Wheeler, J. C., Odewahn, S., & Terrazas, E. 2008b, CBET, 1206, 1

Yuan, F., Quimby, R., Akerlof, C., Wheeler, J. C., Rostopchin, S., & Terrazas, E. 2007h, CBET, 1169, 1

Yuan, F., Quimby, R., Akerlof, C., Wheeler, J. C., Shetrone, M., & Deglman, F. 2007i, CBET, 1178, 1

Yuan, F., Quimby, R., Aretakis, J., Akerlof, C., & Wheeler, J. C. 2007j, ATEL, 1255

Yuan, F., Quimby, R., Aretakis, J., Akerlof, C., & Wheeler, J. C. 2007k, ATEL, 1280

Yuan, F., Quimby, R., Aretakis, J., Akerlof, C., & Wheeler, J. C. 2007l, CBET, 1138, 1

Yuan, F., Quimby, R., Aretakis, J., Akerlof, C., Wheeler, J. C., Caldwell, J., Riley, V., & Terrazas, E. 2007m, CBET, 1112, 1

Yuan, F., Quimby, R., Aretakis, J., Akerlof, C., Wheeler, J. C., & Rau, A. 2007n, CBET, 1136, 1

Yuan, F., Quimby, R., Aretakis, J., Akerlof, C., Wheeler, J. C., Rau, A., & The ROTSE Collaboration. 2007o, ATEL, 1277

Yuan, F., Quimby, R., Chamarro, D., Sisson, M. D., Akerlof, C., & Wheeler, J. C. 2008c, ATEL, 1556

Yuan, F., Quimby, R., Chamarro, D., Sisson, M. D., Akerlof, C., & Wheeler, J. C. 2008d, CBET, 1273, 1

Yuan, F., Quimby, R., Chamarro, D., Sisson, M. D., Akerlof, C., Wheeler, J. C., Caldwell, J., & Riley, V. 2008e, CBET, 1314, 1

Yuan, F., Quimby, R., Chamarro, D., Sisson, M. D., Akerlof, C., Wheeler, J. C., Rostopchin, S., & Deglman, F. 2008f, CBET, 1353, 1

Yuan, F., Quimby, R., Chamarro, D., Sisson, M. D., Akerlof, C., Wheeler, J. C., Shetrone, M., & Terrazas, E. 2008g, CBET, 1395, 1

Yuan, F., Quimby, R., Chamarro, D., Sisson, M. D., Akerlof, C., Wheeler, J. C., & The ROTSE Collaboration. 2008h, ATEL, 1402

Yuan, F., Quimby, R., Chamarro, D., Sisson, M. D., Uecker, A., Akerlof, C., & Wheeler, J. C. 2008i, CBET, 1639, 1

Yuan, F., Quimby, R., Chamarro, D., Sisson, M. D., Uecker, A., Akerlof, C., Wheeler, J. C., Caldwell, J., & Westfall, A. 2008j, CBET, 1513, 1

Yuan, F., Quimby, R., Chamarro, D., Sisson, M. D., Uecker, A., Akerlof, C., Wheeler, J. C., Odewahn, S., & Westfall, A. 2008k, CBET, 1532, 1

Yuan, F., Quimby, R., Chamarro, D., Uecker, A., Sisson, M. D., Akerlof, C., & Wheeler, J. C. 2008l, ATEL, 1690

Yuan, F., Quimby, R., Chamarro, D., Uecker, A., Sisson, M. D., Akerlof, C., & Wheeler, J. C. 2008m, ATEL, 1702

Yuan, F., Quimby, R., Chamarro, D., Uecker, A., Sisson, M. D., Akerlof, C., & Wheeler, J. C. 2008n, CBET, 1502, 1

Yuan, F., Quimby, R., Chamarro, D., Uecker, A., Sisson, M. D., Akerlof, C., Wheeler, J. C., Odewahn, S., & Riley, V. 2008o, CBET, 1505, 1

Yuan, F., et al. 2008p, CBET, 1492, 3

Yuan, F., Quimby, R., McKay, T., Chamarro, D., Sisson, M. D., Akerlof, C., & Wheeler, J. C. 2008q, ATEL, 1515

Yuan, F., et al. 2008r, CBET, 1462, 1

Yuan, F., Quimby, R., Peters, C., & Thorstensen, J. 2007p, CBET, 1059, 1

Yuan, F., et al. 2008s, CBET, 1262, 1

Yuan, F., et al. 2008t, ATEL, 1389

Yuan, F., Quimby, R., Sisson, M. D., Chamarro, D., Akerlof, C., & Wheeler, J. C. 2008u, CBET, 1245, 1

Yuan, F., Quimby, R., Uecker, A., Chamarro, D., Sisson, M. D., Akerlof, C., Wheeler, J. C., Caldwell, J., & Terrazas, E. 2008v, CBET, 1500, 1

Yuan, F., et al. 2010, submitted to ApJ

Yuan, F. & Rujopakarn, W. 2008, GCN, 8536

Yuan, F., et al. 2008w, in American Institute of Physics Conference Series, Vol. 1065, American Institute of Physics Conference Series, ed. Y.-F. Huang, Z.-G. Dai, & B. Zhang, 103–106

Yuan, F., Sisson, M. D., Chamarro, D., Akerlof, C., & Quimby, R. 2008x, ATEL, 1421

Yuan, F., Sisson, M. D., Chamarro, D., Akerlof, C., Quimby, R., Wheeler, J. C., Blondin, S., & Brown, W. 2008y, CBET, 1308, 1

Yuan, F., Vinko, J., Quimby, R., Chamarro, D., Sisson, M. D., Akerlof, C., Pandey, S. B., Wheeler, J. C., & Chatzopoulos, E. 2009a, ATEL, 2128

Yuan, F., Vinko, J., Quimby, R., Chamarro, D., Sisson, M. D., Akerlof, C., Pandey, S. B., Wheeler, J. C., & Chatzopoulos, E. 2009b, CBET, 1875, 1

Yuan, F., Vinko, J., Quimby, R., Chamarro, D., Sisson, M. D., Akerlof, C., Wheeler, J. C., & Chatzopoulos, E. 2009c, CBET, 1775, 1

Yuan, F., Vinko, J., Quimby, R., Chamarro, D., Sisson, M. D., Akerlof, C., Wheeler, J. C., Chatzopoulos, E., & The ROTSE Collaboration. 2009d, ATEL, 2018

Yuan, F., et al. 2009e, CBET, 1666, 1

Zabludoff, A. I., Huchra, J. P., & Geller, M. J. 1990, ApJS, 74, 1

Zhang, B., Fan, Y. Z., Dyks, J., Kobayashi, S., Mészáros, P., Burrows, D. N., Nousek, J. A., & Gehrels, N. 2006, ApJ, 642, 354

Zhang, B., Kobayashi, S., & Mészáros, P. 2003, ApJ, 595, 950

Zhang, B., et al. 2009, ApJ, 703, 1696

Zhang, B.-B., Liang, E.-W., & Zhang, B. 2007, ApJ, 666, 1002

Zhang, X.-H. 2009, Research in Astronomy and Astrophysics, 9, 213

Ziaeepour, H., et al. 2008, GCN, 7936